

AFRL-MN-EG-TR-1999-7054

PENETRATOR CASE FRACTURE PREDICTIVE TECHNOLOGY:
VOLUME I-- DYNAMIC FRACTURE MECHANICS METHODOLOGY

C. H. POPELAR

J. D. WALKER

C. E. ANDERSON, Jr,

G. R. JOHNSON

S. R. BEISSEL

Southwest Research Institute

P. O. Drawer 28510

San Antonio, TX 78228-0510



Alliant Techsystems Inc.

600 Second Street N.E.

Hopkins, MN 55343

CONTRACT NO. FO8630-96-C-0029

JUNE 1999

FINAL REPORT FOR PERIOD MAY 1996 - JUNE 1999

Approved for public release; distribution is unlimited.

AIR FORCE RESEARCH LABORATORY, MUNITIONS DIRECTORATE

Air Force Materiel Command ■ United States Air Force ■ Eglin Air Force Base

DTIC QUALITY INSPECTED 4

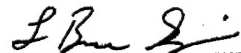
19990913 045

NOTICE

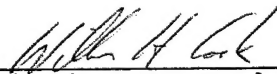
When Government drawings, specifications, or other data are used for any purpose other than in connection with a definitely Government-related procurement, the United States Government incurs no responsibility or any obligation whatsoever. The fact that the Government may have formulated or in any way supplied the said drawings, specifications, or other data, is not to be regarded by implication, or otherwise in any manner construed, as licensing the holder, or any other person or corporation; or as conveying any rights or permission to manufacture, use, or sell any patented invention that may in any way be related thereto.

This technical report is releasable to the National Technical Information Services (NTIS). At NTIS it will be available to the general public, including foreign nations.

This technical report has been reviewed and is approved for publication.



L. Bruce Simpson
Technical Director
Assessments and Demonstrations Division



William H. Cook
Program Manager

If your address has changed, if you wish to be removed from our mailing list, or if your organization no longer employs the addressee, please notify AFRL/MNAC, Eglin AFB FL 32542-6810, to help us maintain a current mailing list.

Do not return copies of this report unless contractual obligations or notice on a specific document requires that it be returned.

REPORT DOCUMENTATION PAGE

Form Approved
OMB No. 0704-0188

Public reporting burden for this collection of information is estimated to average 1 hour per response, including the time for reviewing instructions, searching existing data sources, gathering and maintaining the data needed, and completing and reviewing the collection of information. Send comments regarding this burden estimate or any other aspect of this collection of information, including suggestions for reducing this burden, to Washington Headquarters Services, Directorate for Information Operations and Reports, 1215 Jefferson Davis Highway, Suite 1204, Arlington, VA 22202-4302, and to the Office of Management and Budget, Paperwork Reduction Project (0704-0188), Washington, DC 20503.

1. AGENCY USE ONLY (Leave Blank)			2. REPORT DATE 6/30/99	3. REPORT TYPE AND DATES COVERED Final Report: May 1996 - June 1999
4. TITLE AND SUBTITLE Penetrator Case Fracture Predictive Technology: Volume 1—Dynamic Fracture Mechanics Methodology			5. FUNDING NUMBERS Contract # F08630-96-C-0029 JON: 25020724	
6. AUTHOR(S) C. H. Poplar, J. D. Walker, C. E. Anderson, Jr., G. R. Johnson, S. R. Beissel			8. PERFORMING ORGANIZATION REPORT NUMBER SwRI Report 18-8037/001	
7. PERFORMING ORGANIZATION NAME(S) AND ADDRESS(ES) Southwest Research Institute P.O. Drawer 28510 San Antonio, TX 78228-0510			10. SPONSORING/MONITORING AGENCY REPORT NUMBER AFRL-MN-EG-TR-1999-7054	
9. SPONSORING/MONITORING AGENCY NAME(S) AND ADDRESS(ES) Air Force Research Laboratory Munitions Directorate 101 West Eglin Blvd. Eglin AFB, FL 32542			11. SUPPLEMENTARY NOTES	
12a. DISTRIBUTION/AVAILABILITY STATEMENT Approved for Public Release/Unlimited Distribution			12b. DISTRIBUTION CODE	
13. ABSTRACT (Maximum 200 words) A dynamic fracture mechanics methodology has been implemented into the Lagrangian finite-element hydrocode EPIC. The generalized energy release rate T^* was assumed to be a measure of the crack driving force. This representation for the crack driving force was selected because its generality includes elastic-plastic behavior and inertial effects. In addition to the introduction of the crack driving force, a nodal release algorithm to model the formation of traction-free surfaces produced by a propagating crack was incorporated into EPIC. The dynamic fracture mechanics enhanced EPIC code was used in the generation phase mode to deduce the dynamic fracture toughness from measurements made during high-loading-rate fracture tests of AISI 4340 and AF 1410 steel specimens. The internal consistency of the approach and algorithms was demonstrated by performing application phase analyses of these fracture tests to predict the crack growth history. A second set of experiments was devised, using a different experimental arrangement and specimen geometry, to demonstrate the predictive capability of the methodology. A new dynamic test method was developed—referred to as a dynamic three-point bend test—in which an instrumented, precracked three-point bend specimen is dynamically loaded through a transmitter bar that is struck by a striker bar fired from a gas gun. The length and speed of the striker bar control the duration and intensity of the loading pulse. A finite element model of the experiment was developed. Numerical predictions, using the fracture toughness determined from the independent coupled pressure bar tests, are in relatively good agreement with measured crack growth and strain gage histories, thereby validating the dynamic fracture mechanics computational methodology implemented into EPIC.				
14. SUBJECT TERMS dynamic fracture, fracture mechanics, energy release rate, finite element, EPIC, crack propagation, nodal release, AISI 4340 steel, AF1410 steel, fracture toughness, generation phase, application phase, couple pressure bar test, dynamic three-point bend test, fracture specimen, crack speed, crack growth, crack driving force			15. NUMBER OF PAGES 139	
			16. PRICE CODE	
17. SECURITY CLASSIFICATION OF REPORT Unclassified	18. SECURITY CLASSIFICATION OF THIS PAGE Unclassified	19. SECURITY CLASSIFICATION Unclassified	20. LIMITATION OF ABSTRACT UL	

TABLE OF CONTENTS

	Page
1.0	INTRODUCTION AND EXECUTIVE SUMMARY 1
2.0	DYNAMIC FRACTURE MECHANICS METHODOLOGY 4
2.1	Crack Driving Force 4
2.2	Fracture Criterion 6
2.3	Numerical Modeling of Crack Growth 8
3.0	GENERATION PHASE EXPERIMENTS AND ANALYSES 11
3.1	Heat Treatment 11
3.2	Static Fracture Toughness 13
3.3	Dynamic Fracture Apparatus and Testing Procedure 15
3.3.1	Coupled Pressure Bar Apparatus 15
3.3.2	Test Procedure 18
3.4	Dynamic Fracture Data 20
3.5	Data Reduction 27
3.6	Dynamic Fracture Resistance 31
3.6.1	AISI 4340 Fracture Resistance 33
3.6.2	AF 1410 Fracture Resistance 41
4.0	APPLICATION PHASE EXPERIMENTS AND ANALYSIS 46
4.1	Application Phase Test Method 46
4.1.1	Dynamic Three-Point Bend Apparatus 47
4.1.2	Test Procedure 54
4.2	Dynamic Fracture Data 55
4.3	Application Phase Analyses 67
4.3.1	Modeling Considerations 67
4.3.2	Application Phase Results for AISI 4340 68
4.3.3	Generation Phase Analysis of AISI 4340 Specimen 6 78
4.3.4	An Application Phase Analysis for an AF1410 Three-Point Bend Specimen 89
4.4	An Engineering Model for Determination of the Fracture Toughness 92
5.0	CONCLUSIONS 97
6.0	REFERENCES 101
	APPENDIX A: EXPERIMENTAL DATA FOR AISI 4340 AND AF 1410 A-1
	APPENDIX B: APPLICATION PHASE EXPERIMENTAL DATA FOR AISI 4340 STEELB-1 B-1

LIST OF FIGURES

Figure	Page
2.1 Contour and Domain Used for Computing T^* in Equation (2.1).....	5
3.1 Heat Treatment Schedule for AISI 4340 Specimens	12
3.2 Heat Treatment Schedule for AF 1410 Specimens	12
3.3 Tensile Specimen (Dimensions in Inches)	14
3.4 Comparison of Quasi-Static AISI 4340 Stress-Strain Data from Eglin and SwRI.....	14
3.5 Comparison of Quasi-Static AF 1410 Stress-Strain Data from Eglin and SwRI.....	15
3.6 Compact Tension Specimen (Dimensions in Inches)	16
3.7 Coupled Pressure Bar Specimen (Dimensions in Inches)	17
3.8 Schematic Diagram for the Coupled Pressure Bar Apparatus Used in Conducting Dynamic Fracture Tests	19
3.9 Photograph of Coupled Pressure Bar Setup	19
3.10 Measured Load Line Displacement Record for AF 1410 Specimens CPB1 and CPB2	22
3.11 Measured Crack Opening Displacement Record for AF 1410 Specimens CPB1 and CPB2.....	22
3.12 Measured Strain in AF 1410 Specimen CPB1	23
3.13 Measured Strain in AF 1410 Specimen CPB2.....	23
3.14 Measured Load in Upper Pressure Bar and Load Cell.....	24
3.15 Measured Crack Length Histories in AF 1410 Specimens CPB1 and CPB2	24
3.16 Measured Load Line Displacement Records for AISI 4340 CPB Specimens 1 and 2	26
3.17 Measured Crack Opening Displacement Records for AISI 4340 CPB Specimens 1 and 2	26
3.18 Measured Crack Length Histories in AISI 4340 CPB Specimens 1 and 2	27
3.19 Reduced Load Line Displacement Record for AISI 4340 CPB Specimen 1	29
3.20 Reduced Load Line Displacement Record for AISI 4340 CPB Specimen 2	29
3.21 Comparison of Reduced Load Line Displacement Records for AISI 4340 CPB Specimens 1 and 2.....	30
3.22 Comparison of Reduced Crack Opening Displacement Records for AISI 4340 CPB Specimens 1 and 2	30

3.23	Reduced Crack Length-Time Histories for AISI 4340 CPB Specimens 1 and 2.....	31
3.24	Quadratic Fit to the Crack Growth History for AISI 4340 CPB Specimen 2	32
3.25	Predictor-Corrector Algorithm for the Load Point Displacement.....	34
3.26	Comparison of Measured Load Line Displacement and First Approximation for the Load Point Displacement	35
3.27	Comparison of Computed and Measured COD	36
3.28	Variation of T^* with Time for CPB Specimen 2.....	36
3.29	Variation of Fracture Resistance with Crack Speed Determined from CPB Specimen 2 and a Bilinear Fit to Data.....	37
3.30	Variation of Dynamic Fracture Toughness with Crack Speed for CPB Specimen 2... 37	
3.31	Comparison of Dynamic Fracture Resistance for CPB Specimens 1 and 2.....	39
3.32	Bilinear Representations for the Dynamic Fracture Resistance of CPB Specimens 1 and 2	39
3.33	Comparison of Application Phase Analysis Predictions for the Crack Growth History with the Measured History for AISI 4340 CPB Specimen 1	40
3.34	Comparison of Application Phase Analysis Predictions for the Crack Growth History with the Measured History for AISI 4340 CPB Specimen 2	40
3.35	Measured Load Line Displacement for AF 1410 Specimens CPB2 and CPB6.....	42
3.36	Crack Length-Time History for AF 1410 Specimens CPB2 and CPB6	42
3.37	Measured Crack Opening Displacement for AF 1410 Specimens CPB2 and CPB6... 43	
3.38	Comparison of Predicted and Measured COD for AF 1410 Specimen CPB2.....	43
3.39	Comparison of Predicted and Measured COD for AF 1410 Specimen CPB6.....	44
3.40	Deduced Dynamic Fracture Toughness for AF 1410 Steel.....	44
4.1	Schematic of Application Phase Experimental Setup	48
4.2	Machine Drawing of Three-Point Bend Specimen (Dimensions in inches)	48
4.3	Photograph of Dynamic Three-Bend Specimen Identifying Starter Notch, Side Groove and Relief for COD Gage.....	49
4.4	Close-up View Showing Location of Crack Tip Strain Gage Relative to Starter Crack and Side Groove	50
4.5	Close-up View of Hartrun Crack Gage Applied to Specimen	52
4.6	Comparison of Crack Growth Histories Measured in Test 1 Using Hartrun Crack Ladder Gage and Silk Screen Crack Gage	52
4.7	Overall View of Test Setup Showing Test Bench, Gas Gun, Specimen Holder and Instrumentation.....	53
4.8	Close-up View of Test Apparatus	53

4.9	View of Specimen Positioned in the Specimen Holder	54
4.10	Measured Crack Growth History for Specimen 2.....	57
4.11	Measured Variation of Transmitter Bar Strain for Specimen 2	57
4.12	Measured Variation of the Crack Tip Strain for Specimen 2.....	58
4.13	Measured Variation of the Crack Opening Displacement for Specimen 2	58
4.14	Measured Variation of the Strain at the Pin Support for Specimen 2	59
4.15	Measured Variation of the Strain at the Pin Support for Specimen 4.....	61
4.16	Measured Variation of the Transmitter Bar Strain for Specimen 6	62
4.17	Measured Variation of the Crack Tip Strain for Specimen 6.....	62
4.18	Measured Variation of the Strain at the Pin Support for Specimen 6.....	63
4.19	Measured Crack Growth History for Specimen 6.....	63
4.20	Measured Variation of the Crack Opening Displacement for Specimen 6	64
4.21	Measured Strain Near Center of Initial Ligament of Specimen 6.....	64
4.22	Measured Strain at the Root of the Side Groove in Specimen 6.....	65
4.23	Measured Strain at the Loading Face of Specimen 6, 10 mm from Impact Line	65
4.24	Comparison of the Measured Transmitter Bar Strain for Specimen 2 with that for Specimen 6 Multiplied by the Ratio of the Impact Speed for Specimen 2 to that for Specimen 6	66
4.25	Typical Mesh Used in Modeling of Dynamic Three Point Bend Test.....	69
4.26	Dynamic Fracture Resistance for AISI 4340	69
4.27	Comparison of Measured and Predicted Crack Growth History for Specimen 2 with Low Threshold Resistance	71
4.28	Comparison of Measured and Predicted Transmitter Bar Strains for Specimen 2 with Low Threshold Resistance	71
4.29	Comparison of Measured and Predicted Crack Tip Strains for Specimen 2 with Low Threshold Resistance	72
4.30	Comparison of Measured and Predicted Crack Opening Displacements for Specimen 2 with Low Threshold Resistance	72
4.31	Comparison of Measured and Predicted Strains at Support for Specimen 2 with Low Threshold Resistance	73
4.32	Comparison of Measured and Predicted Crack Growth Histories for Specimen 2 with High Threshold Resistance	74
4.33	Comparison of Measured and Predicted Transmitter Bar Strains for Specimen 2 with High Threshold Resistance	74

4.34	Comparison of Measured and Predicted Crack Tip Strains for Specimen 2 with High Threshold Resistance.....	75
4.35	Comparison of Measured and Predicted Crack Opening Displacements for Specimen 2 with High Threshold Resistance.....	75
4.36	Comparison of Measured and Predicted Strains at Support for Specimen 2 with High Threshold Resistance.....	76
4.37	Comparison of Measured and Predicted Crack Growth for Specimen 5 with High Threshold Resistance.....	77
4.38	Comparison of Measured and Predicted Transmitter Bar Strains for Specimen 5 with High Threshold Resistance	77
4.39	Comparison of Measured and Predicted Crack Tip Strains for Specimen 5 with High Threshold Resistance.....	79
4.40	Comparison of Measured and Predicted Crack Opening Displacements for Specimen 5 with High Threshold Resistance.....	79
4.41	Comparison of Measured and Predicted Strains at Support for Specimen 5 with High Threshold Resistance.....	80
4.42	Comparison of Measured and Predicted Crack Growth for Specimen 6 with High Threshold Resistance.....	80
4.43	Comparison of Predicted and Measured Transmitter Bar Strains for Specimen 6 with High Threshold Resistance	81
4.44	Comparison of Measured and Predicted Crack Tip Strains for Specimen 6 with High Threshold Resistance.....	81
4.45	Comparison of Measured and Predicted Crack Opening Displacements for Specimen 6 with High Threshold Resistance.....	82
4.46	Comparison of Measured and Predicted Strains at Support for Specimen 6 with High Threshold Resistance.....	82
4.47	Comparison of Measured and Predicted Strains at Top of Specimen 6 for High Threshold Resistance.....	83
4.48	Comparison of Measured and Predicted Strain in Side Groove for Specimen 6 with the High Threshold Resistance.....	83
4.49	Comparison of Measured and Predicted Strain Near Center of Initial Ligament for Specimen 6 with the High Threshold Resistance.....	84
4.50	Comparison of Measured and Predicted Transmitter Bar Strains from Generation Phase Analysis of Specimen 6	85
4.51	Comparison of Measured and Predicted Crack Tip Strains from Generation Phase Analysis of Specimen 6.....	85
4.52	Comparison of Measured and Predicted Crack Opening Displacement from Generation Phase Analysis of Specimen 6.....	86

4.53	Comparison of Measured and Predicted Strains at Support of Specimen 6 from Generation Phase Analysis.....	86
4.54	Comparison of Measured and Predicted Strains at the Top Surface of Specimen 6 from Generation Phase Analysis	87
4.55	Comparison of Measured and Predicted Strains in Side Groove from Generation Phase Analysis of Specimen 6	87
4.56	Comparison of Measured and Predicted Strains Near Center of Initial Ligament from Generation Phase Analysis of Specimen 6.....	88
4.57	Comparison of EPIC Computation for the Crack Mouth Opening Displacement with that Given by TADA, <i>et al.</i> [13].	89
4.58	Comparison of EPIC Computation for the Load Point Displacement with that Given by TADA, <i>et al.</i> [13].	90
4.59	Estimate for the Dynamic Fracture Toughness for AF 1410 based upon Static and Couple Pressure Bar Fracture Tests.	91
4.60	Predicted Crack Growth History for AF 1410 Three Point Bend Specimen with an Impact Speed of 50 m/s.....	91
4.61	Predicted Transmitter Bar Strain for AF 1410 Three-Point Bend Specimen with an Impact Speed of 50 m/s	92
4.62	Comparison of Measured and Predicted Crack Opening Displacement for Three-Point Bend Specimen 2.....	94
4.63	Comparison of Measured and Predicted Crack Opening Displacement for Three-Point Bend Specimen 4.....	94
4.64	Comparison of Measured and Predicted Crack Opening Displacement for Three-Point Bend Specimen 5.....	95
4.65	Comparison of Measured and Predicted Crack Opening Displacement for Three-Point Bend Specimen 6.....	95
4.66	Comparison of Present Data with that of Zehnder and Rosakis [11] for AISI 4340 ...	96
A1.	Measured Stress-Strain Data for AISI 4340 Specimen No. 1-1.....	A-3
A2.	Measured Stress-Strain Data for AISI 4340 Specimen No. 1-2.....	A-3
A3.	Measured Stress-Strain Data for AISI 4340 Specimen No. 2-1.....	A-4
A4.	Measured Stress-Strain Data for AISI 4340 Specimen No. 2-2.....	A-4
A5.	Measured Stress-Strain Data for AISI 4340 Specimen No. 3-1.....	A-5
A6.	Measured Stress-Strain Data for AISI 4340 Specimen No. 3-2.....	A-5
A7.	Measured Stress-Strain Data for AF 1410 Specimen No. 1410T61	A-6
A8.	Measured Stress-Strain Data for AF 1410 Specimen No. 1410T11	A-6
A9.	Measured Stress-Strain Data for AF 1410 Specimen No. 1410T31	A-7

A10. Measured Load Versus CMOD in ASTM E399 Test of AISI 4340 Specimen No. 8037-7.....	A-7
A11. Measured Load Versus CMOD in ASTM E399 Test of AISI 4340 Specimen No. 8037-8.....	A-8
A12. Measured Load Versus CMOD in ASTM E399 Test of AF 1410 Specimen No. CT-1.....	A-8
A13. Measured Load Versus CMOD in ASTM E399 Test of AF 1410.....	A-9
A14. Machine Drawing of Coupler (Dimensions in Inches)	A-10
A15. Machine Drawing of Loading Plates (Dimensions in Inches)	A-11
A16. Measured Load Line Displacement in AISI 4340 Specimen 4.....	A-12
A17. Measured Strain in AISI 4340 Specimen 4.....	A-12
A18. Measured Crack Length-Time History in AISI 4340 Specimens 3 and 4	A-13
A19. Measured Load in Bar for Test of AISI 4340 Specimens 3 and 4	A-13
A20. Measured Strain in AISI 4340 Specimen 3.....	A-14
A21. Measured Load Line Displacement in AISI 4340 Specimens 5 and 6.....	A-14
A22. Measured Crack Opening Displacement in AISI 4340 Specimens 5 and 6.....	A-15
A23. Measured Strain in AISI 4340 Specimens 5 and 6.....	A-15
A24. Bar Load and Load Cell Records for Test of AISI 4340 Specimens 5 and 6	A-16
A25. Measured Crack Length-Time History for AISI Specimens 5 and 6.....	A-16
A26. Measured Load Line Displacement in AF 1410 Specimens CPB5 and CPB6	A-17
A27. Measured Crack Opening Displacement in AF 1410 Specimens CPB5 and CPB6	A-17
A28. Measured Strain AF 1410 Specimens CPB5 and CPB6	A-18
A29. Measured Crack Length-Time Histories of AF 1410 Specimens CPB5 and CPB6	A-18
A30. Bar Load and Load Cell Records for Test of AF 1410 Specimens CPB5 and CPB6	A-19
A31. Reduced Load Line Displacement Data for AF 1410 Specimen CPB1.....	A-19
A32. Reduced Strain Data for AF 1410 Specimen CPB1.....	A-20
A33. Reduced Load Line Displacement Data for AF 1410 Specimen CPB2.....	A-20
A34. Reduced Crack Opening Displacement Data for AF 1410 Specimen CPB2.....	A-21
A35. Reduced Strain Data for AF 1410 Specimen CPB2.....	A-21
A36. Reduced Crack Length-Time Histories of AF 1410 Specimens CPB1 and CPB2 ..	A-22
A37. Reduced Load Displacement Data for AF 1410 Specimen CPB5	A-22
A38. Reduced Crack Opening Displacement Data for AF 1410 Specimen CPB5	A-23

A39. Reduced Strain Data for AF 1410 Specimen CPB5.....	A-23
A40. Reduced Load Line Displacement Data for AF 1410 Specimen CPB6.....	A-24
A41. Reduced Crack Opening Displacement Data for AF 1410 Specimen CPB6.....	A-24
A42. Reduced Strain Data for AF 1410 Specimen CPB6.....	A-25
A43. Reduced Crack Length-Time Histories of AF 1410 Specimens CPB5 and CPB6 ..	A-25
B-1. Measured Crack Length History for Specimen 1	B-2
B-2. Measured Transmitter Bar Strain for Specimen 1	B-2
B3. Measured Crack Tip Strain for Specimen 1	B-3
B-4. Measured Crack Opening Displacement for Specimen 1	B-3
B-5. Measured Crack Length History for Specimen 3.....	B-4
B-6. Measured Transmitter Bar Strain for Specimen 3.....	B-4
B-7. Measured Crack Tip Strain for Specimen 3	B-5
B-8. Measured Crack Opening Displacement for Specimen 3	B-5
B-9. Measured Strain at Support for Specimen 3.....	B-6
B-10. Measured Crack Length History for Specimen 4.....	B-6
B-11. Measured Transmitter Bar Strain for Specimen 4.....	B-7
B-12. Measured Crack Tip Strain for Specimen 4.....	B-7
B-13. Measured Crack Opening Displacement for Specimen 4	B-8
B-14. Measured Strain at Support for Specimen 4.....	B-8
B-15. Measured Crack Length History for Specimen 5.....	B-9
B-16. Measured Transmitter Bar Strain for Specimen 5.....	B-9
B-17. Measured Crack Tip Strain for Specimen 5	B-10
B-18. Measured Crack Opening Displacement for Specimen 5	B-10
B-19. Measured Strain at Support for Specimen 5.....	B-11

LIST OF TABLES

Table	Page
3.1 Summary of Dynamic Fracture Tests Performed and Data Captured.....	21
4.1 Summary of Application Phase Dynamic Three-Point Bend Tests	56
A1. Tensile Properties for AISI 4340 and AF 1410 Steels.....	A-2

1.0 INTRODUCTION AND EXECUTIVE SUMMARY

Crucial to the performance of a deep earth penetrator is the preservation of its shape and integrity for delivery of its payload. Therefore, high strength materials are required for these casings. However, high strength in metals is often achieved at the expense of ductility and fracture toughness. It has been observed that high strength casings of deep earth penetrators are subject to crack initiation, followed by rapid crack propagation and fracture that result in loss of penetrator performance. Therefore, optimum performance requires a casing material that possesses sufficient strength to resist deformation, and toughness to resist fracture during penetration. While laboratory experiments can be used to measure and rank the intrinsic strength (i.e., yield and/or ultimate) and fracture toughness of casing materials, the loads on a deep earth penetrator are quite complex, and there is currently no direct means—aside from extensive and costly experimental testing—for establishing the optimum design of strength and fracture toughness for a casing material. Therefore, a capability to perform design studies to assess the potential trade-off of casing strength and fracture toughness is required. Furthermore, it is also desirable to have a methodology that directly relates laboratory strength and fracture toughness measurements to penetrator performance.

The production hydrocode EPIC is often used in the design and analysis of penetrators. This code is capable of performing sophisticated nonlinear dynamic stress and deformation analyses for a variety of loading scenarios. However, heretofore, it did not contain a fracture mechanics capability for predicting influence of dynamic crack initiation and propagation on the overall performance of a penetrator.

The overall objective of this research effort was to develop and implement a validated dynamic fracture mechanics methodology into the explicit finite element hydrocode EPIC. Such a computational tool would enable a designer to:

- evaluate dynamic crack propagation/arrest in a penetrator case during penetration;
- evaluate overall penetrator performance during penetration;
- make informed trade-off decisions of material strength versus fracture toughness for optional design and performance of deep-earth penetrators; and thus,
- provide the basis for rational design and material selection decisions.

To achieve this objective, an integrated computational and experimental effort was initiated. Dynamic fracture mechanics algorithms were developed and implemented into EPIC. The first essential algorithm computes the crack driving force which is taken in the form of a generalized energy release rate. The second algorithm provides for the release of nodes to simulate crack propagation. This algorithm permits two types of related analyses to be performed. The first, termed generation phase analysis, enables deducing the dynamic fracture toughness from measured data in laboratory dynamic fracture tests. The second, termed application phase analysis, permits predicting the crack growth history for a structure when the loading and dynamic fracture toughness are prescribed. The nodal release algorithm was generalized to an element failure algorithm to facilitate computationally efficient three-dimensional dynamic crack propagation analyses.

Two types of dynamic fracture experiments were conducted to establish the dynamic fracture toughness of a material and to validate the dynamic fracture mechanics methodology implemented into EPIC. Both sets of experiments included instrumented fracture specimens that were dynamically loaded. The instrumentation includes crack growth gages for measuring the crack growth-time history, eddy current sensors for measuring the crack opening displacement (all tests) and the load line displacement (one set of tests), and strain gages.

The first set of dynamic fracture experiments (coupled pressure bar tests), using a modified compact tension specimen, was conducted on AISI 4340 and AF 1410 steels; representing high strength, moderate toughness and high strength, high toughness materials, respectively. The dynamic-fracture-mechanics-enhanced version of EPIC was used to perform generation phase analyses of these tests to deduce the dynamic fracture toughness for each material. The methodology is demonstrated to be self-consistent by using the measured load and deduced dynamic fracture toughness as inputs into an application phase analysis to reproduce the measured crack propagation histories.

A second set of experiments was devised, using a different experimental arrangement and specimen geometry, to demonstrate the predictive capability of the methodology. A new dynamic test method was developed—referred to as a dynamic three-point bend test—in which an instrumented, precracked three-point bend specimen is dynamically loaded through a transmitter bar that is struck by a striker bar fired from a gas gun. The length and speed of the striker bar control the duration and intensity of the loading pulse. A finite element model of the experiment was developed. Numerical predictions, using the fracture toughness determined

from the independent coupled pressure bar tests, are in relatively good agreement with measured crack growth and strain gage histories; thereby validating the dynamic fracture mechanics computational methodology implemented into EPIC.

A parametric study was conducted to demonstrate this new computational capability. The example problem is a generic deep earth penetrator striking a concrete target at 305 m/s at 20° to the normal. A through-wall crack is assumed at one of four locations in the casing material (AISI 4340 steel), and the subsequent crack growth histories are computed for each case.

The report is divided into two volumes. Volume I contains a description of the dynamic fracture mechanics methodology, and generation and application phase experiments and analyses. The associated numerical simulations and results are also documented in this volume. Volume II contains a description of the numerical algorithms and their implementation into EPIC, as well as the details and results of the parametric study.

2.0 DYNAMIC FRACTURE MECHANICS METHODOLOGY

This section provides the theoretical basis for the dynamic fracture mechanics approach used in this program. Fracture mechanics requires that the governing equations of motion, constitutive relations, kinematic relations, and initial and boundary conditions be supplemented with a fracture criterion. While the crack is propagating, the fracture criterion demands that there be equilibrium between the force tending to drive the crack—the crack driving force—and the critical value of this parameter which is considered to be a measure of the material's intrinsic resistance to fracture. The fracture criterion provides the equation of motion for the propagating crack tip. Because of the complexity of dynamic fracture mechanics problems, numerical solutions are required for all but the simplest ones.

In the following, descriptions for the crack driving force and the associated fracture criterion are presented. Modeling crack growth within the framework of a finite element analysis is achieved through a nodal release algorithm that simulates the creation of traction-free surfaces produced by the propagating crack tip. The details of the nodal release algorithm depend upon whether the goal of an analysis is to deduce the fracture resistance from a fracture test—termed a generation phase analysis—or to predict the crack growth history in a structural component—referred to as an application phase analysis.

2.1 Crack Driving Force

The dynamic fracture mechanics methodology used in this development is based upon the rate at which energy is released to the crack tip region. The energy release rate represents the crack driving force and this concept was first used by Griffith in his pioneering work on quasi-static fracture [1]. The energy release rate has also been used previously to quantify dynamic crack propagation and arrest [2]. This choice for the crack driving force also offers numerical computational advantages. For example, its dependence upon precise representations for the field quantities near the crack tip, where numerical inaccuracies are usually the greatest, is not as crucial as for other fracture characterizing parameters.

The most general representation for the energy release rate is the T^* integral due to Atluri [3]. The expression for T^* for the propagation of a plane crack in the x_i -direction is

$$T^* = \int_{\Gamma} \left[(\bar{W} + T) n_i - \sigma_{ij} n_j \frac{\partial u_i}{\partial x_j} \right] d\Gamma - \int_{\Omega} \left[\frac{\partial}{\partial x_i} (\bar{W} + T) - \rho \left(\ddot{u}_i \frac{\partial u_i}{\partial x_i} \right) - \sigma_{ij} \frac{\partial^2 u_i}{\partial x_i \partial x_j} \right] d\Omega \quad (2.1)$$

in which x_i are Cartesian coordinates; Γ is an arbitrary contour extending counterclockwise from the lower crack face ($x_2 = 0^-$) around the crack tip to the upper crack face ($x_2 = 0^+$) as depicted in Figure 2.1; n_i are the components of the unit outward normal to the contour Γ ; Ω is the region bounded by the contour Γ , a vanishing small contour surrounding the crack tip Γ^* , and the crack faces connecting these two contours; repeated subscripts denote summation over the range from $i, j = 1$ to 3 ; a superposed dot indicates a partial derivative with respect to time t , u_i are the displacement components; ρ is the mass density; σ_{ij} is the stress tensor; $T = \rho \dot{u}_i \dot{u}_i / 2$ is the kinetic energy density; and \bar{W} is the stress work density

$$\bar{W} = \int_0^t \sigma_{ij} \dot{\epsilon}_{ij} dt \quad (2.2)$$

This representation for the crack driving force includes elasto-plasticity, strain rate (i.e., viscoplasticity effects) and inertial effects. It can be shown that T^* is independent of the choice for the contour Γ . This independence is a product of the divergence theorem that was used to take T^* , evaluated on a vanishingly small contour surrounding the crack tip, and expand it to the more computationally convenient form of Equation (2.1).

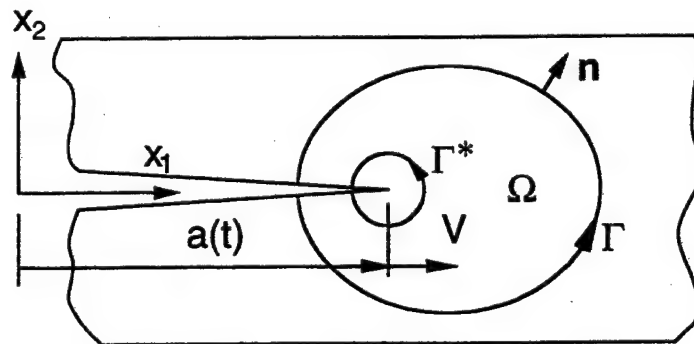


Figure 2.1 Contour and Domain Used for Computing T^* in Equation (2.1).

For a plane fracture problem, in which the x -axis is normal to the crack plane and the z -axis is parallel to and in the direction of crack growth, the unabridged form of Equation (2.1) becomes

$$T^* = \int_{\Gamma} \left[(\bar{W} + T) n_z - \left(\sigma_x n_x \frac{\partial u}{\partial z} + \sigma_z n_z \frac{\partial w}{\partial z} + \tau_{xz} n_x \frac{\partial w}{\partial z} + \tau_{xz} n_z \frac{\partial u}{\partial z} \right) \right] d\Gamma \quad (2.3)$$

$$- \int_{\Omega} \left[\frac{\partial}{\partial z} (\bar{W} + T) - \rho \left(\ddot{u} \frac{\partial u}{\partial z} + \ddot{w} \frac{\partial w}{\partial z} \right) - \left(\sigma_x \frac{\partial^2 u}{\partial x \partial z} + \sigma_z \frac{\partial^2 w}{\partial z^2} + \tau_{xz} \frac{\partial^2 u}{\partial z^2} + \tau_{xz} \frac{\partial^2 w}{\partial x \partial z} \right) \right] d\Omega$$

where u and w are the in-plane displacements in the x and z directions, respectively; n_x and n_z are the directions of the outward normal of the contour Γ ; and σ_x , σ_z and τ_{xz} are the usual in-plane stress components.

Computation of T^* has been incorporated into the numerical code EPIC which employs triangular elements. Numerical integration over the contour Γ in Equation (2.3) is achieved using the trapezoidal rule for each of the boundary segments in counterclockwise order. The scheme requires averaging values from adjacent elements to develop nodal values for the integrand. The integral over the domain Ω is evaluated by using one-point quadrature for each triangular element in Ω . The second-order derivatives of the displacements in Equation (2.3) must be smoothed before application of the quadrature approach. Smoothing is achieved by averaging values of the displacement gradients from adjoining elements at each node, and then linearly interpolating between these nodal values to achieve constant second-order displacement derivatives for each element. This approach is again used for calculating the gradients of the energy densities in Equation (2.3). Dexter and O'Donoghue [4] also used a node averaging method to smooth the gradients of the energy densities and strain fields, and found greatly improved accuracy in computing T^* .

2.2 Fracture Criterion

In general the crack driving force T^* will depend upon the applied loading $P(t)$, the crack length $a(t)$, and geometry b of the cracked component; i.e., $T^* = T^*[P(t), a(t), b]$. The fracture resistance R , which is considered to be a material property, may be a function of the instantaneous crack speed V , thickness h of the component, and temperature Θ ; i.e., $R =$

$R(V, h, \Theta)$. The fracture criterion requires that there be equilibrium between the crack driving force and the fracture resistance for a propagating crack. In this case, the fracture criterion becomes

$$T^* [P(t), a(t), b] = R(V, h, \Theta); V = \dot{a} > 0 \quad (2.4)$$

If $T^* < R$, the crack is at arrest; i.e., $V = 0$.

The dynamic fracture resistance is determined from a laboratory fracture test. In this test the loading $P(t)$ and the crack growth history $a(t)$ are measured. These data serve as inputs to a dynamic fracture mechanics analysis that computes the crack driving force T^* during the fracture event. When the crack growth history is specified; e.g., as when analyzing a fracture test, this type of analysis is referred to as a generation phase analysis. According to the fracture criterion of Equation (2.4), the computed variation of T^* with the crack speed V in a fracture test is the fracture resistance of the material at the test temperature and thickness of the specimen. The fracture resistance is expected to be independent of thickness if conditions of plane strain are satisfied; i.e., if the thickness of the specimen or component is sufficiently large compared to the size of the fracture process zone. If conditions of plane strain are not satisfied, the fracture resistance must be established using a specimen of the same thickness as the component under investigation.

For small scale yielding, it is convenient to define a dynamic fracture toughness K_{ID} as

$$K_{ID} = \sqrt{E'R} \quad (2.5)$$

where

$$\begin{aligned} E' &= \frac{E}{1-\nu^2} && \text{for plane strain} \\ &= E && \text{for plane stress} \end{aligned} \quad (2.6)$$

in which E is the elastic modulus and ν is Poisson's ratio. Rigorously, Equation (2.5) should contain a function of crack speed, but this function is approximately unity for the crack speeds encountered in the tests reported herein.

The converse of the generation phase analysis is the application phase analysis. In this case the loading $P(t)$ of the cracked component and its fracture resistance R are prescribed. The fracture criterion of Equation (2.4) can be viewed as the nonlinear equation of motion governing the propagation of the crack tip. The integration of this equation in a fracture mechanics analysis yields the crack growth history for the body.

2.3 Numerical Modeling of Crack Growth

Clearly, performing a generation phase or an application phase analysis is a complicated mathematical problem that demands a numerical solution except for the simplest of problems. The numerical method requires computing not only the stress, strain and displacement fields but also the crack driving force. Moreover, the numerical method must also properly simulate the unloading of a material element as the crack tip passes through it.

If a crack propagates along a plane of symmetry as, for example, in a fracture specimen, then only one-half of the body need be modeled. A node on the plane of symmetry ahead of the crack tip is restrained by only a normal force for the opening mode of crack propagation. The formation of new traction-free surfaces during dynamic crack propagation is simulated in the finite element model by release of the crack-tip node in accordance with the fracture criterion. When the fracture criterion is satisfied, the restraining force on the crack-tip node must not be released instantaneously. To do so is equivalent to applying an impulse to the node which would lead to spurious ringing in the model. Moreover, it would be impossible to satisfy an energy balance since there would be no mechanism in the model for dissipating energy associated with the fracture process. Therefore, it is necessary to restrain the crack-tip node by a force that monotonically decreases to zero as the crack tip propagates to the next node. Experience indicates that the numerical results are not sensitive to the manner in which the nodal force is decreased so long as it is done so in a reasonable, monotonic smooth manner [2].

An algorithm for the release of the nodal force, that has been used previously, decreases the nodal restraining force linearly with the advance of the crack through the element. For example, in modeling the propagation of the crack tip from node i to node $i+1$ on the crack plane, the nodal force F_i at node i is released according to

$$F_i = F_{io} (1 - \Delta z / L); \quad 0 \leq \Delta z \leq L \quad (2.7)$$

where F_{io} is the nodal restraining force when the crack tip initially encounters node i ; L is the length of the element (distance between node i and $i+1$); and Δz is the extent of crack growth through the element (distance from the node i to the current crack tip). While this nodal release algorithm is used for both generation and application phase analyses, these analyses are distinguished by the way Δz is computed.

In the generation phase analysis the crack growth history $a(t)$ is part of the input. As a result, the time at which the crack tip will be at each node of a finite element model is known *a priori*. Interpolation between crack growth measurements is usually required to establish these times. Fitting the measured crack growth history with an analytical expression (e.g., a polynomial) readily facilitates the interpolation. With these times, the average speed V at which the crack tip traverses the distance between consecutive nodes is computed. This crack speed also permits the determination of the extent of crack growth Δz for each computational cycle as the crack tip extends incrementally from node i to node $i+1$. With Δz determined, the nodal force F_i for each cycle is given by Equation (2.7).

The process for the application phase analysis is more complicated since the crack growth history is not known *a priori*. In this case, the loading $P(t)$ and fracture resistance $R(V)$ are specified and the crack growth history is to be determined. During each computational cycle, the crack driving force T^* is computed. This quantity is equated to the fracture resistance $R(V)$ per Equation (2.4), and $R(V)$ is inverted to yield the instantaneous crack-tip speed V . Unlike the generation phase analysis where the crack speed is constant for all cycles as the tip passes from node i to node $i+1$ (i.e., for $\Delta z < L$), the crack speed here can change with each cycle. The crack-tip location Δz is updated from the crack speed using a forward Euler scheme. This new value for Δz is introduced into Equation (2.7) to determine the nodal force for the next cycle. In this way Equation (2.4) is integrated to determine the crack growth history. This approach assumes that the fracture resistance is a single-valued function of crack speed. If, for example, the fracture resistance is independent of crack speed, then an alternate method must be used; e.g., see Reference [5]. Alternatively, a pragmatic solution is to modify the fracture resistance by giving it a small, negligible dependence on crack speed and use the above, described procedure.

Algorithms for computation of T^* , generation and application phase analyses, and crack growth have been implemented into EPIC. Further descriptions of these algorithms and their use are contained in Volume 2 of this report [6]. Also included in Reference [6] is a description of an element failure method that provides a computationally efficient alternative to the nodal release scheme when the crack path is not known *a priori*.

3.0 GENERATION PHASE EXPERIMENTS AND ANALYSES

AISI 4340 and AF 1410 steels were selected for use in the experimental phase of this program because the former is being used in bomb cases and the latter is being considered for such use. Moreover, their material properties have been previously characterized. When heat treated to a Rockwell hardness of 48 or greater, AISI 4340 is a relatively high strength material (e.g., a yield strength of approximately 1,500 MPa) with intermediate toughness (a plane strain fracture toughness K_{Ic} of about 83 MPa \sqrt{m}). Consequently, this material is expected to exhibit small scale yielding during fracture. It is also a material that has been used previously in dynamic crack propagation and arrest investigations. By contrast AF 1410 is a high strength material (e.g., a yield strength of about 1,600 MPa) with a high toughness (K_{Ic} of approximately 185 MPa \sqrt{m}). That is, it has a yield strength that is comparable to that of 4340, but its toughness is more than twice as great. It is unusual to find a material that has such high yield strength and fracture toughness and AF 1410 provides a contrast to AISI 4340. This is another reason for selecting this material.

Descriptions of the preparation of specimens for uniaxial tensile, quasi-static fracture toughness testing and dynamic fracture toughness testing are given in the following. The coupled pressure bar test apparatus and test procedure are described. Typical data and the procedures used to reduce the data to serve as input into the Generation Phase Analysis Module of EPIC to determine the dynamic fracture toughness are also presented. A complete set of data is contained in Appendix A. Finally, generation phase analyses are performed to deduce the fracture resistance as a function of crack speed from data attained in coupled pressure bar tests.

3.1 Heat Treatment

The Johnson-Cook material parameters for AISI 4340 and AF 1410, required for analyzing dynamic fracture tests of these materials, have been previously established for specific heats. Therefore, sufficient quantities of each material were subjected to the same respective heat treatment to avoid further material characterizations. Heat treatment schedules for AISI 4340 and AF 1410 used in this investigation are depicted in Figures 3.1 and 3.2, respectively.

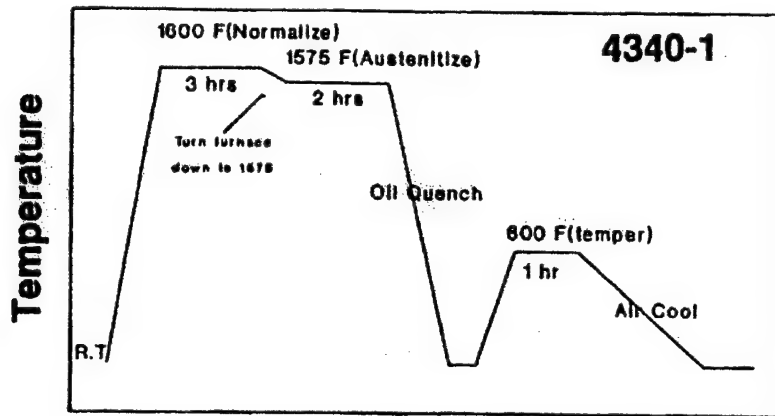
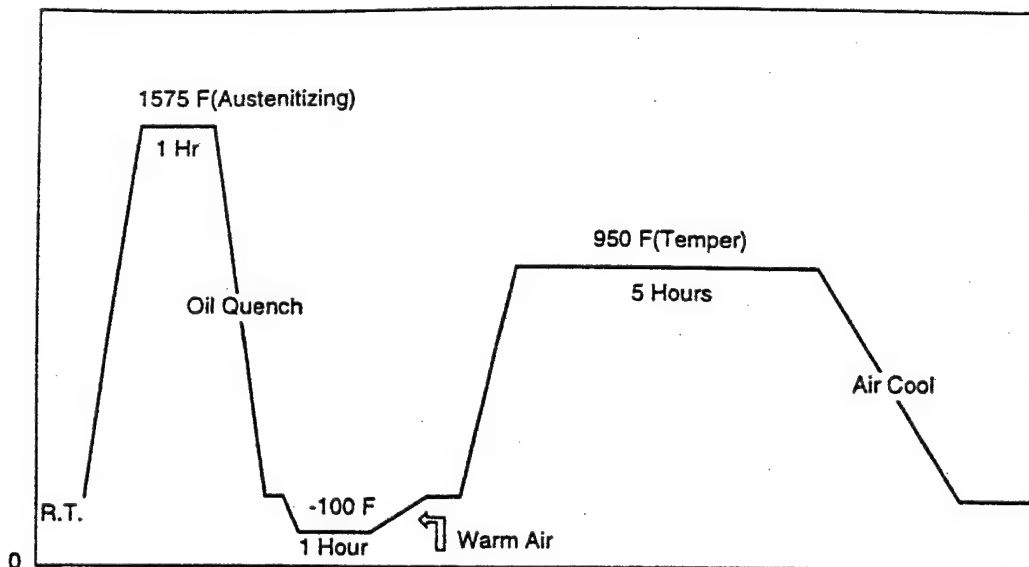


Figure 3.1 Heat Treatment Schedule for AISI 4340 Specimens.



01_T18072

Figure 3.2 Heat Treatment Schedule for AF 1410 Specimens.

To assure that the heat treatments produced the same mechanical properties, uniaxial tensile tests were performed and the measured stress-strain curves were compared with the respective ones from which the Johnson-Cook parameters were previously established. The tensile specimens used in these tests had the dimensions shown in Figure 3.3. Figure 3.4 compares a stress-strain curve measured in this program (denoted by SwRI) and that previously determined (noted as Eglin) for AISI 4340. Figure 3.5 depicts a similar comparison for AF 1410. It is clear that very good agreement exists between the stress-strain responses for the respective materials. Therefore, it is safe to assume that the Johnson-Cook parameters established earlier for these materials may be used in analyses of the dynamic fracture tests of these materials. No significant anisotropy in the stress-strain response was detected in either material. A complete set of measured stress-strain responses for AISI 4340 and AF 1410 are contained in Figures A1 through A9 in Appendix A.

3.2 Static Fracture Toughness

Quasi-static fracture toughness tests were performed on compact tension specimens of the heat treated AISI 4340 and AF 1410 steels following ASTM E399. The dimensions for the specimen are shown in Figure 3.6. These specimens have the same nominal thickness as the coupled pressure bar specimens used in the dynamic tests and also contained approximately 10 percent side-grooves to promote plane strain fracture. Two replications were performed for each material. The thickness of the 4340 specimens was sufficient to satisfy requirements for a valid plane strain fracture toughness K_c per ASTM E399. The measured values of K_c for 4340 were 84.7 MPa \sqrt{m} and 80.0 MPa \sqrt{m} . The values of the stress intensity factor at initiation of crack growth in AF 1410 were 186 MPa \sqrt{m} and 188 MPa \sqrt{m} . According to ASTM E399, the minimum specimen thickness for these initiation values to be valid measures of K_c is 24.9 mm for a yield strength of 1,620 MPa compared to an actual thickness of 21.7 mm. Consequently, the specimen thickness was slightly undersize. It is worth noting that the side grooves virtually eliminated shear lips in these specimens so that these values are representative of the plane strain fracture of the AF 1410 material. Other than the thickness, all the other requirements for a valid K_c were satisfied. The measured load versus crack mouth opening displacement (CMOD) plots for these materials appear in Figures A10 through A13 in Appendix A.

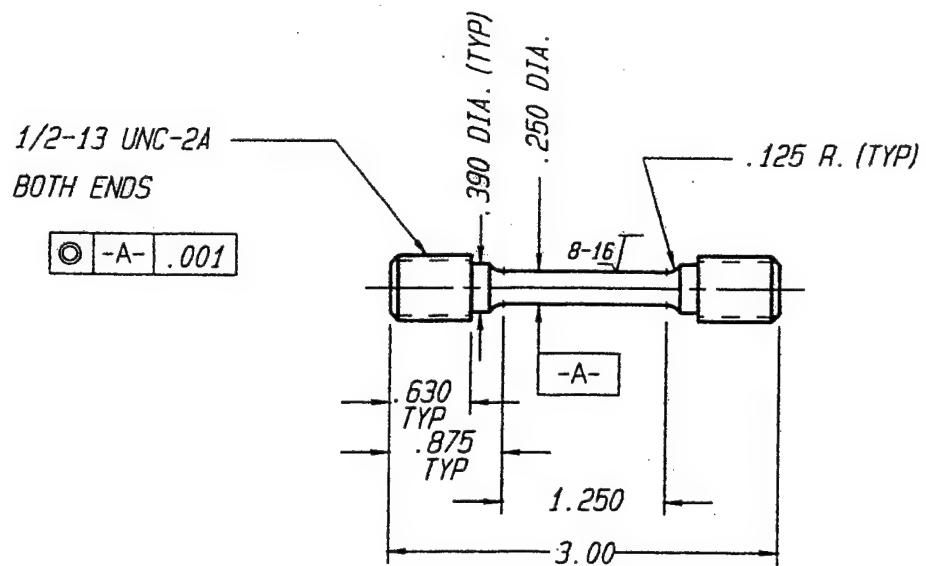


Figure 3.3 Tensile Specimen (Dimensions in Inches).

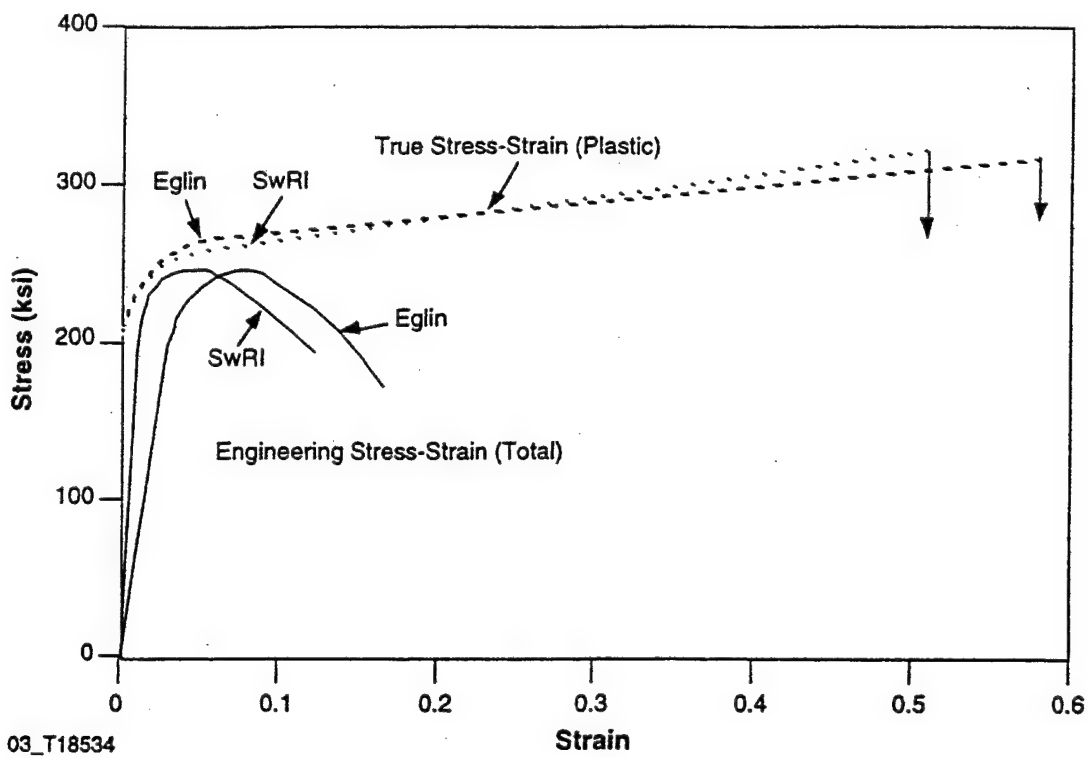


Figure 3.4 Comparison of Quasi-Static AISI 4340 Stress-Strain Data from Eglin and SwRI.

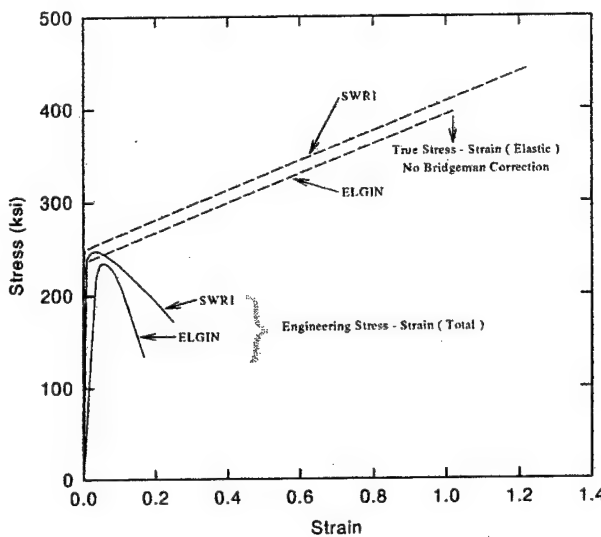


Figure 3.5 Comparison of Quasi-Static AF 1410 Stress-Strain Data from Eglin and SwRI.

3.3 Dynamic Fracture Apparatus and Testing Procedure

3.3.1 Coupled Pressure Bar Apparatus. The coupled pressure bar (CPB) arrangement, developed by Couque, *et al.* [7-8], was used to perform dynamic fracture tests of AISI 4340 and AF 1410 specimens. The fracture specimen used in these tests is a compact tension specimen that has been modified for loading using the coupled pressure bars and to accept an eddy current proximity gage for measuring the crack opening displacement (COD). Figure 3.7 is a machine drawing for this specimen. Pins from the couple pressure bar fixture mate with the 12.7-mm diameter semi-circular notches in the specimen.

The specimen is instrumented in several ways so that its dynamic fracture toughness can be deduced from a test. The relief machined into the bottom face of the starter notch receives an eddy current proximity gage to measure the COD. A KAMAN Instrument Corporation¹ Model 2UB eddy current sensor is used with Model KD 3210-2UB oscillator/demodulator to measure the crack opening displacement. The gage has a linear range over approximately 2.5 mm of displacement. A strain gage, located 10 mm above the tip of the fatigue starter crack, is affixed

¹ KAMAN Instrumentation Corp., 1500 Garden of the Gods Rd., Colorado Springs, CO 80907.

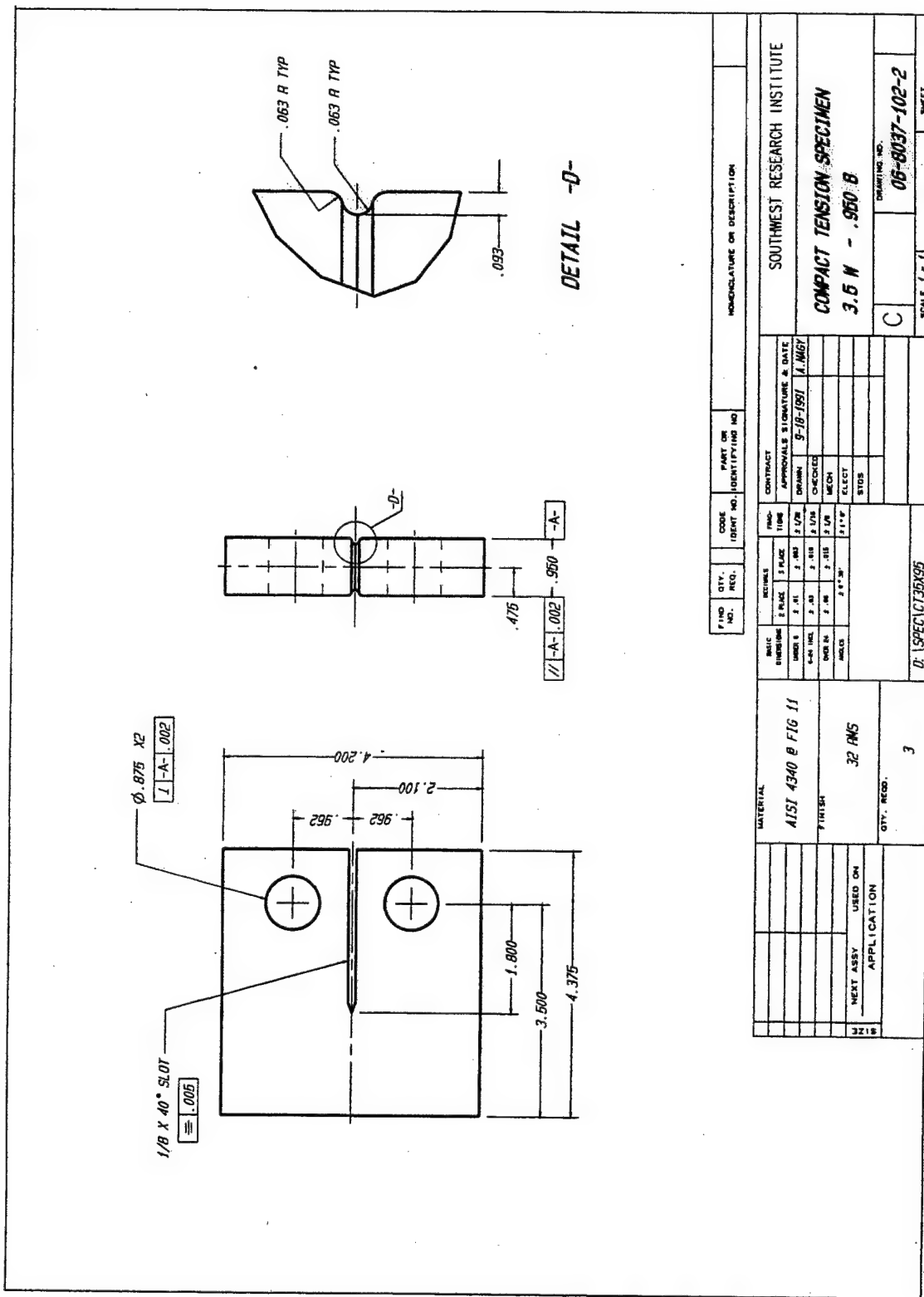


Figure 3.6 Compact Tension Specimen (Dimensions in Inches).

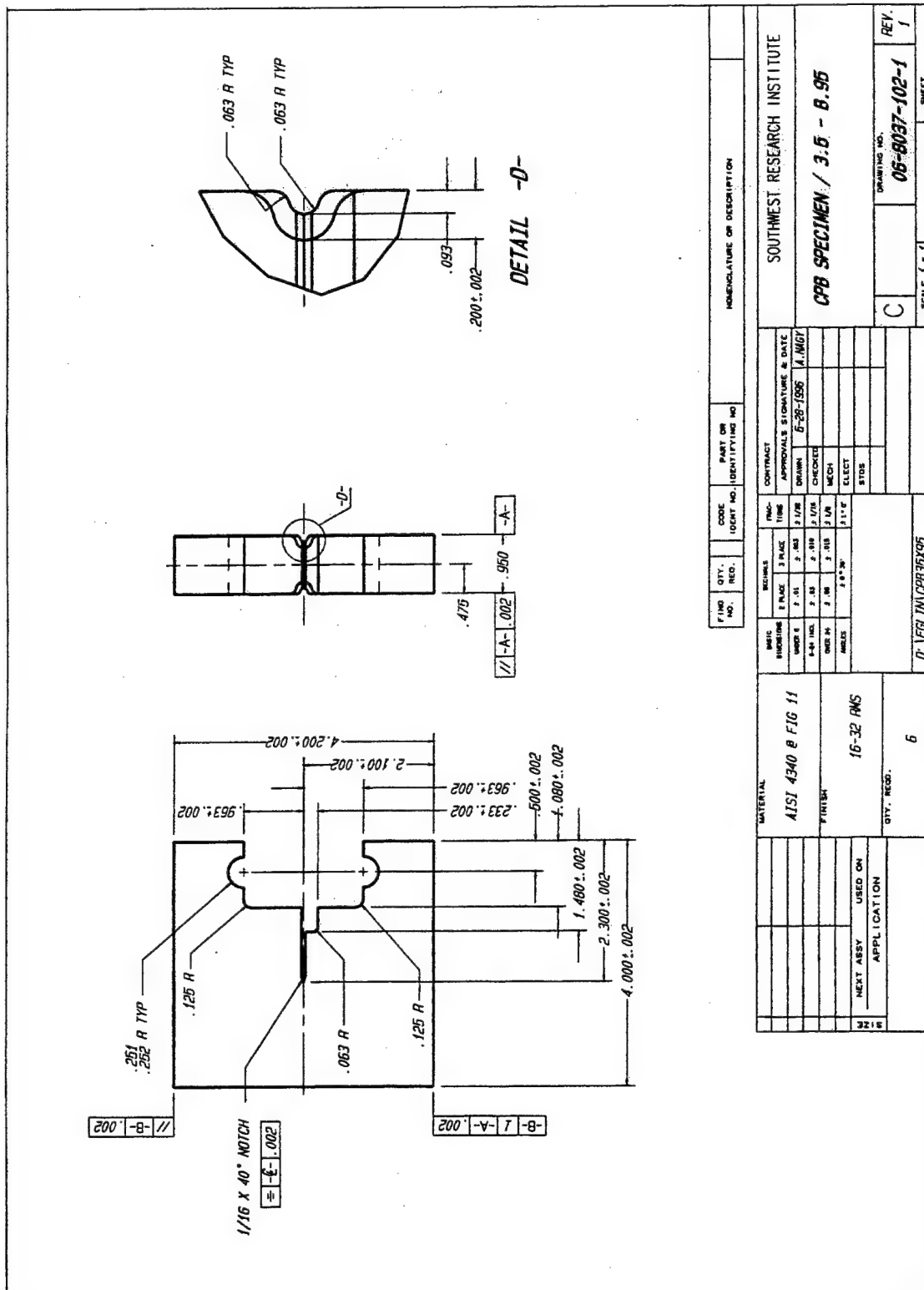


Figure 3.7 Coupled Pressure Bar Specimen (Dimensions in Inches).

to aid in establishing when initiation of crack growth occurred and to serve as a validity check for the analysis. On a lateral surface of the specimen an electrical insulating material, onto which a crack ladder gage is silk screened, is applied. The ladder gage consists of 10 rungs spaced at approximately 3-mm intervals. The electrical continuity of each rung is monitored during a test with a high speed counter that operates at 10 MHz. As the crack propagates through the specimen, it sequentially breaks a rung and disrupts its continuity, and the time of the event is recorded by the counter.

A schematic of the CPB assembly is depicted in Figure 3.8 and a photograph of the setup appears in Figure 3.9. In this configuration, two specimens located opposite each other are tested at a time. Basically, the arrangement consists of two 952-mm long, 38.1-mm diameter bars that are connected by an internally threaded notched round coupler. The inside and outside diameters of the coupler are 22 mm and 41 mm, respectively. The notch depth and radius are designed to support the preload that is applied to the bars. The outside of the coupler is threaded to accept, on either side of the notch, 95-mm square by 19-mm thick loading plates. The plates are separated by approximately 10 mm. Parallel to each edge of a plate are 12.7-mm semi-circular grooves into which 12.7-mm diameter harden pins fit. (Machine drawings for the coupler and loading plate are contained in Figures A14 and A15, respectively, in Appendix A.) The other ends of the bars are placed in the grips of a 890-kN servohydraulic testing machine.

Strain gages are attached to the top bar approximately 127 mm above the coupler. The bar with the strain gages is calibrated so that the load in the bar may be measured during a test. An eddy current gage, one for each specimen, is attached to the top of the bottom plate opposite the semi-circular groove into which the specimen loading pin is placed to measure the load line displacement.

3.3.2 Test Procedure. The test procedure consists of the following operations. A pair of fatigue precracked specimens are instrumented with a strain gage, crack growth ladder gage, and eddy current gage for measuring the COD. The specimen geometry (thickness, net specimen thickness in the side groove, initial crack length, width, height) and positions of the strain gage, each rung of the crack ladder gage, and the eddy current gage are measured and recorded. The strain and eddy current gages for a specimen are connected to the input of a Nicolet digital storage oscilloscope (two oscilloscopes are used in a test). Either the bar strain gage or the load cell is connected to the fourth channel of an oscilloscope. Electrical connections from each rung

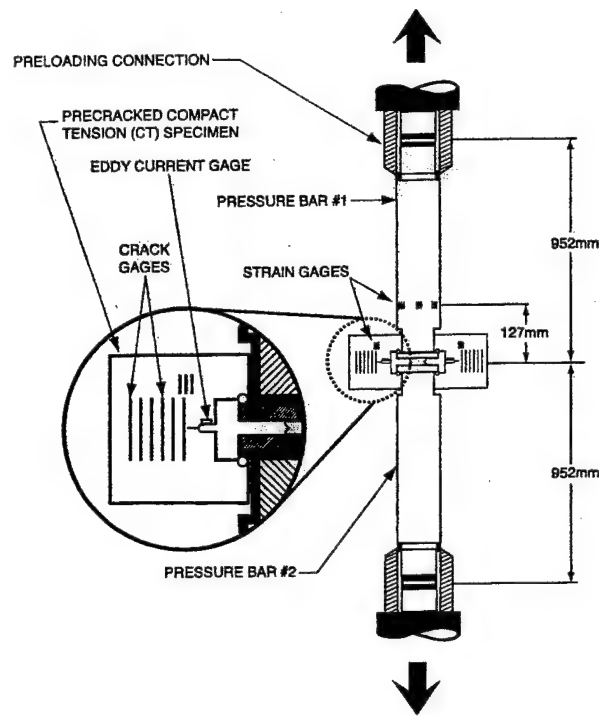


**Figure 3.8 Schematic Diagram for the Coupled Pressure Bar Apparatus
Used in Conducting Dynamic Fracture Tests.**

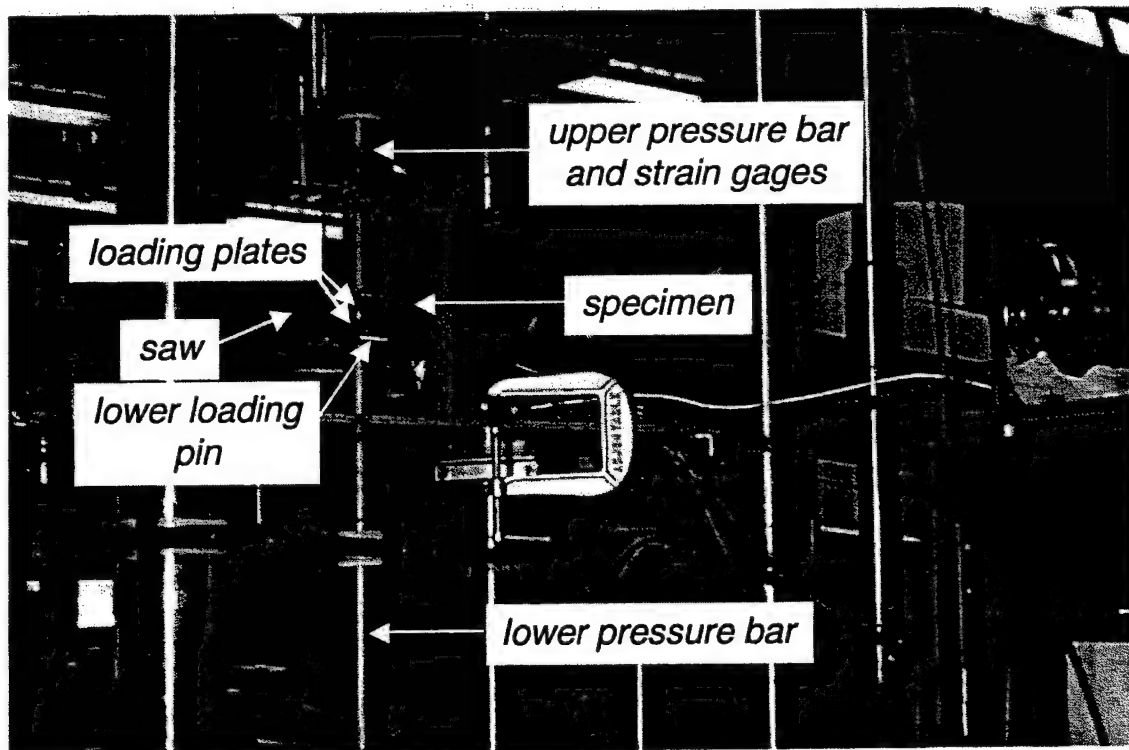


Figure 3.9 Photograph of Coupled Pressure Bar Setup.

of the crack ladder gages are connected to the transient counter. The loss of electrical continuity of the first rung of a ladder gage is used to trigger the oscilloscopes whose pretriggers were set at 400 μ s (except for the very first test in which a pretrigger of 200 μ s was used and proved to be too short).

A preload is selected for the test and the bars are loaded in the load control mode of the testing machine. The preloads used in this investigation were typically either 178 kN or 623 kN. A preload of 400 kN was also used in a further test of AF 1410 since only a pop-in of the crack occurred at the 178-kN preload. The specimens are affixed to the loading pins on the loading plates. All data recording devices are checked and zeroed as required. After proper precautions are taken to contain the broken specimens, the test commences by using a diamond tip saw, driven by an air motor, to produce a thin saw-cut at the root of the notch in the coupler. The cutting continues until insufficient cross sectional area of the coupler remains to support the preload. Unstable fracture in the reduced section causes rapid transfer of the preload (energy stored) in the bars to the test specimens. Depending upon the magnitude of the preload and the fracture toughness of the material, initiation of crack growth followed by complete fracture of the specimen takes from 150 μ s to 300 μ s. The oscilloscope data, in terms of output voltage of the transducer versus time, is written to electronic data files at the conclusion of the test for subsequent analyses. The counter times are manually recorded and written to a data file. A spreadsheet is used to translate the voltage measurements to physical quantities by using appropriately determined calibration factors.

3.4 Dynamic Fracture Data

A total of six specimens were tested for each material. Specimens are tested in pairs in the coupled pressure bar apparatus. Because of electronic recording problems, all of the intended data were not always captured in a test. Table 3.1 summarizes the preload and the data that were gathered for each specimen. Even though some data were not successfully captured, sufficient data were obtained for deducing the fracture toughness except for Specimens 5 and 6 where the pretrigger was inadequate to obtain the initial portion of the data.

Typical measured data obtained from a dynamic fracture test are contained in Figures 3.10 through 3.15 for AF 1410 specimens CPB1 and CPB2. Figure 3.10 shows the variation of the

Table 3.1 Summary of Dynamic Fracture Tests Performed and Data Captured

Specimen No.	Preload (kN)	LLD*	COD	Crack Gages	Strain Gage	Bar Load	Load Cell	Comments
AISI 4340								
1	623	yes	yes	yes	no	No	No	Second oscilloscope failed to capture data
2	623	yes	yes	yes	no	No	No	Second oscilloscope failed to capture data
3	623	no	no	yes	yes	Yes	Yes	LLD and COD gages grounded; test repeated
4	623	yes	no	yes	yes	Yes	Yes	COD gage grounded; test repeated
5	178	yes	yes	yes	yes	Yes	Yes	Trigger delay too short; missed initiation
6	178	yes	yes	yes	yes	Yes	Yes	Trigger delay too short; missed initiation
AF 1410								
CPB1	623	yes	no	yes	yes	Yes	Yes	COD gage destroyed during test
CPB2	623	yes	yes	yes	yes	Yes	Yes	
CPB3	178	yes	yes	yes	yes	Yes	Yes	Only crack pop-in occurred; no dynamic crack propagation
CPB4	178	Yes	yes	yes	yes	Yes	Yes	Only crack pop-in occurred; no dynamic crack propagation
CPB5	400	Yes	yes	yes	yes	Yes	Yes	LLD gage failed during test
CPB6	400	Yes	yes	yes	yes	Yes	Yes	

* LLD = Load Line Displacement

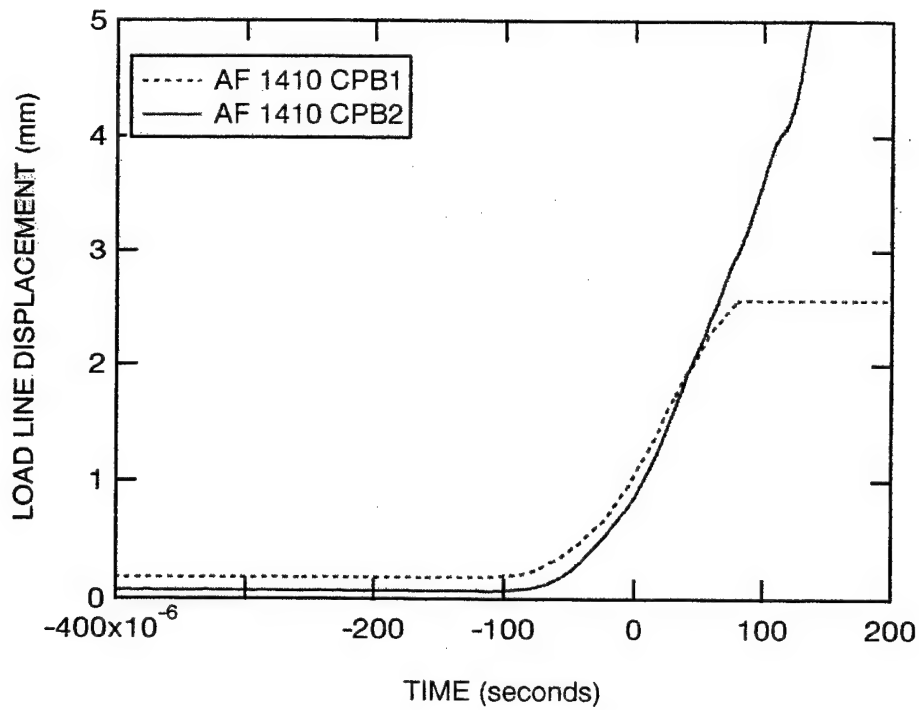


Figure 3.10 Measured Load Line Displacement Record for AF 1410 Specimens CPB1 and CPB2.

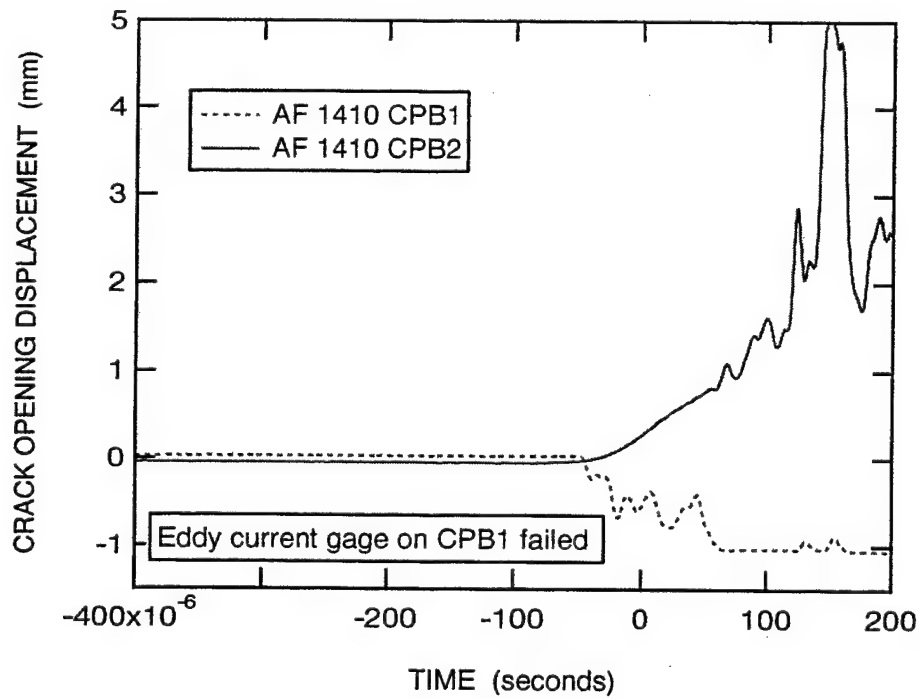


Figure 3.11 Measured Crack Opening Displacement Record for AF 1410 Specimens CPB1 and CPB2.

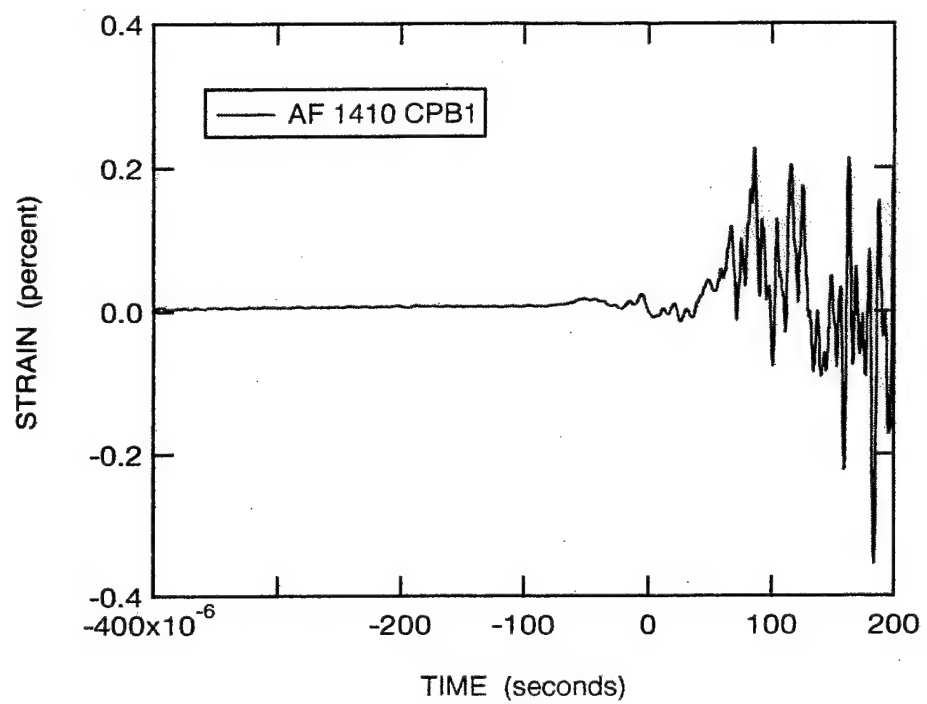


Figure 3.12 Measured Strain in AF 1410 Specimen CPB1.

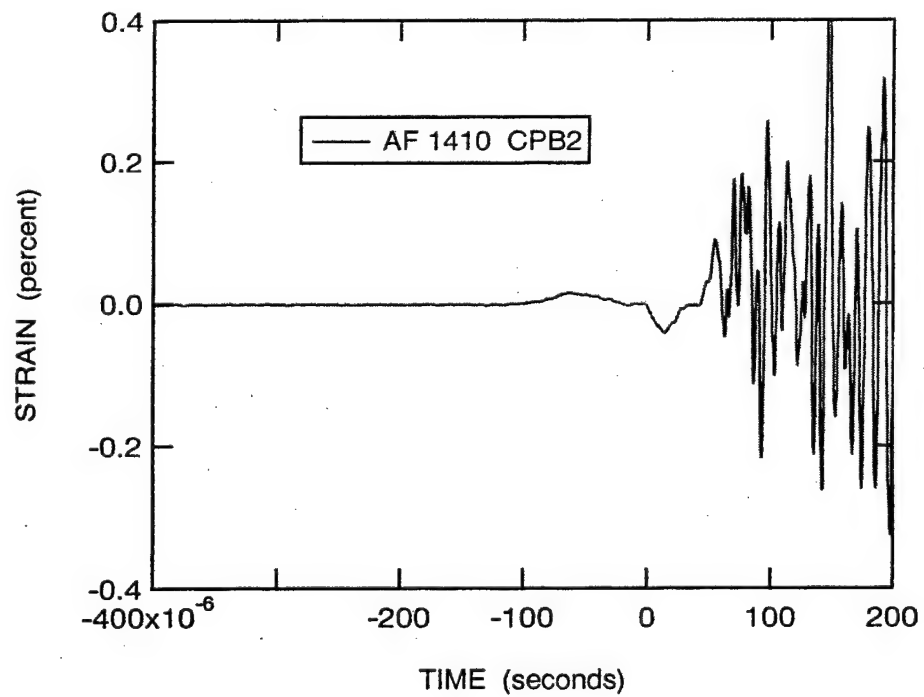


Figure 3.13 Measured Strain in AF 1410 Specimen CPB2.

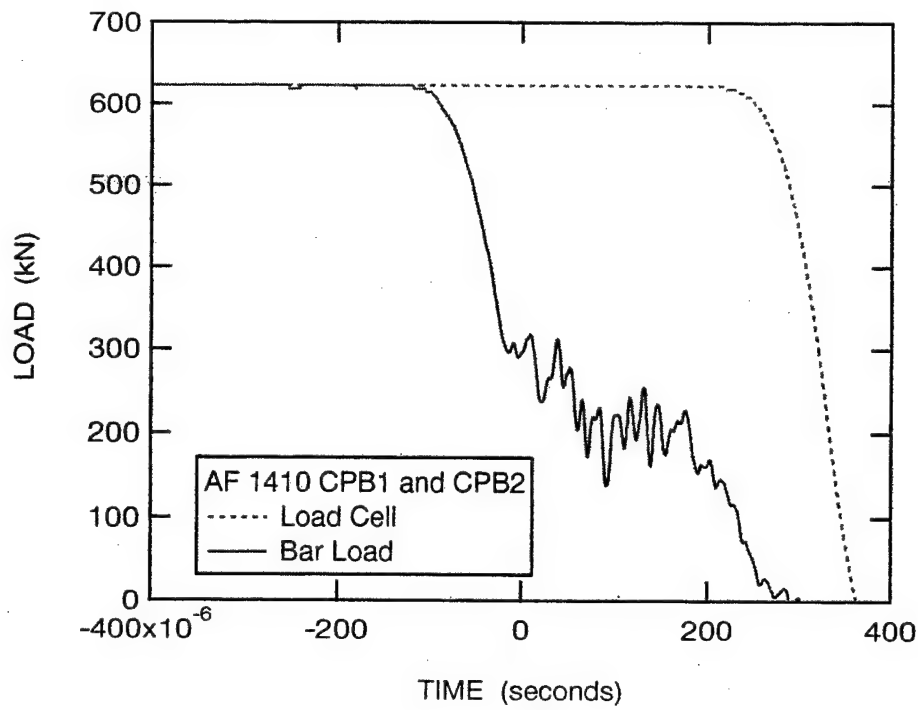


Figure 3.14 Measured Load in Upper Pressure Bar and Load Cell.

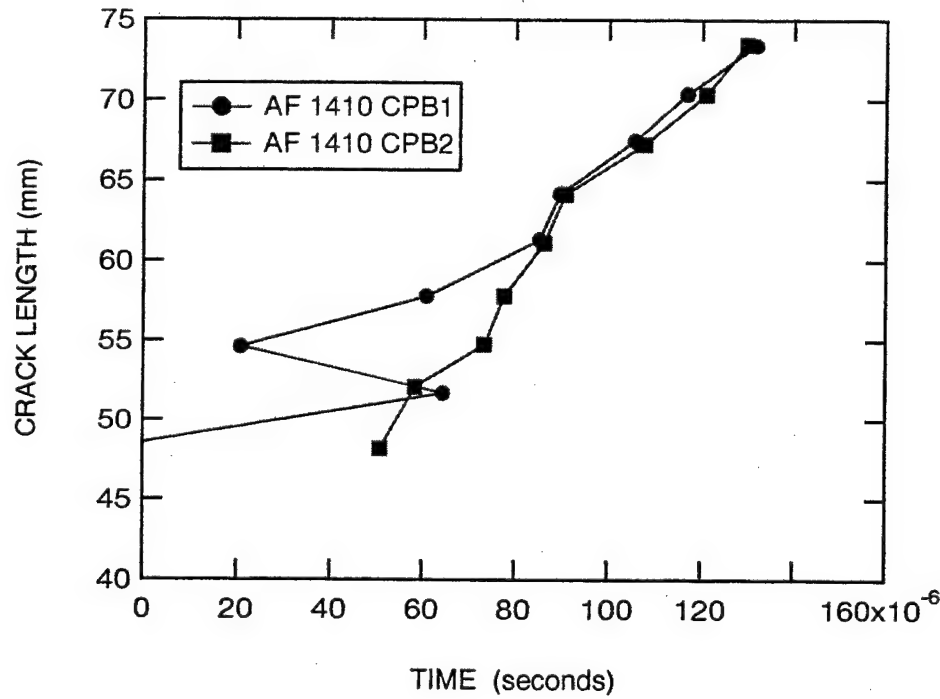


Figure 3.15 Measured Crack Length Histories in AF 1410 Specimens CPB1 and CPB2.

measured load line displacement with time. Note that zero time denotes when the trigger for capturing the data occurred. The actual loading of the specimens commenced earlier. The load line displacement data for AF 1410 CPB1 is clipped after 80 μ s and likely indicates failure of the eddy current gage. As noted in Figure 3.11 the eddy current proximity gage on CPB1 for measuring the COD also failed. Figures 3.12 and 3.13 depict the measured strain gage output for specimens CPB1 and CPB2, respectively. Figure 3.14 shows the measured load in the bar as determined from its strain gages, and the load cell to which the bar is attached. Because the load cell is located approximately 800 mm from the strain gages on the bar, there is a time delay between the response of the measured bar load and load cell. Moreover, the significantly smoother record for the load cell indicates that its frequency response is much lower than that of the bar and is insufficient for reliable dynamic measurements. The load in the bar begins to decrease at approximately -97 μ s and this time is nearly that at which the load line displacements for CPB1 and CPB2 start to increase in Figure 3.10. This is approximately the time at which loading of the specimens commenced. Finally, Figure 3.15 depicts the measured crack length time history. The mean crack speeds in specimens CPB1 and CPB2 were 190 m/s and 314 m/s, respectively.

Figures 3.16 through 3.18 depict the data for AISI 4340 CPB Specimens 1 and 2 for the same preload of 623 kN. (Once again zero time denotes when the trigger occurred.) These figures can be contrasted with Figure 3.10, 3.11 and 3.15, respectively. The load line displacement histories for AISI 4340 and AF 1410 are very similar to approximately 50 μ s which suggests that the initial rate of loading of the materials is expected to be the same for equal preloads under small scale yielding. The load line displacement records following crack initiation will depend upon the dynamic fracture toughness of the material. The average crack growth rates for Specimen 1 and 2 are 504 m/s and 450 m/s, respectively, and are considerably greater than the measured values for AF 1410. Clearly, the dynamic fracture toughness of AISI 4340 is significantly less than for AF 1410. An examination of Figure 3.16 indicates that the load line displacement of Specimen 1 begins to increase—signifying initiation of loading—at approximately -80 μ s compared to about -70 μ s for Specimen 2.

Data for other tests are contained in Figures A16 through A30 in Appendix A.

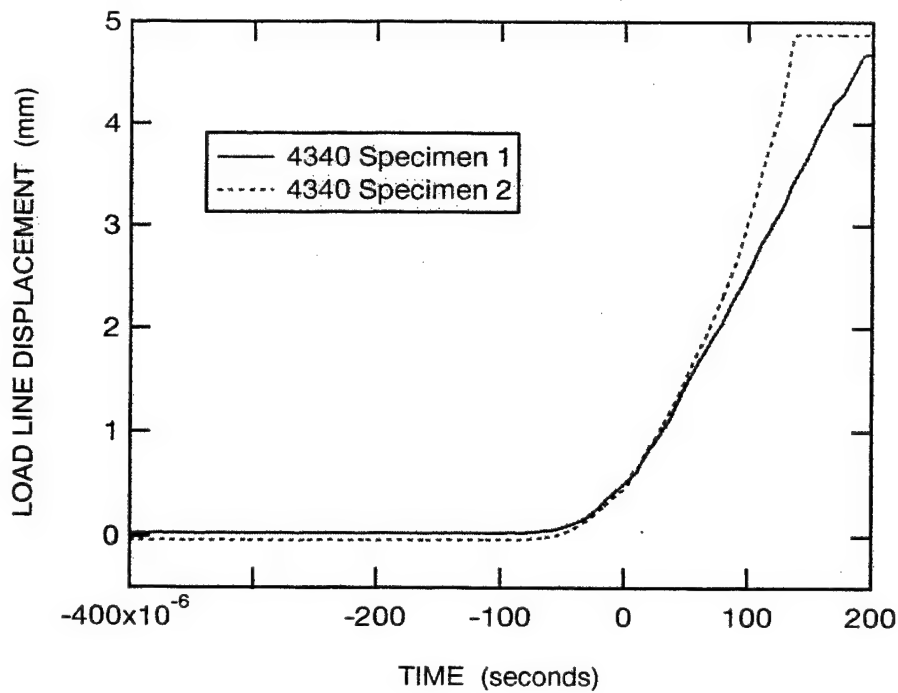


Figure 3.16 Measured Load Line Displacement Records for AISI 4340 CPB Specimens 1 and 2.

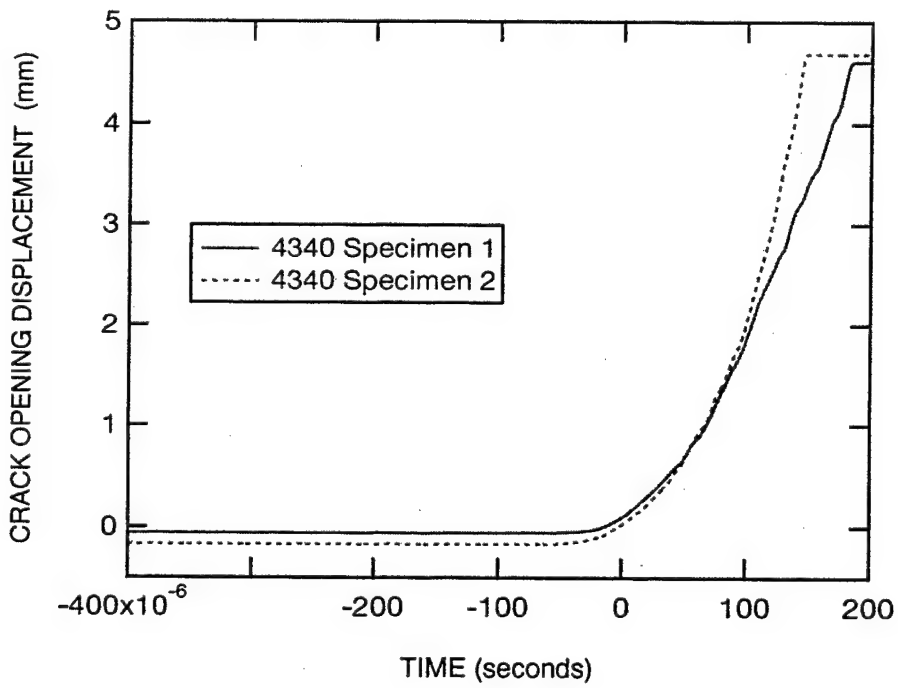


Figure 3.17 Measured Crack Opening Displacement Records for AISI 4340 CPB Specimens 1 and 2.

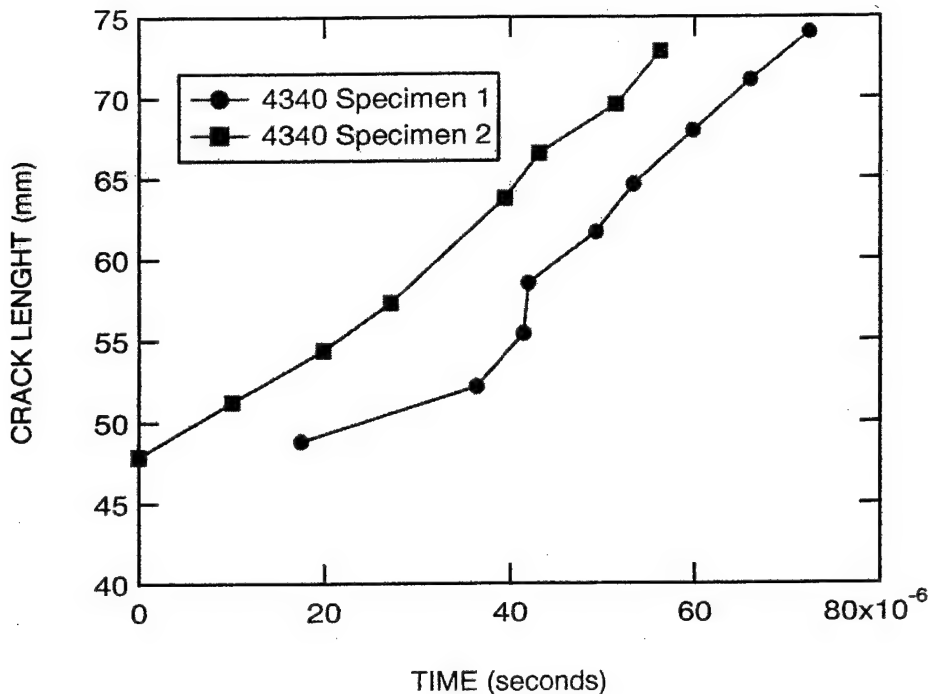


Figure 3.18 Measured Crack Length Histories in AISI 4340 CPB Specimens 1 and 2.

3.5 Data Reduction

A numerical simulation of the coupled pressure bar experiment is necessary for deducing the fracture toughness for a rapidly propagating crack. The required time-dependent experimental data that serve as input to the simulation are the load point displacement-time (actually load point velocity for EPIC) and the crack length-time histories. The measured COD-time history and/or the strain gage-time history are used in the analysis as a consistency or validation check of the numerical simulation.

It is necessary to establish from the experimental records the time at which loading of the specimen commenced. The time for initiation of the event is taken to be the time at which the load line displacement record departs from its initial value. Establishing this time is difficult because the initial rate of change of the load line displacement is very small. Therefore, small changes in the load line displacement; say, due to slight electrical noise or other experimental error, can lead to a degree of uncertainty for the initiation time. It should be noted that the load line displacement is not necessarily the load point displacement (i.e., the displacement at the

point of loading of the specimen) for the specimen because of deformations of the loading plates, pin contact surfaces, etc., and potential slack in the load train. The load point displacement is likely to be less than the load line displacement and delayed slightly relative to the latter. Since it is the load point displacement that serves as input to the numerical analysis, proper consideration of such effects must be made in an analysis of the test.

An algorithm has been developed for establishing the initiation time from the load line displacement record. A linear regression analysis of the load line displacement data indicates that

$$\Delta = (a + bt)^2 \quad (3.1)$$

in which Δ is the load line displacement and t is time, represents a very good fit to the data after initiation of loading through the measured crack propagation phase. In this procedure an estimate for the initiation time t_i is made from the load line displacement record. This point and the following data are translated so that it passes through the origin of the Δ - t space. A least square fit of Equation (3.1) to this record is made. If the fit does not render $\Delta = 0$ at $t = 0$, a new estimate for the initiation time t_{oi} is made for which $\Delta = 0$ (i.e., $t_{oi} = -a/b$). The data is translated again so that this new point passes through the origin and the process is repeated. Usually, there is no need to repeat the process a third time.

Figures 3.19 and 3.20 depict the results of applying this algorithm to the data in Figure 3.16. Also shown in these figures are the least square fits of Equation (3.1) to the data in Figure 3.16 and the initiation time t_i for loading. The remaining data for these specimens are translated so that the respective points at t_i pass through their origins. For example, the translated data for AISI 4340 Specimens 1 and 2 are depicted in Figures 3.21 through 3.23. The diamonds in Figures 3.21 and 3.22 denote the time at which the first rung of the respective crack ladder gage failed. The load line displacement at initiation of crack growth in Specimen 1 was about 10 percent greater than that for Specimen 2; while the COD's at initiation of crack growth are nearly identical. The close agreement is an indicator of the good replication for these specimens. Data of the kind in Figures 3.21 and 3.23 serve as input data to EPIC when analyzing the specimens to determine the dynamic fracture resistance, and the data in Figure 3.22 serve as the consistency check or validation of the simulation.

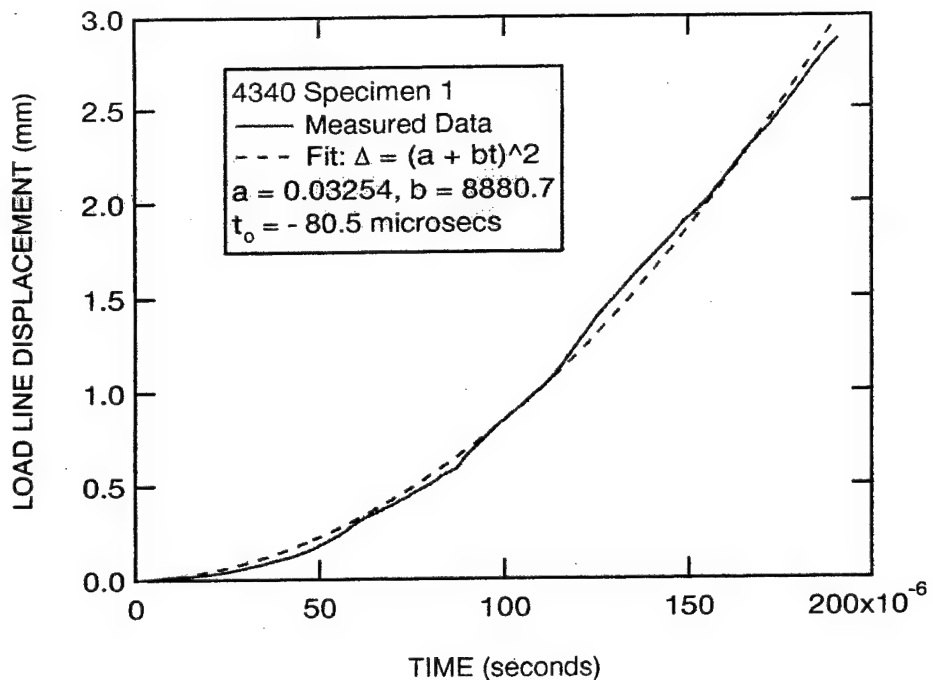


Figure 3.19 Reduced Load Line Displacement Record for AISI 4340 CPB Specimen 1.

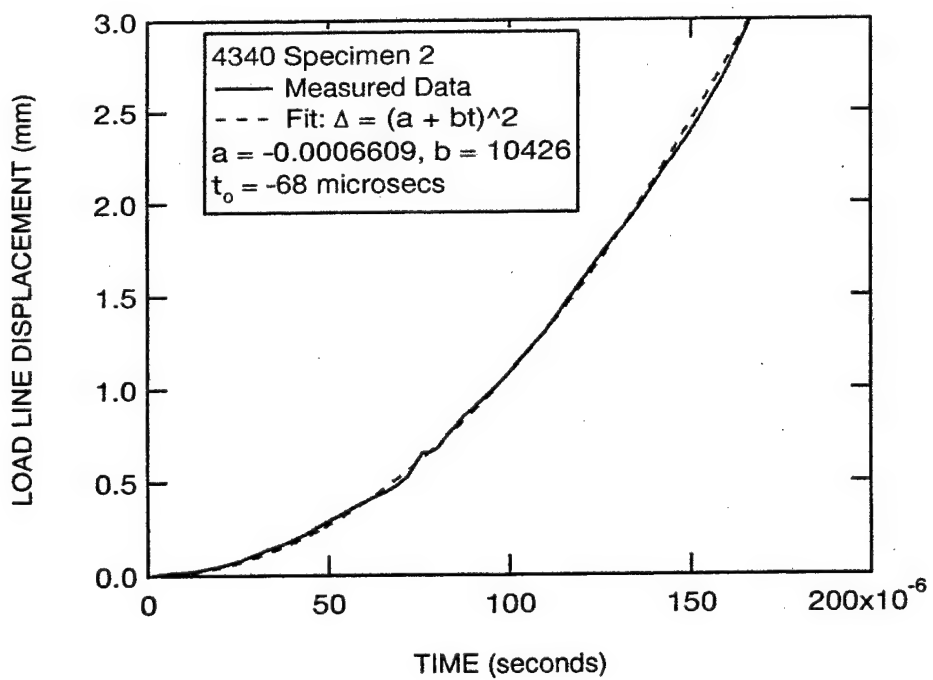


Figure 3.20 Reduced Load Line Displacement Record for AISI 4340 CPB Specimen 2.

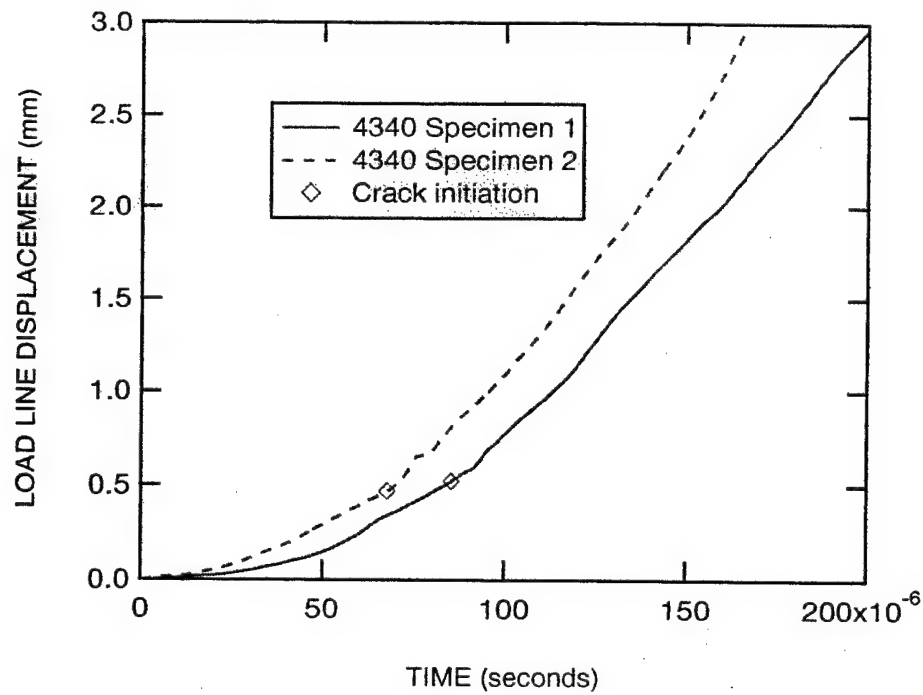


Figure 3.21 Comparison of Reduced Load Line Displacement Records for AISI 4340 CPB Specimens 1 and 2.

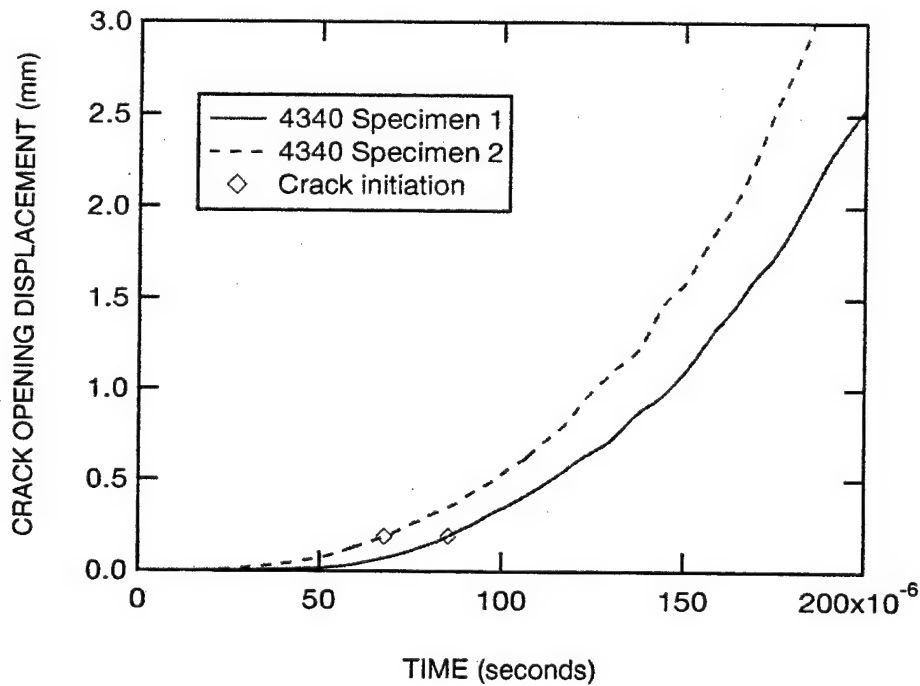


Figure 3.22 Comparison of Reduced Crack Opening Displacement Records for AISI 4340 CPB Specimens 1 and 2.

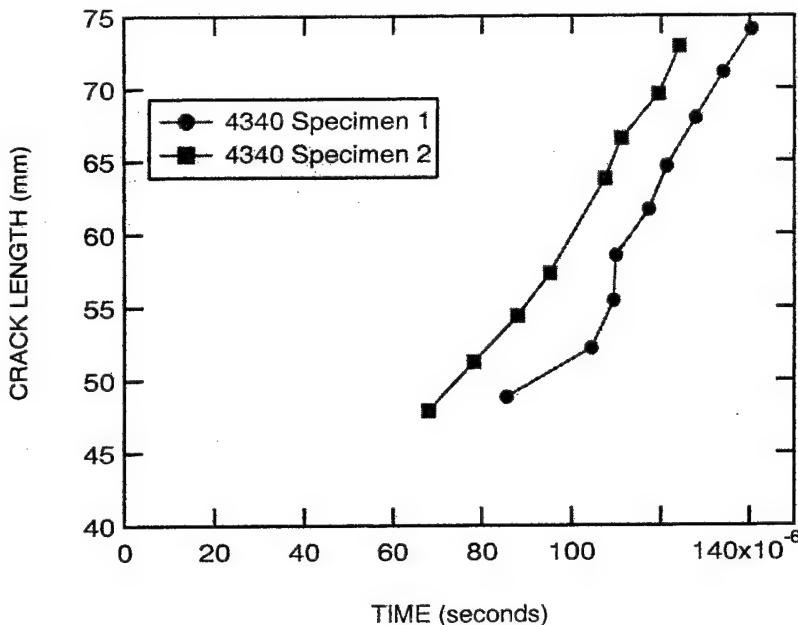


Figure 3.23 Reduced Crack Length-Time Histories for AISI 4340 CPB Specimens 1 and 2.

The reduced data for the other tests can be found in Figures A31 through A43 in Appendix A.

3.6 Dynamic Fracture Resistance

While the crack is propagating, the fracture criterion of Equation (2.4) requires equilibrium between the crack driving force as measured by T^* and the dynamic fracture resistance R of the material. Since it is impossible to measure the dynamic fracture resistance, it must be established through a generation phase analysis of data measured in fracture experiments. The load point displacement and crack growth histories, along with the specimen's geometry and material properties, serve as input to an EPIC model of the fracture specimen. EPIC computes T^* that is equal to R during crack propagation. It is through such an analysis that the dynamic fracture resistance is determined.

In these computations, the measured crack growth history is fit with a second-degree polynomial to enable interpolation between discrete measurements of the crack tip position with time. Such a fit provides a linear variation of crack speed with time. For example, Figure 3.24 depicts a quadratic fit to the measured crack tip history for AISI 4340 Specimen 2. This fit is

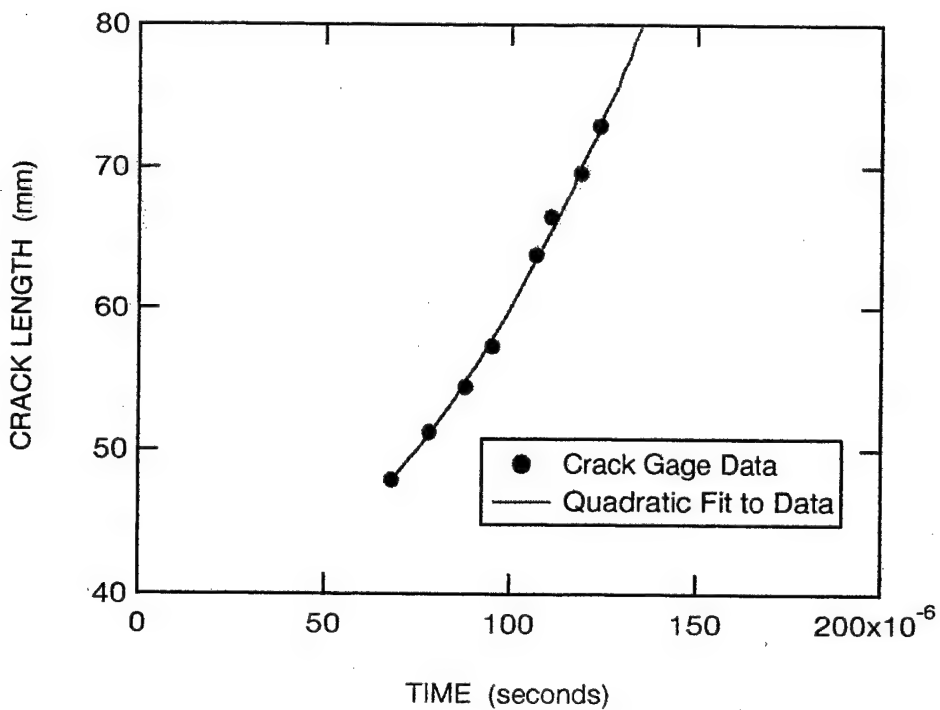


Figure 3.24 Quadratic Fit to the Crack Growth History for AISI 4340 CPB Specimen 2.

used to determine the time in EPIC at which the crack tip arrives at a crack plane node and the increment Δz for use in Equation (2.7) for each computational time step.

Direct measurement of the displacement of the specimen at the point of application of the load; i.e., the load *point* displacement (LPD), in the coupled pressure bar test is impossible. Only the load line displacement (i.e., the displacement at a point on the line through the load points, but somewhat removed from the point of application of the load) can be measured. Nevertheless, it is the LPD that is required in a generation phase analysis. Therefore, a predictor-corrector algorithm was developed to estimate the LPD from the measured load line displacement (LLD). The algorithm uses the COD as a metric for assessing the adequacy of the estimated LPD. The process starts by using the measured LLD as a first approximation for the LPD, which is used in EPIC to compute the COD. The computed COD is compared with the measured COD. If the difference between the computed and measured COD fails to meet an acceptance criterion, the LPD is corrected and the process is repeated until the criterion is satisfied.

Figure 3.25 graphically illustrates the algorithm. It should be noted that the differences depicted in this figure have been exaggerated for purposes of clarity. As depicted in Figure 3.25a, the load line displacement is expected to be greater than the load point displacement due to the compliance of the load train. The algorithm starts with the load line displacement as a first approximation for the load point displacement (see Figure 3.25a). The generation phase analysis is used to compute the COD which is compared with the measured COD as depicted in Figure 3.25b. Note that the computed COD (e.g., point A) from this approximation to the LPD occurs before the same measured value (Point B) because the LLD (e.g., point C in Figure 3.25a) precedes the LPD (point D). The goal is to have A and B coincide; i.e., the predicted COD equals the measured COD. For the coupled pressure bar specimens used in this investigation, it takes approximately 10 μ s for a wave to travel from the load point (pin) to the position of the COD proximity gage. If a causal relation is assumed between the LPD and COD, then the LPD that produced the COD at point A must have occurred 10 μ s earlier; i.e., point C in Figure 3.25a. The LPD is corrected by translating point C parallel to the time axis to point D by an amount equal to the difference in time between points A and B. For this specific case, the time at D equals the time at B less 10 μ s. This process is repeated for other points on the computed COD curve to generate a new prediction for the LPD history. The EPIC generation phase analysis is repeated with this new LPD history and a second COD is computed. Usually very good agreement (much better than that depicted schematically in Figure 3.25b) is attained between the newly computed COD and the measured value. If necessary, the process can be repeated again to obtain improved correspondence between the measured and computed COD. Modifications are made to the previous estimate for LPD to attain an updated or corrected LPD to be used in the computations.

After acceptable correspondence between the computed and measured COD data is attained, the crack driving force T^* , which in turn is equal to the resistance R during crack growth, is computed. A cross plot of R against crack speed V establishes the dynamic fracture resistance for the material. For small scale yielding, dynamic fracture toughness K_{ID} is determined from the fracture resistance using Equation (2.5).

3.6.1 AISI 4340 Fracture Resistance. The dashed curve in Figure 3.26 is the experimentally measured load line displacement in a coupled pressure bar test of 4340 Specimen 2. This curve represents a first approximation to the load point displacement. The solid curve is the corrected

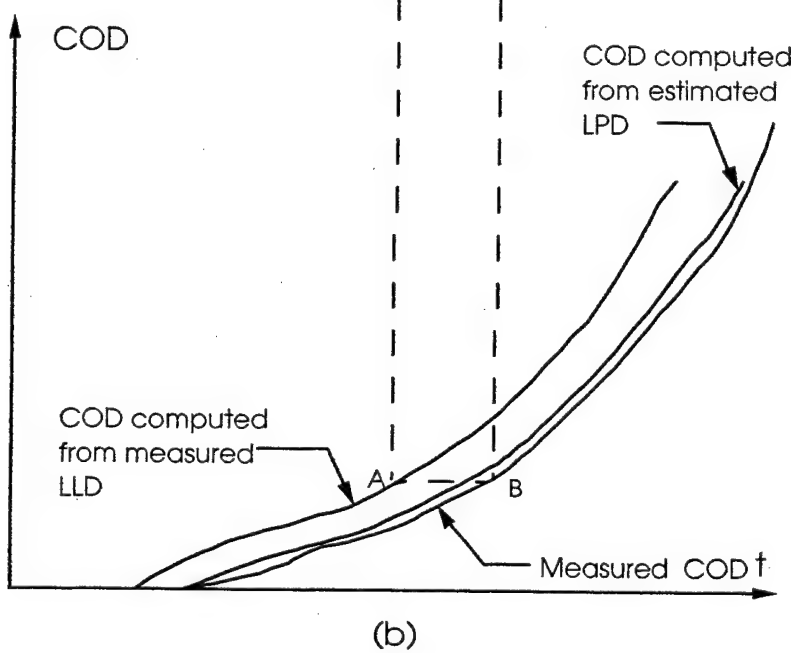
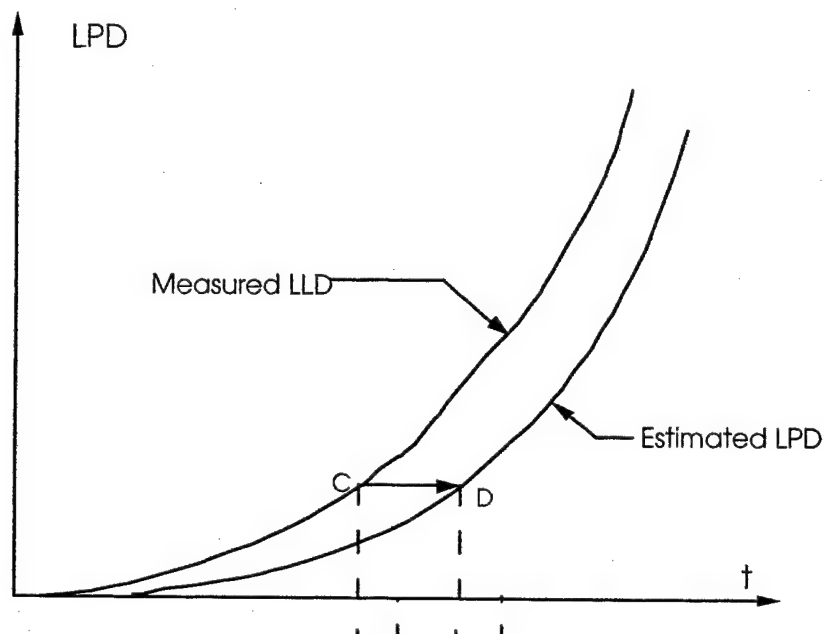


Figure 3.25 Predictor-Corrector Algorithm for the Load Point Displacement.

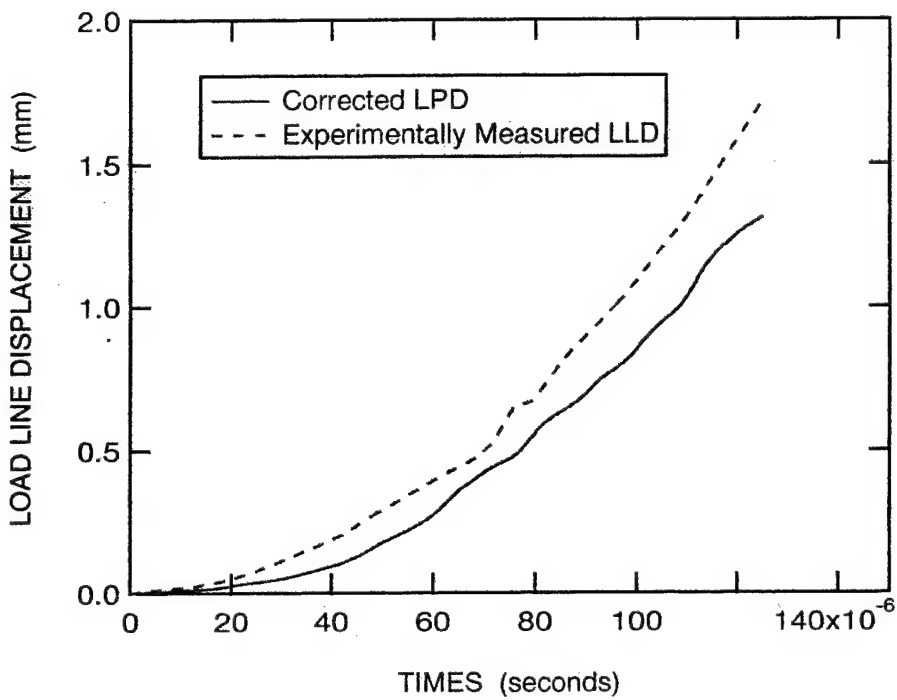


Figure 3.26 Comparison of Measured Load Line Displacement and First Approximation for the Load Point Displacement.

load point displacement using the above algorithm. Figure 3.27 compares the EPIC computed COD using this load point displacement with the measured COD. The agreement between the two is very good. The variation of T^* with time is shown in Figure 3.28. The results show a gradual increase of T^* to approximately 68 μ s after which there is a slight decrease signifying initiation of crack growth. The slight jaggedness of the curve following crack initiation is indicative of numerical modeling of crack propagation. From the point of initiation of crack growth onward, the fracture criterion requires that crack driving force equal the dynamic fracture resistance; i.e., $T^* = R$ for $V > 0$. As depicted in Figure 3.29, the fracture resistance may be cross plotted against the crack speed to establish the fracture resistance as a function of crack speed. The dashed curve is a bilinear fit to the data. Alternatively, Equation (2.5) can be used to develop the fracture toughness as shown in Figure 3.30. The decrease in the fracture resistance for crack speeds greater than about 550 m/s does not seem realistic since the fracture resistance is expected to be a single valued function of the crack speed. This discrepancy may be the result of experimental errors; e.g., in measuring the crack tip position as a function of time and then

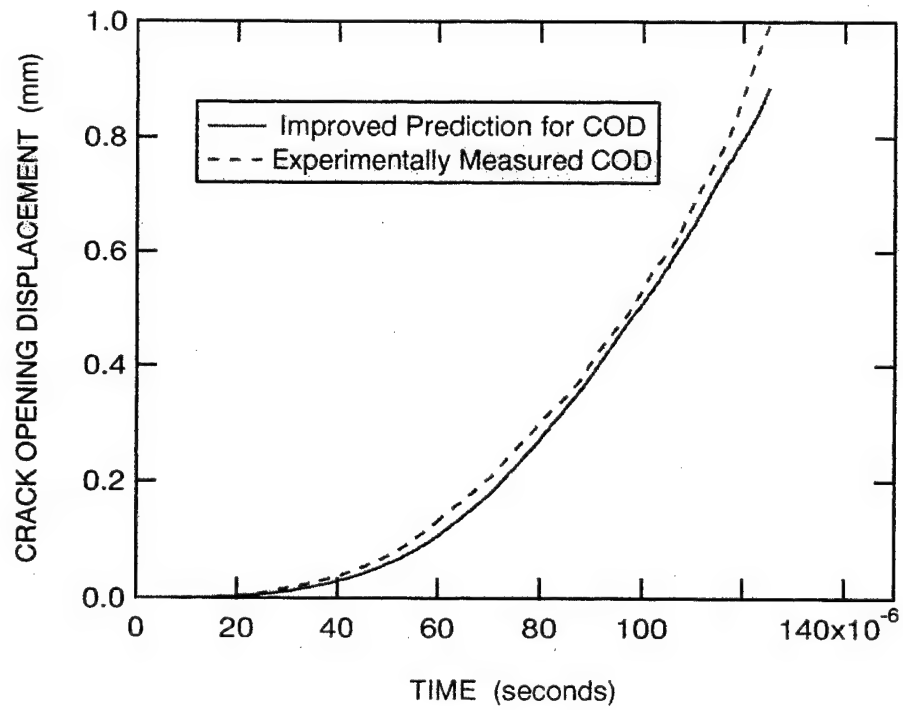


Figure 3.27 Comparison of Computed and Measured COD.

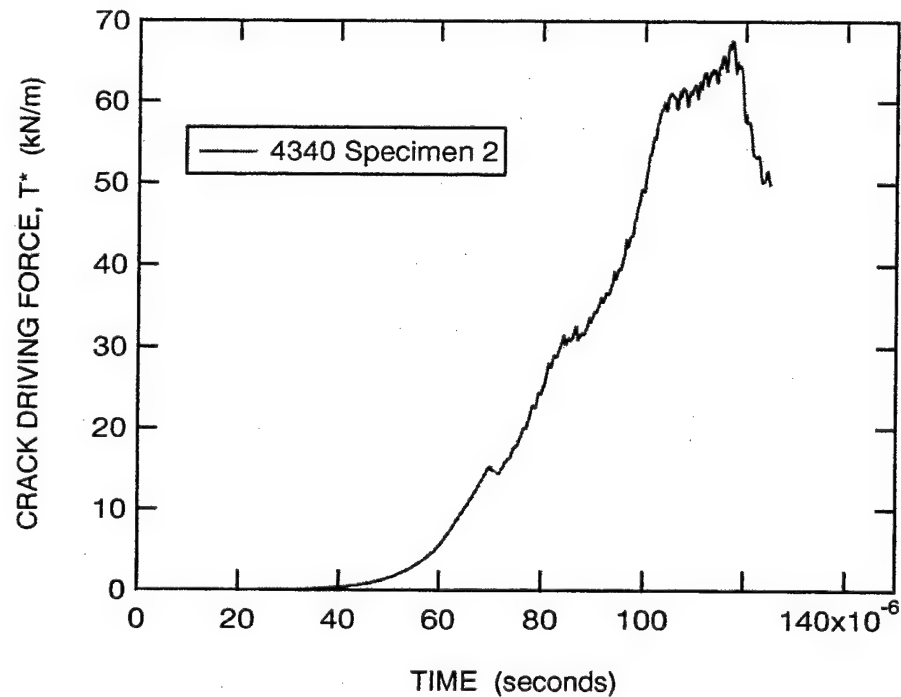


Figure 3.28 Variation of T^* with Time for CPB Specimen 2.

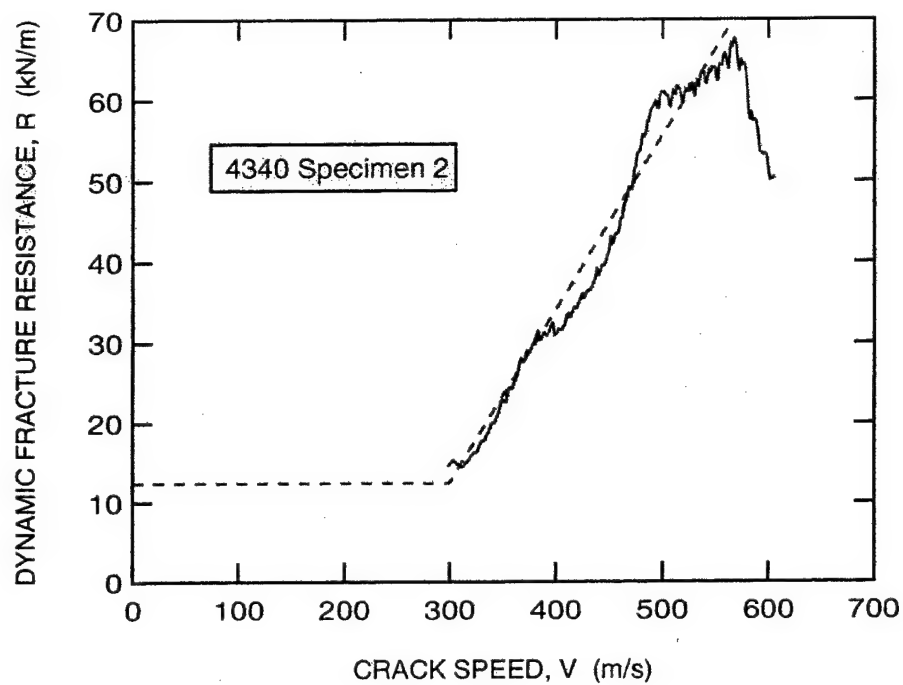


Figure 3.29 Variation of Fracture Resistance with Crack Speed Determined from CPB Specimen 2 and a Bilinear Fit to Data.

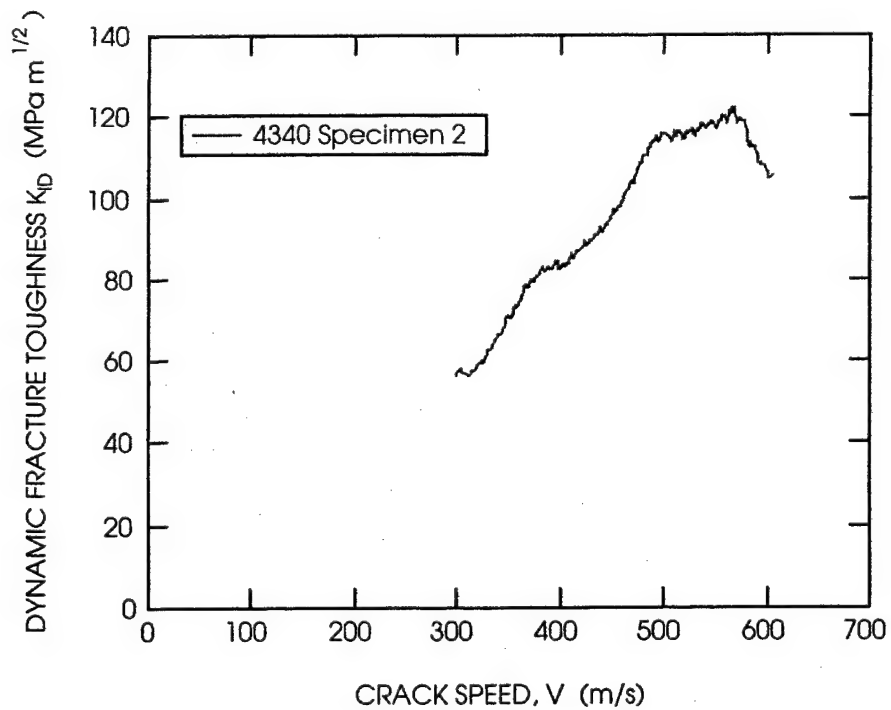


Figure 3.30 Variation of Dynamic Fracture Toughness with Crack Speed for CPB Specimen 2.

numerically differentiating it to obtain a crack speed greater than the actual speed. The fracture resistance developed from Specimen 1 in Figure 3.31 exhibits similar characteristics.

The dynamic toughness K_{ID} developed from these tests varies from approximately 50 to 130 MPa \sqrt{m} over the range of crack speeds of 300 to 600 m/s. These toughness values are in general agreement with those reported by Kanninen, *et al.* [9] for this range of crack speeds, but are less than the values 110 to 175 MPa \sqrt{m} over the crack speeds of 200 to 700 m/s reported by Couque, *et al.* [10] for AISI 4340 steel. The present dynamic toughness tends to be greater than that measured by Zehnder and Rosakis [11] using the method of caustics. Hence, the present values fall within those reported by other investigators for this material.

To check that all the calculations are consistent, application phase analyses using the developed dynamic fracture resistance as a function of crack speed were performed to compute the crack growth history. The fracture resistances for Specimens 1 and 2, respectively, are approximated by the straight lines in Figure 3.32. These representations for the fracture resistances and the respective deduced load point displacements were used in application phase analyses to compute the crack growth histories for Specimens 1 and 2 in Figures 3.33 and 3.34, respectively. Clearly there is good agreement between the measurements and the predictions over the region for which crack growth measurements exist. This agreement confirms the internal consistency of the generation phase and application phase algorithms.

Note, however, that the application phase analysis predicts for both specimens that the crack speed decreases following the last measured crack position, approximately 15 mm from the back surface of the specimen. This is in contrast to what is expected if the measured crack growth history is extrapolated quadratically. An Imacon 468 digital camera was used to capture six images of Specimen 2 during its dynamic fracture test. The crack tip position measured from these images is also plotted in Figure 3.34. These data indicate that the crack speed indeed slows as predicted by the application phase analysis. Moreover, there is favorable agreement between the application phase predictions and the measurements. If anything, these measured crack lengths likely underestimate the actual crack length because of the difficulty of identifying the actual crack tip in the images. These additional data and the favorable comparison between the predicted and measured crack growth histories further support the validity of the approach since the Imacon data were not previously used in the generation phase analysis. Furthermore, these

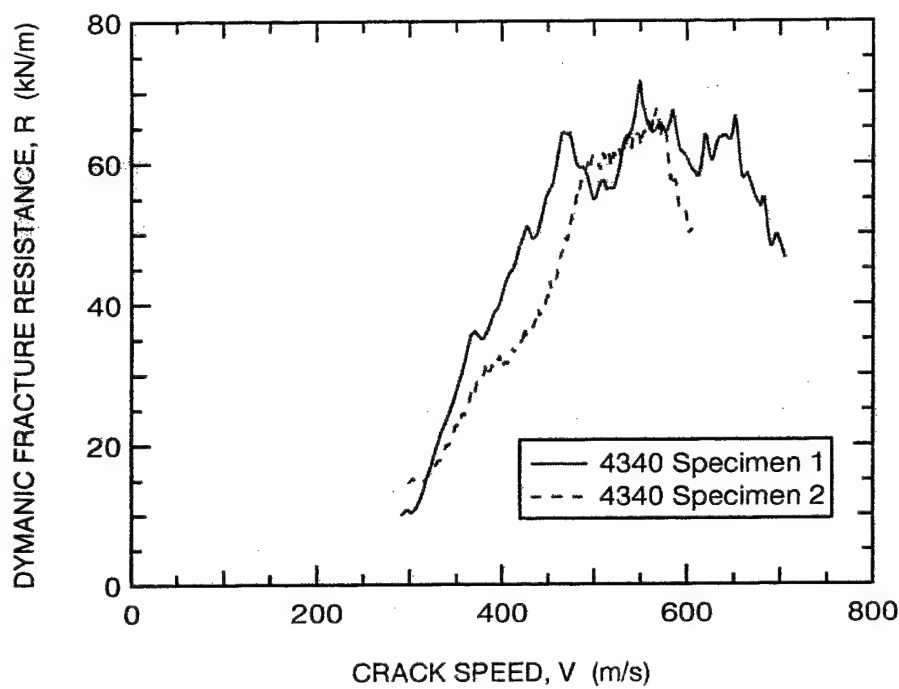


Figure 3.31 Comparison of Dynamic Fracture Resistance for CPB Specimens 1 and 2.

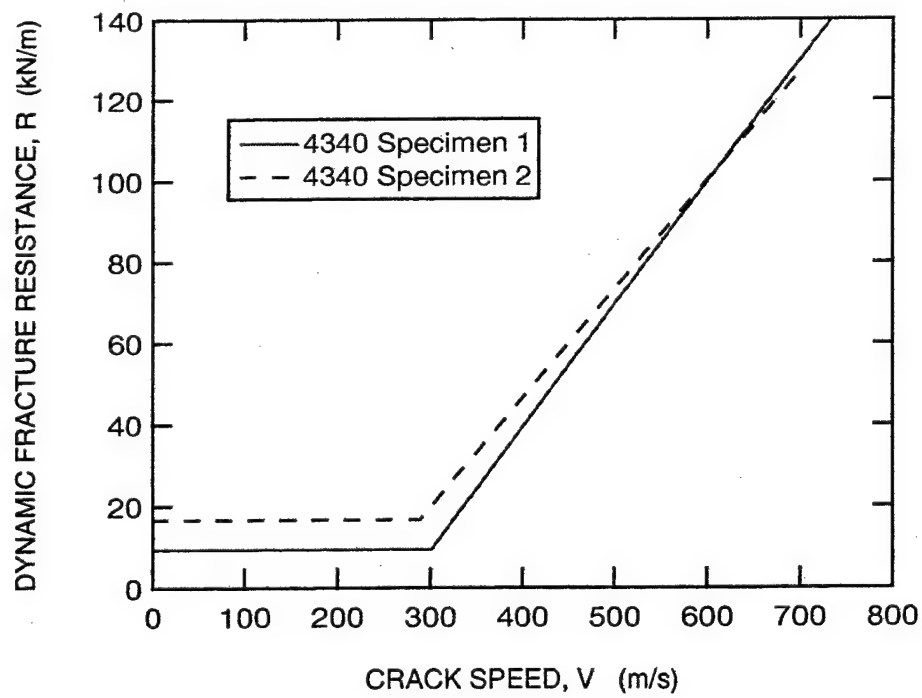


Figure 3.32 Bilinear Representations for the Dynamic Fracture Resistance of CPB Specimens 1 and 2.

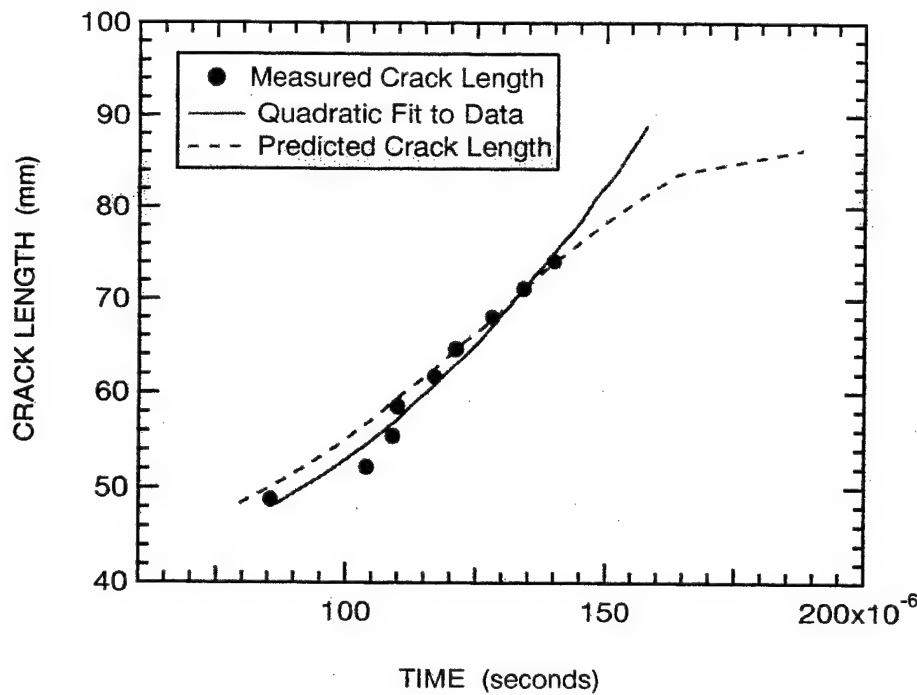


Figure 3.33 Comparison of Application Phase Analysis Predictions for the Crack Growth History with the Measured History for AISI 4340 CPB Specimen 1.

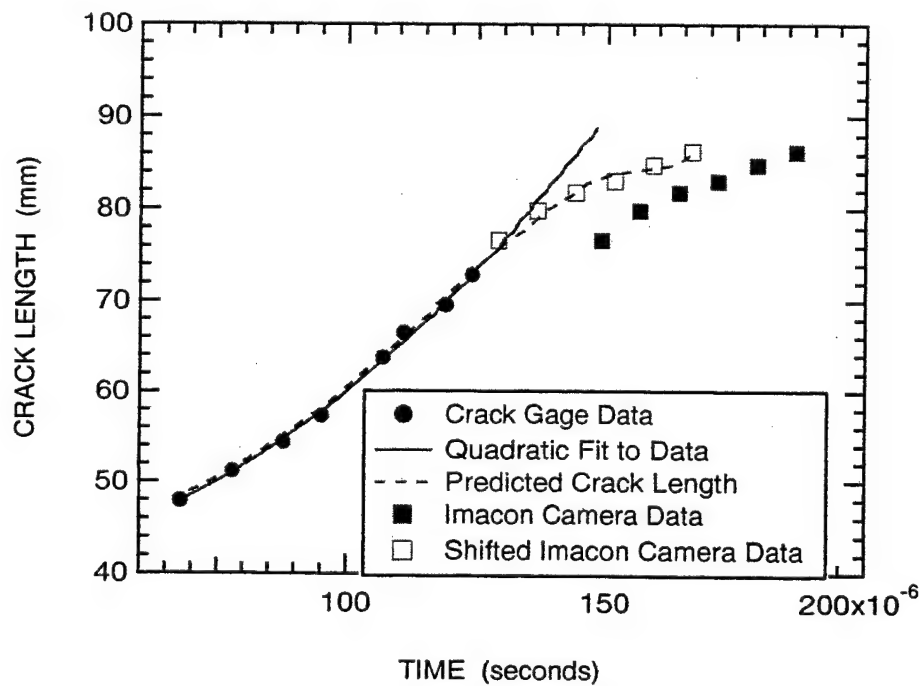


Figure 3.34 Comparison of Application Phase Analysis Predictions for the Crack Growth History with the Measured History for AISI 4340 CPB Specimen 2.

data show, consistent with the predictions, that the crack tip does decelerate as it approaches the rear surface of the specimen.

If the measured crack lengths from images captured with the Imacon camera occurred 20 μ s earlier, these data (represented by the open points) follow exactly the predictions as demonstrated in Figure 3.34. Unfortunately, there is no overlap in the crack gage data and the Imacon images. A definitive reason for a possible time shift this large is unknown and is only subject to conjecture.

3.6.2 AF 1410 Fracture Resistance. Generation phase analyses were also performed to determine the fracture resistance for the AF 1410 steel. Essential data for performing these analyses are measured load line displacement, crack growth and crack opening displacement histories. Table 3.1 reveals that these data are only available for Specimens CPB2 and CPB6 and are depicted in Figures 3.35, 3.36 and 3.37, respectively. Note that the measured COD histories contain rather larger oscillations after initiation of crack growth that were not evident in the tests for AISI 4340 and may not be real. It is clear from these figures that the larger preload, 623 kN for CPB2 versus 400 kN for CPB6, produced much larger responses for CPB2. In both cases the cracks propagated at nearly constant speeds.

Again, the measured LLD was used as a first approximation for the LPD in the predictor-corrector algorithm. Figures 3.38 and 3.39 compare the prediction of the COD with the measured data for CPB2 and CPB6, respectively. Figure 3.40 depicts the variation of the dynamic fracture resistance for each specimen with crack speed. The rapid variation of the fracture toughness is not real and is likely due to the strong oscillations in the measured COD history. Secondary effects are due to imprecision in the measurements of the crack growth history and differentiating it to determine the crack speed. It is believed that a better measure of the fracture toughness is represented by the mean or average for each specimen which are represented by the solid points in this figure. The average fracture toughness determined for the faster propagating crack in Specimen CPB2 is approximately 7 percent less than that determined for the slower propagating crack in CPB6. The fracture toughness is expected to increase with increasing crack speed. This difference is likely due to uncertainties in the measurements and the analysis of the data. The average dynamic toughness of approximately 260 MPa \sqrt{m} , determined

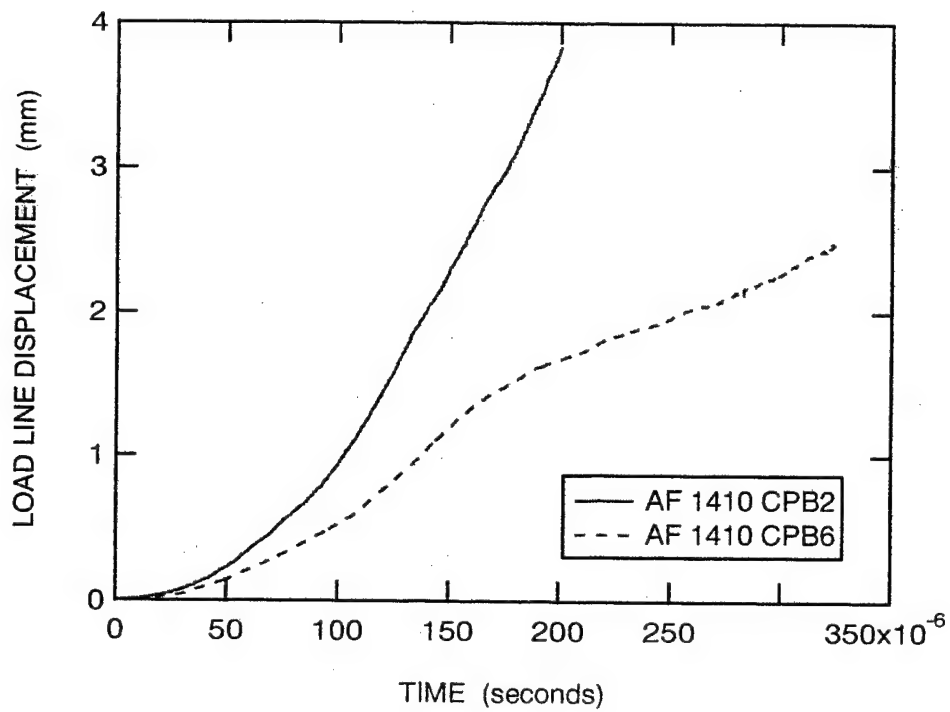


Figure 3.35 Measured Load Line Displacement for AF 1410 Specimens CPB2 and CPB6.

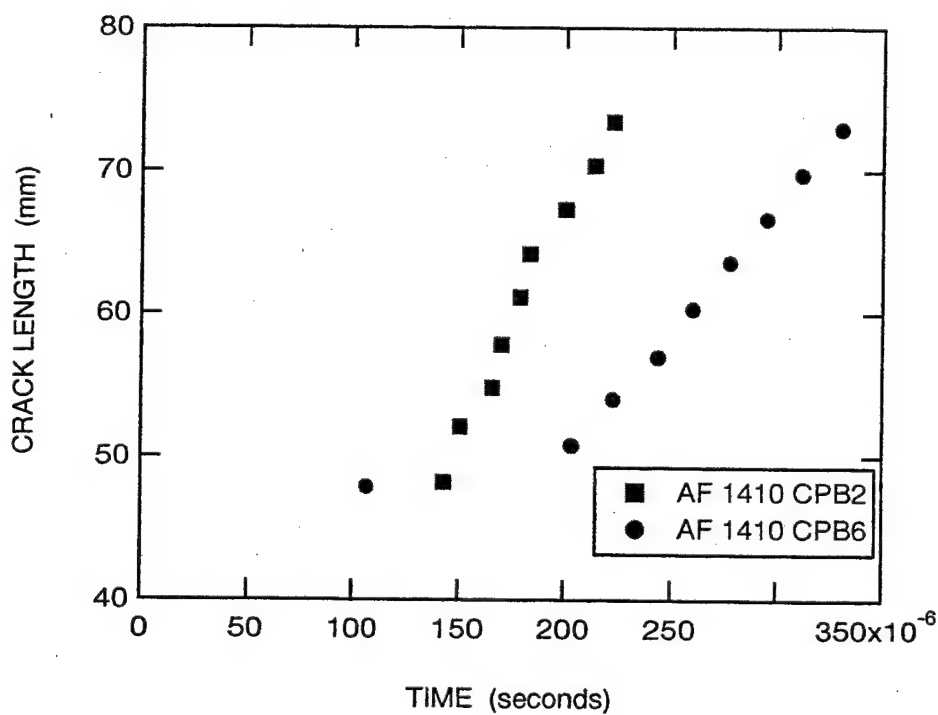


Figure 3.36 Crack Length-Time History for AF 1410 Specimens CPB2 and CPB6.

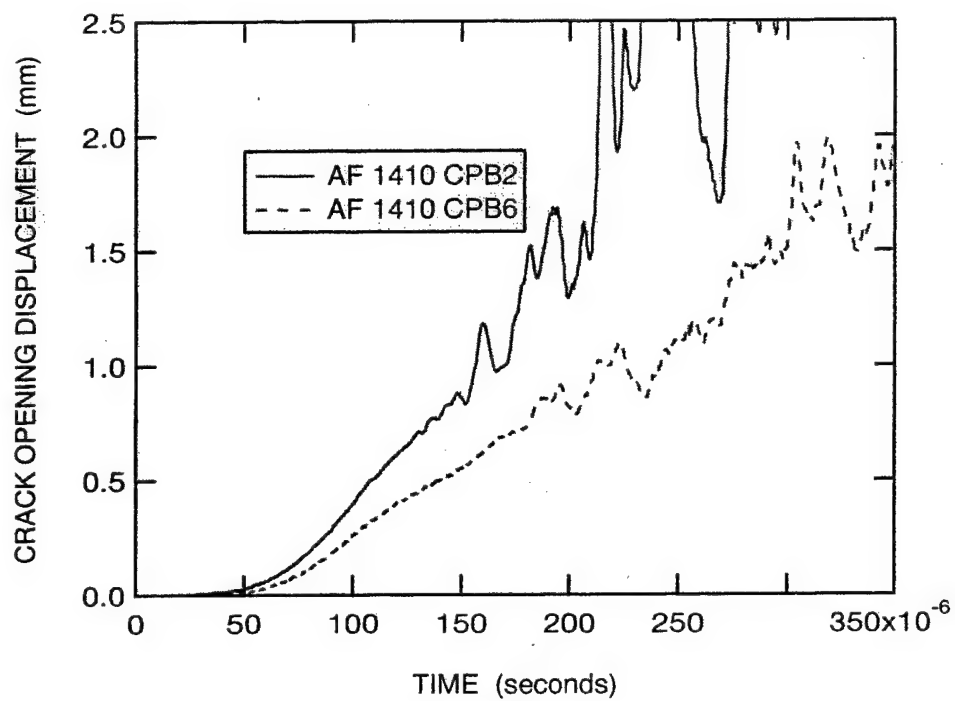


Figure 3.37 Measured Crack Opening Displacement for AF 1410 Specimens CPB2 and CPB6.

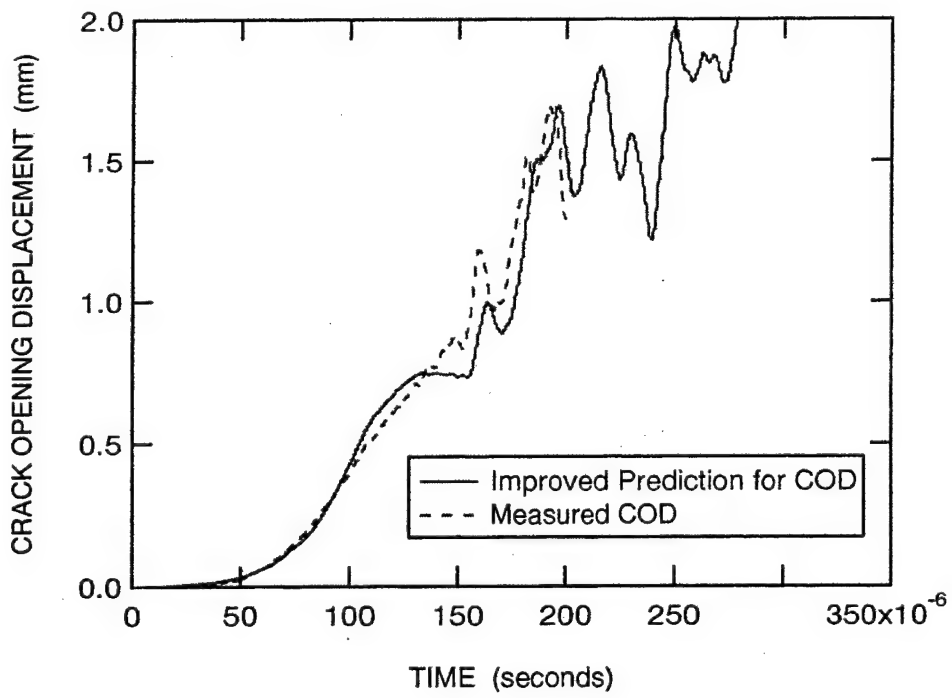


Figure 3.38 Comparison of Predicted and Measured COD for AF 1410 Specimen CPB2.

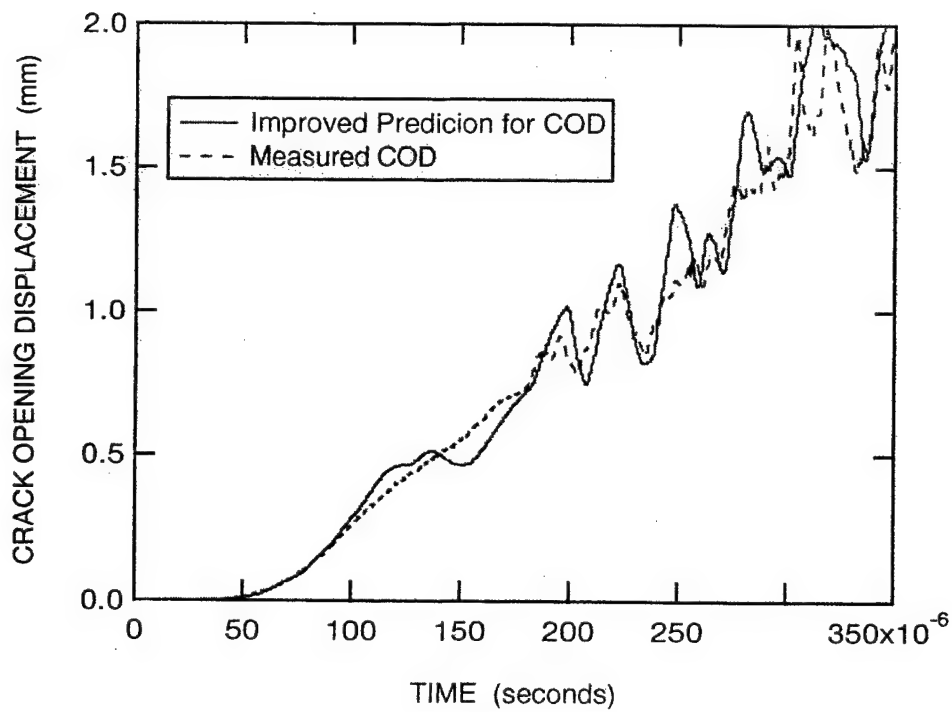


Figure 3.39 Comparison of Predicted and Measured COD for AF 1410 Specimen CPB6.

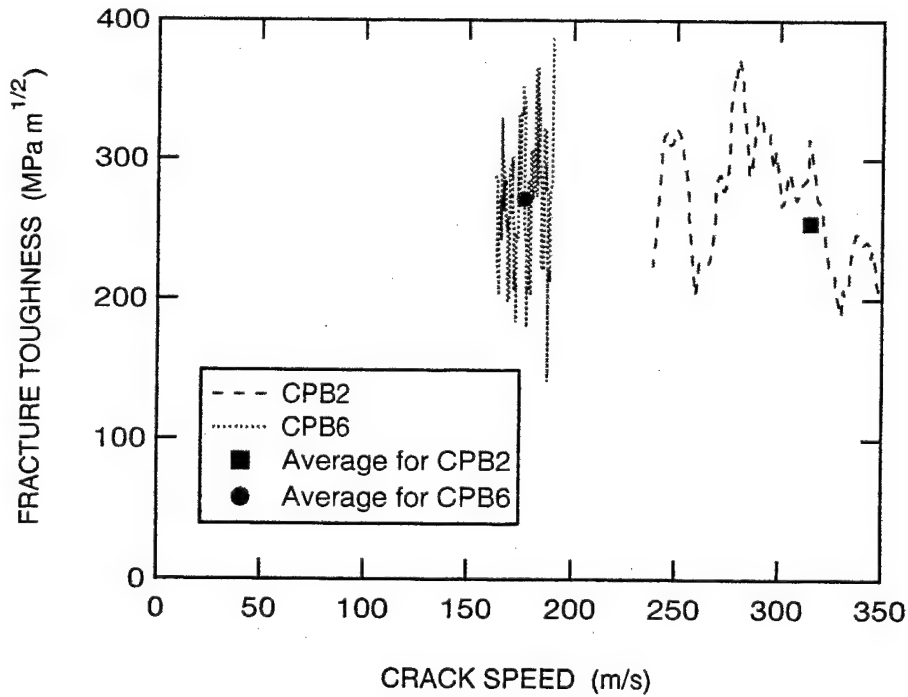


Figure 3.40 Deduced Dynamic Fracture Toughness for AF 1410 Steel.

from these tests, compares with the measured static initiation value of $187 \text{ MPa}\sqrt{\text{m}}$. These results suggest the fracture toughness for a running crack in AF 1410 is greater than its static value.

4.0 APPLICATION PHASE EXPERIMENTS AND ANALYSES

The internal consistency between the generation and application phase algorithms in EPIC has been previously demonstrated for the coupled pressured bar specimen. While this consistency is necessary, it is not sufficient to validate the dynamic fracture mechanics methodology. The purpose of the application phase experiments and analyses is to validate the methodology. The validation requires that the dynamic fracture resistance toughness data, derived from generation phase experiments, be transferable to predict the rapid crack growth history in another component of the same material subjected to a different type of loading; i.e., to ensure similitude is satisfied. Application phase tests are designed to aid in the validation of the methodology and the appropriateness of the measure for the crack driving force and its critical value, the fracture resistance. The crack propagation history is typically used as a metric for assessing the methodology by comparing measured and predicted histories.

The application phase experiment should possess the same attributes as the generation phase experiment. The experiment should have well defined, unambiguous boundary and loading conditions, and be relatively easy and inexpensive to perform. The test specimen and method of loading, however, should differ from that used in generation phase experiments for determining the dynamic fracture toughness. Since the fracture toughness may depend upon the thickness of the specimen if conditions of plane strain fracture are not satisfied, the specimens used in the generation and application phase tests must have the same thickness.

In the following, a description of the application phase experiment is presented. A series of six tests of AISI 4340 steel was conducted to develop a test protocol, an understanding of dynamic fracture phenomenon in this experiment, and data for use in verifying the dynamic fracture mechanics methodology. Typical data gathered in these tests are presented in the following; data from other experiments are contained in Appendix B. Finally, the dynamic fracture mechanics methodology used in this investigation is evaluated by comparing predicted and measured crack growth histories.

4.1 Application Phase Test Method

A notched three-point bend specimen is often used in laboratory fracture tests. To produce a rapidly propagating crack, the specimen is usually loaded using a drop weight machine or a pendulum machine, similar to a Charpy machine but much larger by comparison. Precise

measurements of the loads applied to the specimen in these tests are usually difficult. The interpretation and the analysis of the experiment are often confounded by intermittent loss of contact between the specimen and supports and/or anvil. A variation of the split Hopkinson bar arrangement [12] has been used to determine dynamic fracture initiation toughness using a bend specimen comparable in size to a Charpy specimen. Quasi-static loading of a specimen with a blunt starter notch has been used to create a supercritical condition to produce a rapidly propagating crack as it initiates from the notch. The energy available to drive the crack under displacement controlled loading is limited by the elastic energy stored in the specimen prior to initiation of crack growth and is proportional to the size of the specimen. While this method suffices for high strength, low toughness materials, it is inadequate for lower strength, higher toughness materials because it is virtually impossible to store sufficient elastic energy to drive the crack through the specimen.

A new dynamic fracture test method was developed in this research effort and is depicted schematically in Figure 4.1. Briefly, an instrumented, precracked three-point bend specimen is dynamically loaded through a transmitter bar that is struck by an impact or striker bar fired from a gas gun. The duration and intensity of the loading pulse delivered to the transmitter bar and ultimately to the specimen is controlled by the length and speed of the striker bar. This test arrangement has several advantages over other dynamic fracture test methods. While it does require a gas gun, it is, otherwise, relatively simple to perform. The initial and boundary conditions for the test are well defined. Although it was developed as an application phase test, it can also be employed as a generation phase test for determining the fracture toughness. Detailed descriptions of this test apparatus and method are presented in the following sections.

4.1.1 Dynamic Three-Point Bend Apparatus. The fracture specimen used in these experiments is a precracked three-point bend specimen. A machine drawing of the specimen appears in Figure 4.2, and Figure 4.3 contains a photograph of the specimen. The planar dimensions of the specimen are approximately 50 mm by 200 mm. The specimen has the same nominal thickness (approximately 25 mm) as the modified compact tension specimen used in the generation phase coupled pressure bar experiments. It contains a centrally located, through-thickness, machine notch that is approximately 16-mm deep. One face of the notch is relieved to accept an eddy current proximity gage for measuring the crack opening displacement (COD) during the dynamic fracture event. This specimen, like the generation phase specimen, contains side grooves that

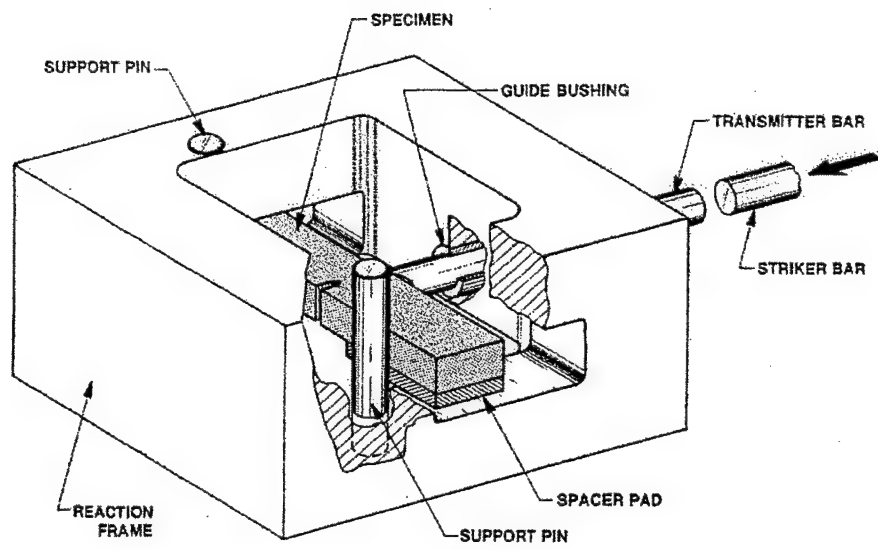
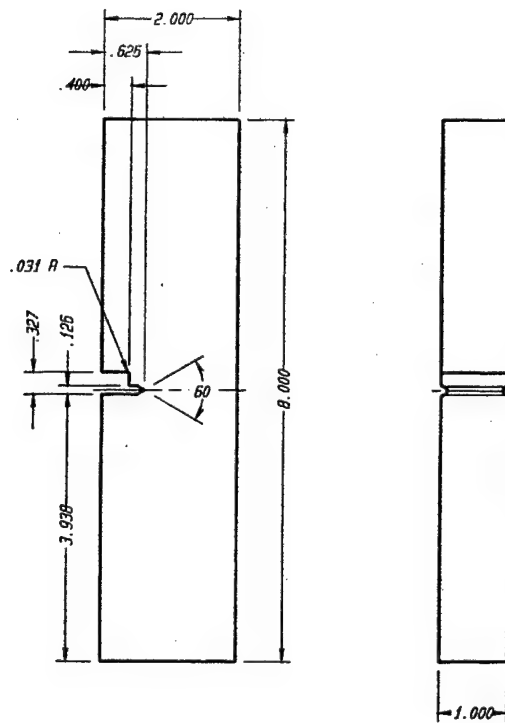


Figure 4.1 Schematic of Application Phase Experimental Setup.



**Figure 4.2 Machine Drawing of Three-Point Bend Specimen
(Dimensions in Inches).**

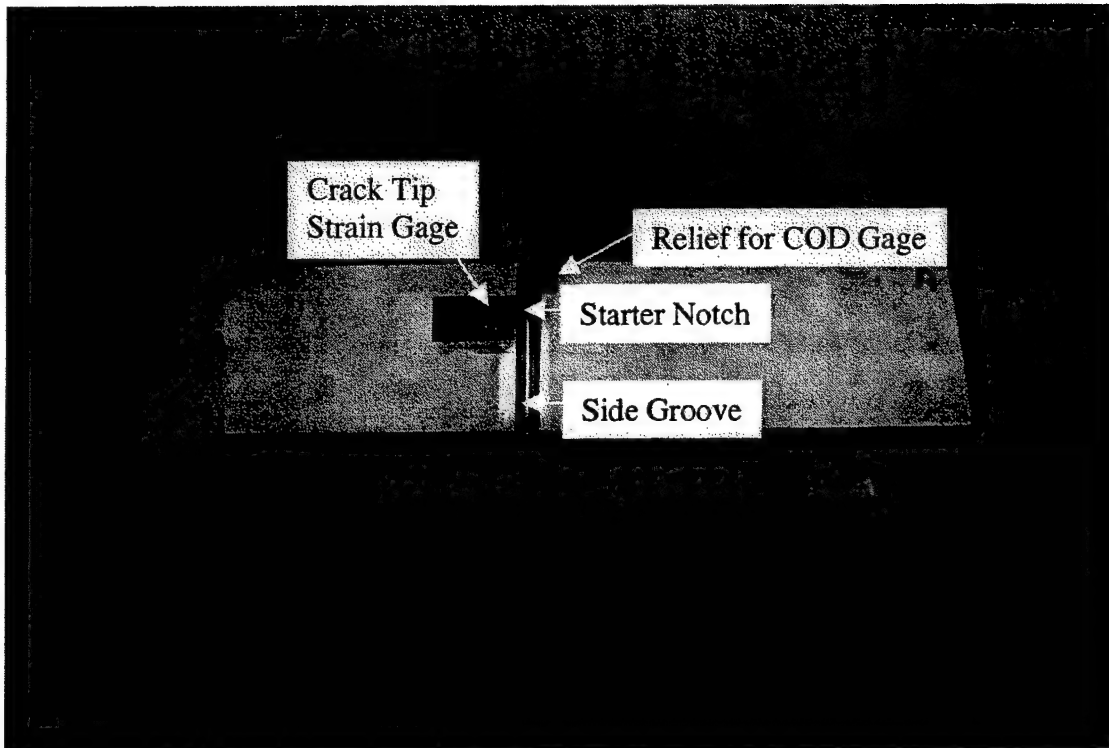


Figure 4.3 Photograph of Dynamic Three-Bend Specimen Identifying Starter Notch, Side Groove and Relief for COD Gage.

have approximately 10 percent relief on each side of the specimen. These grooves are used to promote plane strain fracture and preclude bifurcation or curving of the crack during the test.

A sharp fatigue crack is produced at the base of the machined notch by cyclically loading the specimen between a maximum stress intensity factor of approximately 60 percent of the plane strain fracture toughness K_{Ic} and a minimum stress intensity factor equal to 10 percent of the maximum value (i.e., R-ratio equal to 0.1). The fatigued crack is typically grown approximately 1.5 mm beyond the machine notch.

The specimen is instrumented in several ways. One strain gage is located approximately 10 mm opposite the fatigue crack tip (see Figure 4.4). A KAMAN Instrument Corporation Model 2UB eddy current sensor is used with Model KD 3210-2UB oscillator/demodulator to measured the crack opening displacement. The sensor is 10.8 mm in diameter and 6.35 mm thick. This COD gage has a linear range over approximately 2.5 mm of displacement. After calibrating the sensor, it is bonded with epoxy cement to the relief in the starter notch. These two devices are typically used to assess the veracity of an analysis of the event. A second strain

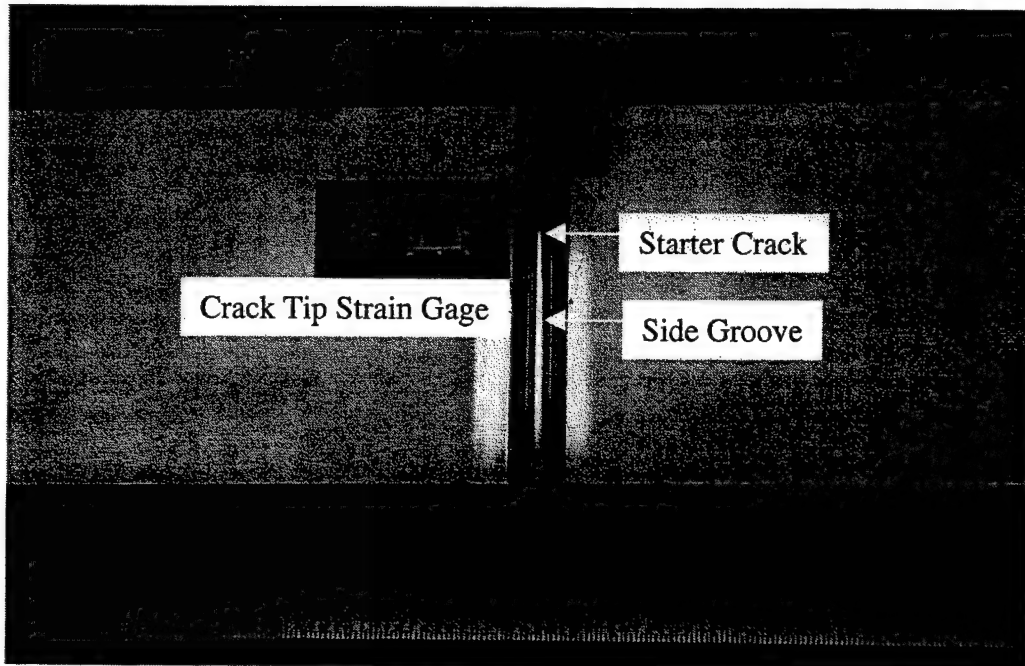


Figure 4.4 Close-up View Showing Location of Crack Tip Strain Gage Relative to Starter Crack and Side Groove.

gage is applied to the specimen about 6 mm above the point of contact at the support pin to ascertain whether or not the specimen lifts off the support during the fracture event.

A crack gage is applied to the lateral surface of the specimen to measure the crack growth history. The previous method of silk screening the gage onto the specimen used in the coupled pressure bar test is a tedious and laborious process for a side-grooved specimen. Therefore, Hartrun Corporation¹ was commissioned to manufacture a crack ladder gage to SwRI specifications. The 50-mm long crack gage consists of 40 equally spaced thin metallic rungs, 0.25-mm wide and located 1.27 mm on centers, deposited on a thin, flexible, electrically insulated substrate.

The gage may be cut to length as required for different length of ligament. The gage is bonded to the specimen in much the same way that a strain gage is applied. A side groove of a specimen was used as a form to cast a polyurethane piece that conforms to the shape of the side groove. This piece is used to facilitate placing the crack gage in the base of the side groove and

¹ Hartrun Corp., St. Augustine, FL.

holding it there while the epoxy cement cures. Figure 4.5 shows a specimen with the Hartrun crack gage. The crack tip gage is on the backside and is not visible in this view.

In a test, each rung of the crack gage is wired into a high speed transient counter, operating at 10 MHz, to monitor the electrical continuity of each rung and to record the time when a rung is broken by the propagating crack tip. Specimen 1 was prepared with a Hartrun ladder gage on one side of the specimen and a silk-screened gage on the other, and the measured crack growth histories with the two gages in a test were compared. The crack position versus time recorded using these gages overlap very nicely as depicted in Figure 4.6 and produced the same crack growth history. Therefore, the Hartrun crack gages proved to be successful and were used to measure the crack growth history in subsequent tests.

A ladder gage with 24 rungs can be applied to the bend specimen. Since the high-speed transient counter used in the tests only accommodates 18 channels, not all rungs can be monitored. Typically, each rung except for every third one between the first five and last four rungs is used in a test. This arrangement permits measurement of the crack growth to be made over the entire ligament. An exception was for Specimen 2 where the first 17 rungs and the last one were monitored (two anomalies in the measurement occurred in this test).

In a test, a three-point bend specimen is contained within a massive steel base fixture as shown in Figure 4.1. The specimen is supported by two 25.4-mm diameter pins made of a high-grade alloy steel and located 165 mm on centers. The 254-mm long by 25.35-mm diameter transmitter bar and 138.7-mm long by 25.32-mm diameter striker bar are made from VASCOMAX 350 CVM, a maraging steel with a yield strength of approximately 2.3 GPa. The end of the transmitter bar in contact with the specimen is machined to produce a line load. Spacer plates are used to position the specimen in the fixture.

The supporting base fixture is bolted to the flange of a large wide flange beam on which a gas gun is mounted. Figure 4.7 contains an overall view of the setup showing the test bench, gas gun, specimen supporting base fixture and instrumentation while Figure 4.8 provides a closer view of the supporting fixture. The fixture is aligned so that the axes of the transmitter and striker bars are collinear. The speed of the striker bar as it exits the gun barrel has been calibrated against the gas pressure in the gun. By adjusting the pressure, the striker bar's speed can be controlled; two photodiodes are used to provide an accurate measurement of the impact speed. Depending upon the length of the striker bar, speeds up to 120 m/s can be attained with

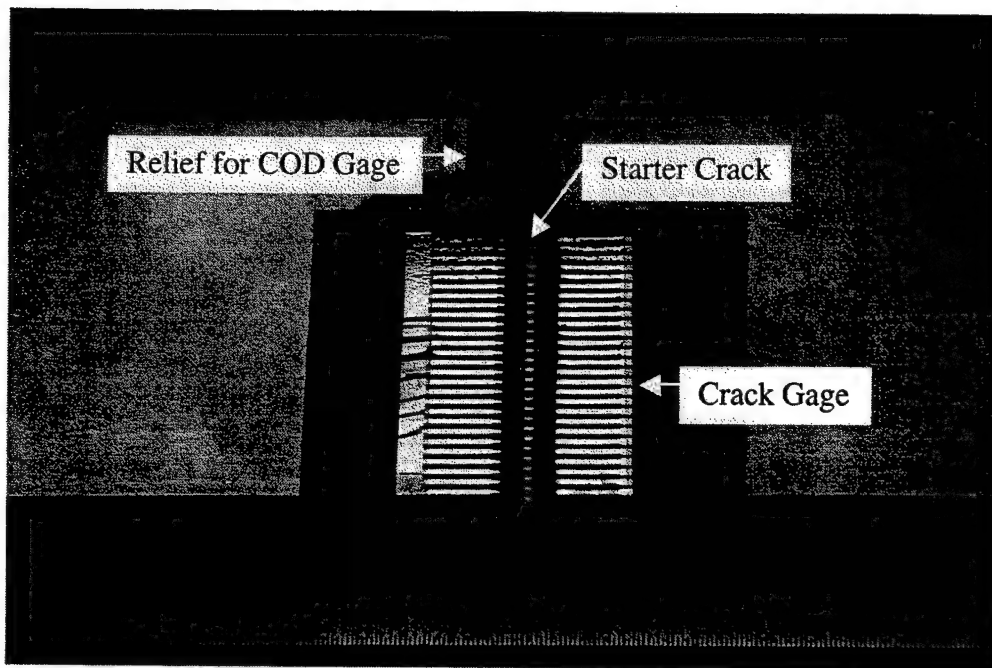


Figure 4.5 Close-up View of Hartrun Crack Gage Applied to Specimen.

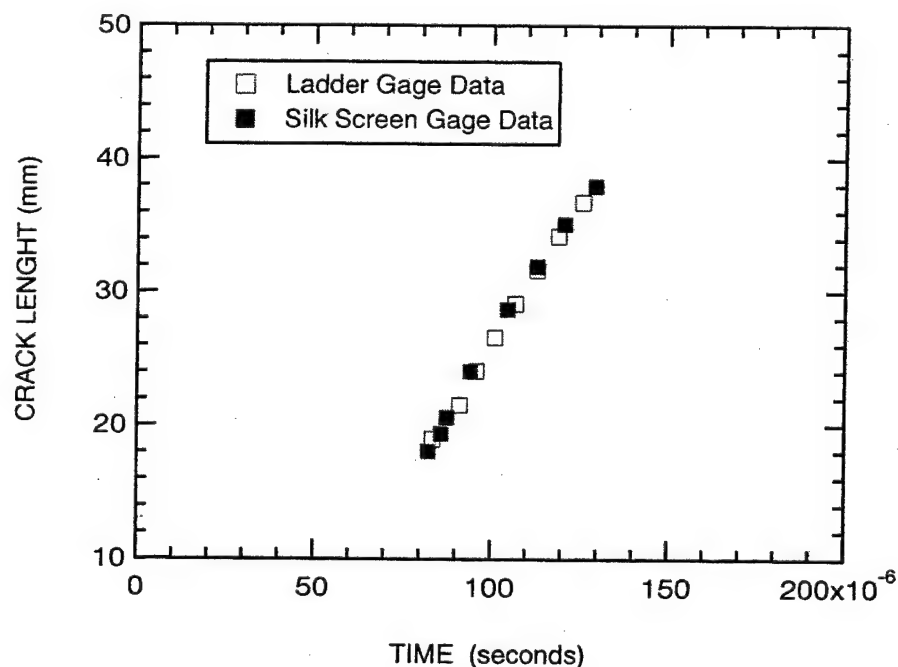


Figure 4.6 Comparison of Crack Growth Histories Measured in Test 1 Using Hartrun Crack Ladder Gage and Silk Screen Crack Gage.

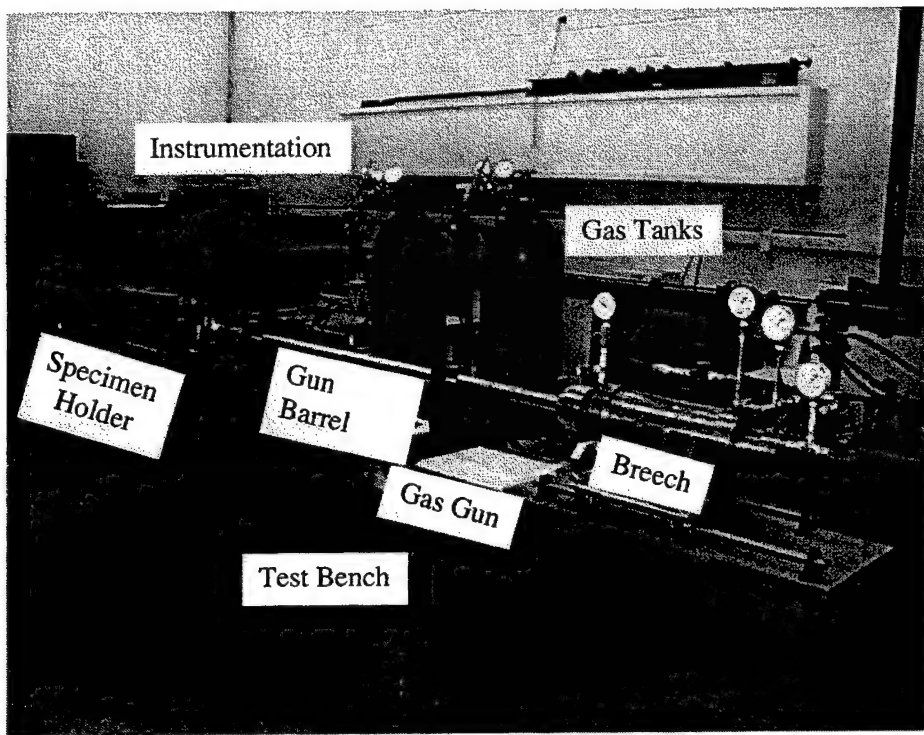


Figure 4.7 Overall View of Test Setup Showing Test Bench, Gas Gun, Specimen Holder and Instrumentation.

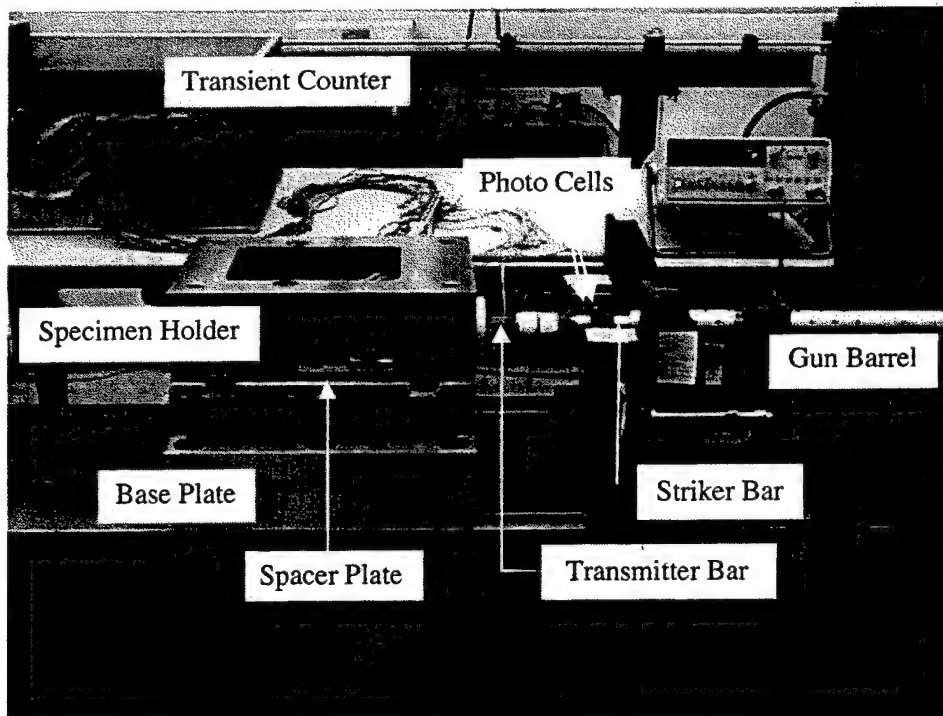


Figure 4.8 Close-up View of Test Apparatus.

this gas gun. However, the maximum speed of the striker bar is limited to approximately 90 m/s to avoid yielding the bars. The length of the striker bar and its speed determine, respectively, the duration and intensity of the generated loading pulse.

4.1.2 Test Procedure. The fatigue precracked, three-point bend test specimen is instrumented with a crack growth ladder gage, an eddy current proximity gage for measuring the COD, and strain gages opposite the crack tip and a support pin. The specimen geometry (length, height, thickness, net thickness in the side groove, and initial crack length) and positions of the strain gages and locations of the rungs of crack gage are measured and recorded. The specimen is placed in the supporting fixture and positioned so that the starter notch and the axis of the transmitter bar are properly aligned. Figure 4.9 shows the crack gage and eddy current proximity gage on the specimen positioned in the supporting fixture. The crack tip gage is on the backside and is not visible. A cover plate is placed on the fixture prior to a test to contain the fractured specimen.

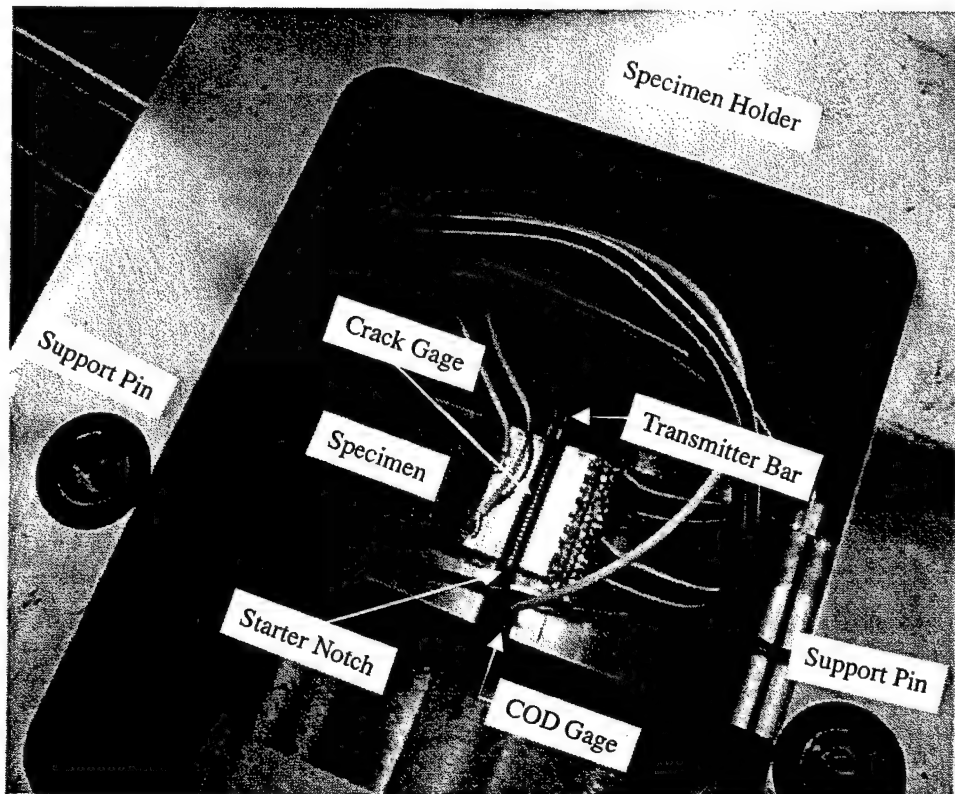


Figure 4.9 View of Specimen Positioned in the Specimen Holder.

The specimen and transmitter bar strain gages are connected to separate high speed strain conditioners typically used in elastic wave propagation tests. The outputs from these conditioners and from the eddy current proximity gage are connected into the four channels of a Nicolet digital storage oscilloscope. The sampling interval of the oscilloscope is set at 0.2 μ s. Electrical connections from each rung of the crack gage are made to the transient counter. The loss of electrical continuity of the first rung of the crack gage triggers the oscilloscope whose pretrigger is set at 300 μ s.² After the second test, a fourth strain gage was placed on the face of the transmitter bar to record the instant of impact between it and the striker bar. The output from this gage is connected to a second Nicolet oscilloscope that is slaved with the first one. In this way, the instant of impact is measured.

A speed for the striker bar is selected and the gas gun is pressurized according to the calibration for the specific striker bar. A dedicated timer is used to record the signals from the photodiodes, from which the actual speed of the striker is determined. All data recording devices are checked and strain gages zeroed as required. When all systems are ready, the gun is fired. The oscilloscope data are saved on a floppy diskette and transferred to a spreadsheet at the conclusion of the test. The transient counter times, defining the sequential failure of rungs of the crack gage, are manually recorded and entered onto the same spreadsheet.

4.2 Dynamic Fracture Data

A total of six specimens were tested and the test conditions are summarized in Table 4.1 along with the time of impact between the striker and transmitter bars, and the deduced time for initiation of crack growth. The latter time is determined by extrapolating the measured crack growth history to the measured initial crack length. In all of these tests, except the first one where the trigger was off the transmitter bar strain gage output, time equal to zero corresponds to breaking of the first rung of the crack gage.

² An exception was the first test in which the output from the strain gage on the transmitter bar was used to trigger the oscilloscope, independently of the crack growth measurements. This made the task of synchronizing the measured oscilloscope signals with the crack growth difficult and introduces a degree of uncertainty. This procedure was abandoned in favor of triggering off the first rung of the crack gage so that all signals are automatically synchronized.

Table 4.1 Summary of Application Phase Dynamic Three-Point Bend Tests

Specimen No.	Specimen Thickness (mm)	Side-Groove Width (mm)	Initial Crack Length (mm)	Striker Speed (m/s)	Impact Time (μs)	Crack Initiation Time (μs)
1	24.33	19.71	17.69	36.96	-12.5	82.5 ^(a)
2	24.35	19.71	17.41	30.47	-107.7	-1.7
3	24.37	19.71	17.26	30.47	-138	-34 ^(b)
4	24.35	19.71	17.26	31.77	-103	-0.7
5	24.35	19.71	17.42	87.58	-82.2	0
6	24.37	19.66	17.32	20.77	-127.5	-0.7

^(a) In this test, the measurements were triggered off the strain gage on the transmitter bar which takes place approximately 12.5 μs after impact. The crack growth measurements were made independently of this trigger, and the measurements and crack growth history were synchronized using the peak in the measured crack tip strain as an indicator of crack initiation. Crack initiation is estimated to occur at 82.5 μs. Subsequent tests were triggered off the breaking of the first rung of the crack gage so that all recorded data have a common time line.

^(b) In this test the first two rungs on the crack gage failed after initiation of crack growth because of inadequate bonding between the gage and specimen. A comparison of the measured crack growth data for the replicate Test 4 indicates that crack initiation likely occurred at approximately -34 μs.

Typical data recorded during Test 2 are depicted in Figures 4.10 through 4.14. The specimen's length, height and full thickness are 203.2 mm, 50.8 mm and 24.35 mm, respectively. The thickness of the specimen at the base of the side groove is 19.71 mm. The initial crack length including the fatigue precrack was 17.41 mm. In this test, the striker bar was launched with a speed of 30.47 m/s.

Figure 4.10 shows the measured crack growth history. The crack propagates at nearly a constant speed of 324 m/s and complete fracture of the specimen takes place in approximately 100 μs. Extrapolation of the data to the initial crack length indicates that initiation of crack growth occurred at -1.7 μs.

Figure 4.11 displays the variation of the strain on the surface of the transmitter bar with time. The strain gage is located 63.5 mm from the impact end. The first evidence of straining detected by this gage occurs at -95.2 μs. Since it takes approximately 12.5 μs for a longitudinal wave travelling at 5,000 m/s to propagate from the impact end to the strain gage on the transmitter bar, then the impact occurred at -107.7 μs. Classical one-dimensional wave theory indicates that the striker bar should produce a strain pulse with an amplitude of 0.3% and a duration of approximately 55 μs in the transmitter bar. Radial inertia, neglected in the one-dimensional wave theory, causes the rise of the pulse to occur slightly sooner followed by an overshoot and

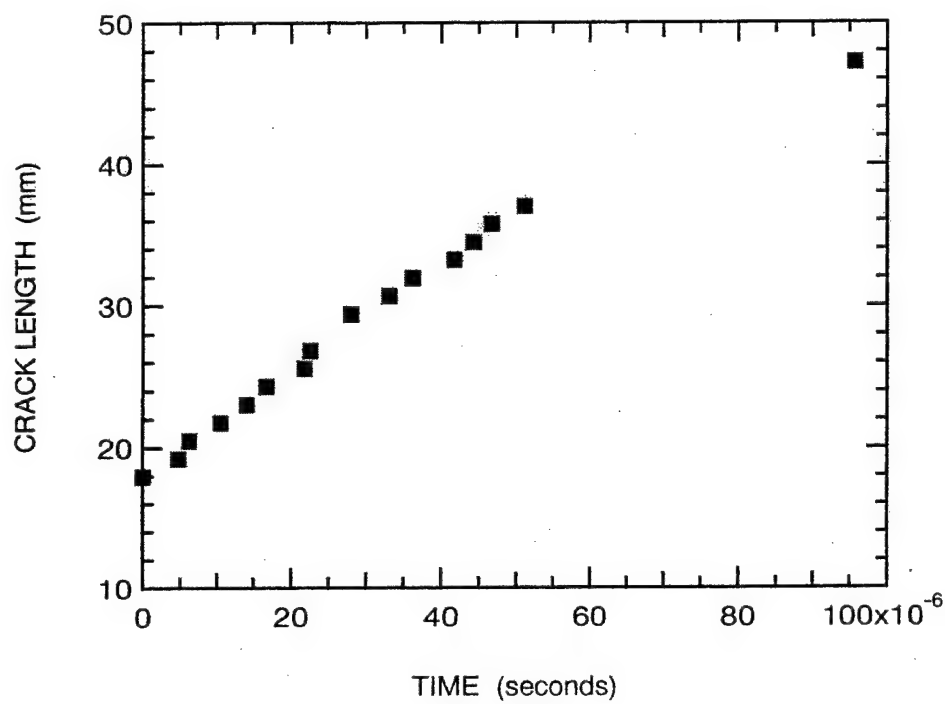


Figure 4.10 Measured Crack Growth History for Specimen 2.

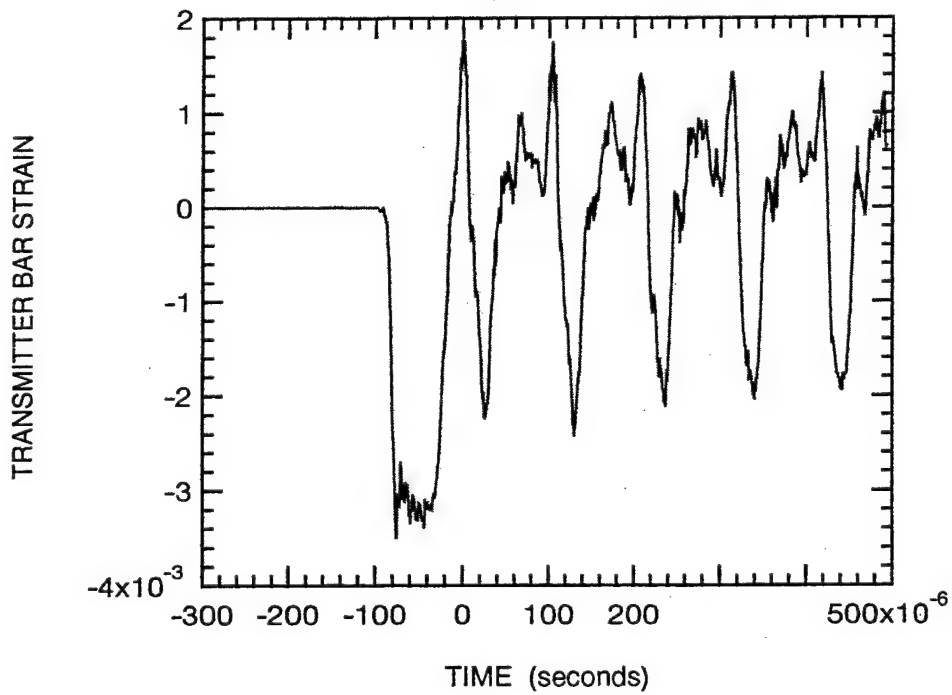


Figure 4.11 Measured Variation of Transmitter Bar Strain for Specimen 2.

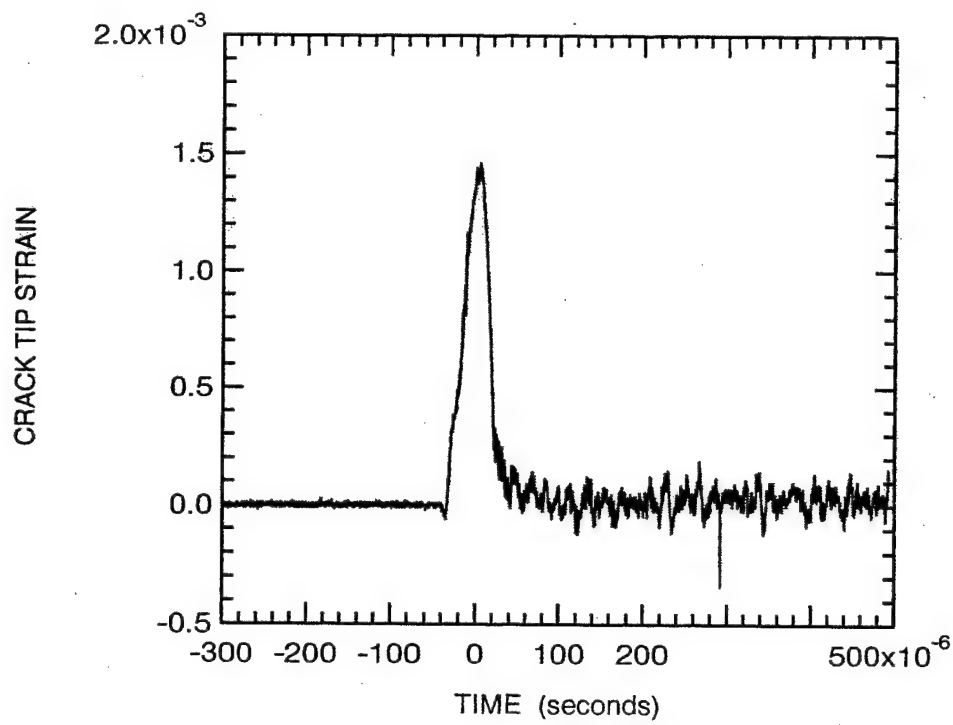


Figure 4.12 Measured Variation of the Crack Tip Strain for Specimen 2.

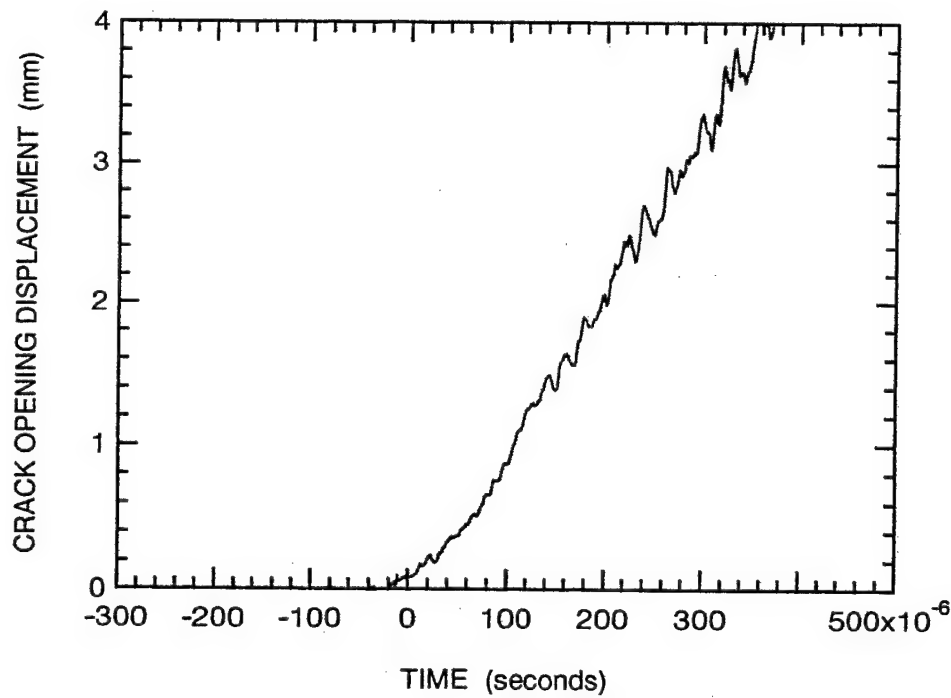


Figure 4.13 Measured Variation of the Crack Opening Displacement for Specimen 2.

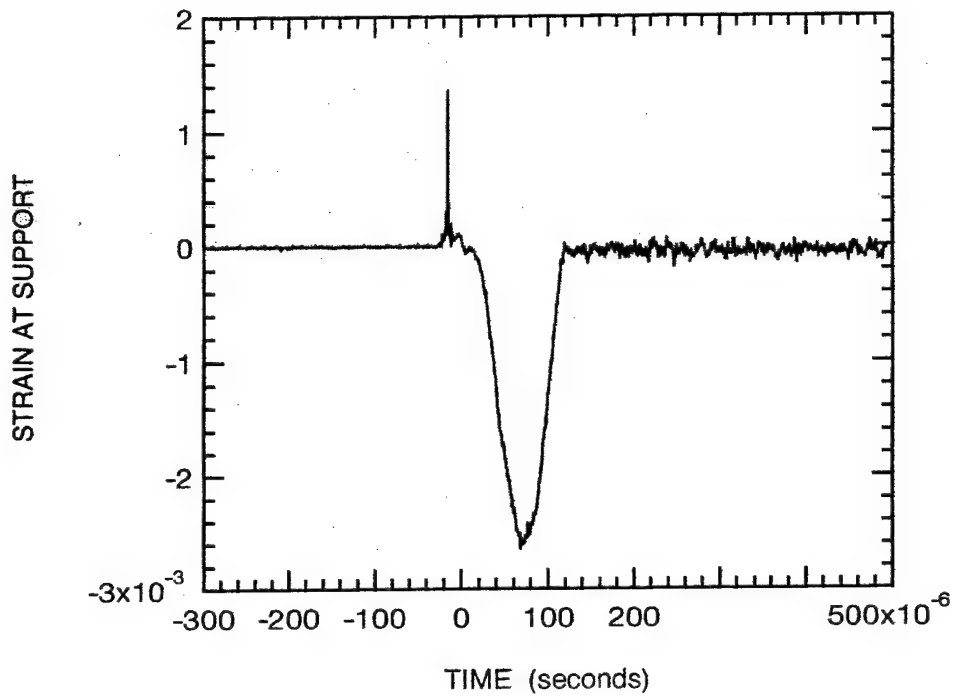


Figure 4.14 Measured Variation of the Strain at the Pin Support for Specimen 2.

subsequent oscillatory behavior. When consideration is given to the latter, the first part of the measured amplitude and pulse duration agree with the simple wave theory estimates.

While complete fracture of the specimen occurred at approximately 100 μ s, it takes about 37.5 μ s (the time for a wave to propagate from the specimen end of the transmitter bar to the strain gage) for this information to be communicated to the strain gage on the transmitter bar. Therefore, the measured strain in the bar for times greater than approximately 138 μ s reflects the propagation of a wave trapped within the bar. The period of oscillation is approximately 105 μ s and is in good agreement with the round trip flight time for a longitudinal wave in a 254-mm long bar.

Figure 4.12 depicts the strain measured at a site opposite the initial crack tip at a distance of 10 mm. A very rapid rise in the strain occurs as the specimen is loaded through the transmitter bar. Initiation of crack growth can be identified with the first peak of the strain. The material in the neighborhood of the path of the crack quickly unloads and reduces the strain as the crack tip passes.

The measured crack opening displacement (COD) in this test appears in Figure 4.13. The COD commences increasing at approximately $-40\text{ }\mu\text{s}$ into the event and attains a value of approximately 0.9 mm at the end of the fracture event at $100\text{ }\mu\text{s}$.

Figure 4.14 shows the measured strain at a point 6 mm above the support pin. The spike in the measured signal is thought to be due to electrical noise and not real. The signal indicates initially small tensile strains followed by much larger compressive strains that ultimately decrease to zero at approximately $119\text{ }\mu\text{s}$. This time is in excellent agreement with the value obtained when the time of flight of approximately $19\text{ }\mu\text{s}$ for a wave to travel from the load point to the support pin is added to the $100\text{-}\mu\text{s}$ fracture event. Except for the initial tensile straining, the results indicate that the specimen remains in contact with the support pin during the fracture event.

Since the initial small tensile strains might be interpreted as indicating that the specimen separated from the support pin, a modification was made to the support fixture to prevent the specimen from lifting off the support pins. A 19-mm diameter ball bearing is placed at mid thickness against the specimen opposite each support pin. The ball, which makes only a point contact with the specimen, is held in place by a 19-mm diameter rod that fits into a hole bored into the specimen support fixture. A cup was machined into one end of the rod to support the bearing and the other end of the rod was backed by a set screw to keep the bearing in contact with the specimen. The rod had a reduced cross section that serves as a weak link to avert potential damage if pieces should bind in the fixture.

Tests 3 and 4 used this arrangement. Figure 4.15 shows the measured support strain for Test 4 which replicates Test 2 with this support system. Even in this case for which lift-off is prevented, tensile straining occurs initially. Subsequent numerical simulations also predict a similar behavior, with the analysis predicting no lift-off. A comparison of this trace with that in Figure 4.14 shows excellent agreement in the measured strains over the period of interest. It is concluded that lift-off of the specimen only occurred after the crack had propagated through the specimen. Therefore, the ball bearing support arrangement was not used hereafter.

Test 5 was conducted at an impact speed of 87.58 m/s which is near the upper limit for which plastic yielding of the bars will not occur. This resulted in a much more dynamic and violent event that destroyed the COD gage (e.g., see Figures B21 through B25 in Appendix B). The nonuniform crack speed exceeded 570 m/s initially and slowed to less than 40 m/s near the end of the fracture event.

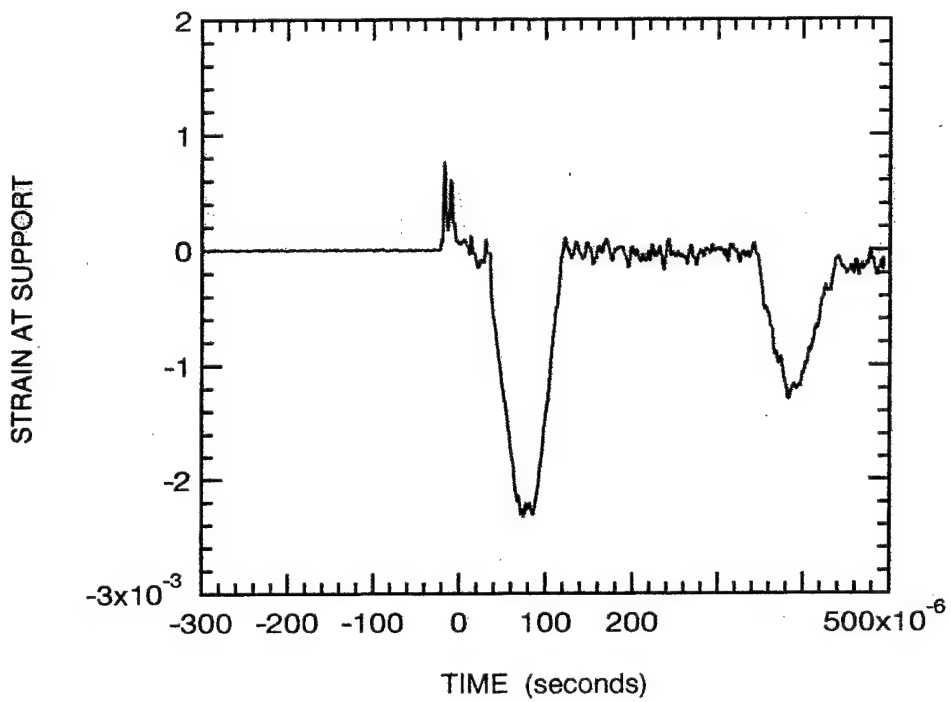


Figure 4.15 Measured Variation of the Strain at the Pin Support for Specimen 4.

During the course of performing numerical simulations of the application phase tests, it was decided that additional strain measurements would be advantageous. Therefore, three more strain gages were applied to Specimen 6. One strain gage was placed in the root of the side groove at the mid-point of the initial remaining ligament (i.e., 17.45 mm from loading (top) face of the specimen). A second strain gage was placed 10 mm opposite the site of this one and inline with the crack tip gage. The third strain gage was centered on the loading face of the specimen 10 mm from the point of impact.

The striker bar speed in Test 6 was 20.77 m/s compared to, for example, 30.47 m/s in Test 2. The data from this test appear in Figures 4.16 through 4.23. Again, the recorded transient spikes are thought to be due to electrical noise since they all occur at approximately the same time for this set of gages. The crack speed was nearly constant at 290 m/s over the major portion of the fracture event.

When the measured transmitter bar strain in Test 6 is increased by the ratio of the striker bar speed in Test 2 to that in Test 6 (i.e., by the ratio 30.47/20.77), there is very good correspondence between this value and the measured transmitter bar strain in Test 2. Figure 4.24 depicts this

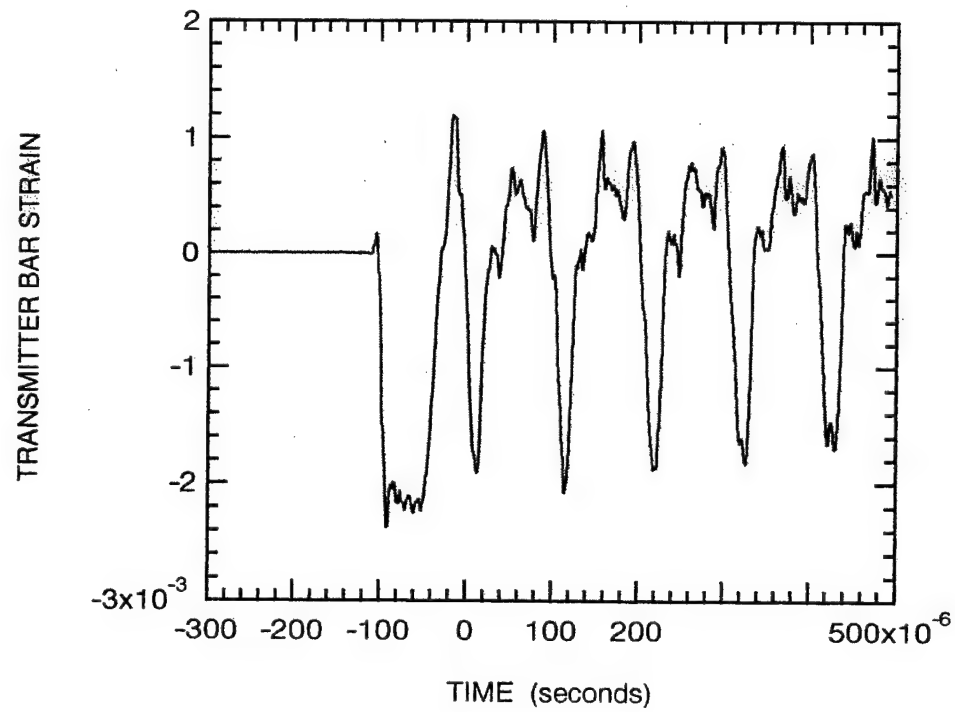


Figure 4.16 Measured Variation of the Transmitter Bar Strain for Specimen 6.

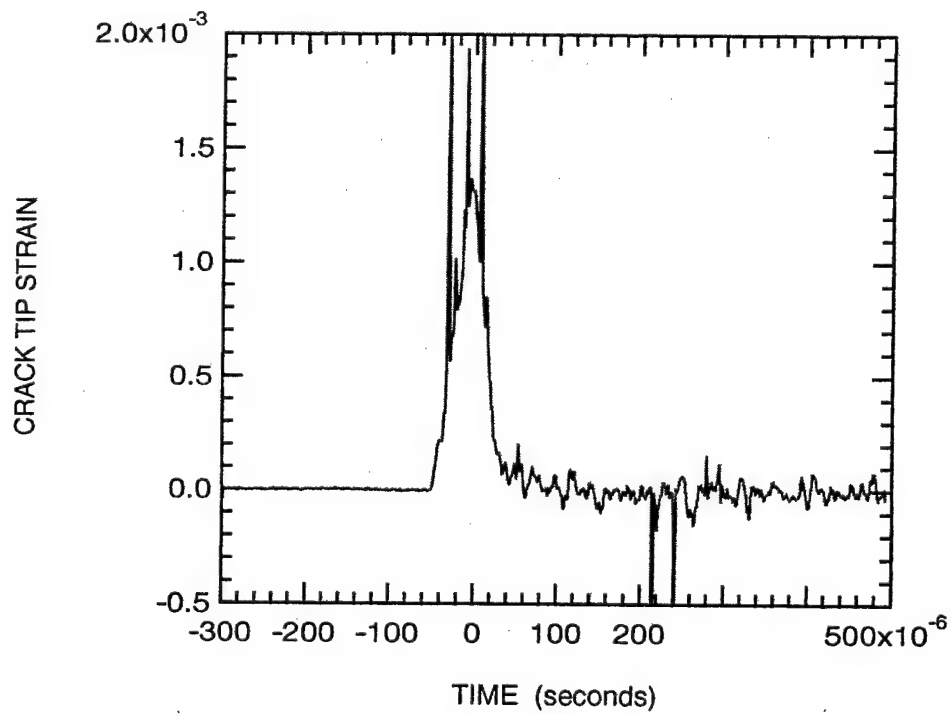


Figure 4.17 Measured Variation of the Crack Tip Strain for Specimen 6.

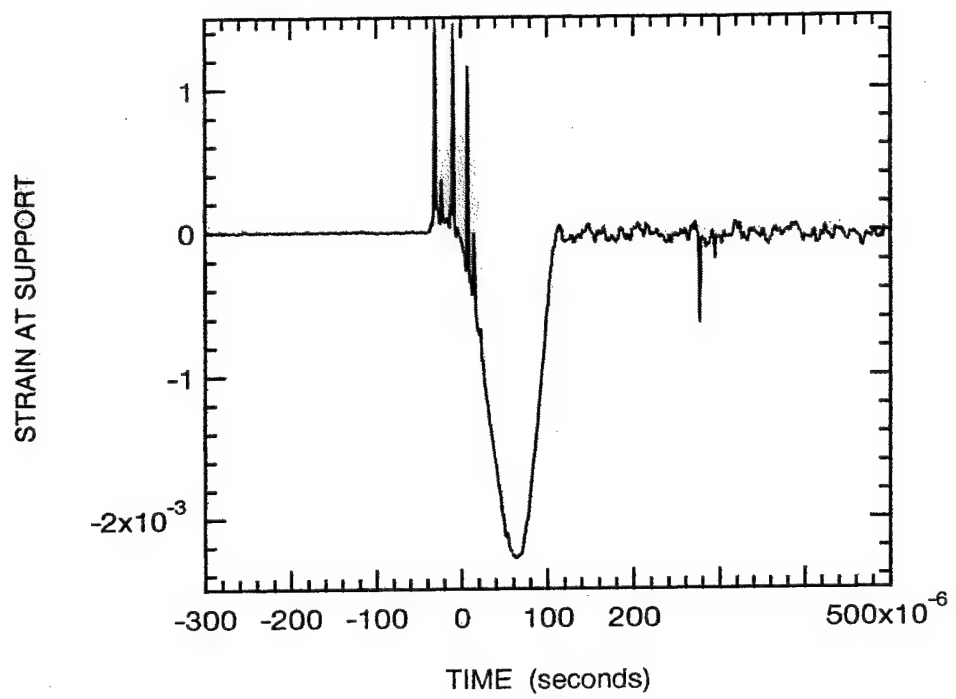


Figure 4.18 Measured Variation of the Strain at the Pin Support for Specimen 6.

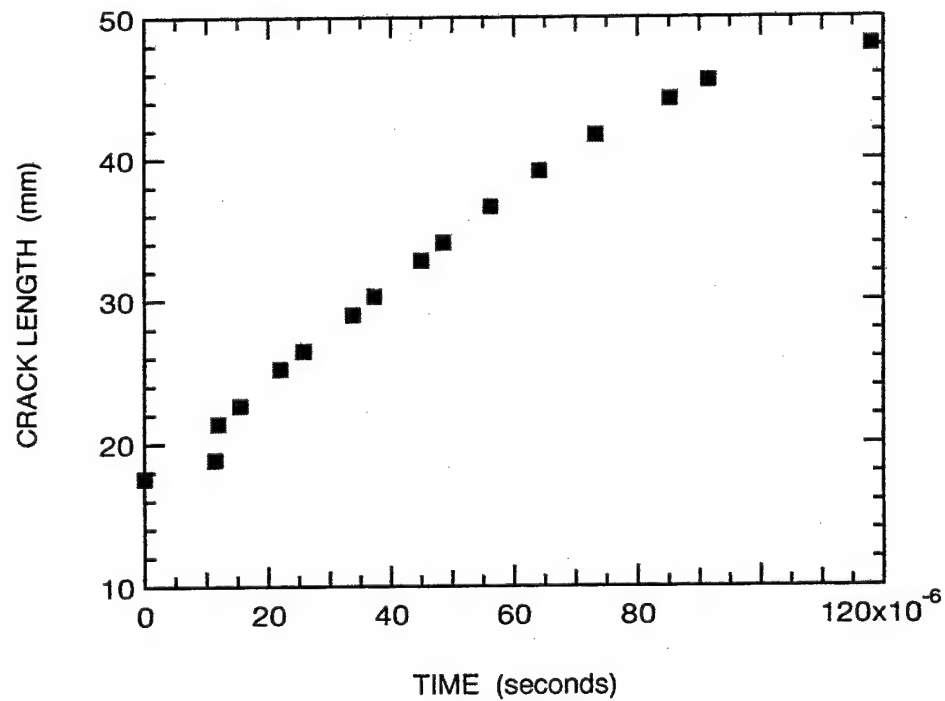


Figure 4.19 Measured Crack Growth History for Specimen 6.

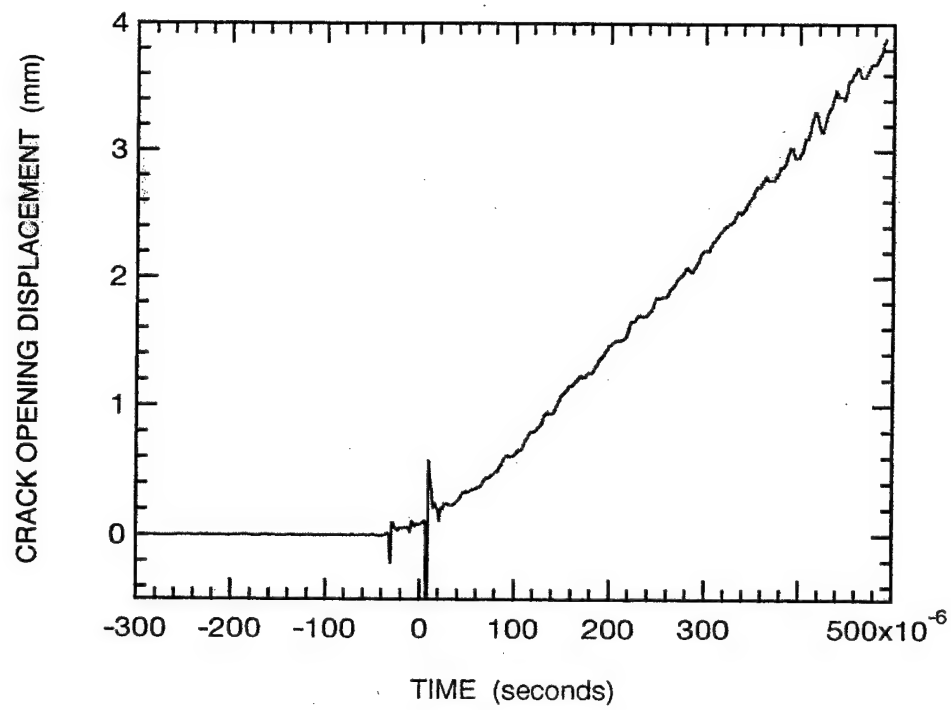


Figure 4.20 Measured Variation of the Crack Opening Displacement for Specimen 6.

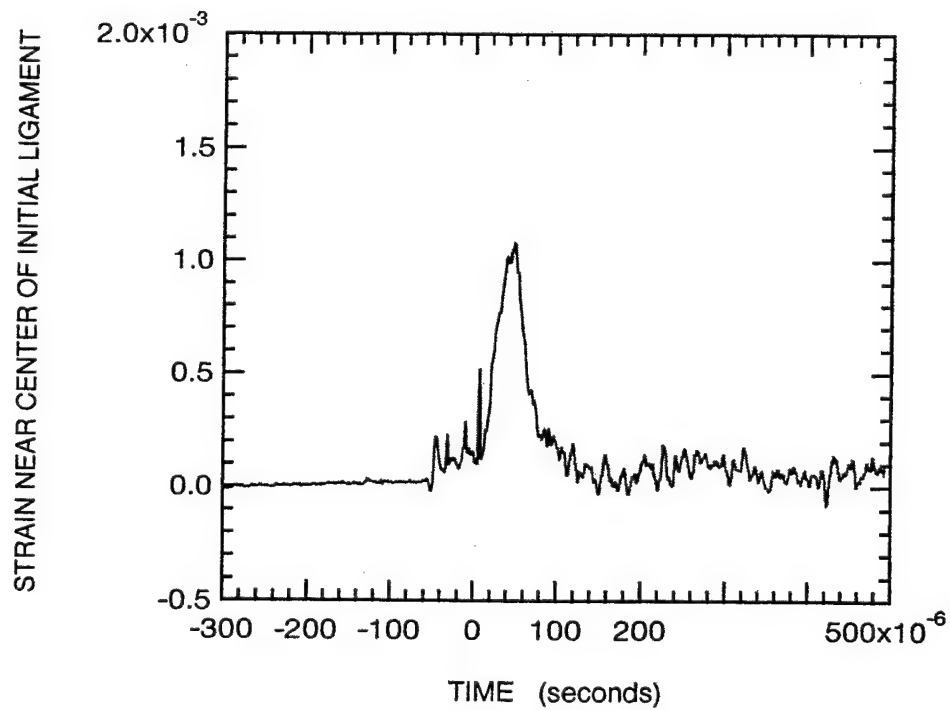


Figure 4.21 Measured Strain Near Center of Initial Ligament of Specimen 6.

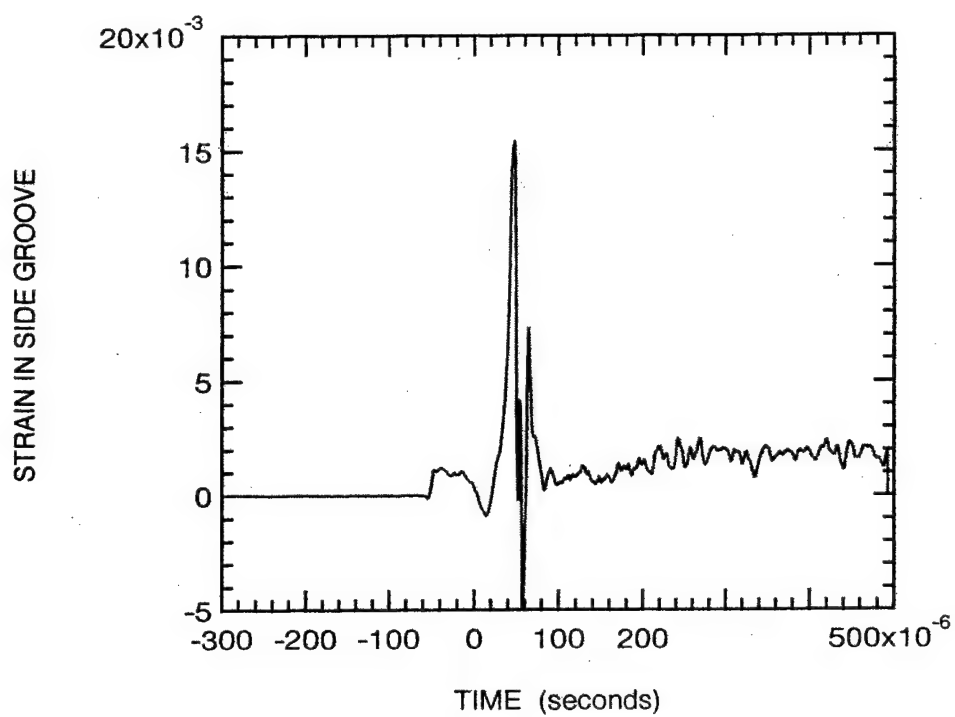


Figure 4.22 Measured Strain at the Root of the Side Groove in Specimen 6.

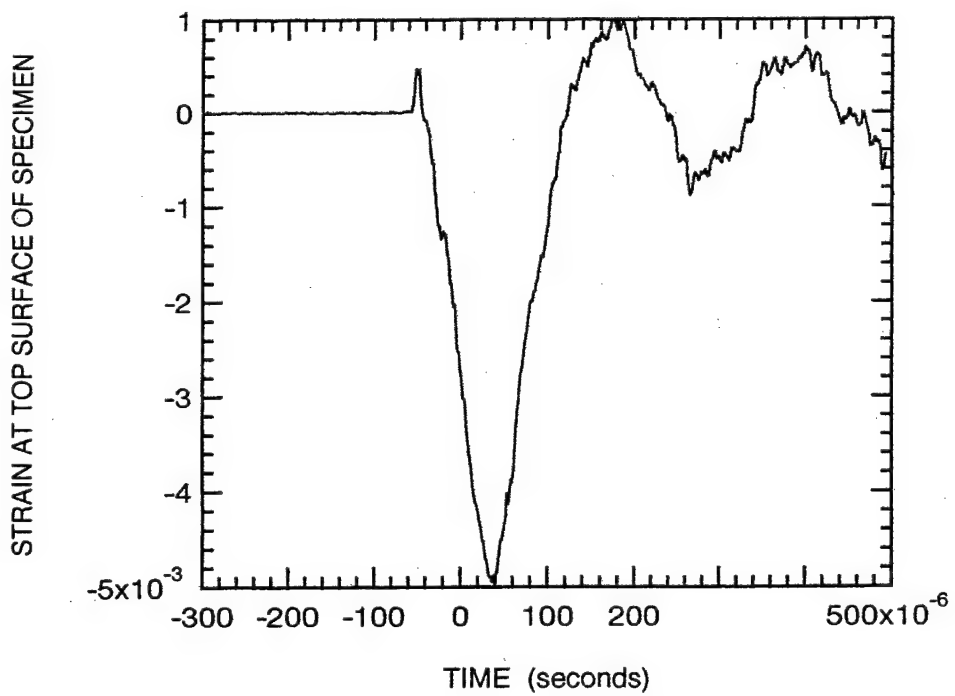


Figure 4.23 Measured Strain at the Loading Face of Specimen 6, 10 mm from Impact Line.

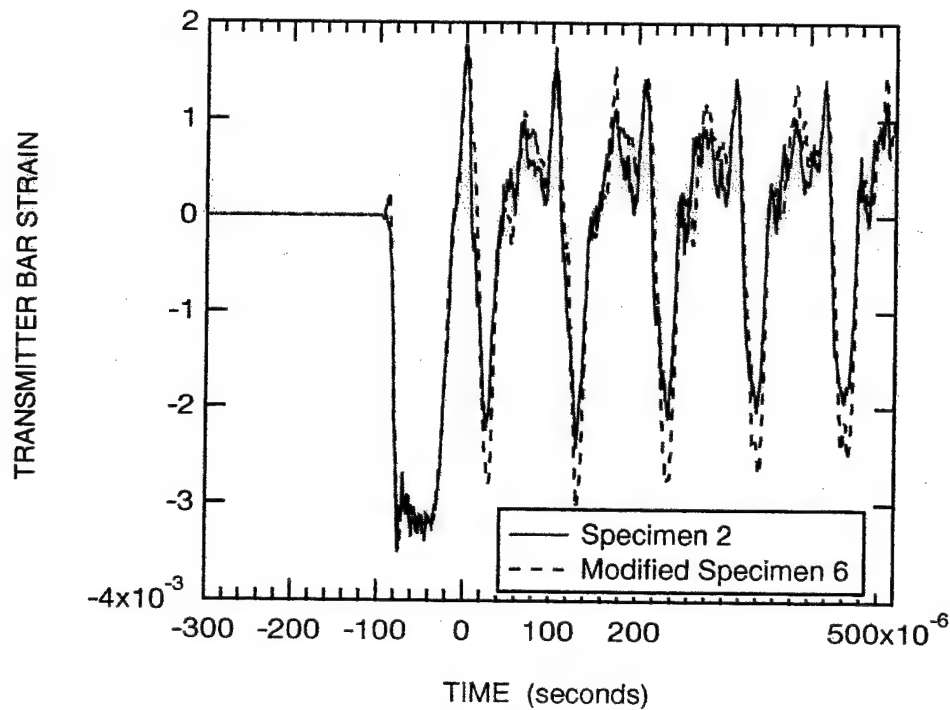


Figure 4.24 Comparison of the Measured Transmitter Bar Strain for Specimen 2 with that for Specimen 6 Multiplied by the Ratio of the Impact Speed for Specimen 2 to that for Specimen 6.

comparison. Note in making this comparison, the data from Test 6 were shifted along the time axis because the time of impact relative to crack initiation is greater for the smaller impact speed. As expected there is excellent agreement for the first 75 μ s (the round-trip time for a longitudinal wave to travel from the strain gage to the specimen end and return) since the strain gage is sensing the effects of linear elastic wave propagation. But even afterwards, there is good correspondence, with the maximum modified compressive strain for Specimen 6 exceeding the maximum compressive strain for Specimen 2. Other small differences are due to variances in the crack propagation histories for the two specimens and perhaps other slight inelastic effects. The periods of oscillations in both cases are virtually identical. The good correspondence between these results reflects on the consistency among these tests. Similar consistent results were attained in comparisons with the other tests; however, the Specimen 5 data tend to exhibit rather larger oscillations because of the more forceful impact.

4.3 Application Phase Analyses

Application phase analyses were performed for the AISI 4340 steel, dynamic three-point bend test. A two-dimensional plane strain EPIC model was developed that explicitly includes the striker bar, transmitter bar, specimen and the support pins. A plane strain model was selected because of the small scale yielding, plane strain (flat) fracture that occurs in this material.

4.3.1 Modeling Considerations. The round cross sections of the striker and transmitter bars and the side grooves in the specimen required special considerations since they are not readily modeled as two dimensional. The cross sections of the striker and transmitter bar were modeled as rectangles. The width of each bar was 25.4 mm (the nominal thickness of the specimen) and the height was determined so that their cross sectional areas are the same as those in the tests. The nose of the transmitter bar was modeled as an ellipse³. Because of the high yield strength of these bars, they were assumed to be linear elastic. The plane strain assumption leads to predicted longitudinal wave speed in the bars that exceeds the measured speed and that predicted by classical one-dimensional wave propagation theory by about 10 percent. As a result, the predicted loading pulse produced in the transmitter bar was also about 10 percent shorter. Since the loading pulse governs the loading of the specimen, it was necessary to adjust the elastic properties of the bars so that the computed loading pulse replicated the measured pulse. This was done by decreasing the reported shear modulus and bulk modulus for the bar material from 77.5 GPa and 163.9 GPa, respectively, to 62.8 GPa and 132.8 GPa while keeping the density of the material constant at 7823 kg/m³ for steel. Poisson's ratio of 0.2958 is used for all materials. This change uniformly reduces all of the wave propagation speeds in the bars.

The side groove in the specimen has the effect of reducing the strength and stiffness in the reduced section relative to the full thickness. This is modeled in the two-dimensional analysis by reducing the yield strength and elastic moduli material by the ratio of the net thickness in the side groove to the full thickness of the specimen (0.81). The density of the material is also reduced by the same factor so that the wave speeds in the side-groove region are the same as in the bulk

³ In a few computations the nose was modeled as an ogive, but this resulted in too soft of a system due to local yielding of the specimen at the contact point and further computations using this nose were abandoned.

of the specimen. The shear and bulk moduli and density used for the side groove region are 63.3 GPa, 133.9 GPa and 6390 kg/m³, respectively, compared to 77.5 GPa, 163.9 GPa and 7823 kg/m³ for the remainder of the specimen. The computation of T^* also accommodates release of energy over the reduced area of the side groove.

In initial computations, the Johnson-Cook model and reported properties for AISI 4340 steel were used. However, the computations showed that the plastic strain in the crack tip region was typically less than 1 percent. The determination of the parameters in the Johnson-Cook model are based upon much larger plastic strains and the model does not fit the measured stress-strain curve for small strains (e.g., ~ 1%). At these small strains there is very little strain hardening; therefore, hardening was neglected. The yield strength was taken to be 1,510 MPa in the bulk of the specimen whereas a reduced yield strength of 1,230 MPa was used for the side groove region.

The pins supports are considered to be linear elastic and to have the above elastic properties of the specimens. The center line of the pin is assumed to be fixed against translation in the plane. The contact between the pin and the specimen is taken to be frictionless.

4.3.2 Application Phase Results for AISI 4340. Application phase analyses were conducted for AISI 4340 three-point bend Specimens 2, 5 and 6. These tests represent intermediate, high and low striker impact speeds. The finite element model and mesh used in these computations are depicted in Figure 4.25. Because of vertical symmetry only one-half of the system is modeled. Loading occurs by the striker bar impacting the transmitter bar which in turn is in contact with the three-point bend specimen. Separations of the striker bar from the transmitter bar, the transmitter bar from the specimen, and the specimen from the support pins are permitted. In addition to the material properties discussed above, the initial striker bar speed must be specified.

The fracture resistance used in these computations is the bi-linear form determined from CPB Tests 1 and 2 for AISI 4340 steel described in Section 3.6 and depicted in Figure 4.26. In the following, two different representations for the fracture resistance are investigated. The first is an average of the resistances determined in Tests 1 and 2 and is that depicted by the small dashed curve having a threshold value of 13 kN/m. The other is that shown by the dot-dash curve which is identical to the previous one except that the threshold value corresponds to the measured static initiation fracture resistance of 32 kN/m.

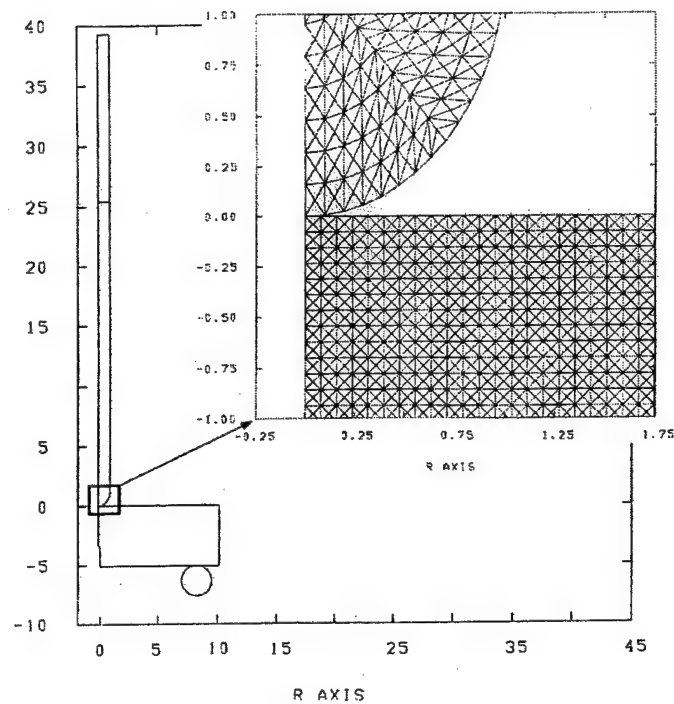


Figure 4.25 Typical Mesh Used in Modeling of Dynamic Three-Point Bend Test.

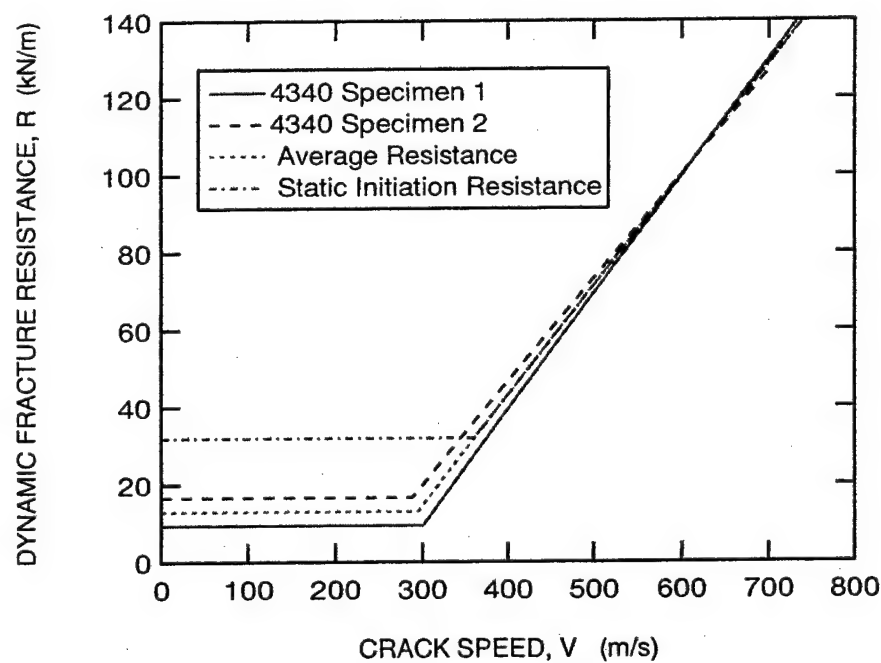


Figure 4.26 Dynamic Fracture Resistance for AISI 4340.

The following compares the predictions with the measurements for Specimen 2 when the fracture resistance with the lower threshold value is used. Figure 4.27 compares the computed and measured crack lengths. (NB Since time equals zero in the following plots corresponds to the time of impact, the measured data are shifted to reflect this change.) The predicted initiation of crack growth occurs at approximately 93 μ s whereas the measured initiation took place about 107 μ s after impact. Following initiation of crack growth, the predicted crack growth rate is slightly greater than the measured rate. The predicted crack growth subsequently diverges from the measured history. Near the end of the event, the predicted crack growth appears to come to a momentary halt and reinitiates whereas there was no evidence of a halt in the experiment. This artifact may be due to the intersection of contours, used in computing T^* , with the face of the specimen to produce unreliable values of T^* . Nonetheless, the predicted time of complete fracture agrees favorably with the measured time, but this may be fortuitous.

Figure 4.28 compares the predicted and measured transmitter bar strain. For times less than about 132 μ s, the agreement is very good; for greater times, there is disparity between the predictions and the measurements. This disparity is due primarily to the premature prediction of crack initiation. It takes approximately 38 μ s for a signal from the crack tip to be detected by the transmitter bar strain gage. When this time is added to the predicted crack initiation time of 93 μ s, a value of 131 μ s is obtained which is in agreement with the time of departure between the predicted and measured strains.

Figure 4.29 compares the predicted and measured crack tip strains. This strain gage is closer to the crack tip and therefore responds sooner to initiation of crack growth. There is very good agreement between the predicted and measured strains for time less than about 93 μ s when initiation of crack growth is predicted. Because of the predicted premature initiation, the predicted strain never attains the maximum measured value.

Figure 4.30 contrasts the predicted and measured crack opening displacement. The predicted COD is nearly twice that of the measured value. One might expect larger predicted COD because of the earlier predicted crack initiation, but as will become apparent with further comparisons this has become a troublesome problem with the predictions. Finally, Figure 4.31 compares the predicted and measured strains at the support. The lack of correspondence between the two is probably due to the predicted early initiation of crack growth.

A larger value for the threshold value of the fracture resistance will delay the time for initiation of crack growth. Therefore, computations were repeated for Specimen 2 using the

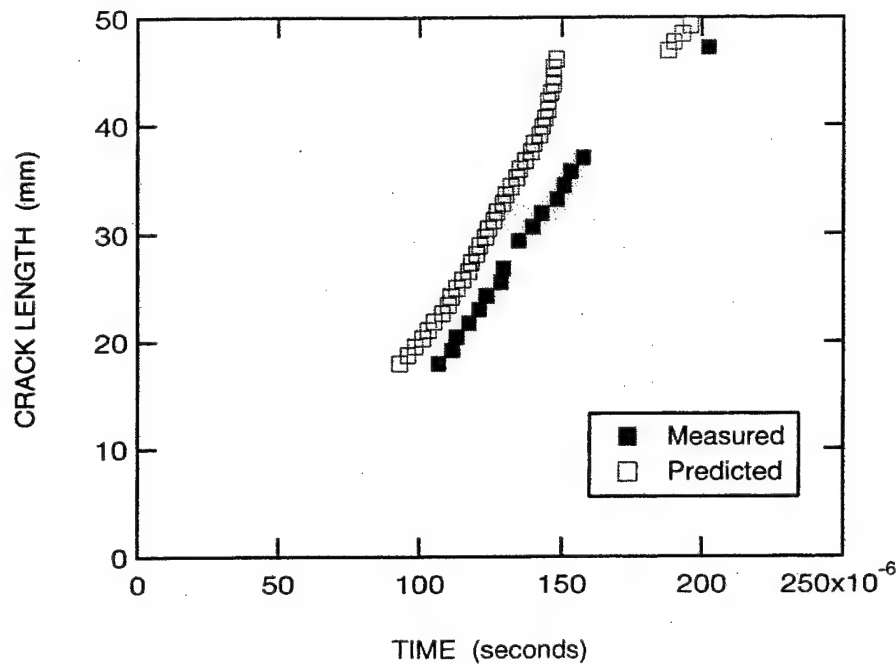


Figure 4.27 Comparison of Measured and Predicted Crack Growth History for Specimen 2 with Low Threshold Resistance.

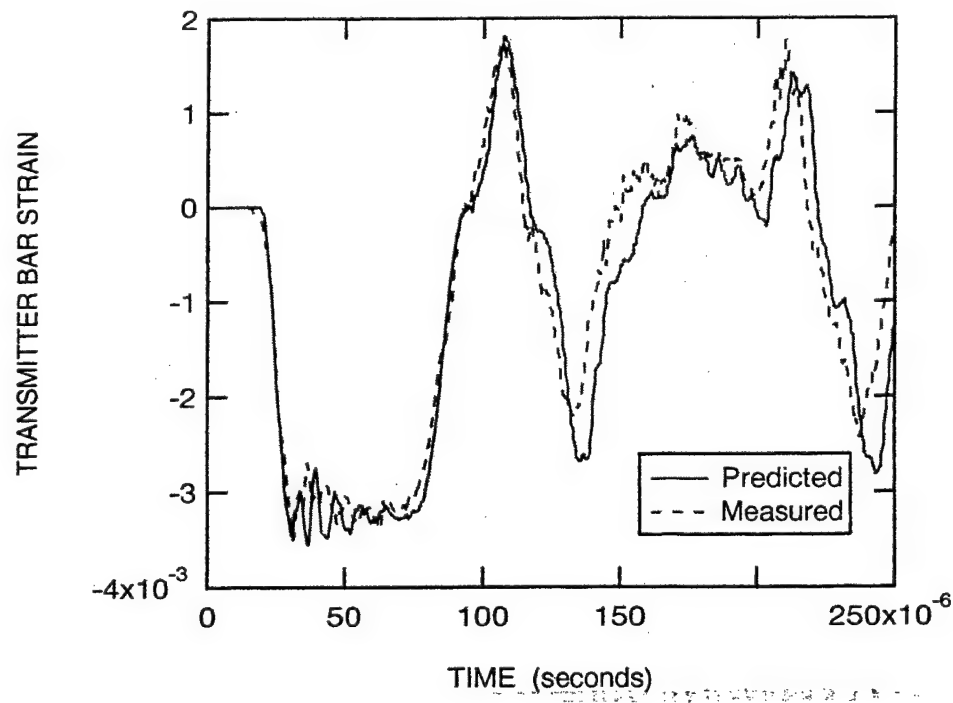


Figure 4.28 Comparison of Measured and Predicted Transmitter Bar Strains for Specimen 2 with Low Threshold Resistance.

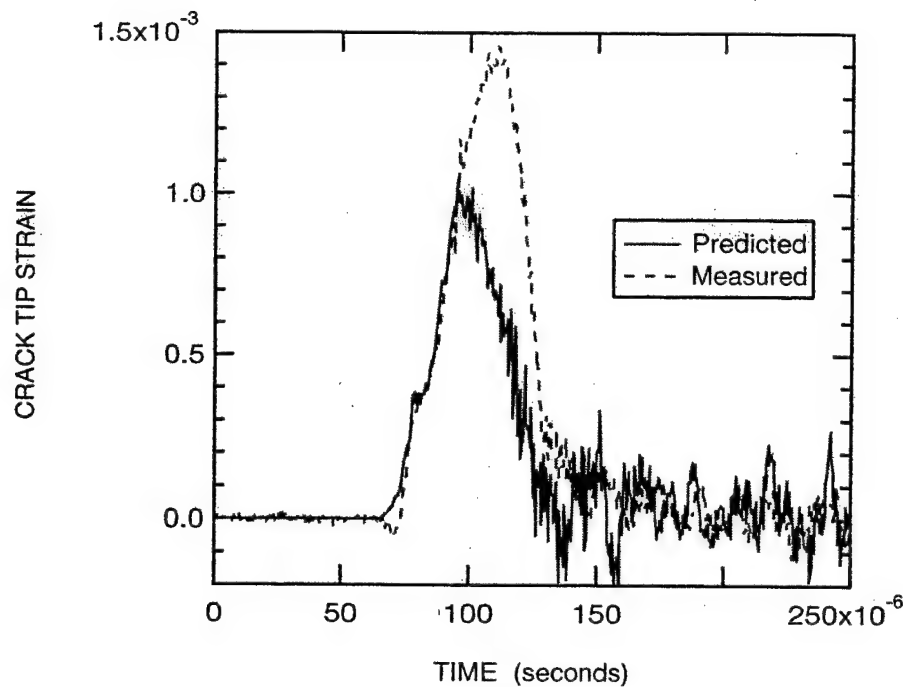


Figure 4.29 Comparison of Measured and Predicted Crack Tip Strains for Specimen 2 with Low Threshold Resistance.

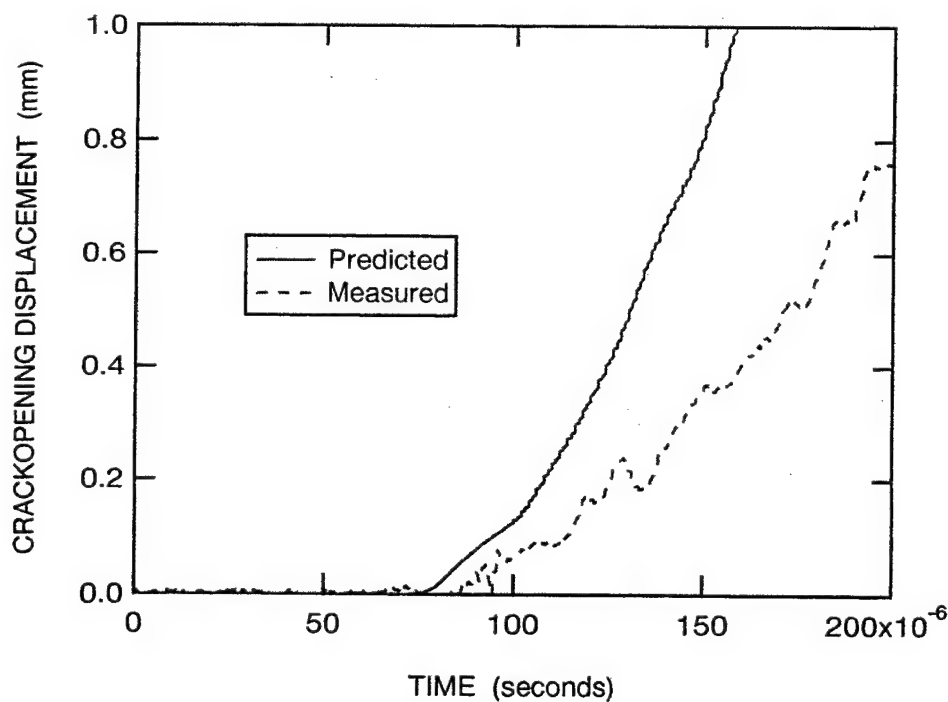


Figure 4.30 Comparison of Measured and Predicted Crack Opening Displacements for Specimen 2 with Low Threshold Resistance.

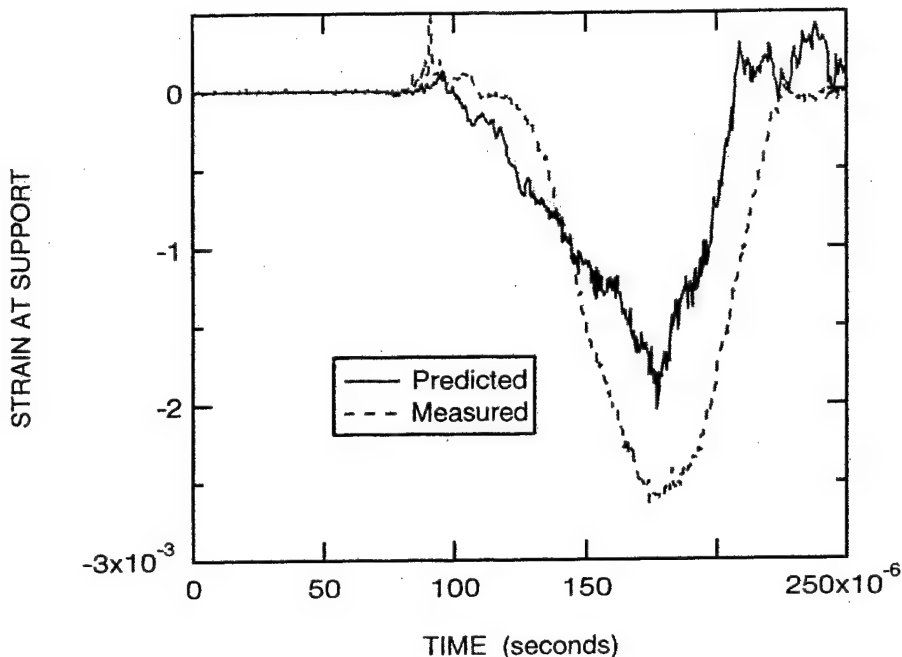


Figure 4.31 Comparison of Measured and Predicted Strains at Support for Specimen 2 with Low Threshold Resistance.

fracture resistance defined by the upper threshold value, corresponding to the static initiation resistance, in Figure 4.26. Figure 4.32 compares the predicted and the measured crack length. The predicted initiation occurs approximately 4 μ s before the measured crack initiation time (compared to 14 μ s in the previous example). The initial predicted and measured crack growth rates are very close. The predicted crack growth increases faster than the measured growth near the end of the event and once again exhibits a momentary halt so that the predicted and measured times of complete fracture are very similar.

As Figure 4.33 indicates, the agreement between predicted and measured transmitter bar strains is somewhat improved. The correspondence between the predicted and measured crack tip strains in Figure 4.34 is markedly better with the prediction almost agreeing exactly with the measurement. Clearly, the threshold value for the initiation fracture resistance has an important effect on the results. Figure 4.35 compares the predicted and measured crack opening displacement. Surprisingly, the larger initiation resistance had very little influence on the predicted crack opening displacement, which in this case is still nearly twice the measured value. It is not clear why better agreement is not attained when the correspondence of the crack tip strains is so good. Figure 4.36 shows a slight improvement in the predicted strain at the support.

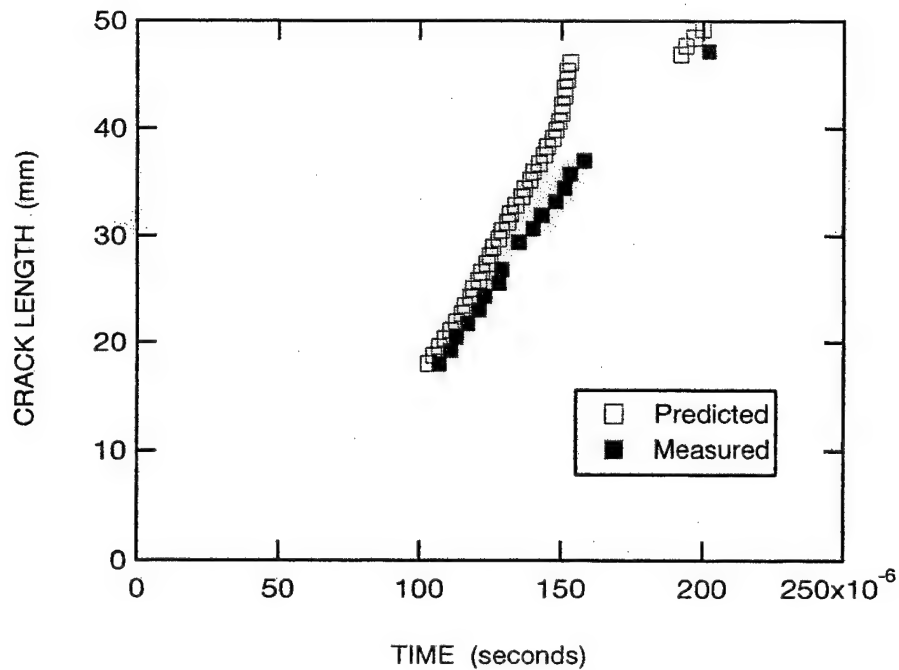


Figure 4.32 Comparison of Measured and Predicted Crack Growth Histories for Specimen 2 with High Threshold Resistance.

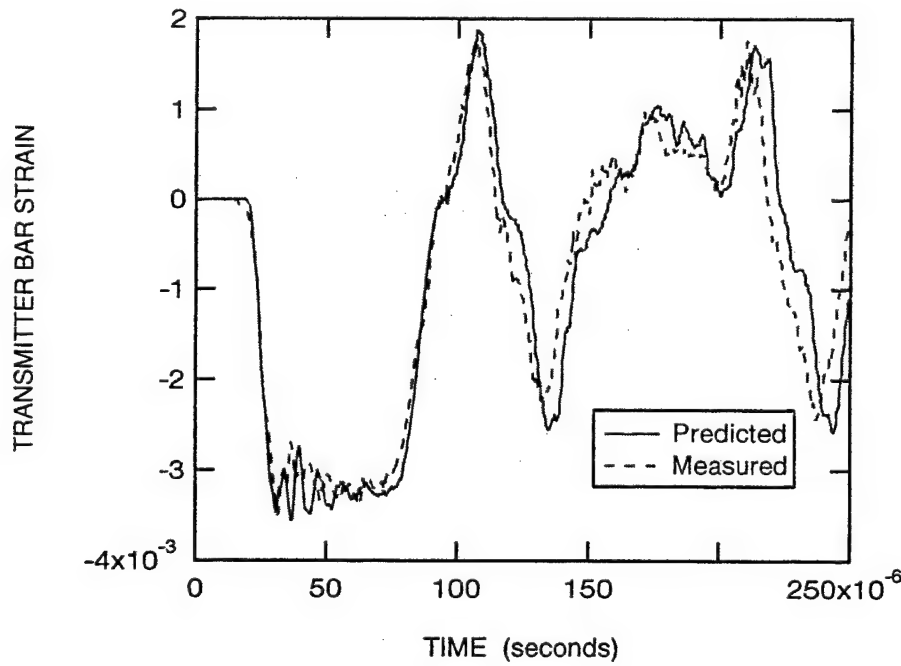


Figure 4.33 Comparison of Measured and Predicted Transmitter Bar Strains for Specimen 2 with High Threshold Resistance.

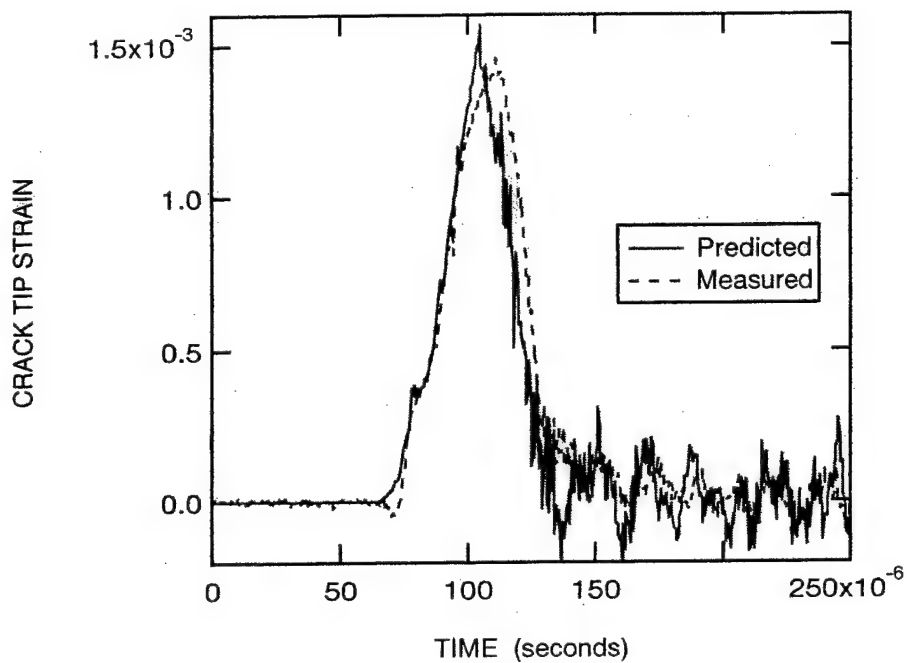


Figure 4.34 Comparison of Measured and Predicted Crack Tip Strains for Specimen 2 with High Threshold Resistance.

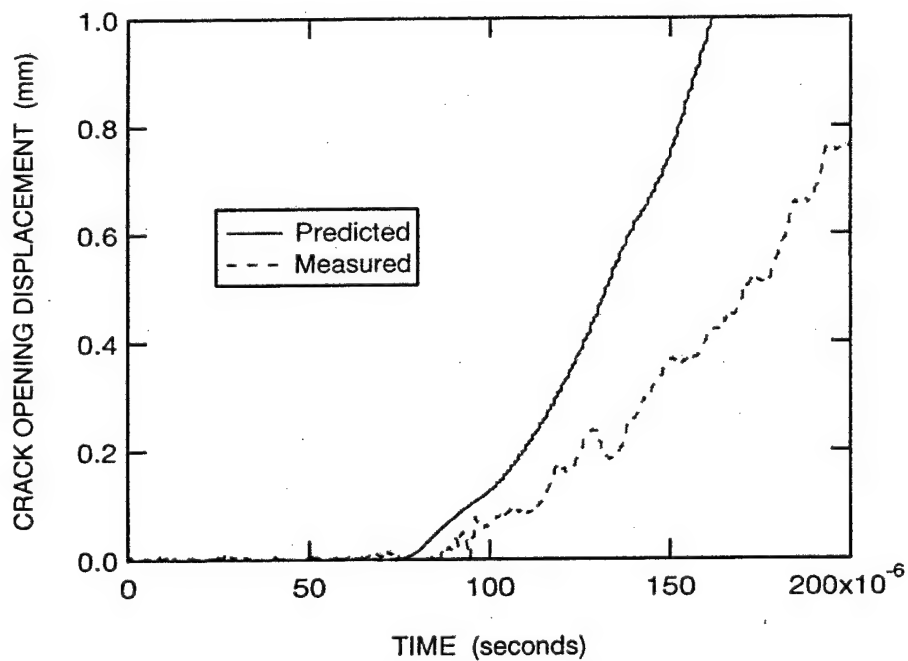


Figure 4.35 Comparison of Measured and Predicted Crack Opening Displacements for Specimen 2 with High Threshold Resistance.

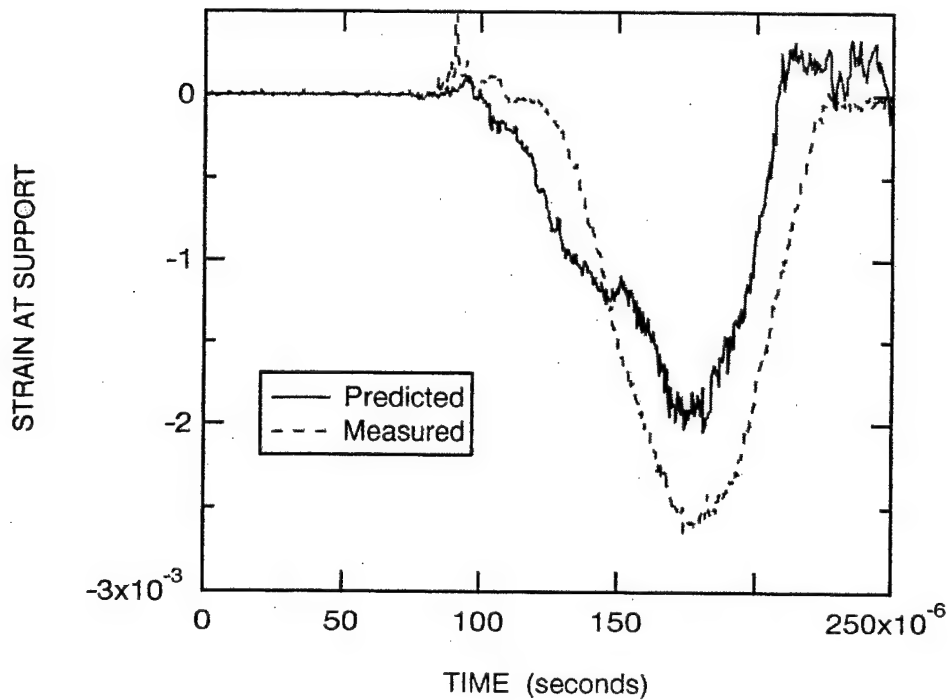


Figure 4.36 Comparison of Measured and Predicted Strains at Support for Specimen 2 with High Threshold Resistance.

In summary, it appears that the increased initiation fracture toughness resulted in significant improvement of the predicted crack growth history and the crack tip strain, but produced only minor improvements for the transmitter bar strain, crack opening displacement and strain at the support.

An application phase analysis was performed for Specimen 5 for which the impact speed of the striker bar was 87.6 m/s. Again, this analysis was performed for the larger initiation fracture resistance in Figure 4.26. Figure 4.37 is a comparison of the predicted and measured crack growth history. The predicted and measured initiation time and the initial crack growth are in very good agreement, but the predicted rate of growth exceeds the measured rate later in the event, and again, the computation indicates a momentary halt in propagation that is not observed. Moreover, the predicted crack growth does not slow near the end of the event as was measured in the test. The prediction indicates that the fracture event is completed after approximately 122 μ s whereas the actual event lasted about twice as long. In general, as shown in Figure 4.38, there is reasonably good agreement between the predicted and measured transmitter bar strains. The measured strains exhibit larger oscillations than the predicted strains. This high impact speed

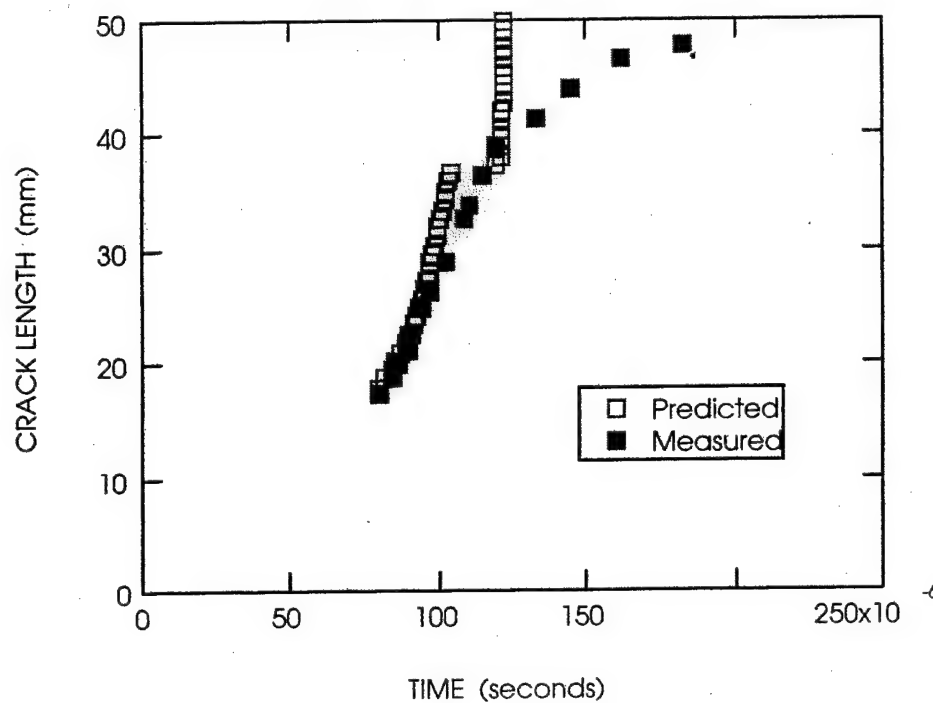


Figure 4.37 Comparison of Measured and Predicted Crack Growth for Specimen 5 with High Threshold Resistance.

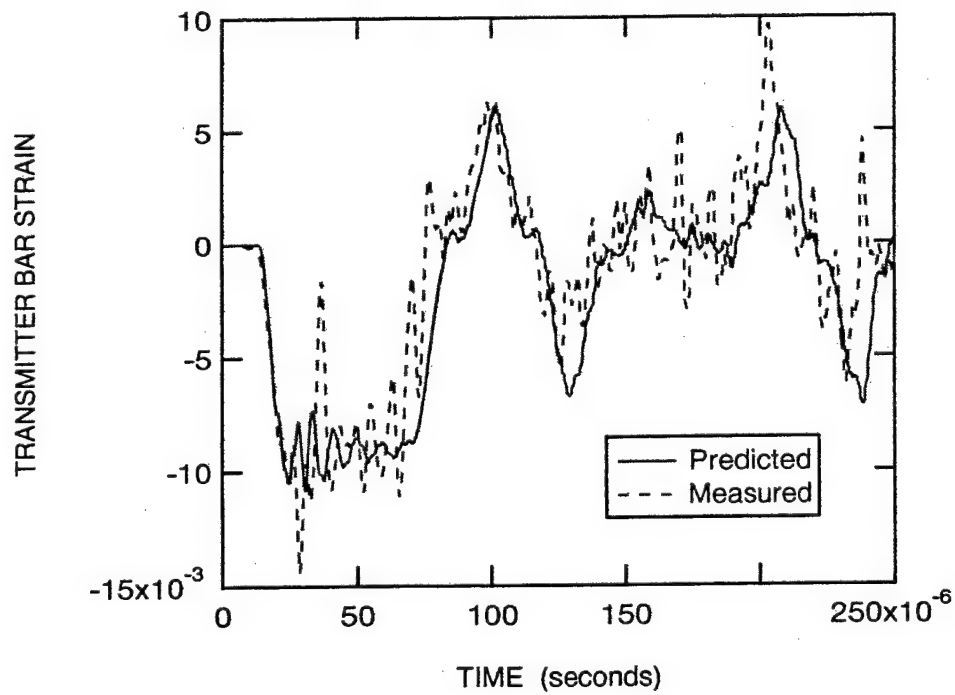


Figure 4.38 Comparison of Measured and Predicted Transmitter Bar Strains for Specimen 5 with High Threshold Resistance.

produced a very dynamic event that taxed the capabilities of the experiment and may be responsible for some of the measured large oscillations. As observed in Figure 4.39, reasonably good agreement exists between the predicted and measured crack tip strains. Once more, the predicted crack opening displacement in Figure 4.40 greatly exceeds the measured value. Finally, the predicted and measured strains at the support are compared in Figure 4.41. The correlation is rather poor. It appears that the predicted strains occurred sooner than the measured ones. This may be due to the greater predicted crack growth rate.

The final application phase analysis of AISI 4340 was performed for Specimen 6, which was instrumented with additional strain gages. The application phase analysis was conducted for the larger initiation fracture resistance. Figure 4.42 shows that predicted crack growth rate agrees favorably with the measured rate. The predicted initiation is approximately 12 μ s before that observed and is primarily responsible for the subsequent differences between the two crack growth histories. Figure 4.43 displays very good agreement between the predicted and measured transmitter bar strains. While Figure 4.44 indicates reasonably good agreement between the predicted and measured crack tip strains, Figure 4.45 illustrates a similar discrepancy between the predicted and measured crack opening displacements that has been observed in previous application phase analyses. Figure 4.46 demonstrates fairly good initial agreement between the predicted and measured strains at the support that deteriorates during the latter stages of the event. The agreement between the predicted and measured strains on the top surface of the specimen in Figure 4.47 is generally good. Figures 4.48 and 4.49 contrast, respectively, the predicted and measured strains in the side groove and near the center of the initial ligament. The predicted peak strains occur earlier than the measured ones because the predicted crack extension takes place sooner.

While there is not universal agreement, some very good agreement between the predicted quantities of the application phase analyses and measurements has been demonstrated. For example, the predicted crack growth history, which is generally of most interest, is usually in good agreement with the measured history.

4.3.3 Generation Phase Analysis of AISI 4340 Specimen 6. A concern in the above analyses is the large discrepancy between the predicted and measured crack opening displacement; particularly, when there is good agreement for the crack tip strain. Clearly, the application phase analysis is dependent upon the fracture resistance that is used as input. In the above analyses the fracture resistance developed from the coupled pressure bar experiments was used. To eliminate

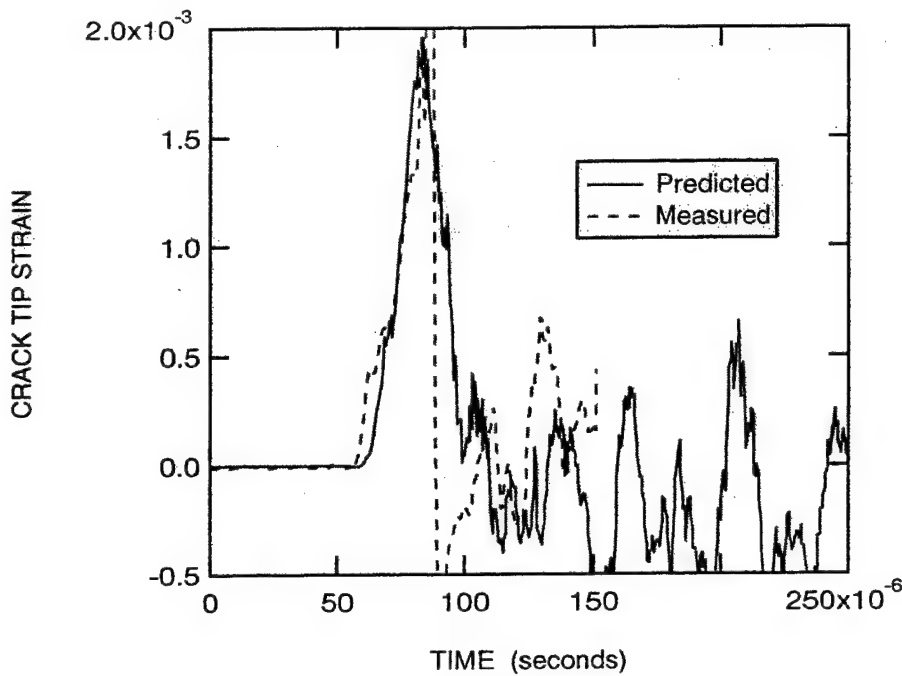


Figure 4.39 Comparison of Measured and Predicted Crack Tip Strains for Specimen 5 with High Threshold Resistance.

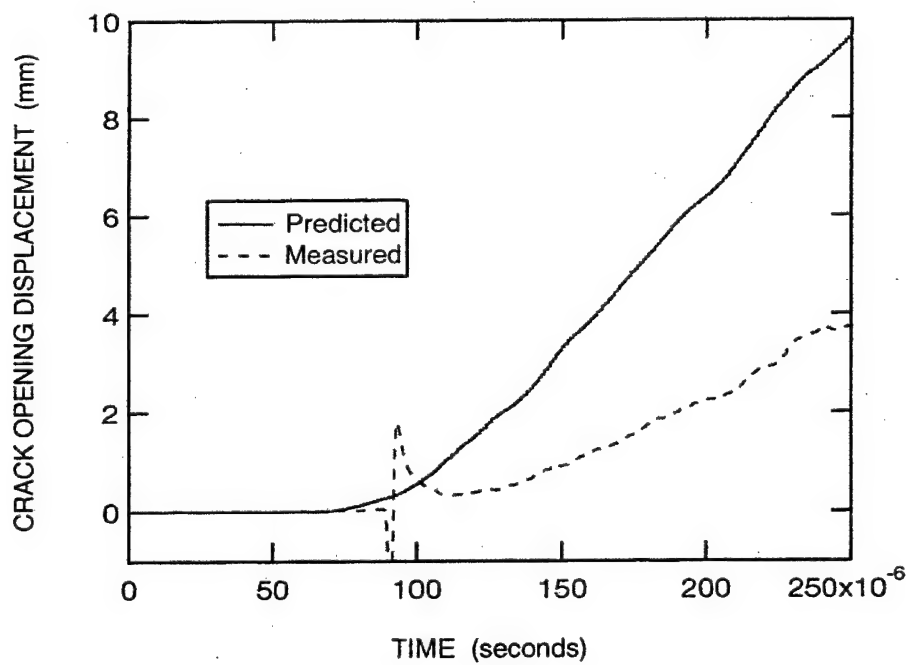


Figure 4.40 Comparison of Measured and Predicted Crack Opening Displacements for Specimen 5 with High Threshold Resistance.

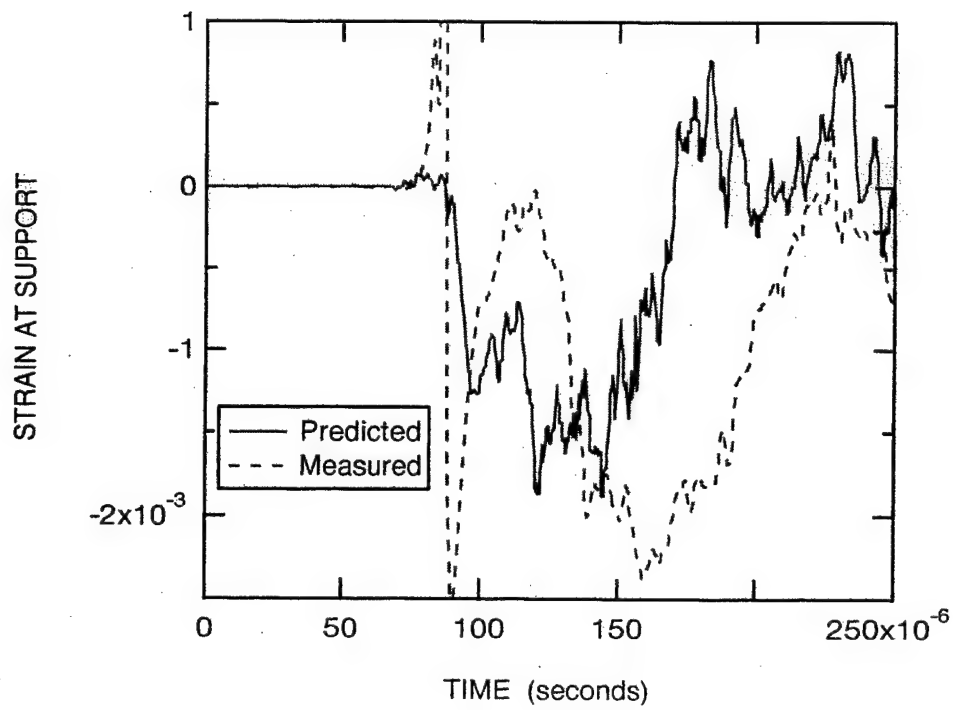


Figure 4.41 Comparison of Measured and Predicted Strains at Support for Specimen 5 with High Threshold Resistance.

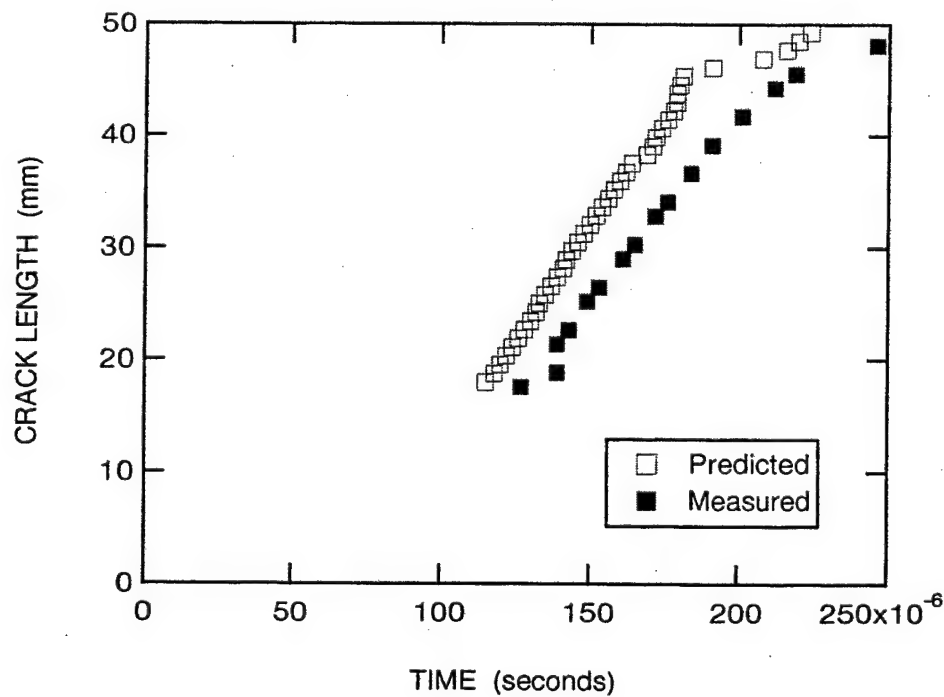


Figure 4.42 Comparison of Measured and Predicted Crack Growth for Specimen 6 with Larger Threshold Resistance.

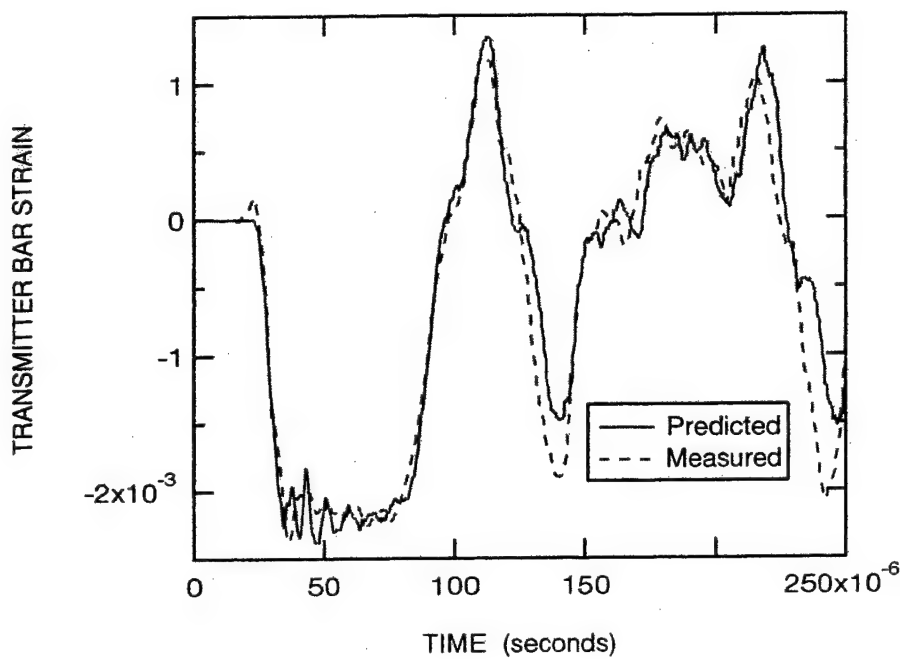


Figure 4.43 Comparison of Predicted and Measured Transmitter Bar Strains for Specimen 6 with High Threshold Resistance.

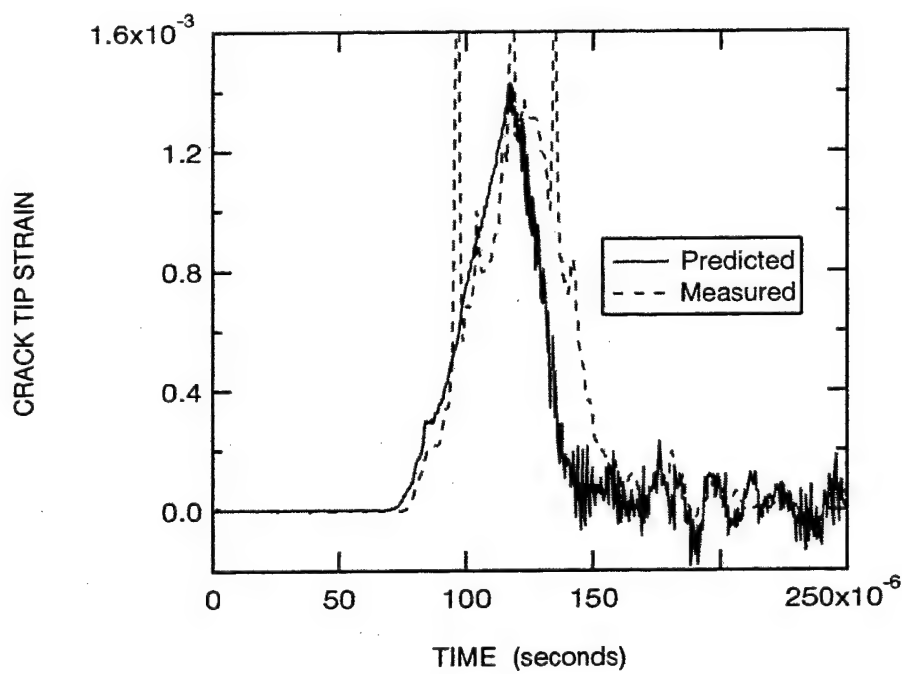


Figure 4.44 Comparison of Measured and Predicted Crack Tip Strains for Specimen 6 with High Threshold Resistance.

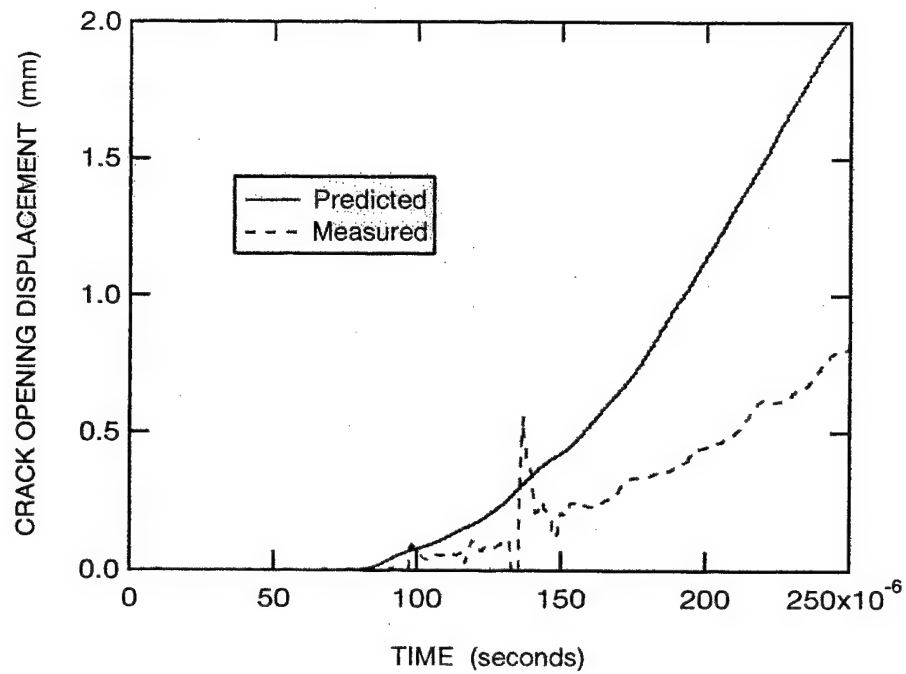


Figure 4.45 Comparison of Measured and Predicted Crack Opening Displacements for Specimen 6 with High Threshold Resistance.

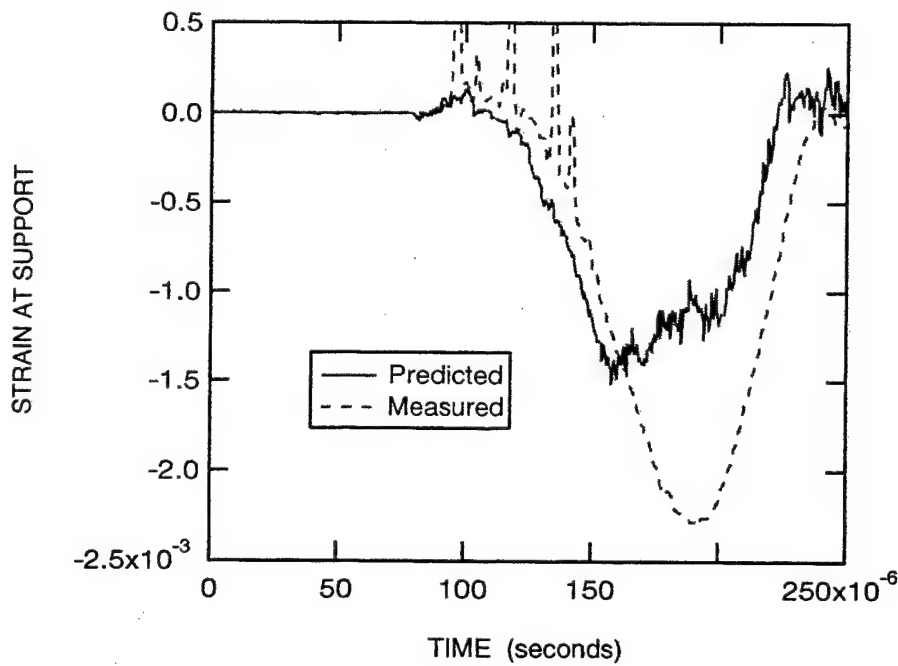


Figure 4.46 Comparison of Measured and Predicted Strains at Support for Specimen 6 with High Threshold Resistance.

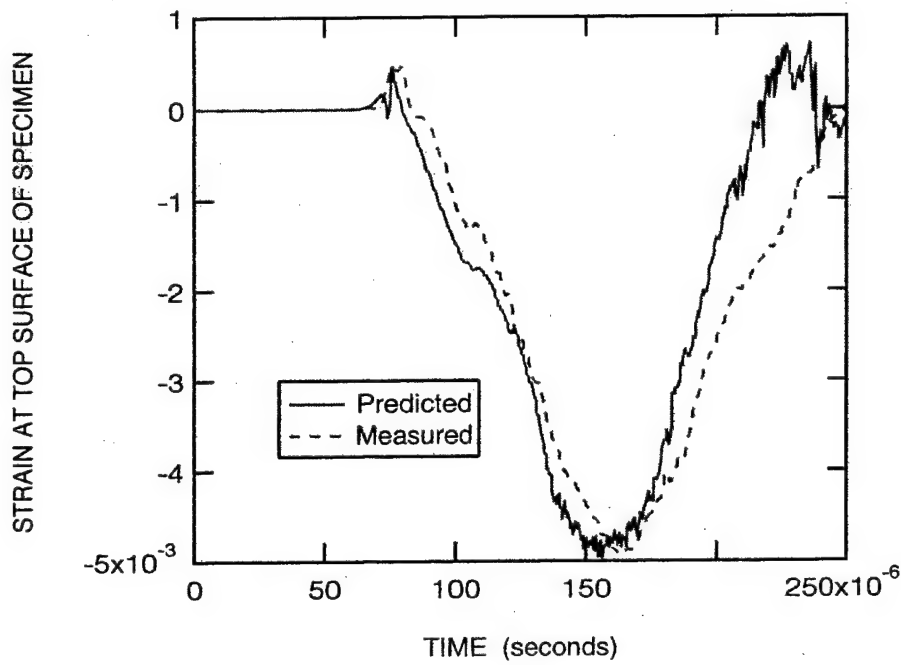


Figure 4.47 Comparison of Measured and Predicted Strains at Top of Specimen 6 for High Threshold Resistance.

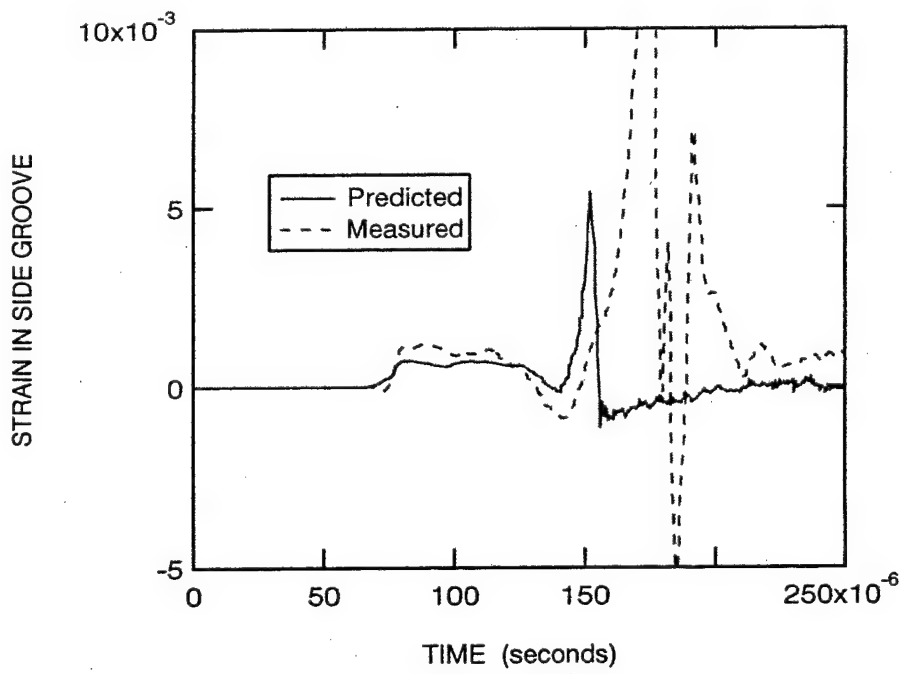


Figure 4.48 Comparison of Measured and Predicted Strain in Side Groove for Specimen 6 with the High Threshold Resistance.

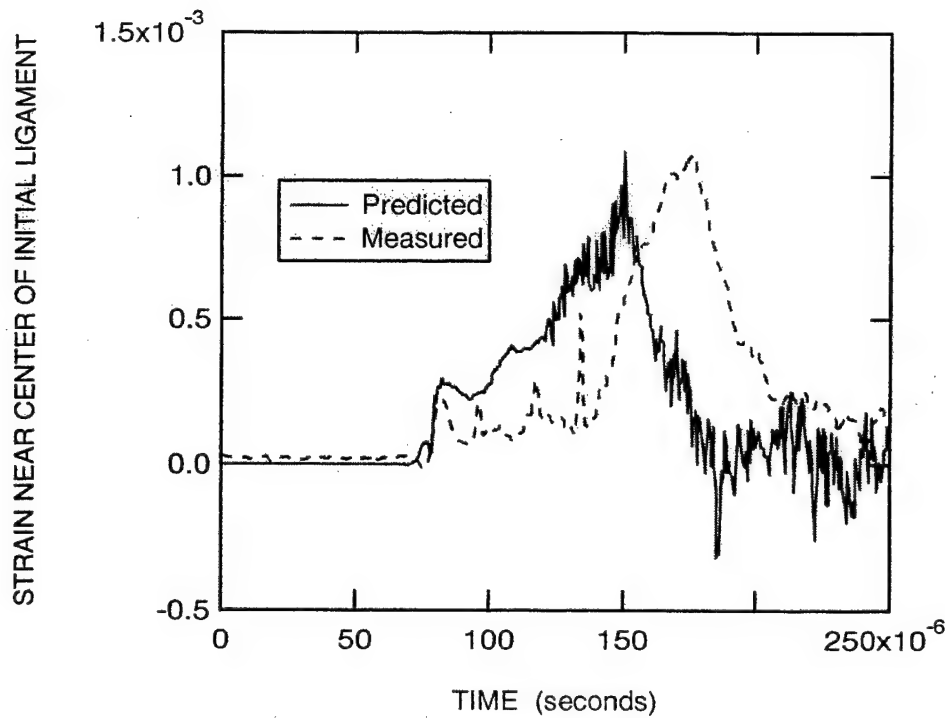


Figure 4.49 Comparison of Measured and Predicted Strain Near Center of Initial Ligament for Specimen 6 with the High Threshold Resistance.

this variable from consideration, a generation phase analysis was performed for Specimen 6. The measured crack growth history of Figure 4.42 was used as input in this analysis. A more refined mesh in the side-groove region was also employed in these computations.

The agreement between the predicted and measured transmitter bar strains in Figure 4.50 is quite good. Figure 4.51 compares the predicted and measured crack tip strains. In general the agreement is very good except that the maximum predicted strain exceeds the measured value by approximately 33 percent. While there is better agreement between the predicted and measured crack opening displacements in Figure 4.52, the predicted value still exceeds the measured value by approximately 65 percent. The agreement between the predicted and measured strains at the support in Figure 4.53 is judged satisfactory with the difference due to the earlier predicted response. The agreement between the predicted and measured strains at the top of the specimen, illustrated in Figure 4.54, is very good. The predicted and measured strains in the side groove and near the middle of the initial ligament exhibit good agreement as evident in Figures 4.55 and 4.56, respectively.

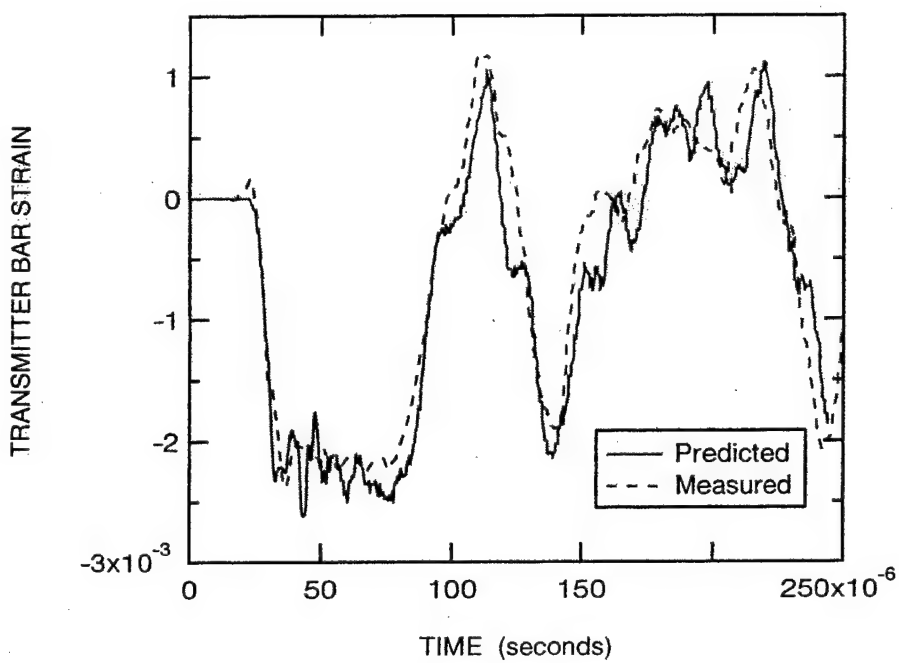


Figure 4.50 Comparison of Measured and Predicted Transmitter Bar Strains from Generation Phase Analysis of Specimen 6.

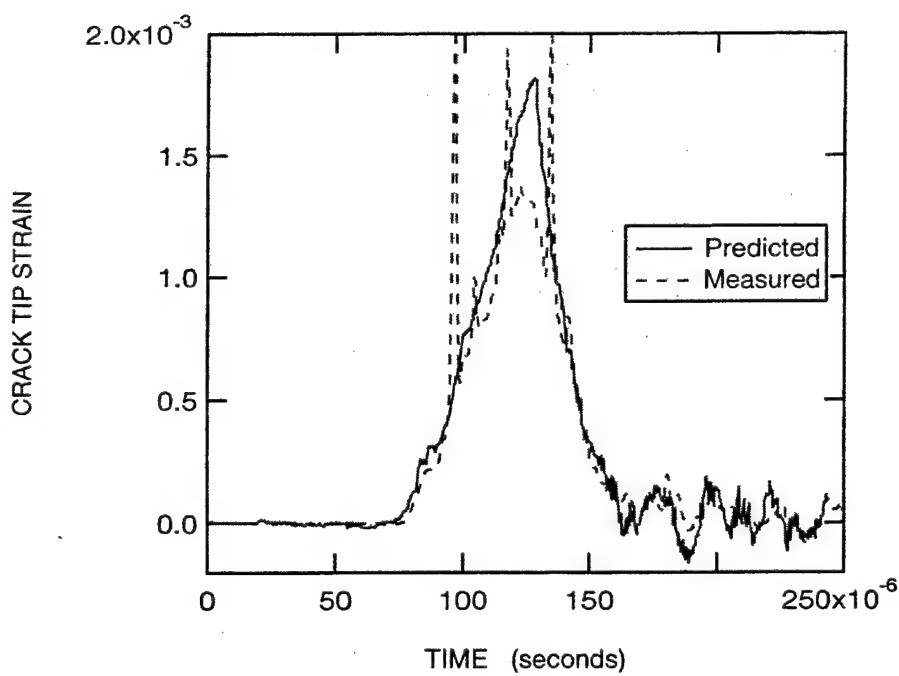


Figure 4.51 Comparison of Measured and Predicted Crack Tip Strains from Generation Phase Analysis of Specimen 6.

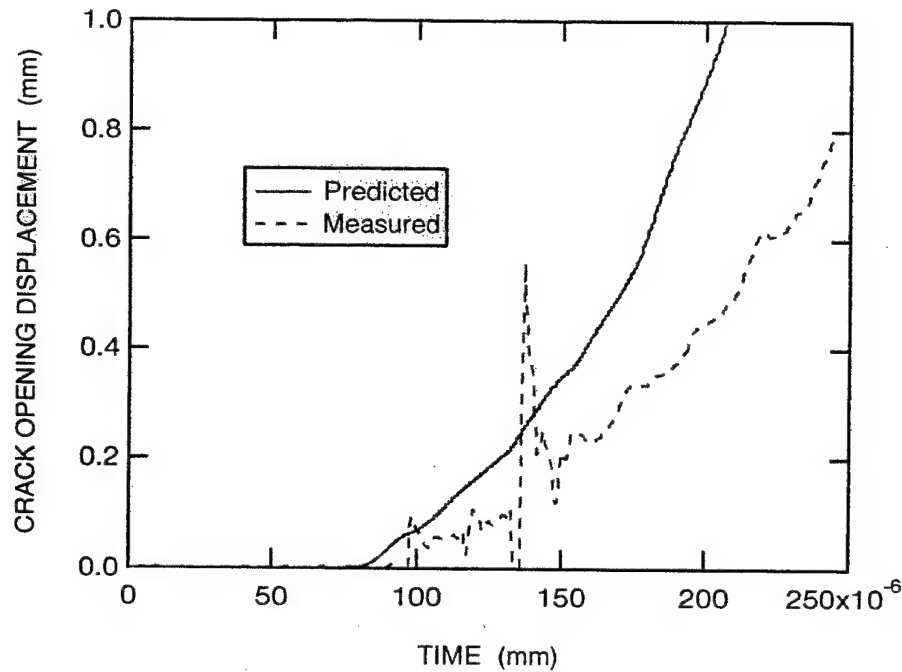


Figure 4.52 Comparison of Measured and Predicted Crack Opening Displacement from Generation Phase Analysis of Specimen 6

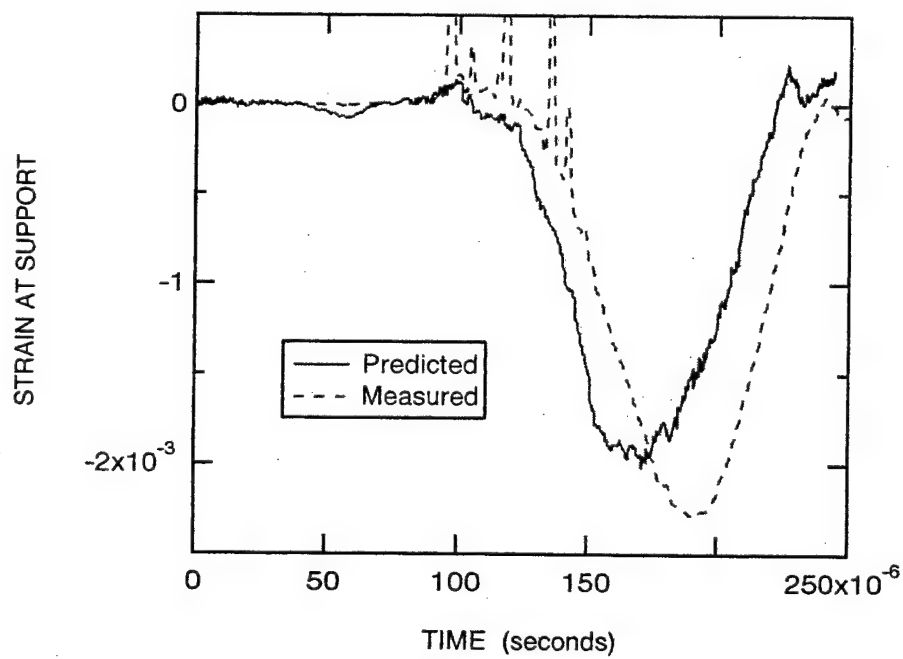


Figure 4.53 Comparison of Measured and Predicted Strains at Support of Specimen 6 from Generation Phase Analysis.

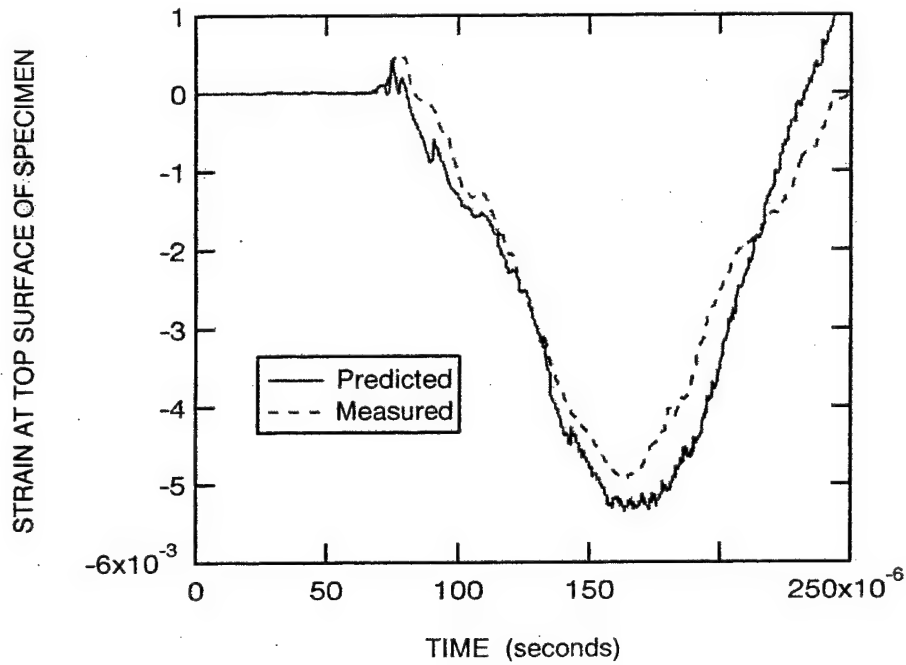


Figure 4.54 Comparison of Measured and Predicted Strains at the Top Surface of Specimen 6 from Generation Phase Analysis

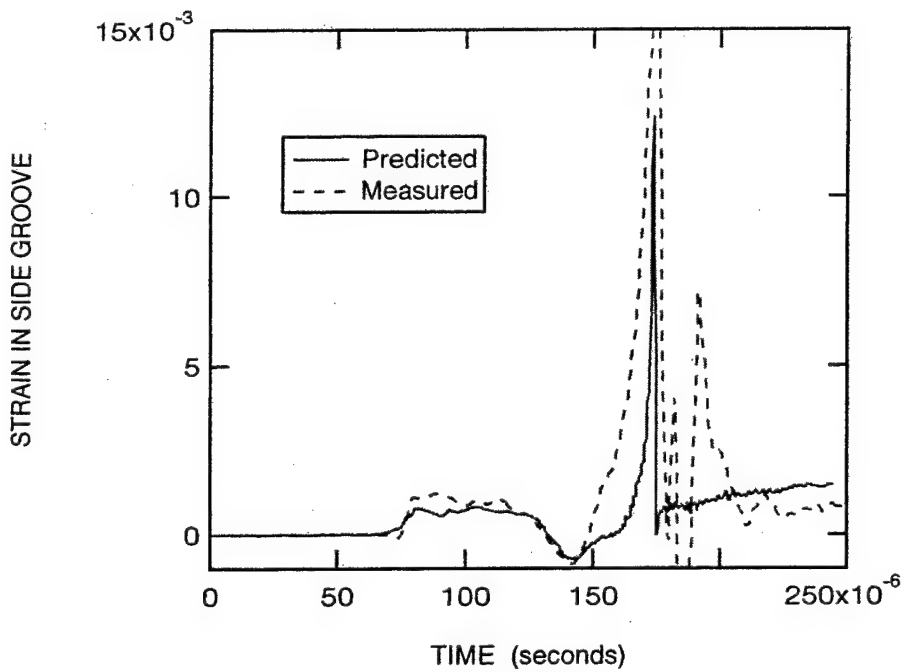


Figure 4.55 Comparison of Measured and Predicted Strains in Side Groove from Generation Phase Analysis of Specimen 6.

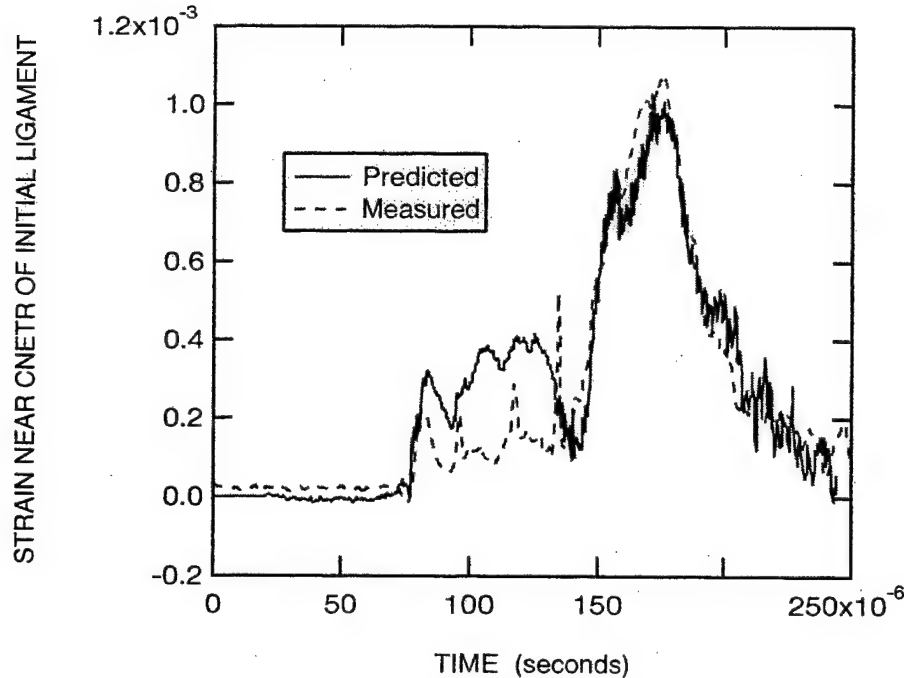


Figure 4.56 Comparison of Measured and Predicted Strains Near Center of Initial Ligament from Generation Phase Analysis of Specimen 6.

While there tends to be good agreement between the predictions and measurements, the discrepancies between the measured and predicted crack opening displacements and the crack tip strains in this generation phase analysis is disconcerting. Even though the fracture mechanics algorithms have undergone debugging, it was decided to use EPIC to perform a quasi-static, plane strain analysis of a three-point bend fracture specimen. The height and span of the steel specimen were 25.4 mm and 101.6 mm, respectively, and the length of the central crack was 12.7 mm. The load point displacement was prescribed to increase slowly with time. Tada, *et al.* [13] present the crack mouth opening displacement (CMOD) and the load point displacement due to the crack for this geometry. The load point displacement with no crack (e.g., see Timoshenko and Goodier [14]) must be added to the latter to obtain the total load point displacement.

Figure 4.57 compares the EPIC computed crack mouth opening displacement with that given by Tada, *et al.* The stress intensity factor is related to T^* computed in EPIC by

$$K = \left[\frac{ET^*}{1-\nu^2} \right]^{1/2} \quad (4.1)$$

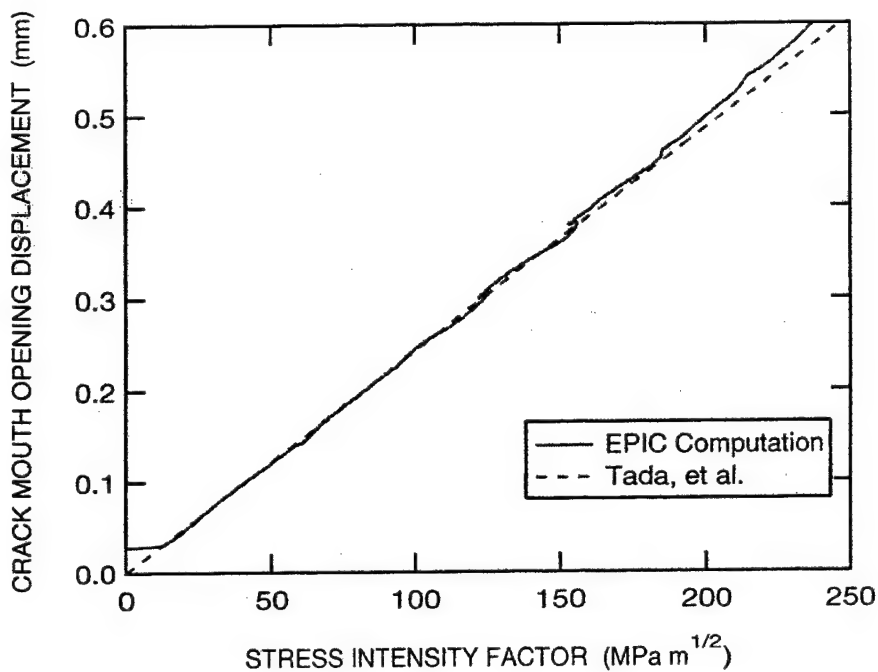


Figure 4.57 Comparison of EPIC Computation for the Crack Mouth Opening Displacement with that Given by Tada, *et al.*[13].

where E is the elastic modulus and ν is Poisson's ratio. Excellent agreement is obtained. The EPIC computed variation of the stress intensity factor with the load point displacement is depicted in Figure 4.58. The slight waviness of the computed results is due to small oscillations produced by the dynamic code for the rate of loading used in this simulation. The agreement with the solution of Tada, *et al.* is extremely good.

These results indicate that the connection between the crack driving force and the crack mouth opening displacement is being handled properly by EPIC, and it is unlikely that the above differences between the predicted and measured crack opening displacements can be attributed to an algorithm or programming error. Instead, it is felt that the source of the problem is an impedance error introduced in the simulation by modeling wave motion in the round transmitter bar as plane strain. Further modeling studies and refinements will be necessary to mitigate this problem.

4.3.4 An Application Phase Analysis for an AF1410 Three-Point Bend Specimen. An application phase analysis is performed in the following to ascertain if the dynamic three-point bend test can be used to study dynamic fracture in the high strength, high toughness AF 1410 steel. The fracture resistance data for this material are limited and consist of the measured quasi-

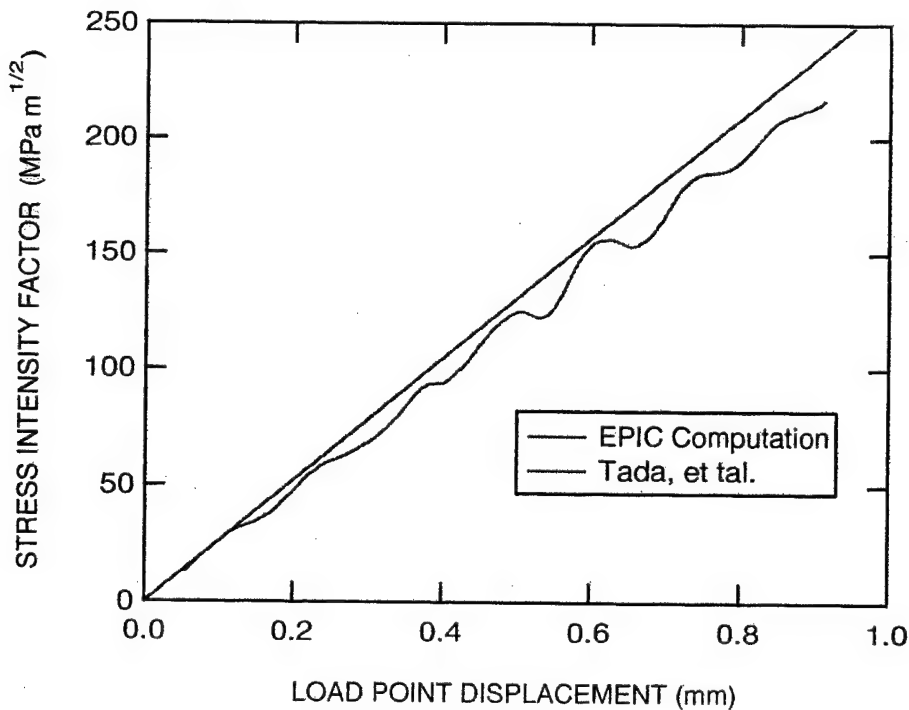


Figure 4.58 Comparison of EPIC Computation for the Load Point Displacement with that Given by Tada, et al. [13].

static resistance and the dynamic fracture resistance deduced from coupled pressure bar tests for Specimens 2 and 6. Based upon these data, the straight line in Figure 4.59 represents an estimate for the variation of fracture resistance with crack speed. In the computation, the length of the striker bar is reduced to 101.6 mm and its impact speed is 50 m/s. The shorter striker bar is recommended for future tests because it enables a simpler interpretation of the transmitter bar strain signal by separating wave reflections from the various interfaces and surfaces. This will permit determining the load transmitted to the specimen which can be compared with the predicted load. Thus, it may be possible to adjust the impedance of the plane strain model of the transmitter bar to match that for the actual bar.

Figure 4.60 depicts that predicted crack growth history. Initiation of crack propagation occurs about 111 μ s after impact, and the subsequent rate of crack growth is nearly constant at approximately 220 m/s. This crack speed is comparable to that produced in the coupled pressure bar tests for this material. These results suggest that it is possible to use the dynamic three-point bend test to study the fracture of AF 1410 and other high toughness materials. Figure 4.61 shows the transmitter bar strain. The shorter striker bar reduces the pulse duration in the

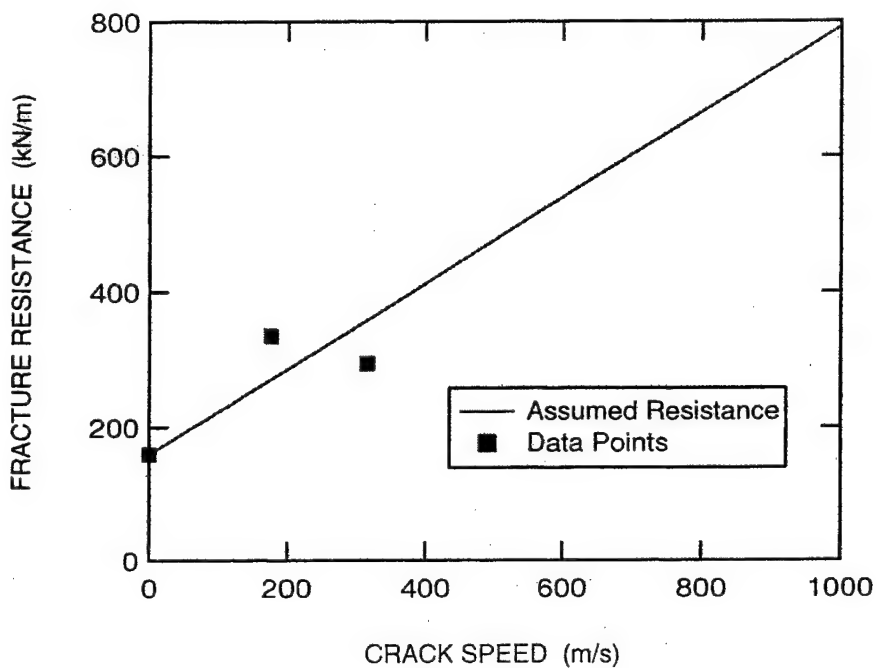


Figure 4.59 Estimate for the Dynamic Fracture Toughness for AF 1410 based upon Static and Couple Pressure Bar Fracture Tests.

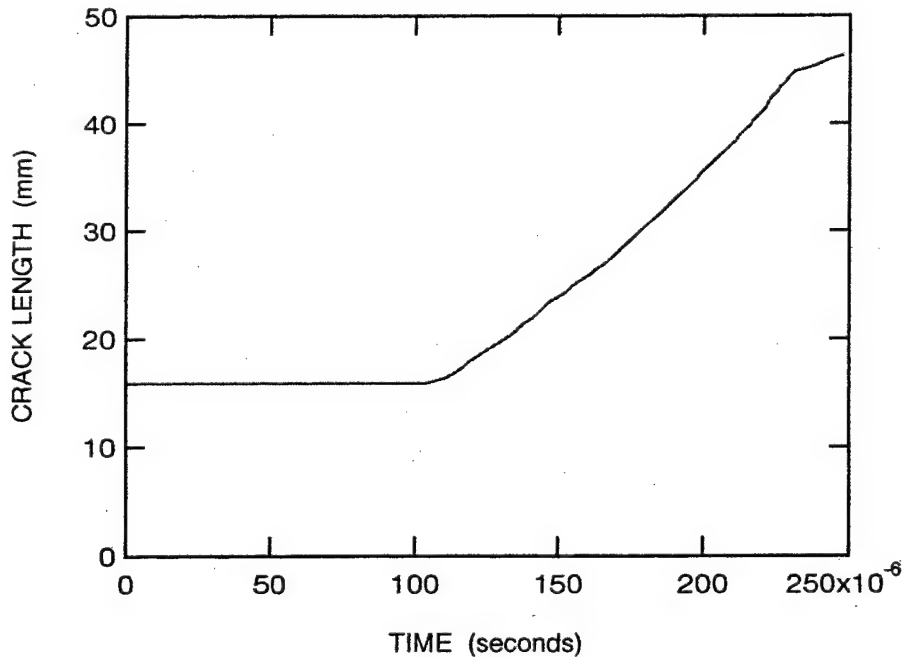


Figure 4.60 Predicted Crack Growth History for AF 1410 Three-Point Bend Specimen with an Impact Speed of 50 m/s.

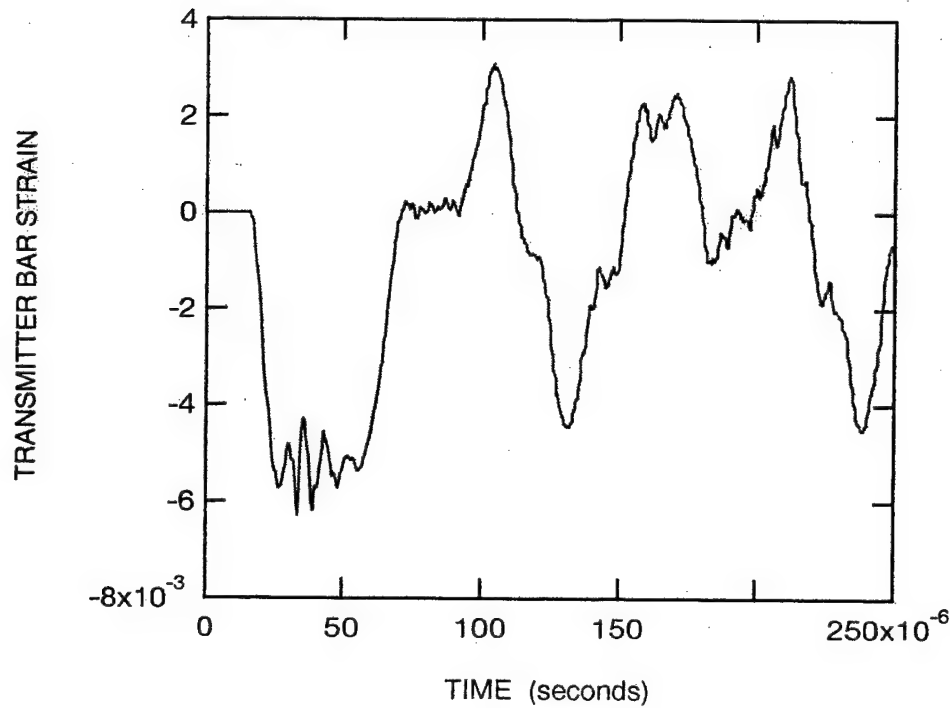


Figure 4.61 Predicted Transmitter Bar Strain for AF 1410 Three-Point Bend Specimen with an Impact Speed of 50 m/s.

transmitter bar. Consequently, in contrast with measured results with the 138.7-mm long striker bar, there is now a well-defined plateau commencing about 72 μ s. Following the plateau is the reflected signal from the transmitter bar-specimen interface.

4.4 An Engineering Model for Determination of the Fracture Toughness

A simple quasi-dynamic model is presented for determining the fracture toughness from dynamic three-point bend tests for materials exhibiting small scale yielding. The crack tip opening displacement for plane strain can be written as

$$\delta_t = \frac{(1-\nu^2)K^2}{2E\sigma_o} \quad (4.2)$$

where σ_o is the flow stress, and the stress intensity factor K equals the fracture toughness for the propagating crack. The crack mouth opening displacement may be expressed as

$$\delta_{c\text{mod}} = \frac{4aV_1(a/W)(1-\nu^2)K}{\sqrt{\pi a}EF(a/W)} \quad (4.3)$$

where a is the crack length, W is the height of the specimen, and according to Tada, *et al.* [13]

$$F(x) = \frac{1.99 - x(1-x)(2.15 - 3.93x + 2.7x^2)}{\sqrt{\pi}(1+2x)(1-x)^{3/2}} \quad (4.4)$$

and

$$V_1(x) = 0.76 - 2.28x + 3.87x^2 - 2.04x^3 + 0.66/(1-x)^2 \quad (4.5)$$

Assuming that the crack faces remain straight, the COD can be approximated by

$$COD = \frac{(a+c-d)\delta_{c\text{ mod}}}{a+c} \quad (4.6)$$

where

$$c = \frac{a\delta_t}{\delta_{c\text{ mod}} - \delta_t} \quad (4.7)$$

and d is the distance from the edge of the specimen to where the COD is measured, which for the specimens used in this investigation is 5 mm.

For an assumed value of the fracture toughness and the measured crack length, Equations (4.2) through (4.7) can be used to calculate the COD which may be compared with the measured value or, conversely, these equations can be solved iteratively to determine the toughness for measured COD and crack length. The former method for $E = 200$ GPa, $\nu = 0.3$, $\sigma_0 = 1.51$ GPa, and $K_{ID} = 88$ MPa \sqrt{m} is used to compute the COD for the measured crack length history of three-point bend Specimen 2. Figure 4.62 compares the predicted COD with the measured values through fracture of this specimen. The agreement is very good and similar correspondence was obtained for Specimens 4, 5 and 6 as shown in Figures 4.63, 4.64 and 4.65, respectively. In the latter the agreement between predictions and measurements tends to deteriorate for deep cracks.

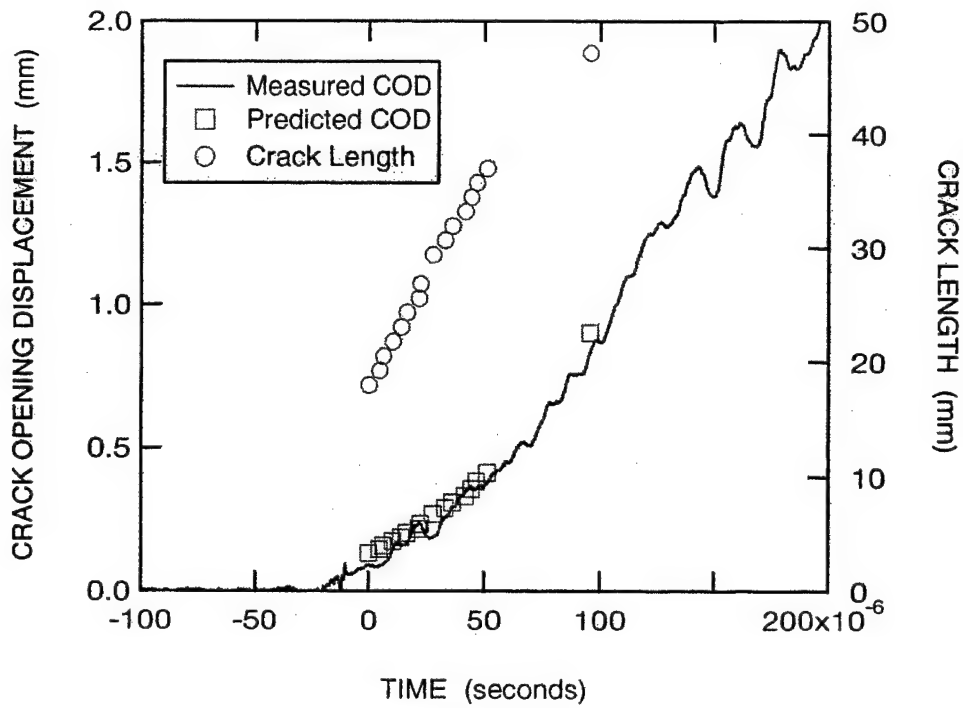


Figure 4.62 Comparison of Measured and Predicted Crack Opening Displacement for Three-Point Bend Specimen 2.

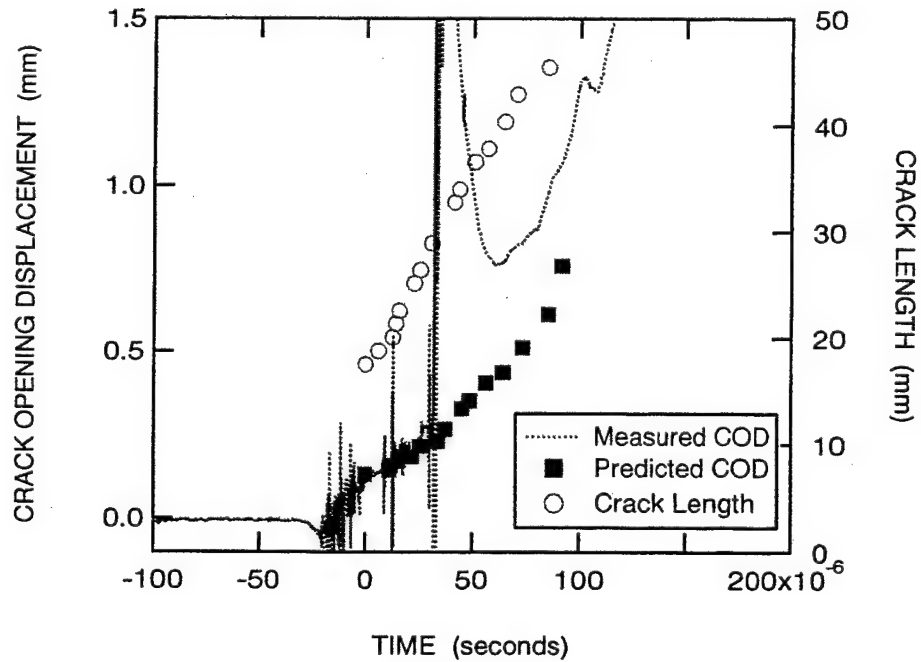


Figure 4.63 Comparison of Measured and Predicted Crack Opening Displacement for Three-Point Bend Specimen 4.

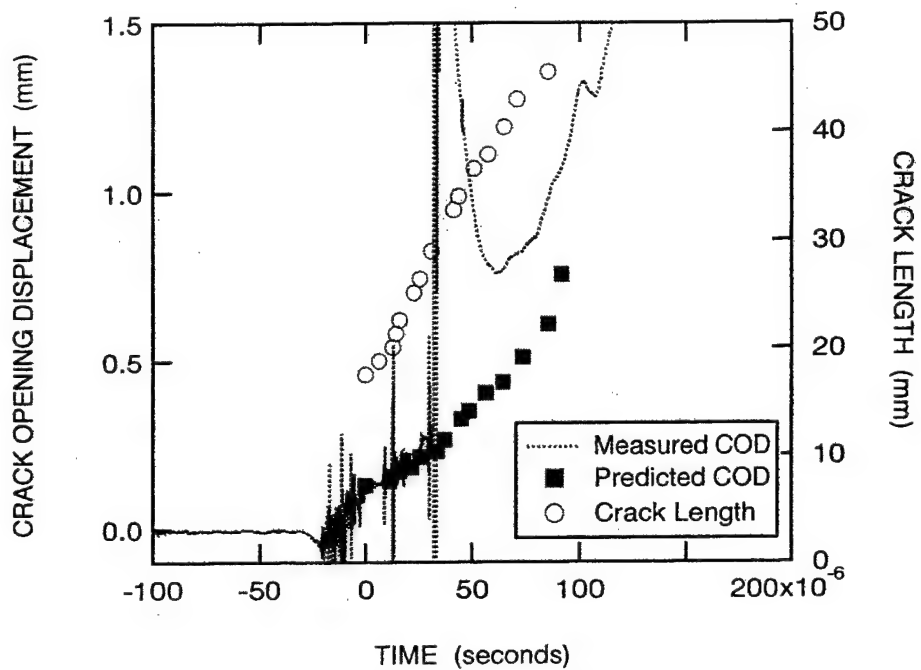


Figure 4.64 Comparison of Measured and Predicted Crack Opening Displacement for Three-Point Bend Specimen 5.

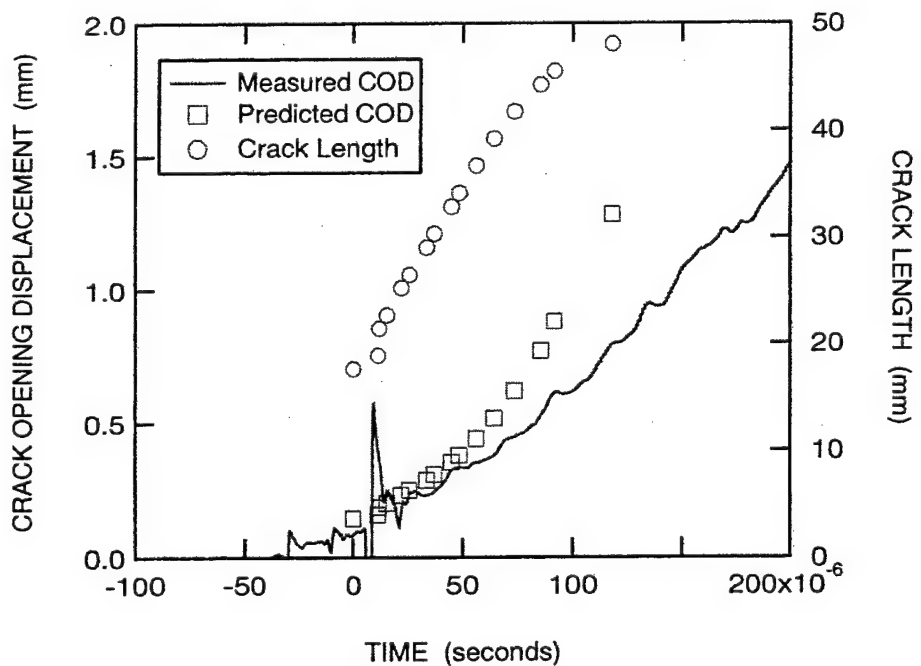


Figure 4.65 Comparison of Measured and Predicted Crack Opening Displacement for Three-Point Bend Specimen 6.

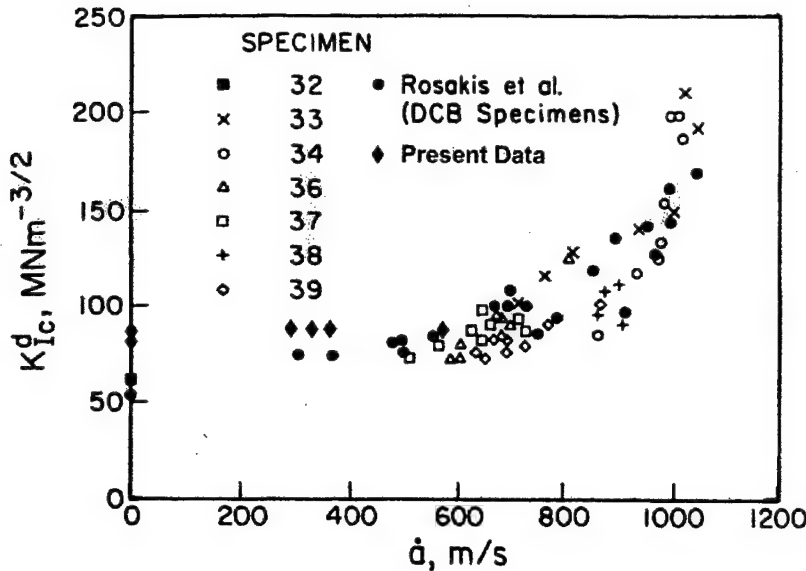


Figure 4.66 Comparison of Present Data with that of Zehnder and Rosakis [11] for AISI 4340.

This may be due to plasticity effects that violate the conditions of small scale yielding. This is apparently the case in Figure 4.64 for Specimen 5 where the COD prior to complete fracture is very large (~ 4 mm). The assumed toughness $K_{ID} = 88 \text{ MPa}\sqrt{\text{m}}$ is in good agreement with the toughness data developed by Zehnder and Rosakis [11] in Figure 4.66 for AISI 4340. Using only the crack-tip singular stress fields, the computed crack tip strain for $K = K_{ID} = 88 \text{ MPa}\sqrt{\text{m}}$ at crack initiation is 0.14 percent and 0.16 percent for plane strain and plane stress, respectively. These values are in good agreement with the measured peak crack tip strain of approximately 0.14 percent at initiation. This model provides a simple means for determining the fracture toughness in lieu of numerical generation phase analysis.

5.0 CONCLUSIONS

A state-of-the-art dynamic fracture mechanics methodology was successfully implemented into the explicit finite element hydrocode EPIC and validated. In this methodology the crack driving force is described by the generalized energy release rate T^* that includes elasto-plasticity, strain rate and inertia effects. An algorithm was developed to calculate T^* from the nodal displacements and stresses routinely computed in EPIC. A nodal release algorithm was also implemented to simulate the propagation of a crack whose directions is known *a priori*; e.g., in a laboratory fracture test. This methodology permits performing a generation phase analysis to deduce the dynamic fracture toughness from measured laboratory data. The methodology also includes an application phase analysis to predict the crack growth-time history in a structure for a specified loading and dynamic fracture resistance. The nodal release algorithm was generalized to an element-failure method that enables computationally efficient three dimensional simulations of through-thickness fracture of penetrator casings. EPIC with the implemented dynamic fracture mechanics methodology can be used to conduct parametric computations to assess the performance of different casing materials for deep earth penetrators, and to perform trade-off studies of strength versus toughness.

Coupled pressure bar tests were performed to determine the dynamic fracture toughnesses of AISI 4340 and AF 1410 steels. Generation phase analyses, using the dynamic-fracture-mechanics-enhanced version of EPIC, of these tests were conducted to deduce the dynamic fracture toughnesses of these steels. For AISI 4340, the dynamic fracture toughness varied from 50 to 130 MPa/m over the range of crack speeds from 300 to 600 m/s. These toughness values tend to fall in the range reported by other investigators for this material. In contrast, the dynamic fracture toughness of the AF 1410 steel was found to be more than twice as great. This is remarkable because the yield strengths of the tested AISI 4340 and AF 1410 steels are very comparable and it is unusual for a material to possess high strength as well as high toughness.

A dynamic three-point bend test was developed as an application phase test for validating the dynamic fracture mechanics methodology. The magnitude and duration of the loading is controlled by the speed and length of the striker bar fired by a gas gun. Tests were conducted for the AISI 4340 material. Dynamic fracture toughness data, obtained from generation phase analysis of the couple pressure bar tests, were used in an application phase analyses of these experiments. In general, good agreement between the predicted and measured crack growth and

strain histories was obtained, and therefore, the dynamic fracture mechanics methodology was validated.

However, the predicted crack opening displacement in these analyses invariably was nearly twice the measured value even when very good agreement between predicted and measured crack tip strains was achieved. It is noteworthy this difference exists irrespective of the fracture mechanics since it exists prior to initiation of crack growth. While extensive investigations were conducted to ascertain the origins for such a large disparity, no definitive explanation was found. It is believed that a prime contributor to the problem is the plane strain simulation of the round transmitter bar and its nose which does not adequately model its impedance and, consequently, the load dynamically transferred from the transmitter bar to the specimen. This is thought to be the case because when EPIC was used to perform a quasi-static analysis of a notched bend bar for which there is no ambiguity in the loading, the agreement of the computations with the known solution was exceptional. A possible solution to the problem is to use a three-dimensional model of the test in place of the two-dimensional plane strain model used in this investigation.

While the dynamic three-point bend test was designed as an application phase experiment, it became apparent during the course of this investigation that it could also be used as a generation phase experiment. An application phase analysis for AF 1410 predicted that it is possible to fracture this material using the new experimental arrangement. It was also demonstrated that a shorter striker bar could still deliver enough energy to fracture a specimen of this tough material. A shorter strike bar (e.g., a 100-mm bar compared to 138-mm bar used in this investigation) also has the advantage that it may be possible to deduce the loading history of the specimen from the transmitter strain gage and aid in resolving the aforementioned impedance problem. The addition of a second set of strain gages to the transmitter bar may also prove beneficial in this regard.

A simple engineering model was developed that enables the deduction of the fracture toughness from the crack opening displacement and crack growth histories measured in the dynamic three-point bend test without the need for a numerical simulation of the test. This analytical method is based upon small scale yielding and, consequently, is limited to high strength, low-to-moderately tough materials; e.g., as demonstrated for AISI 4340.

All dynamic fracture tests have their advantages and disadvantages. Relative to the coupled pressure bar (CPB) test, the dynamic three-point bend test developed in this program has

a relatively simple test arrangement. The set up is easy and, therefore, experiments are substantially cheaper to perform. It does require a gas gun capable of launching a 25-mm diameter bar at speeds upwards of 90 m/s. It is simple to control the loading pulse by adjusting the speed and length of the striker bar. The boundary and initial conditions are well defined, although there is some uncertainty about how to model the round transmitter bar in two dimensions. Since cracks in these tests, at least for AISI 4340 steel, tend to propagate at a constant speed, multiple tests are required to quantify the dependence of the fracture resistance on crack speed. The strength of the bars and capacity of the gas gun limit the attainable crack speed. While this test is unproven for high toughness materials such as AF 1410, analyses indicate that it should be applicable for these materials.

This is contrasted to the CPB apparatus that requires a large load frame (~900 kN capacity) to store energy to drive the crack. Crack speed, for a given material, is limited by the capacity of the load frame. A range of crack speeds is sampled in the test; thus, fewer tests are required for toughness-crack speed determination. Although two specimens are tested simultaneously, available instrumentation channels are now divided between the two specimens (for the same number of recording channels, more detailed crack growth measurements are possible for the dynamic three-point bend test). The test arrangement is complex, and test set up is tedious, with more opportunity for problems. There are also safety issues involved in the large preload, and cutting of the notched coupler. There exist uncertainties in the loading conditions since the load point displacement is not measured directly, but must be inferred from a load line displacement measurement.

Therefore, the simplicity of the dynamic three-point bend experiment, as compared to using the coupled pressure bar apparatus, outweighs the extra costs of additional tests that must be conducted to obtain fracture toughness as a function of crack speed. Being a new test methodology, however, there remains some questions regarding the dynamic three-point bend experiment; but it is believed that these questions will be resolved with further experience.

In summary, a dynamic fracture mechanics methodology has been incorporated into the explicit, time-dependent, finite element hydrocode EPIC, and validated in an integrated experimental and computational research effort. The technology developed in this effort will enable the Air Force to evaluate dynamic crack propagation/arrest in a penetrator case; to evaluate overall penetrator performance during penetration; to make informed trade-off decisions

of material strength versus fracture toughness; and to provide the basis for rational design and material selection decisions.

6.0 REFERENCES

1. Griffith, A.A., "The Phenomena of Rupture and Flow in Solids," *Philosophical Transactions of the Royal Society*, A221, pp. 163-198, 1920.
2. Kanninen, M.F. and Popelar, C.H., *Advanced Fracture Mechanics*, Oxford University Press, New York, 1985.
3. Atluri, S.N., Nishioka, T., and Nagagaki, M., "Incremental Path-Independent Integrals in Inelastic and Dynamic Fracture Mechanics," *Engineering Fracture Mechanics*, Vol. 20, 209-244, 1984.
4. Dexter, R.J. and O'Donoghue, P.E., "Computational Procedures and Energy Integral for Dynamic Fracture in Viscoplastic Materials," *Engineering Fracture Mechanics*, Vol. 44, pp. 591-607, 1993.
5. Jung, J., Ahmad, J., Kanninen, M.F., and Popelar, C.H., "Finite Element Analysis of Dynamic Crack Propagation," *Failure Prevention and Reliability-1981*, ASME, New York, pp. 7-12, 1981.
6. Johnson, G.R., Beissel, S.R., Anderson, C.E., Popelar, C.H., and Walker, J.D, *Penetrator Case Fracture Predictive Technology: Volume 2—Numerical Algorithms and Computations*, AFRL-MN-EG-TR-1999-xxxx, Air Force Research Laboratory, June 1999.
7. Couque, H., Hudak, S.J., Jr., and Lindholm, U.S., "On the Use of Coupled Pressure Bars to Measure the Dynamic Fracture Initiation and Crack Propagation Toughness of Pressure Vessel Steels," *Journal de Physique*, Suplément No. 9, Tome 49, pp. C3-347-C3-352, 1998.
8. Couque, H., Dexter, R.J., and Hudak, S.J., Jr., "Using Small Specimens to Measure Dynamic Fracture Properties of High Toughness Steels," *Rapid Load Fracture Testing, ASTM STP 1130*, pp. 24-36, 1992.
9. Kanninen, M.F., Hudak, S.J., Jr., Couque, H.R., Dexter, R.J., and O'Donoghue, P.E., "Viscoplastic-Dynamic Crack Propagation: Experimental and Analysis Research for Crack Arrest Applications in Engineering Structures," *International Journal of Fracture*, Vol. 42, pp. 239-260, 1990.
10. Couque, H., Leung, C.P., and Hudak, S.J., Jr., "Effect of Planar Size and Dynamic Loading Rate on Initiation and Propagation Toughness of a Moderate-Toughness Steel," *Engineering Fracture Mechanics*, Vol. 47, pp. 249-267, 1994.
11. Zehnder, A.T. and Rosakis, A.J., "Dynamic Fracture Initiation and Propagation in 4340 Steel under Impact Loading," *International Journal of Fracture*, Vol. 43, pp. 271-285, 1990.
12. Yokoyama, T., "Determination of Dynamic Fracture-Initiation Toughness Using a Novel Impact Bend Test Procedure," *Journal of Pressure Vessel Technology*, Vol. 115, pp. 389-397, 1993.

13. Tada, H., Paris, P.C., and Irwin, G.R., *The Stress Analysis of Cracks Handbook*, Second Edition, Paris Productions Inc., St. Louis, MO, 1985.
14. Timoshenko, S., and Goodier, J.N., *Theory of Elasticity*, Second Edition, McGraw-Hill, New York, 1951.

APPENDIX A
EXPERIMENTAL DATA FOR AISI 4340 AND AF 1410

Table A1. Tensile Properties for AISI 4340 and AF 1410 Steels.

Tensile Properties

06-8037

4340		
Spec No.	.2% Yield (ksi)	Ultimate (ksi)
1-1	217.414	246.623
1-2	217.238	246.567
2-1	217.794	246.993
2-2	220.628	250.434
3-1	216.904	244.985
3-2	216.470	244.749
Avg	217.741	246.725

1410		
Spec No.	.2% Yield (ksi)	Ultimate (ksi)
1410T11	239.530	250.340
1410T31	231.170	241.070
1410T61	240.360	255.860
Avg	237.020	249.090

tensprop.wks

Tensile Specimen No.1-1
Init.=.2503"/Final=.1935", Rate=8.70e-04

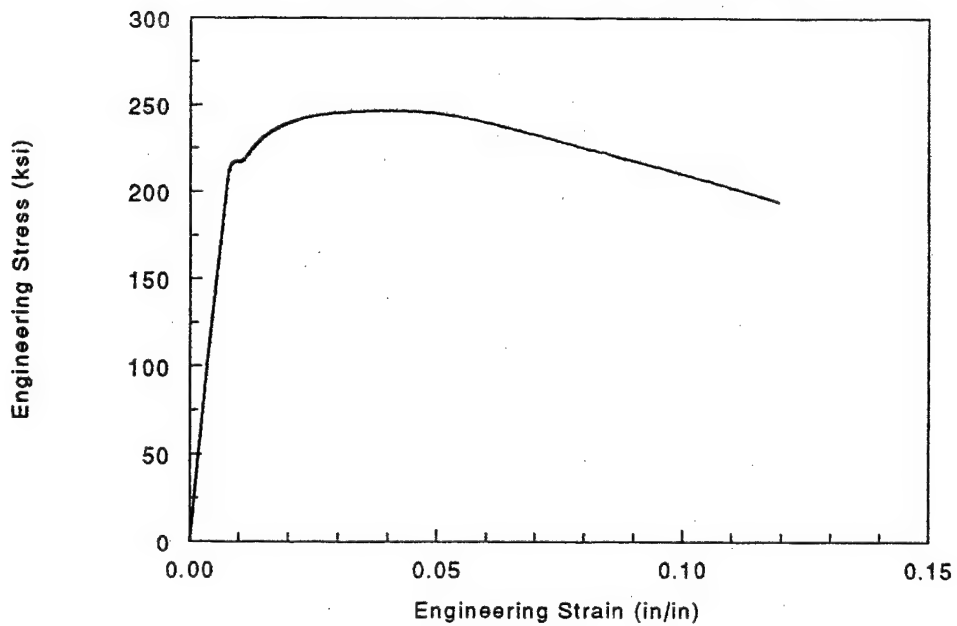


Figure A1. Measured Stress-Strain Data for AISI 4340 Specimen No. 1-1.

Tensile Specimen No.1-2
Init = .2502"/Final=.1960", Rate=8.50e-04

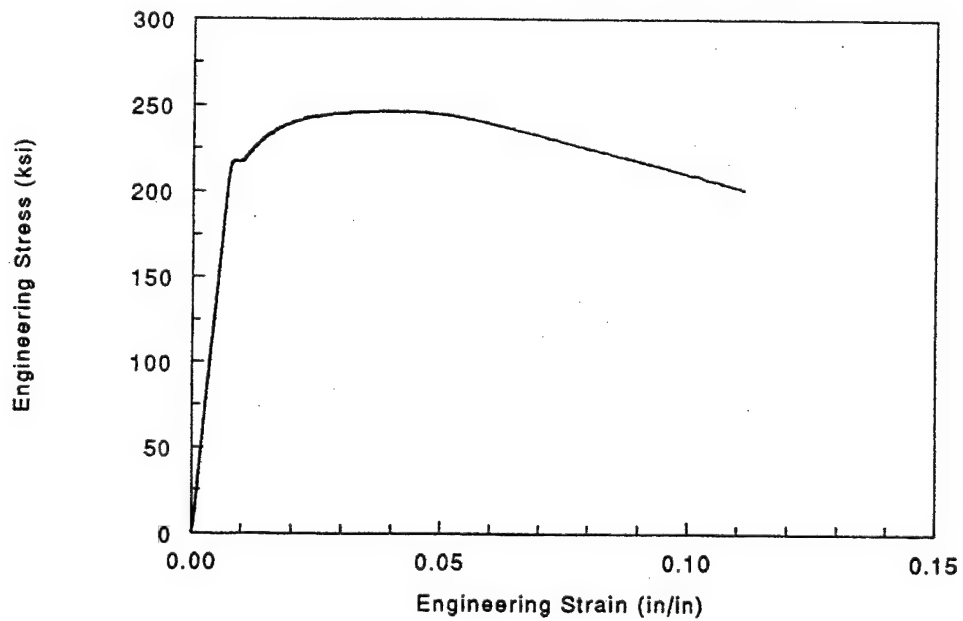


Figure A2. Measured Stress-Strain Data for AISI 4340 Specimen No. 1-2.

Tensile Specimen No.2-1

Init.=.2504"/Final=.1920", Rate=8.95e-04

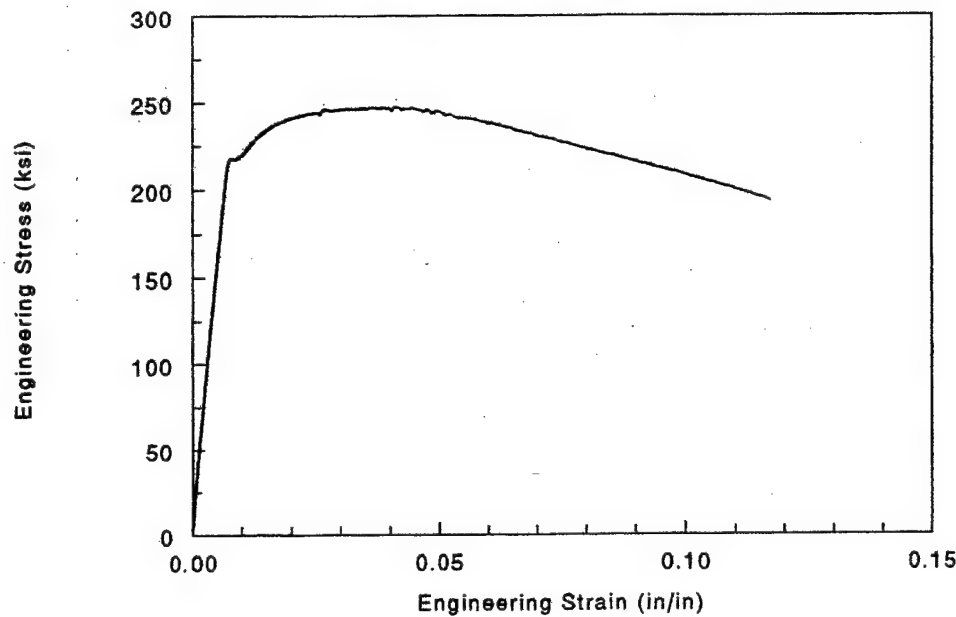


Figure A3. Measured Stress-Strain Data for AISI 4340 Specimen No. 2-1.

Tensile Specimen No.2-2

Init.=.2503"/Final=.200", Rate=8.54e-04

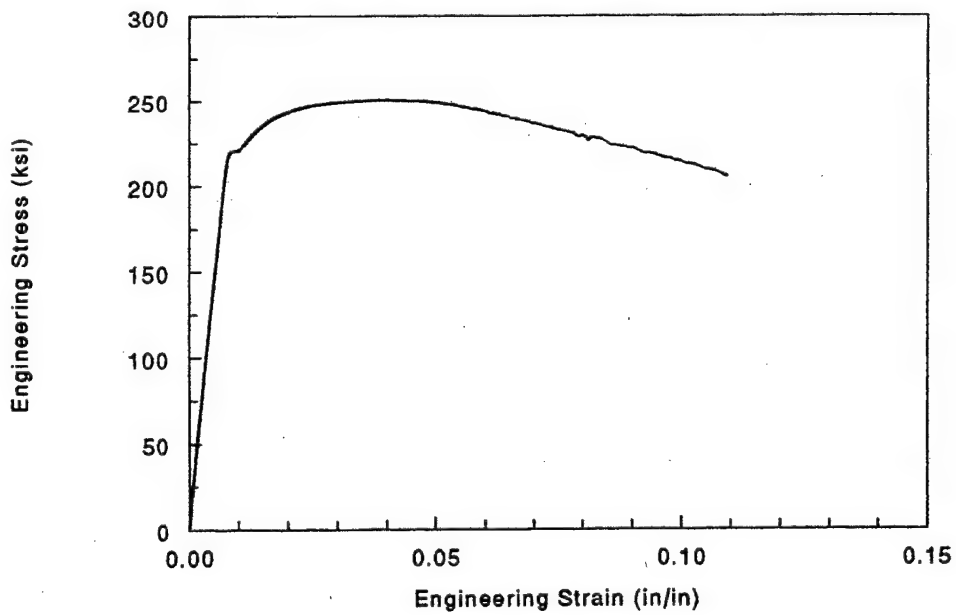


Figure A4. Measured Stress-Strain Data for AISI 4340 Specimen No. 2-2.

Tensile Specimen No.3-1

Init.=.2501"/Final=.1925", Rate=8.96e-04

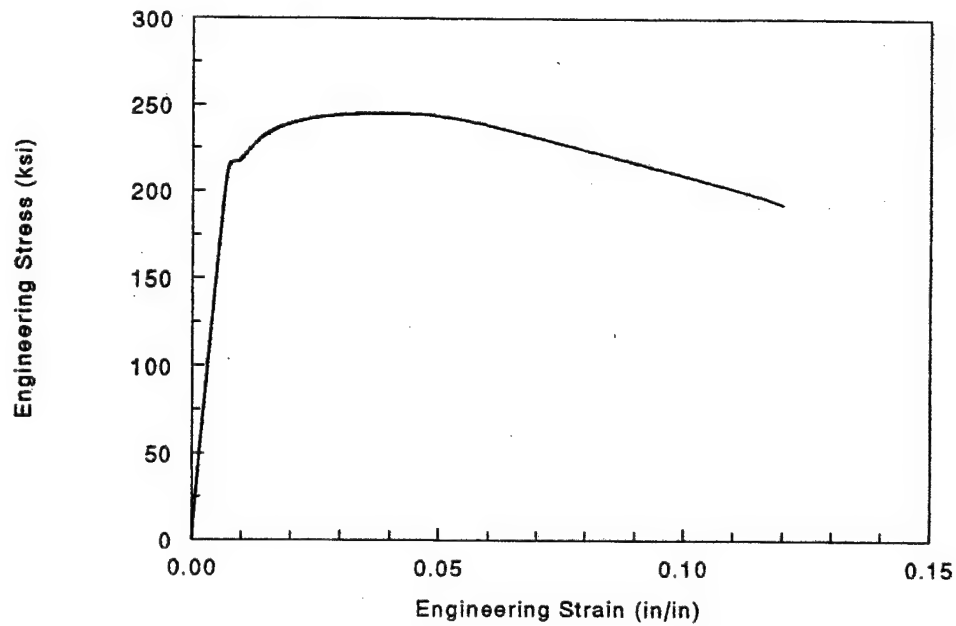


Figure A5. Measured Stress-Strain Data for AISI 4340 Specimen No. 3-1.

Tensile Specimen No.3-2

Init.=.2503"/Final=.1935", Rate=8.82e-04

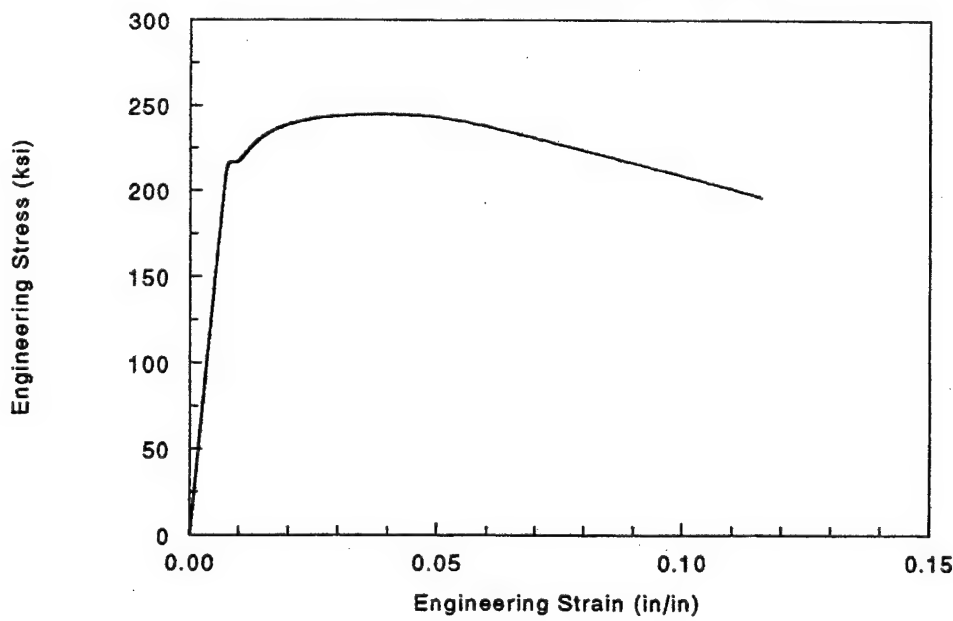


Figure A6. Measured Stress-Strain Data for AISI 4340 Specimen No. 3-2.

Tensile Specimen No.1410T61
Init.=.2507"/Final=.1365"

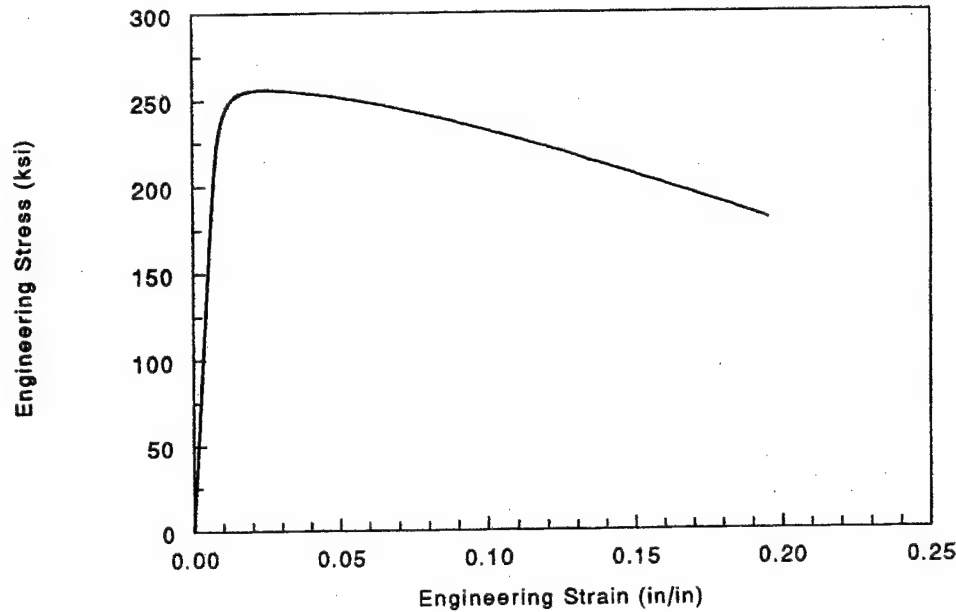


Figure A7. Measured Stress-Strain Data for AF 1410 Specimen No. 1410T61.

Tensile Specimen No.1410T11
Init.=.2506"/Final=.1375"

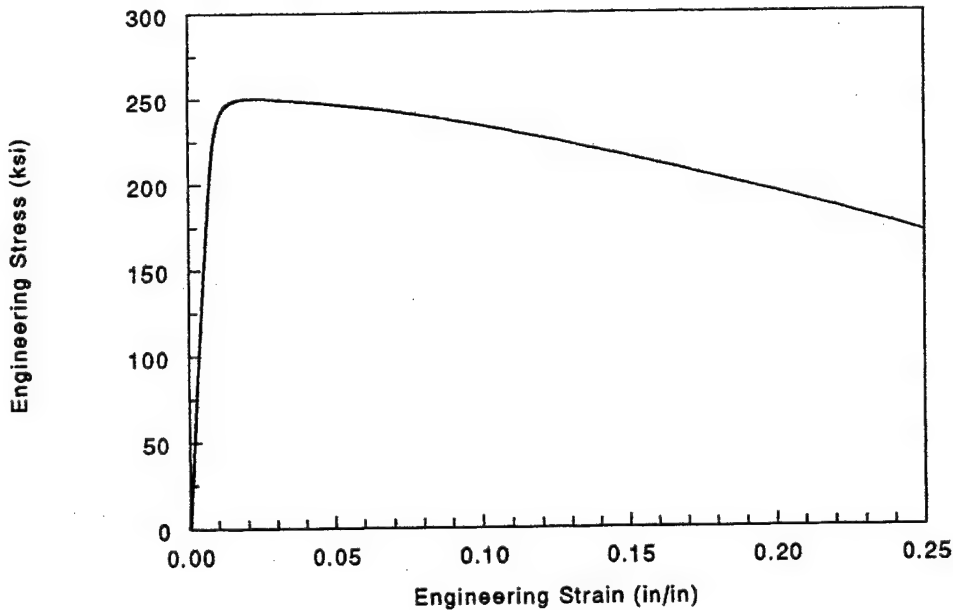


Figure A8. Measured Stress-Strain Data for AF 1410 Specimen No. 1410T11.

Tensile Specimen No.1410T31

Init.=.2507"/Final=.1345"

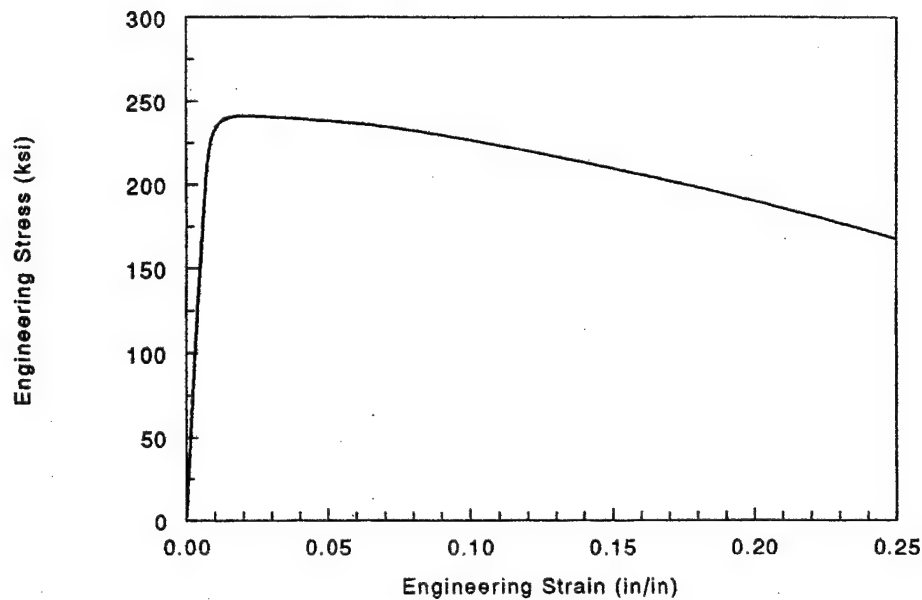


Figure A9. Measured Stress-Strain Data for AF 1410 Specimen No. 1410T31.

Fracture Toughness No.8037-7

Material: 4340 at Room Temperature

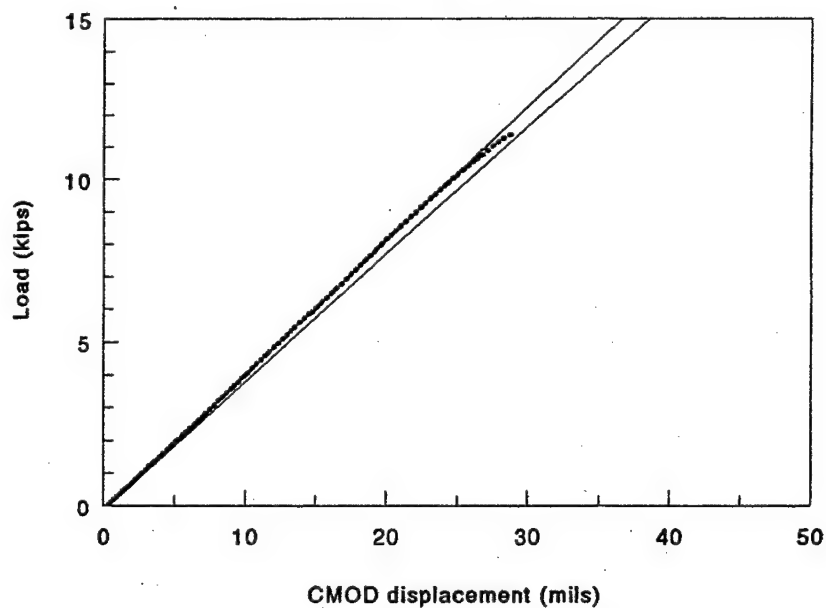


Figure A10. Measured Load Versus CMOD in ASTM E399 Test of AISI 4340 Specimen No. 8037-7.

Fracture Toughness No.8037-8

Material: 4340 at Room Temperature

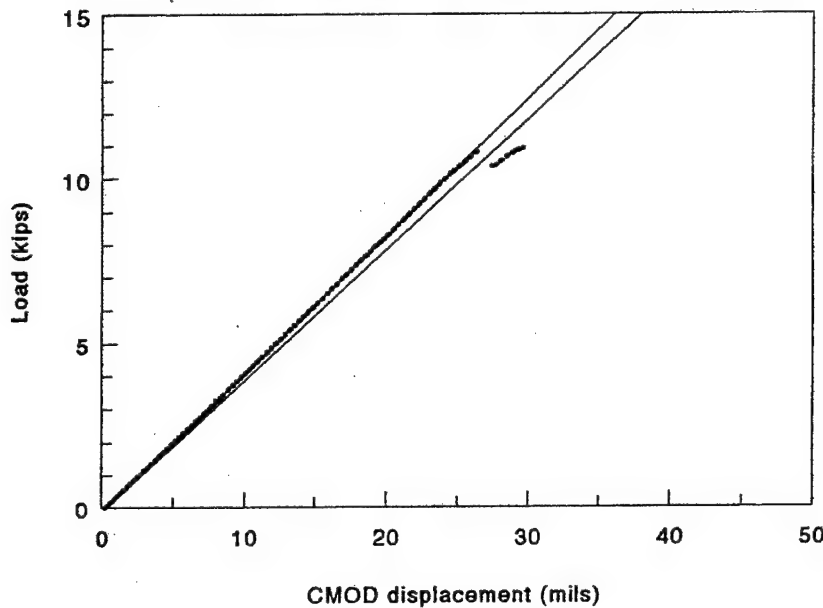


Figure A11. Measured Load Versus CMOD in ASTM E399 Test of AISI 4340 Specimen No. 8037-8.

Fracture Toughness Specimen No.CT-1

AF1410 Material 8-6-97

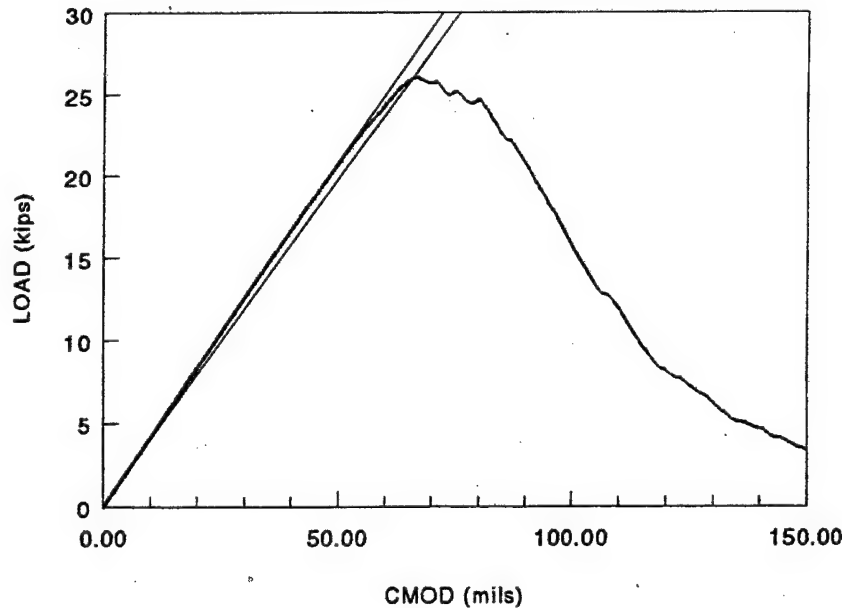
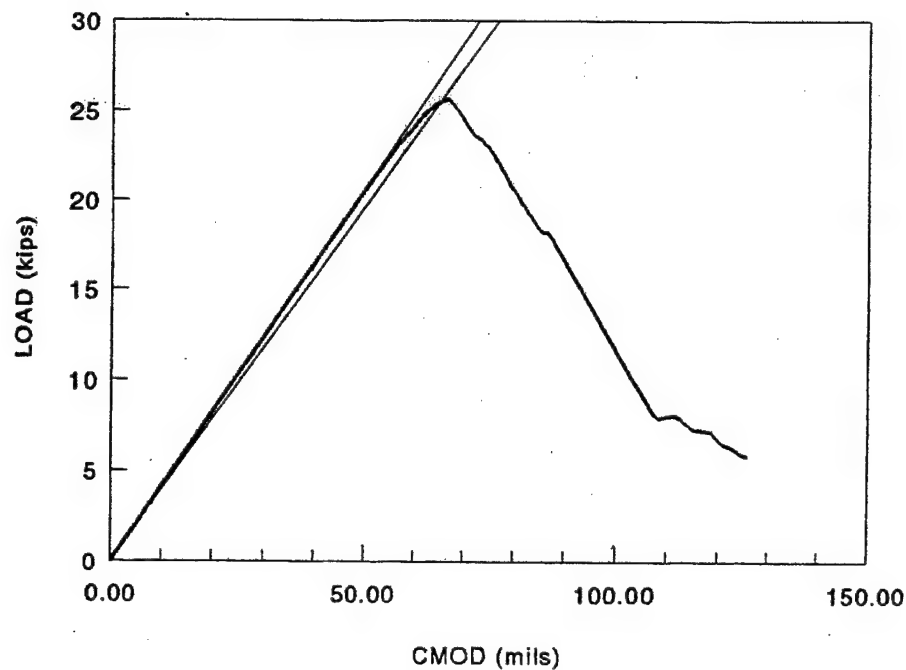


Figure A12. Measured Load Versus CMOD in ASTM E399 Test of AF 1410 Specimen No. CT-1.

Fracture Toughness Specimen No. CT-2
AF1410 Material 8-6-97



**Figure A13. Measured Load Versus CMOD in ASTM E399
Test of AF 1410 Specimen No. CT-2.**

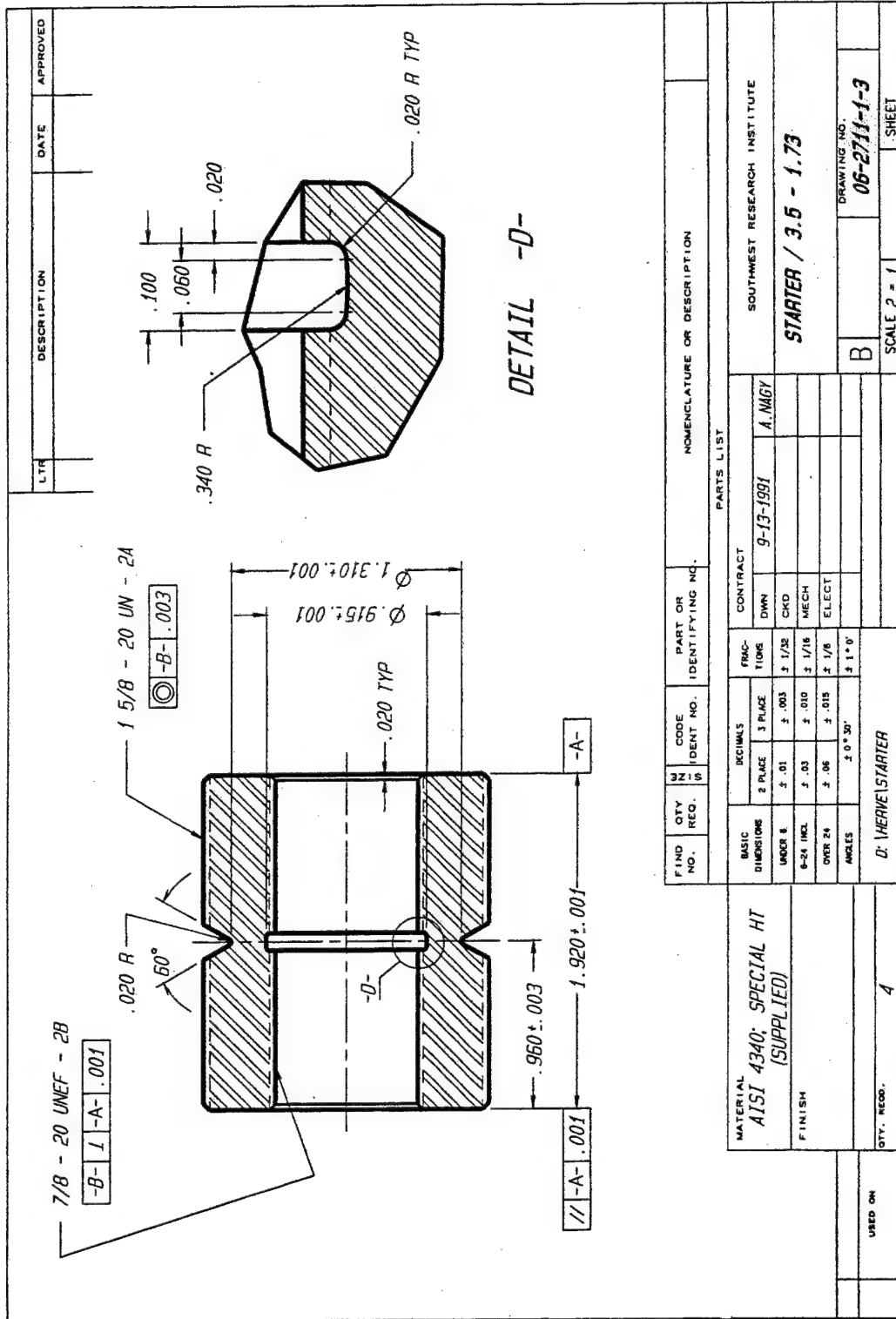


Figure A14. Machine Drawing of Coupler (Dimensions in Inches).

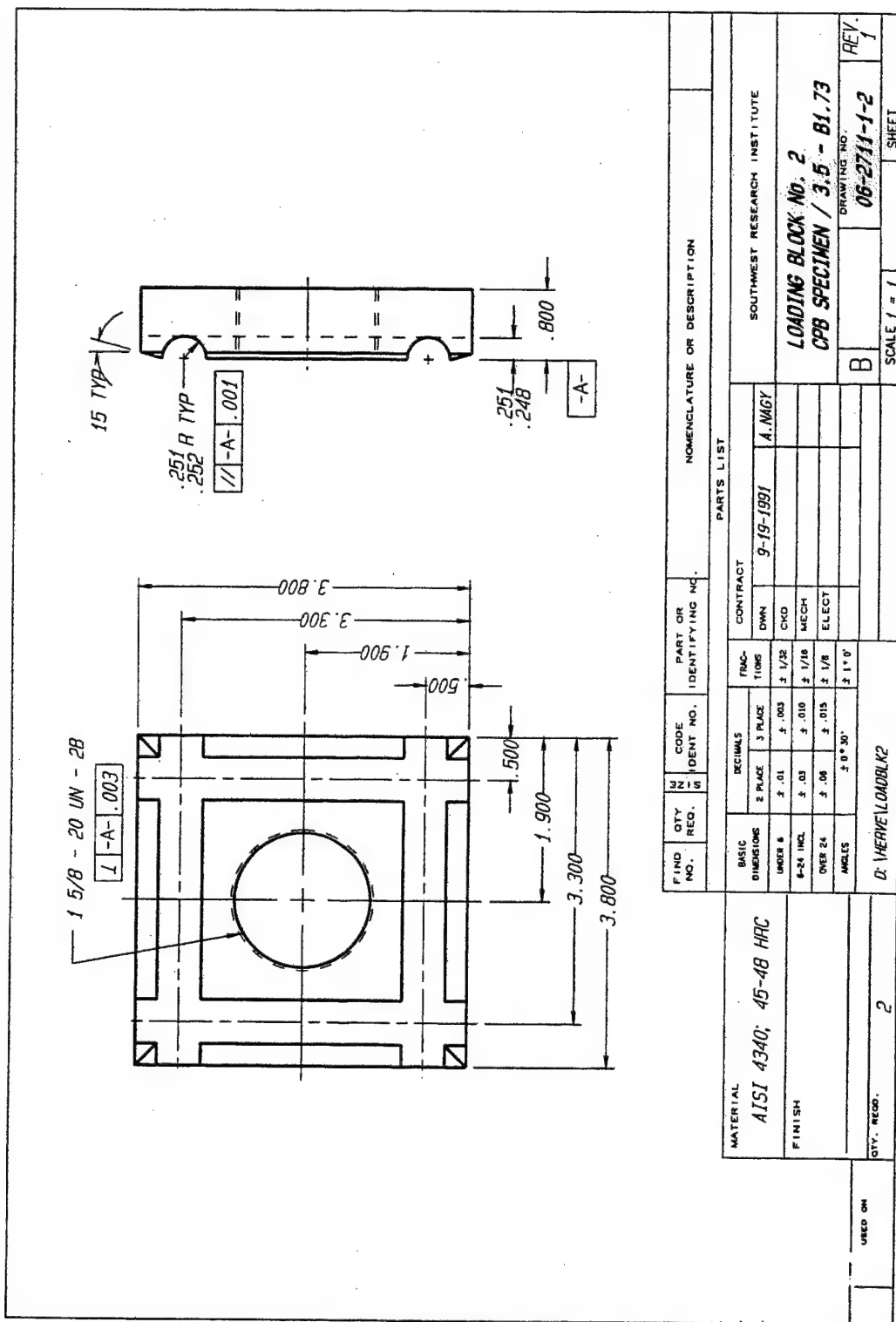


Figure A15. Machine Drawing of Loading Plates (Dimensions in Inches).

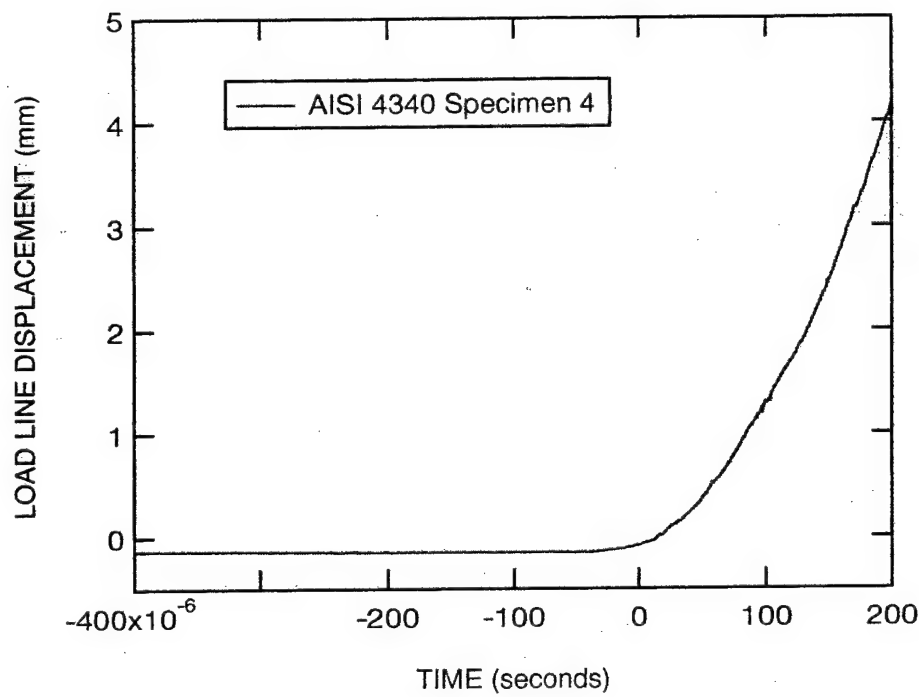


Figure A16. Measured Load Line Displacement in AISI 4340 Specimen 4.

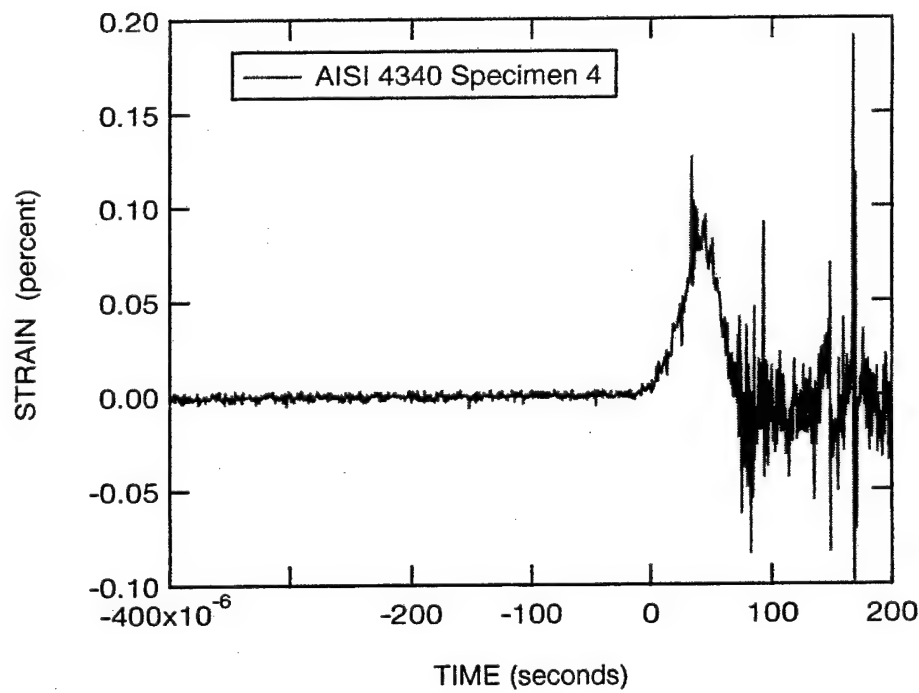


Figure A17. Measured Strain in AISI 4340 Specimen 4.

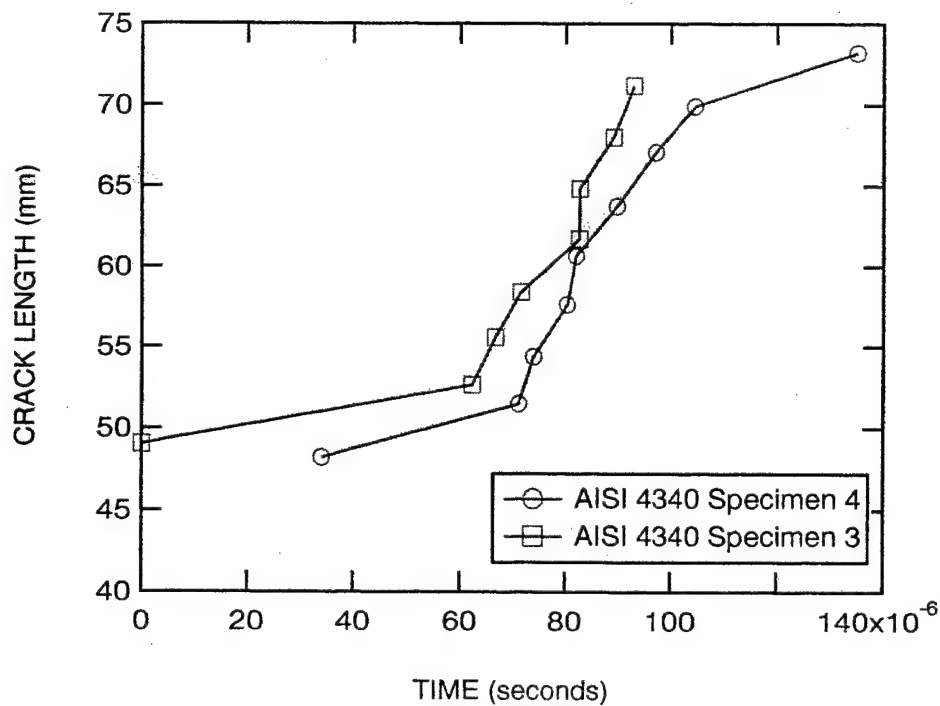


Figure A18. Measured Crack Length-Time History in AISI 4340 Specimens 3 and 4.

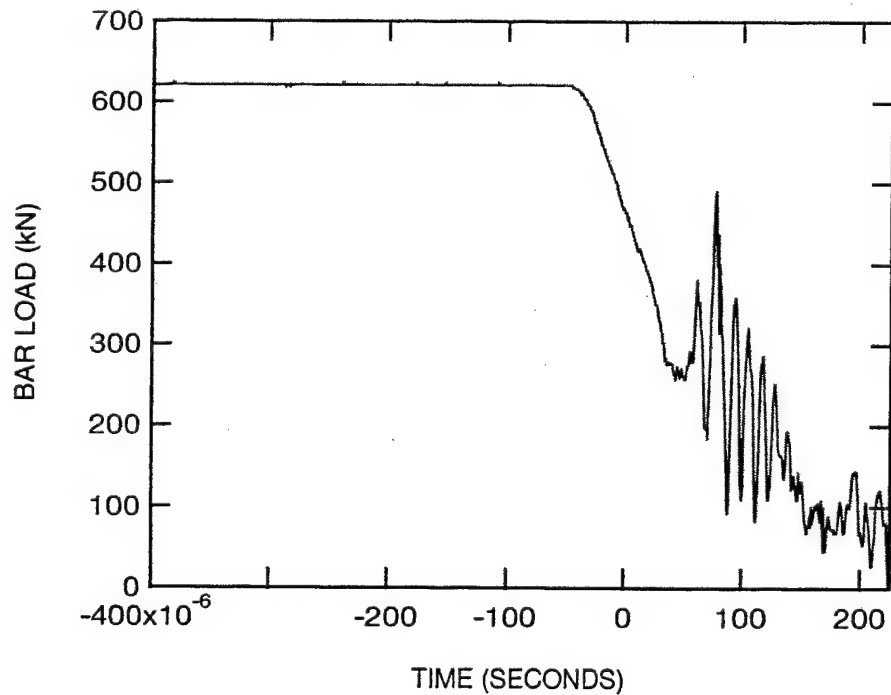


Figure A19. Measured Load in Bar for Test of AISI 4340 Specimens 3 and 4.

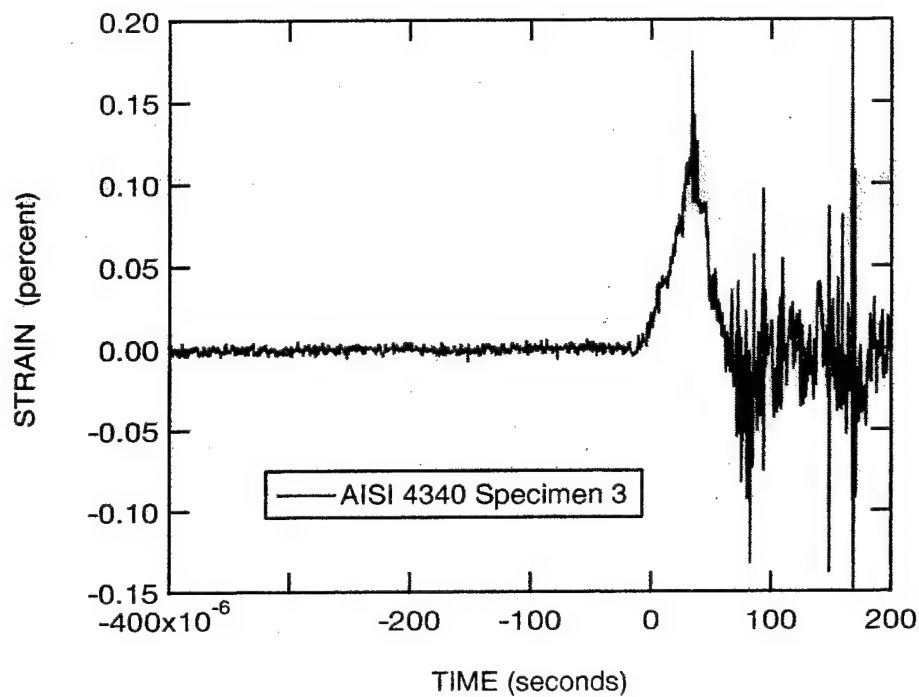


Figure A20. Measured Strain in AISI 4340 Specimen 3.

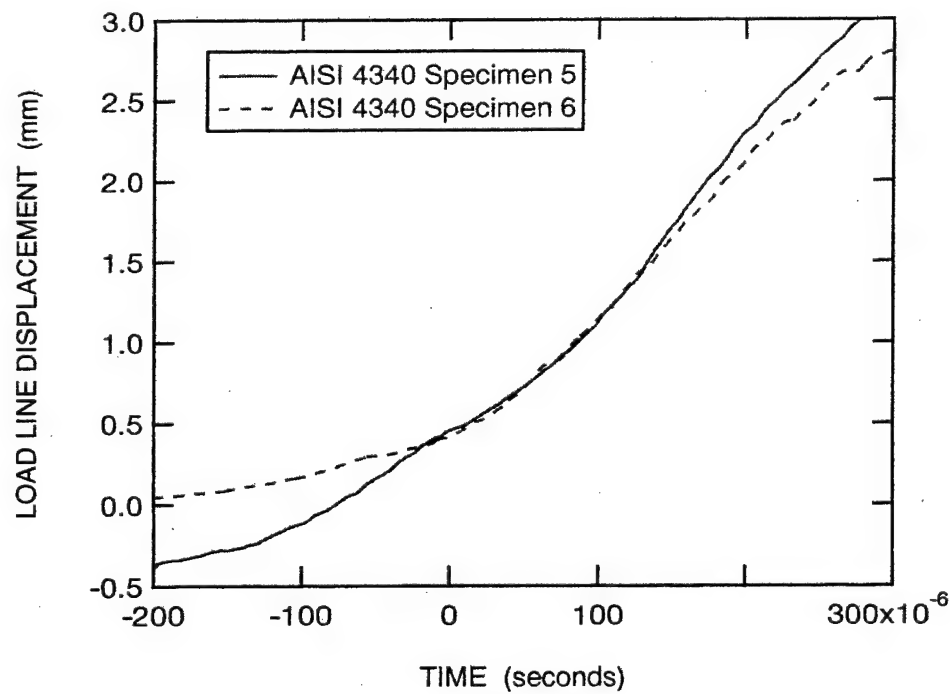


Figure A21. Measured Load Line Displacement in AISI 4340 Specimens 5 and 6.

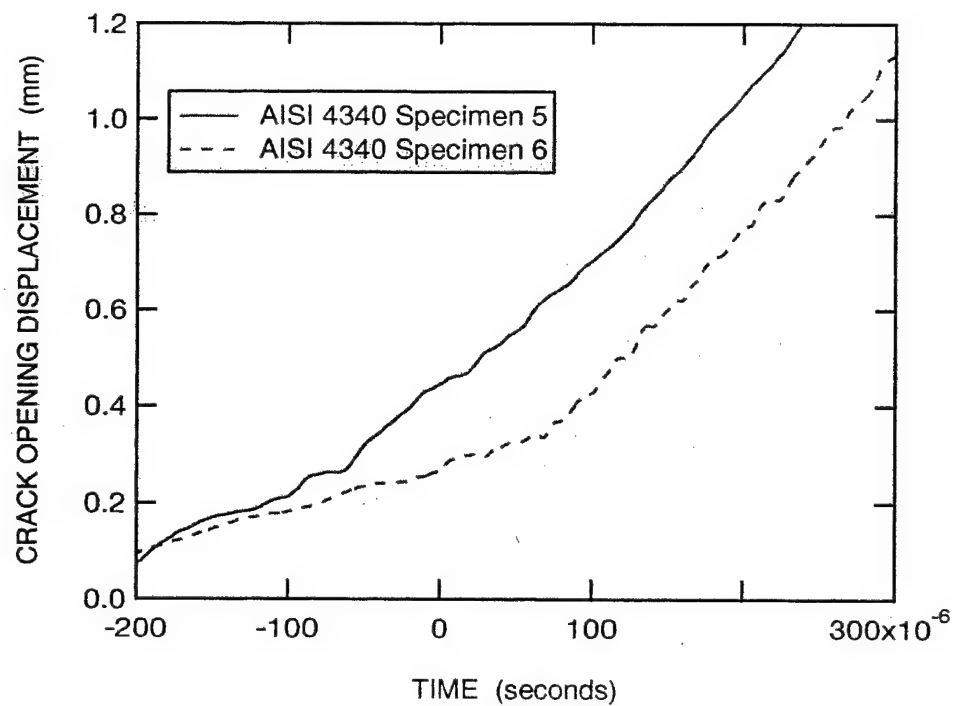


Figure A22. Measured Crack Opening Displacement in AISI 4340 Specimens 5 and 6.

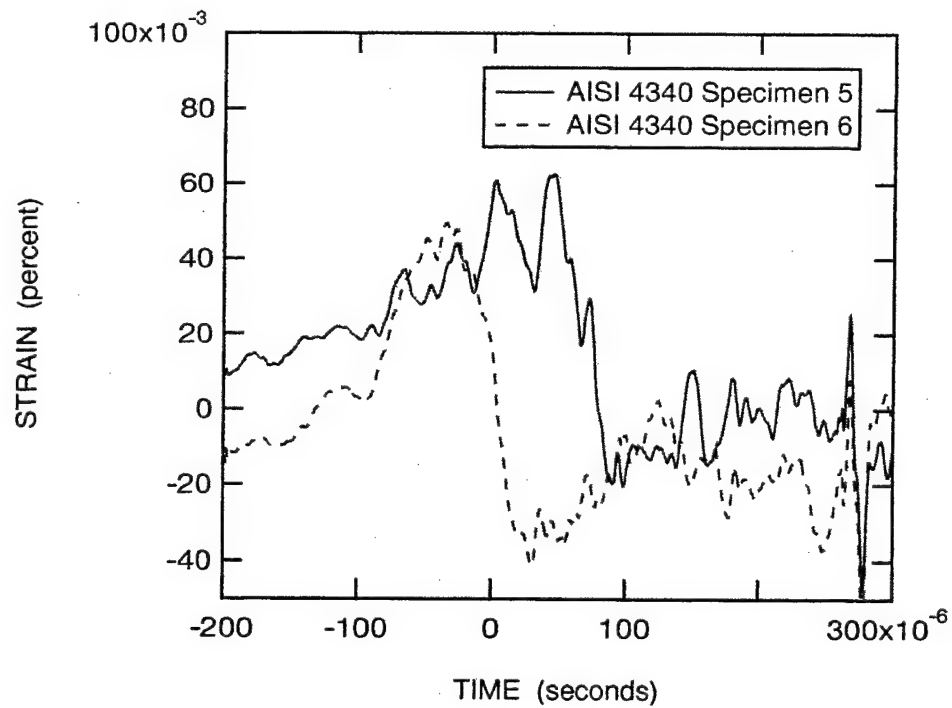


Figure A23. Measured Strain in AISI 4340 Specimens 5 and 6.

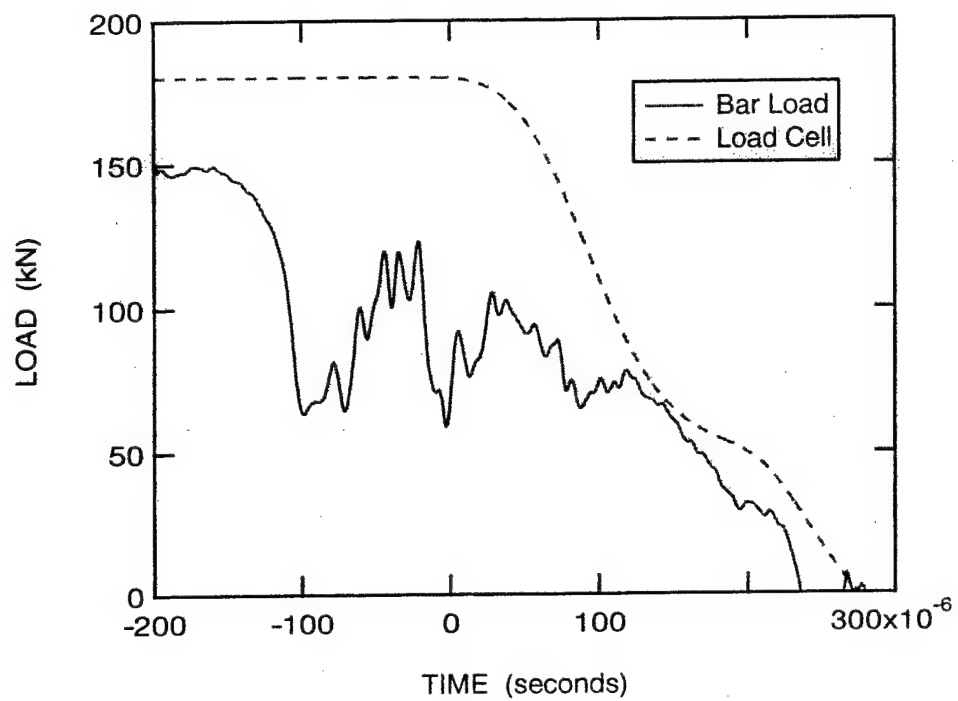


Figure A24. Bar Load and Load Cell Records for Test of AISI 4340 Specimens 5 and 6.

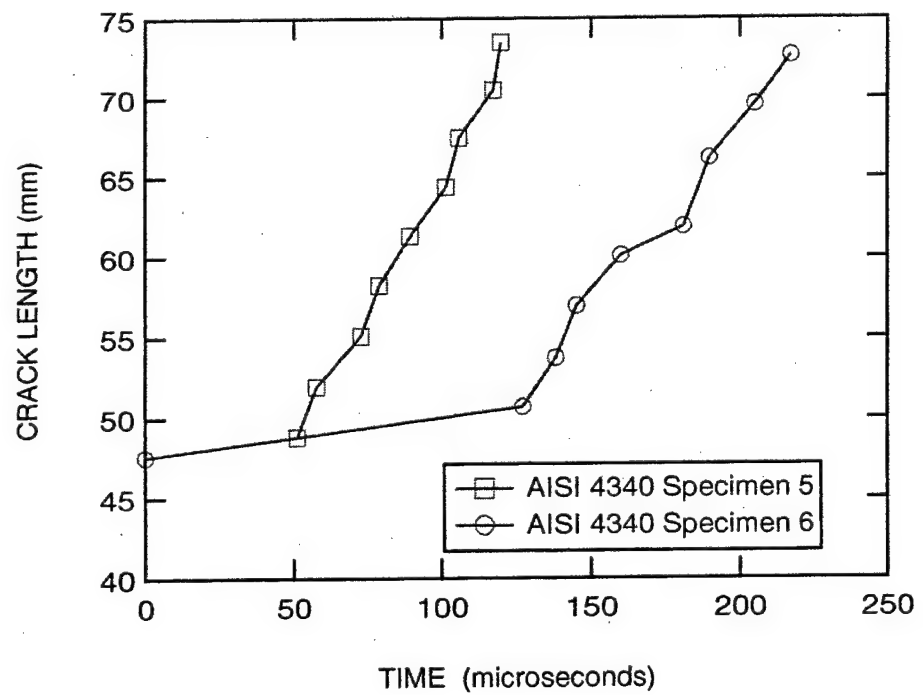


Figure A25. Measured Crack Length-Time History for AISI Specimens 5 and 6.

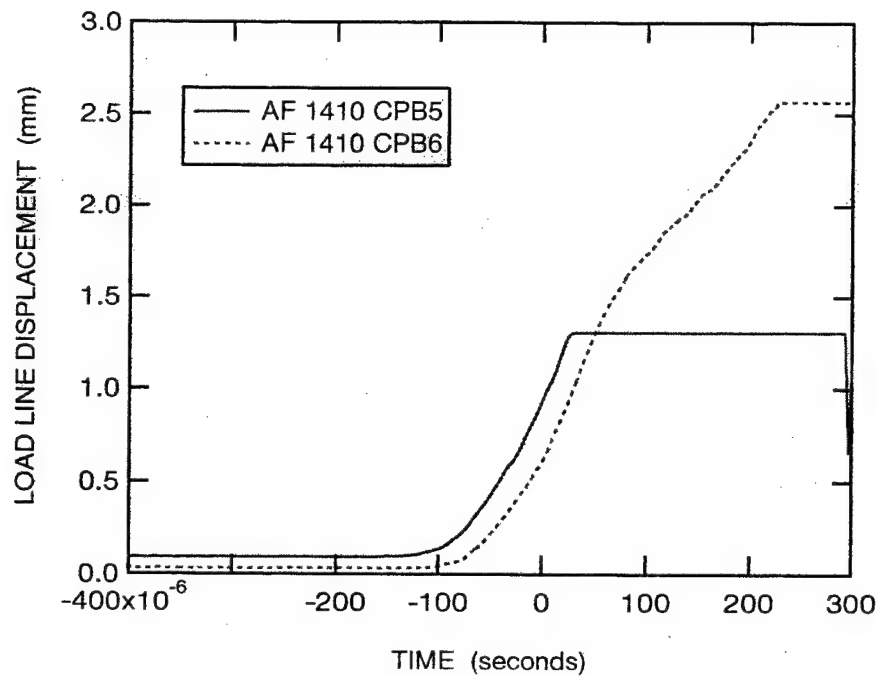


Figure A26. Measured Load Line Displacement in AF 1410 Specimens CPB5 and CPB6.

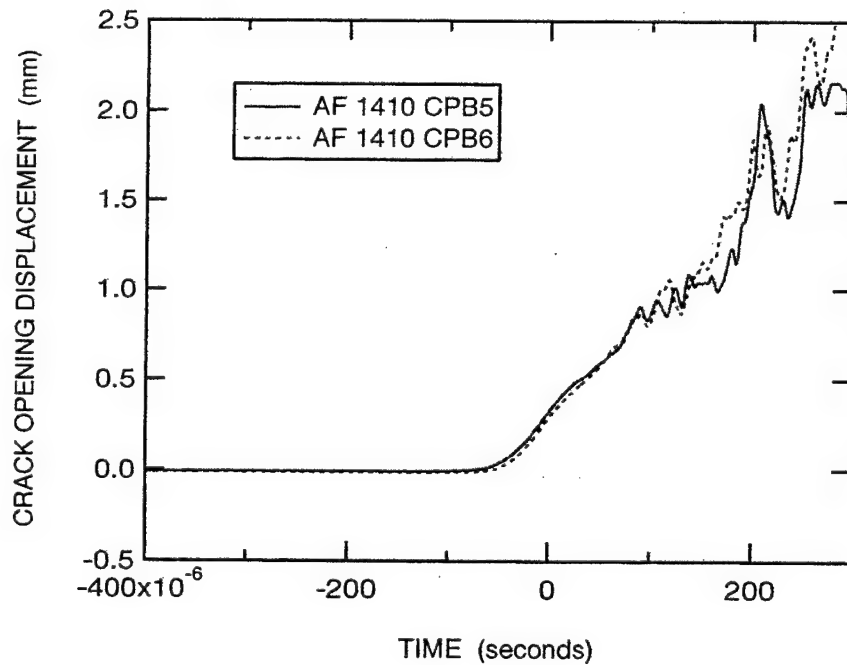


Figure A27. Measured Crack Opening Displacement in AF 1410 Specimens CPB5 and CPB6.

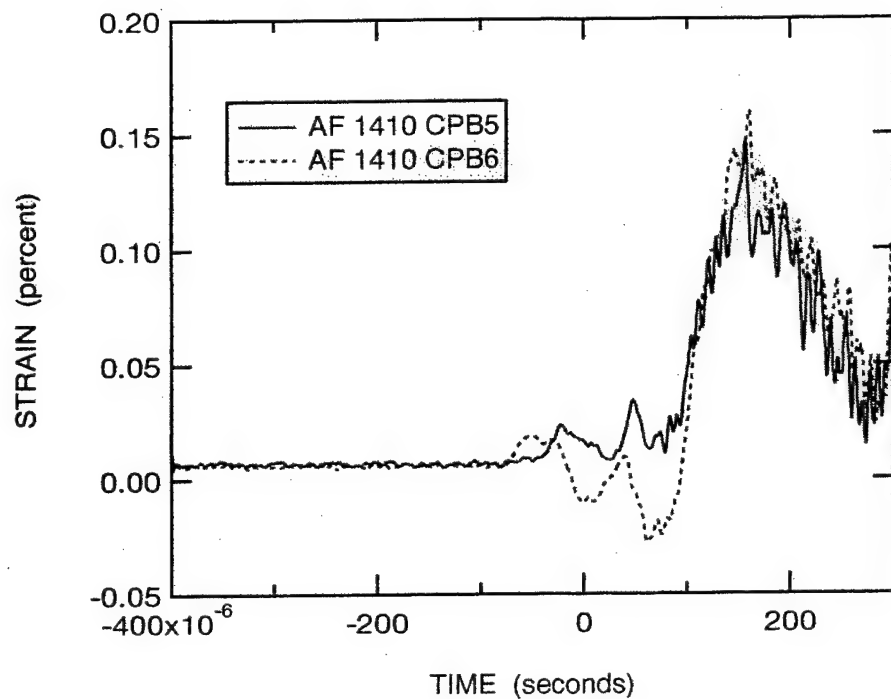


Figure A28. Measured Strain AF 1410 Specimens CPB5 and CPB6.

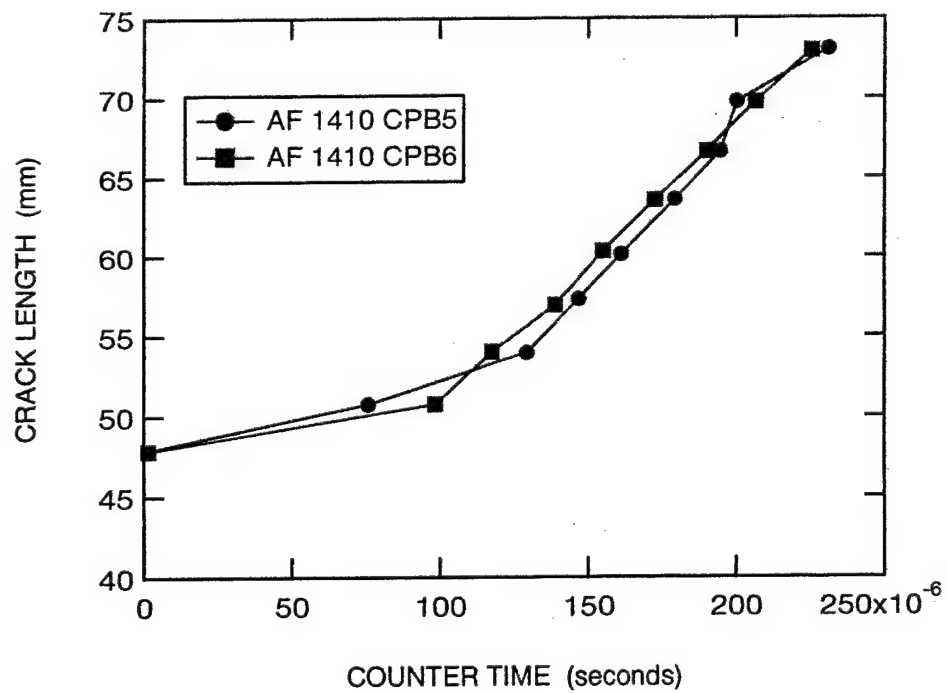


Figure A29. Measured Crack Length-Time Histories of AF 1410 Specimens CPB5 and CPB6.

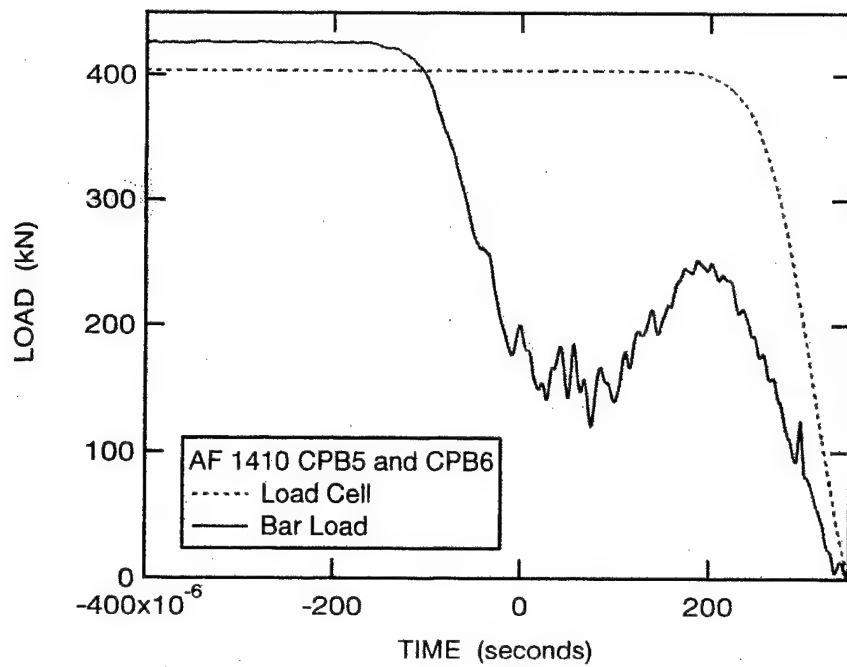


Figure A30. Bar Load and Load Cell Records for Test of AF 1410 Specimens CPB5 and CPB6.

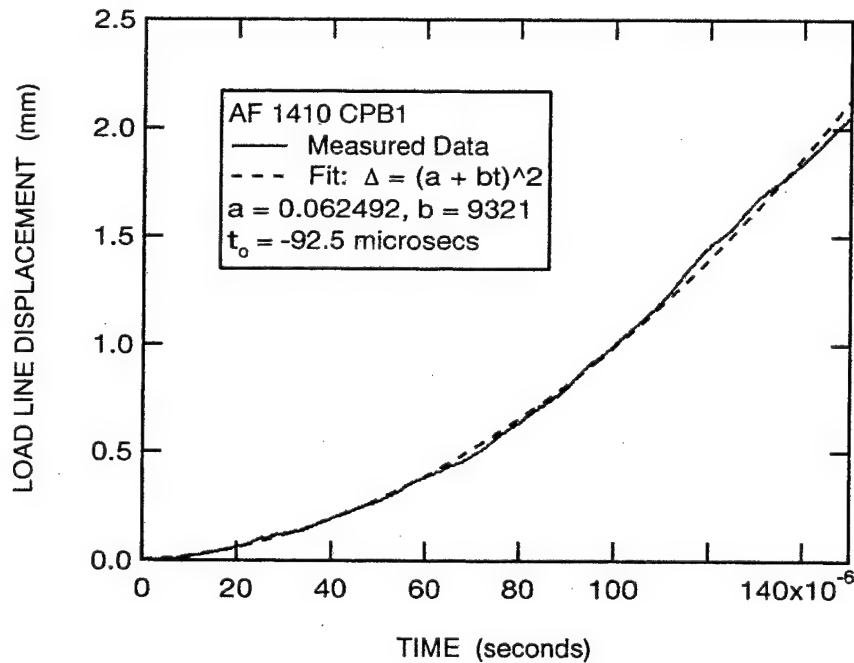


Figure A31. Reduced Load Line Displacement Data for AF 1410 Specimen CPB1.

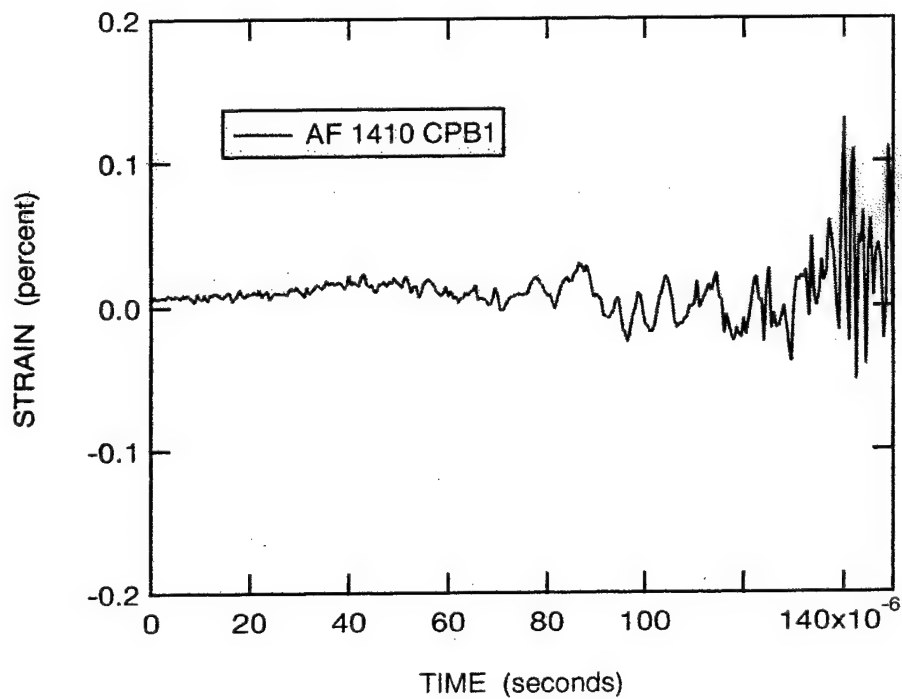


Figure A32. Reduced Strain Data for AF 1410 Specimen CPB1.

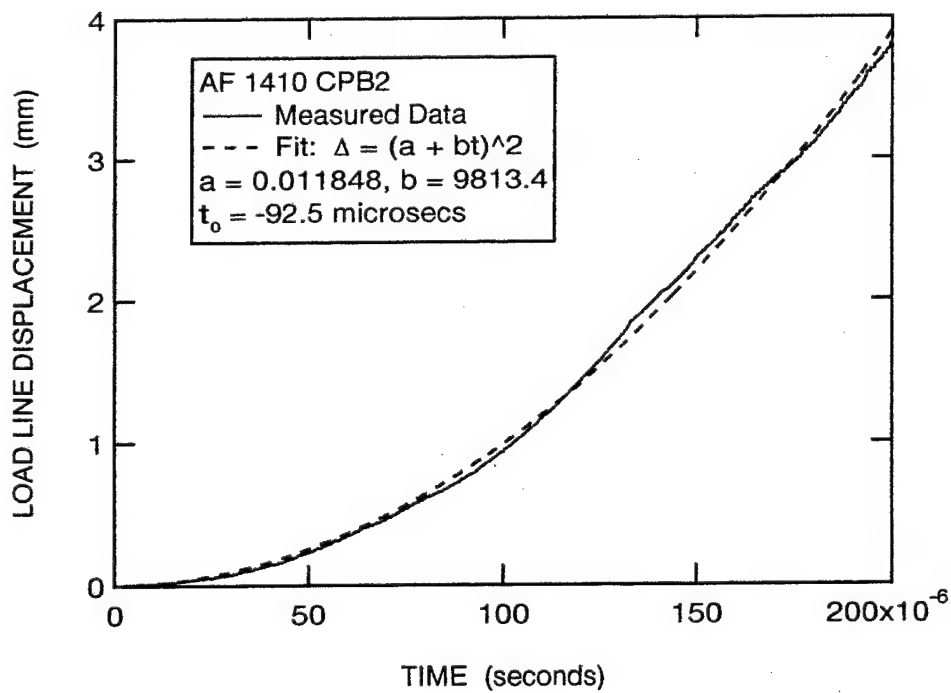


Figure A33. Reduced Load Line Displacement Data for AF 1410 Specimen CPB2.

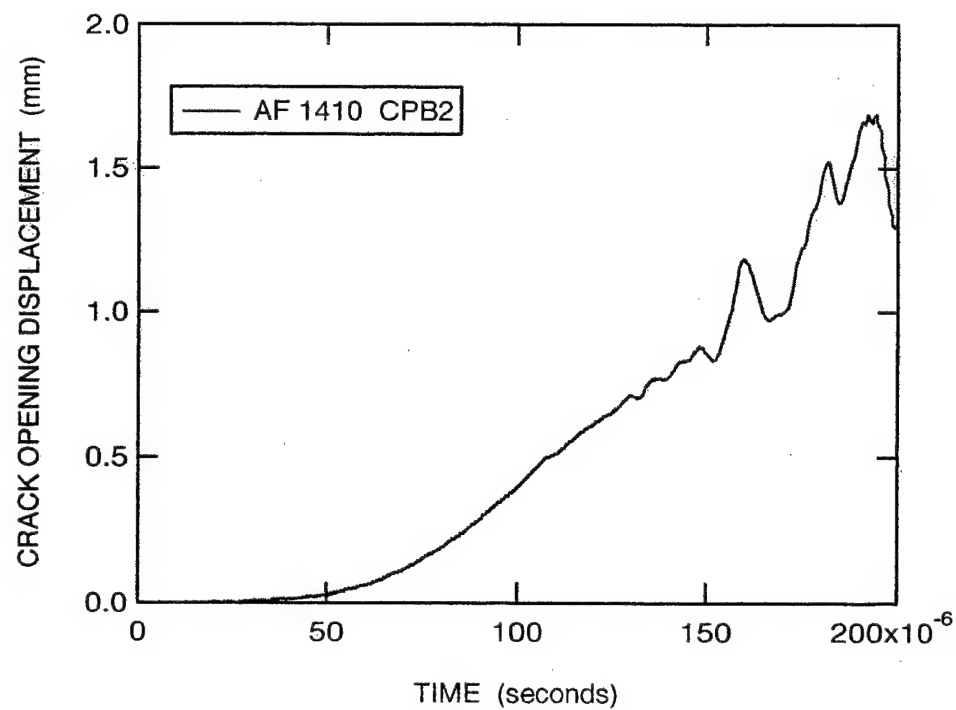


Figure A34. Reduced Crack Opening Displacement Data for AF 1410 Specimen CPB2.

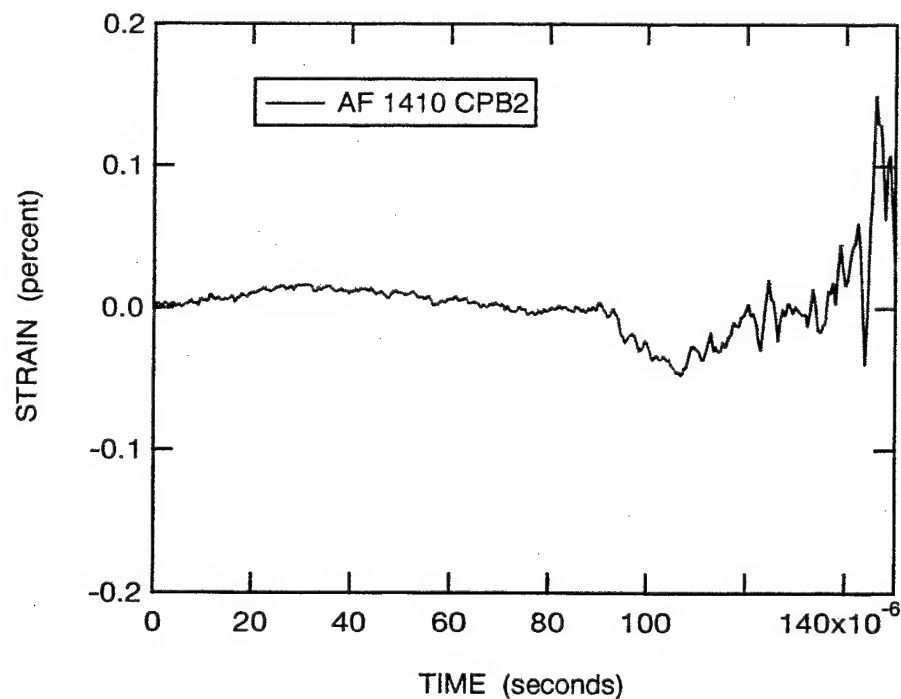


Figure A35. Reduced Strain Data for AF 1410 Specimen CPB2.

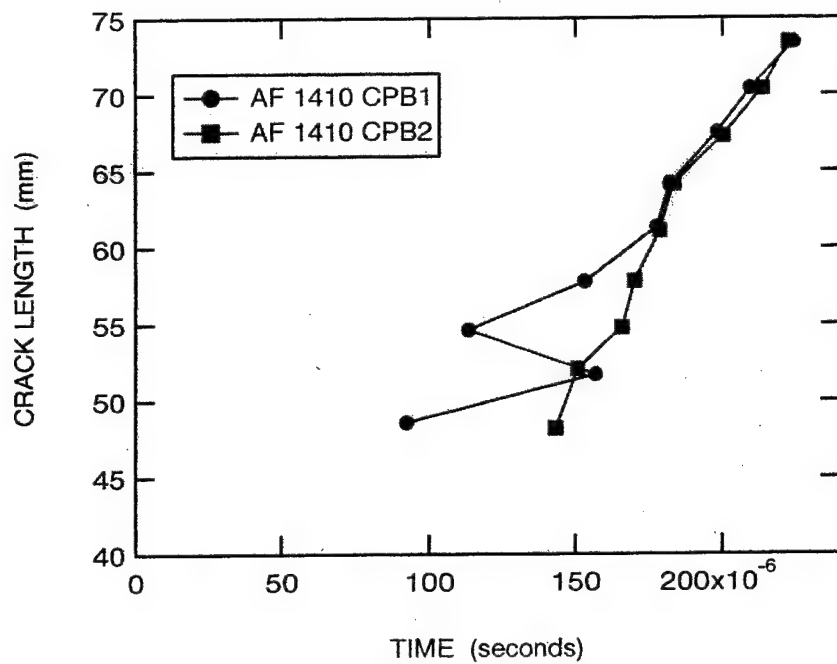


Figure A36. Reduced Crack Length-Time Histories of AF 1410 Specimens CPB1 and CPB2.

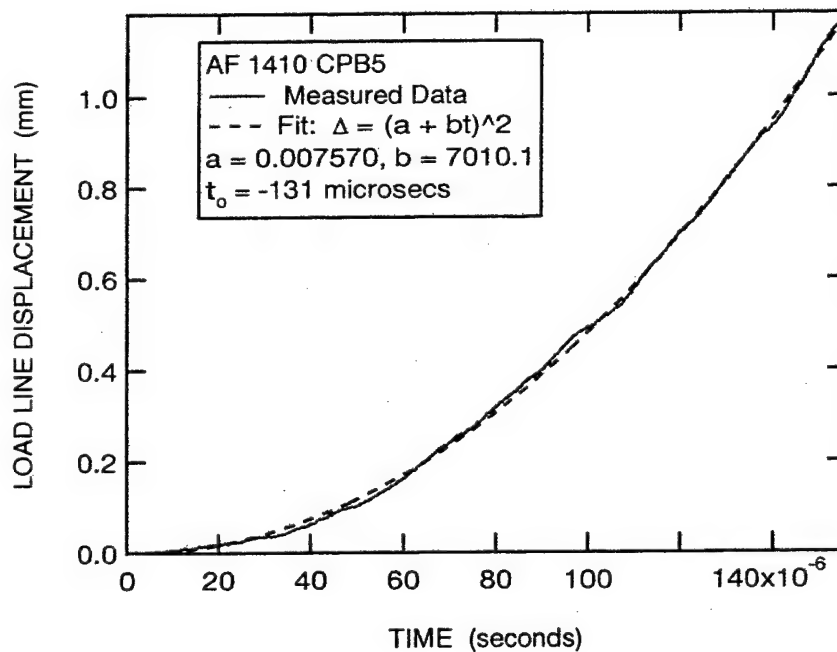


Figure A37. Reduced Load Displacement Data for AF 1410 Specimen CPB5.

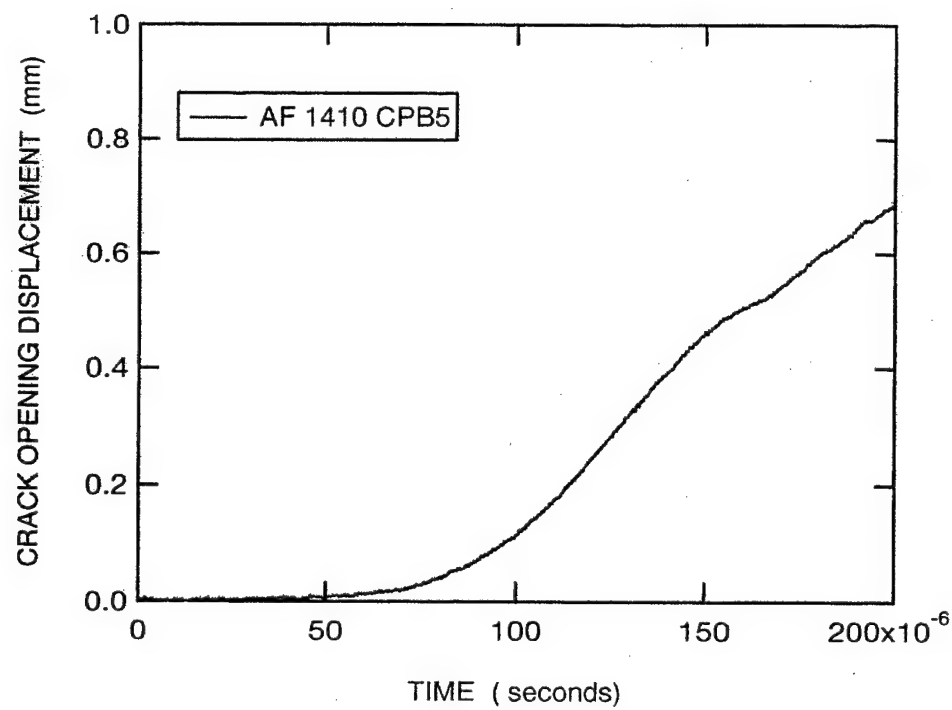


Figure A38. Reduced Crack Opening Displacement Data for AF 1410 Specimen CPB5.

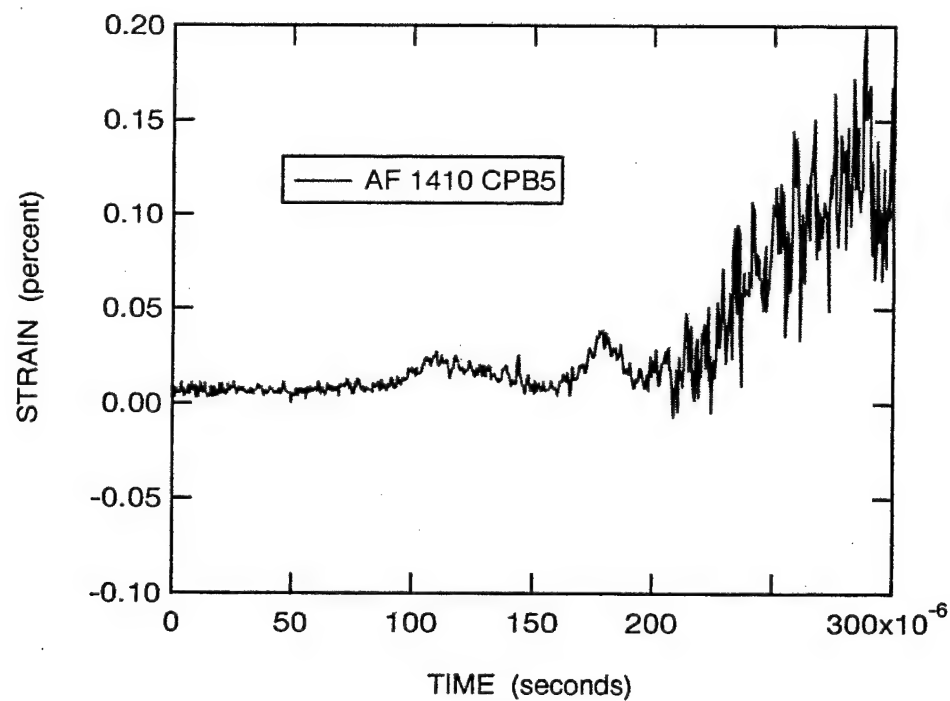


Figure A39. Reduced Strain Data for AF 1410 Specimen CPB5.

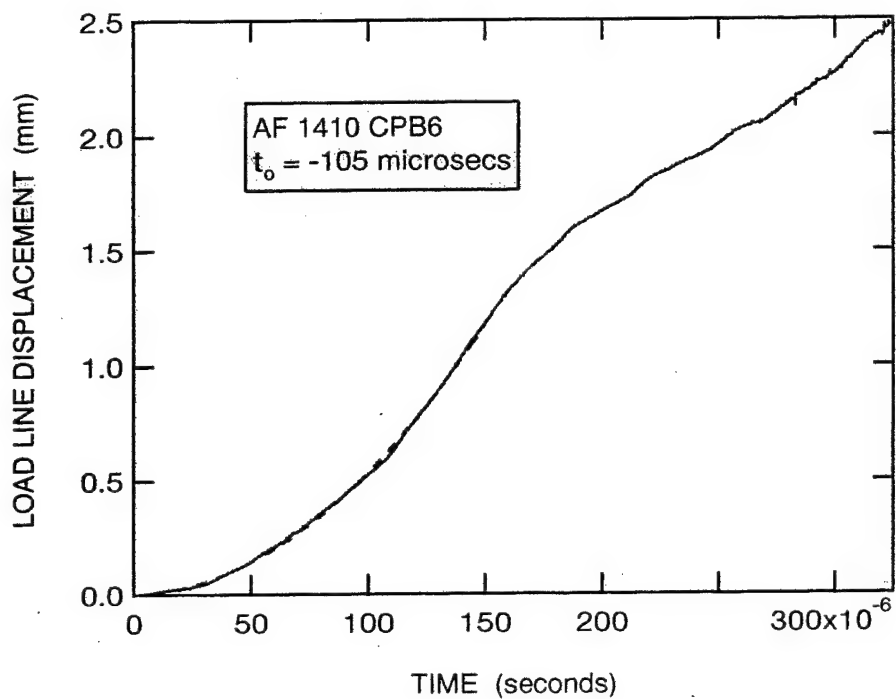


Figure A40. Reduced Load Line Displacement Data for AF 1410 Specimen CPB6.

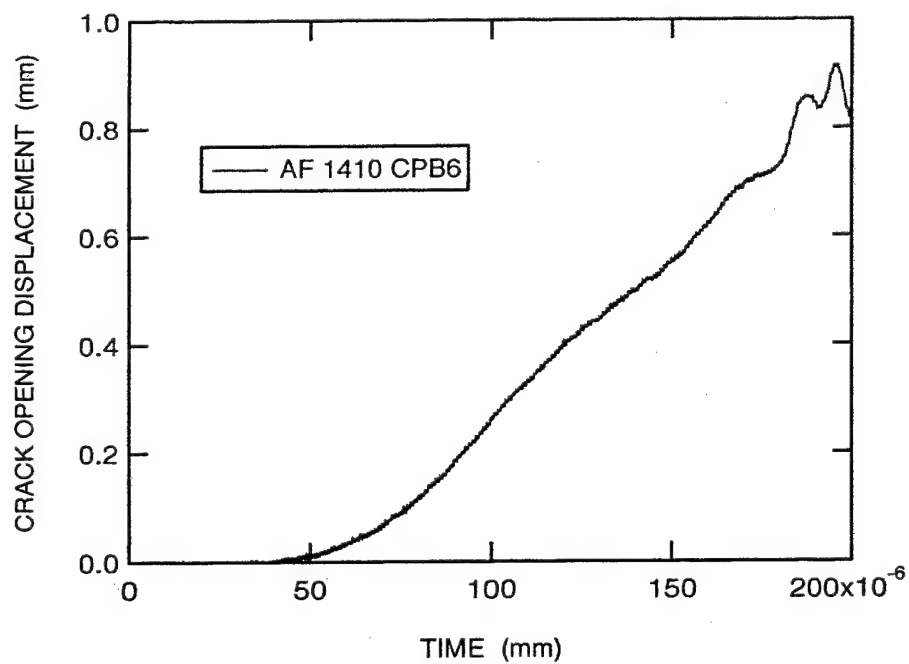


Figure A41. Reduced Crack Opening Displacement Data for AF 1410 Specimen CPB6.

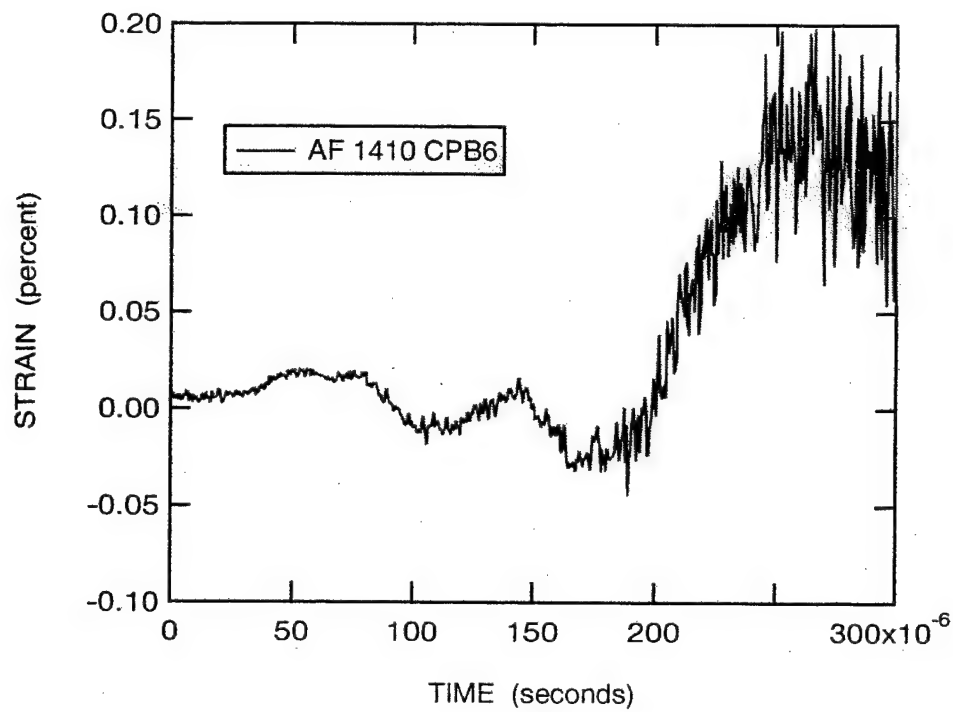


Figure A42. Reduced Strain Data for AF 1410 Specimen CPB6.

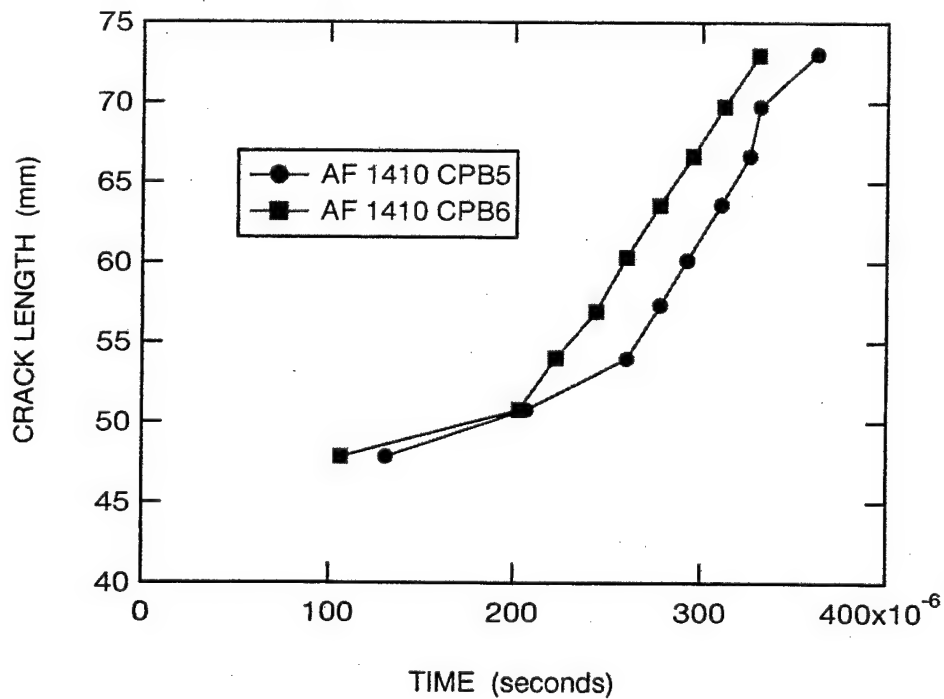


Figure A43. Reduced Crack Length-Time Histories of AF 1410 Specimens CPB5 and CPB6.

APPENDIX B

APPLICATION PHASE EXPERIMENTAL DATA

FOR AISI 4340 STEEL

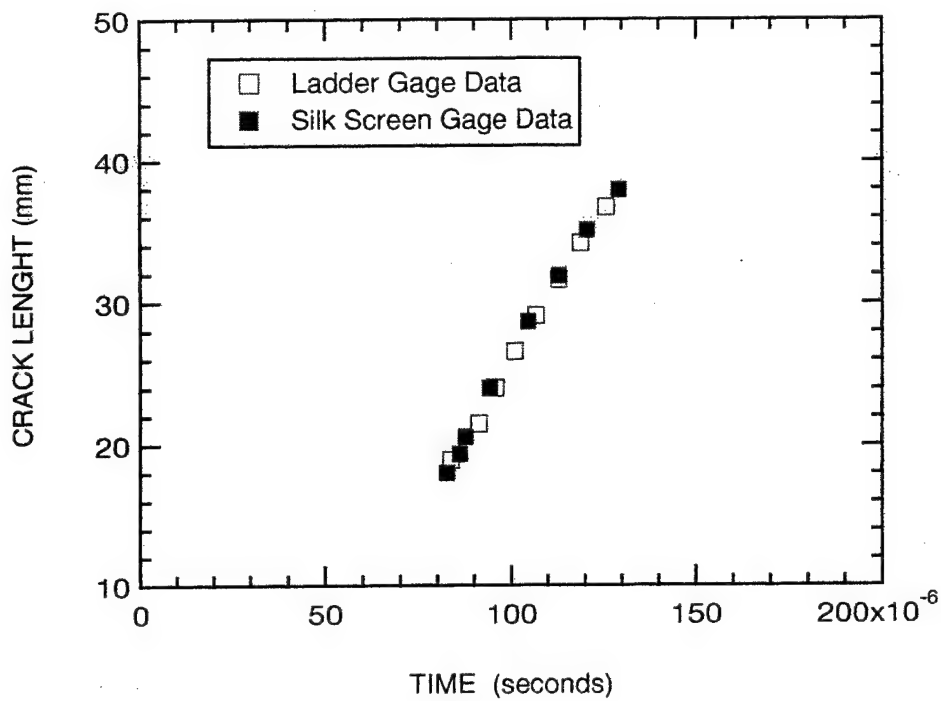


Figure B1. Measured Crack Length History for Specimen 1.

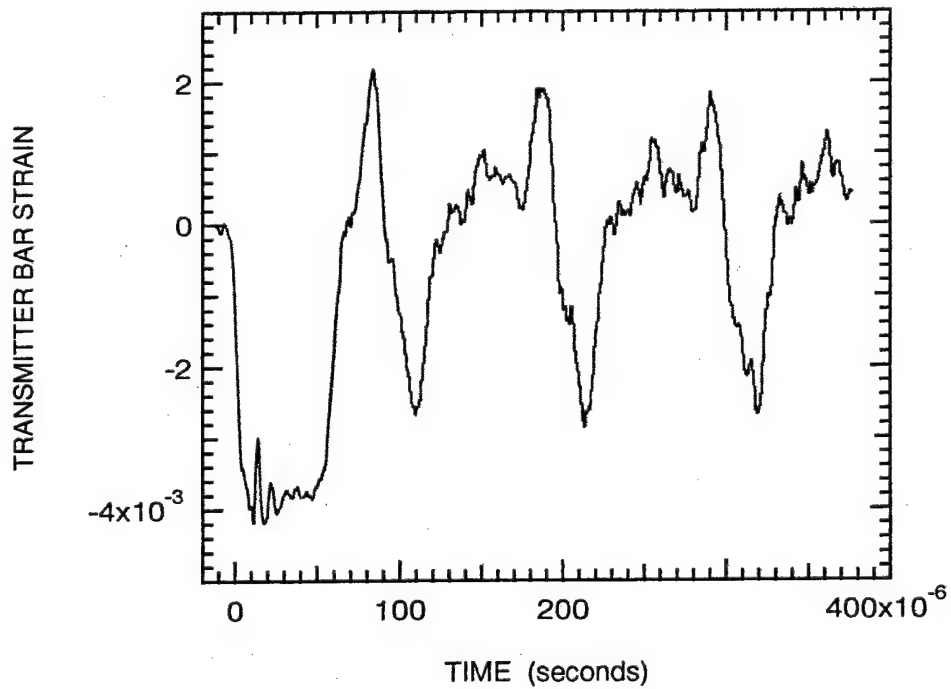


Figure B2. Measured Transmitter Bar Strain for Specimen 1.

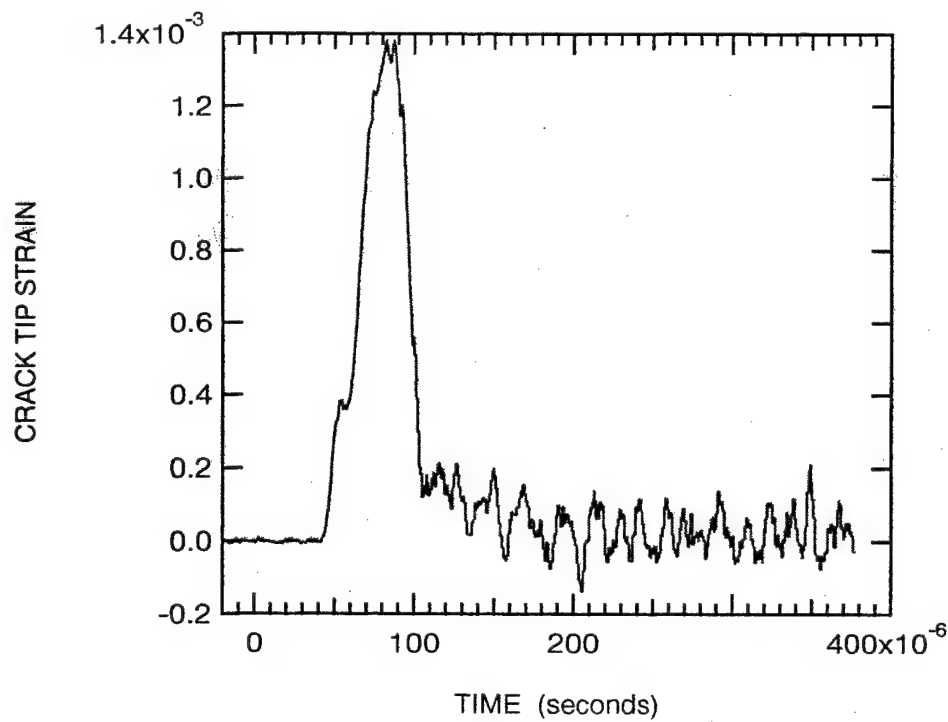


Figure B3. Measured Crack Tip Strain for Specimen 1.

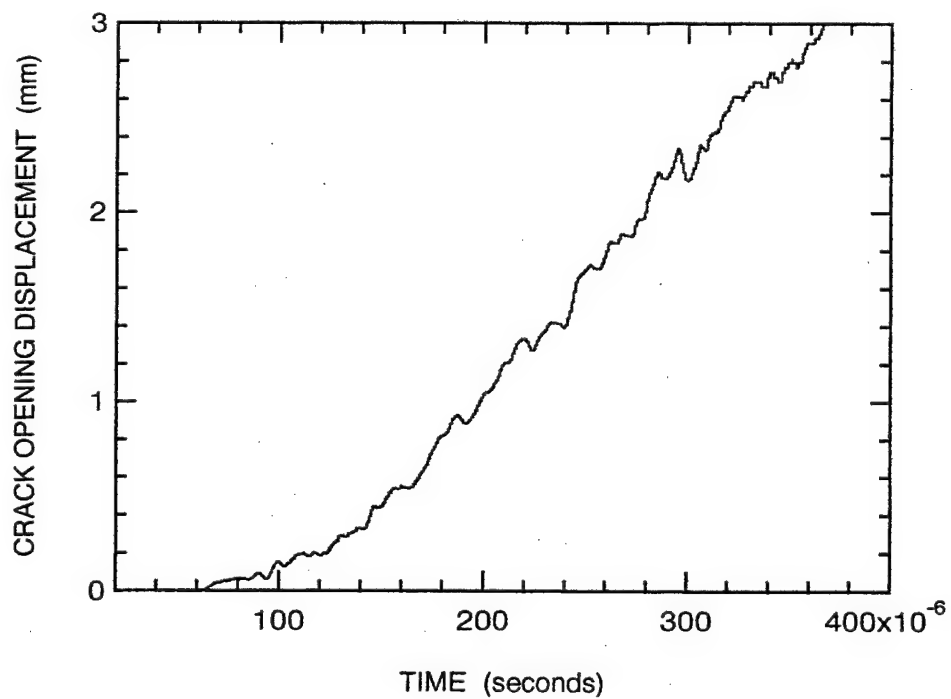


Figure B4. Measured Crack Opening Displacement for Specimen 1.

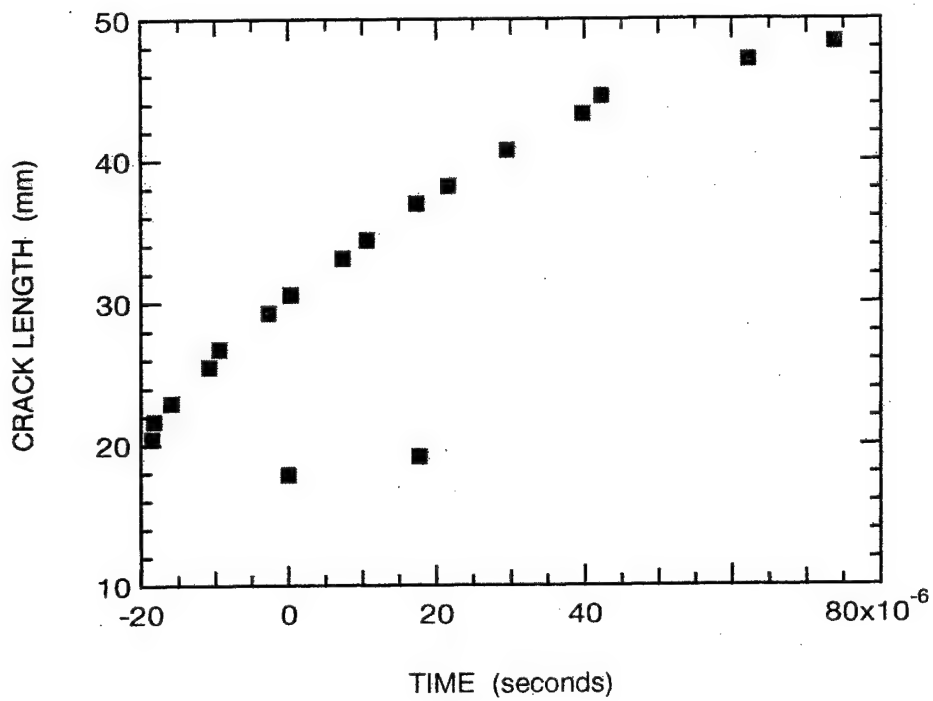


Figure B5. Measured Crack Length History for Specimen 3.

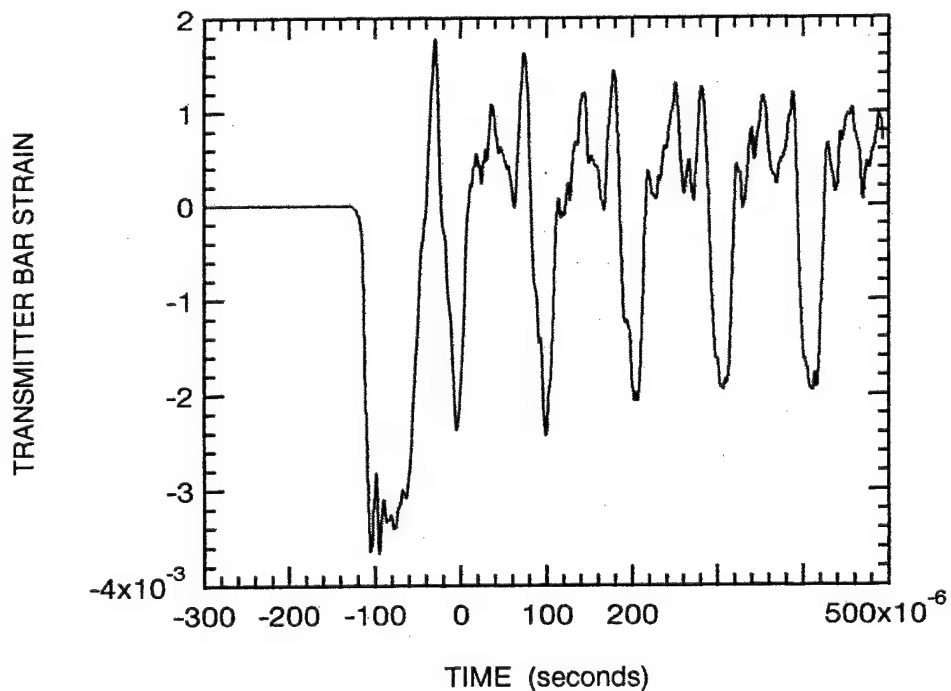


Figure B6. Measured Transmitter Bar Strain for Specimen 3.

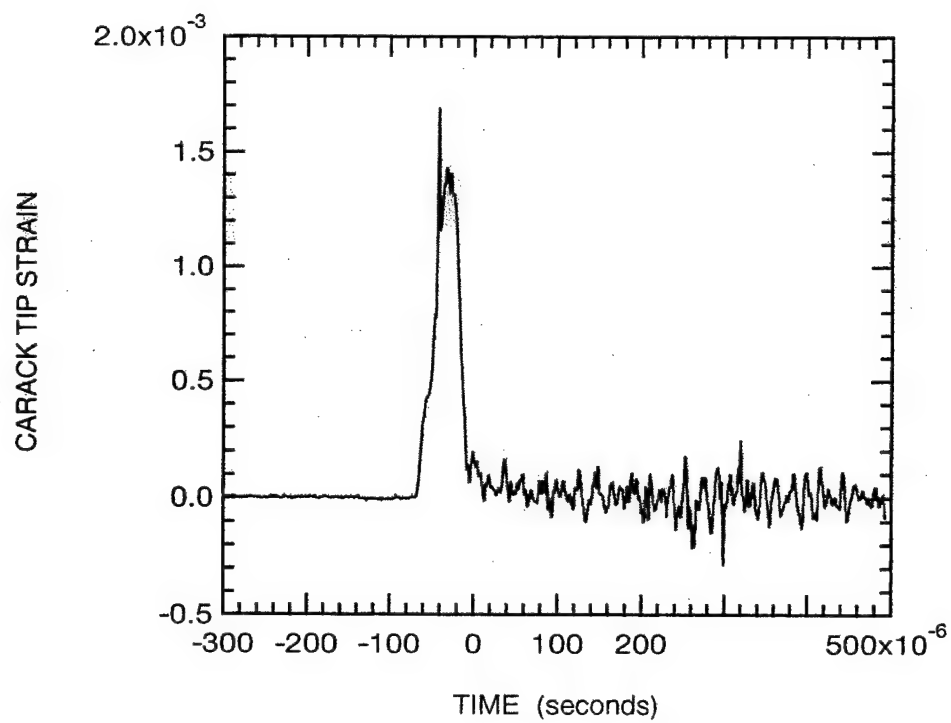


Figure B7. Measured Crack Tip Strain for Specimen 3.

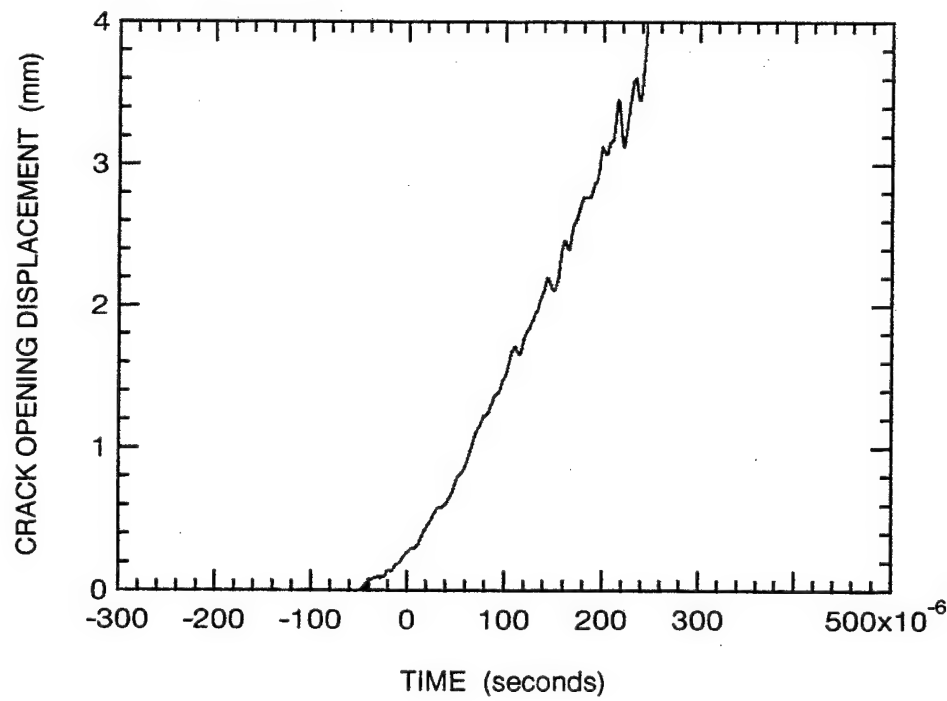


Figure B8. Measured Crack Opening Displacement for Specimen 3.

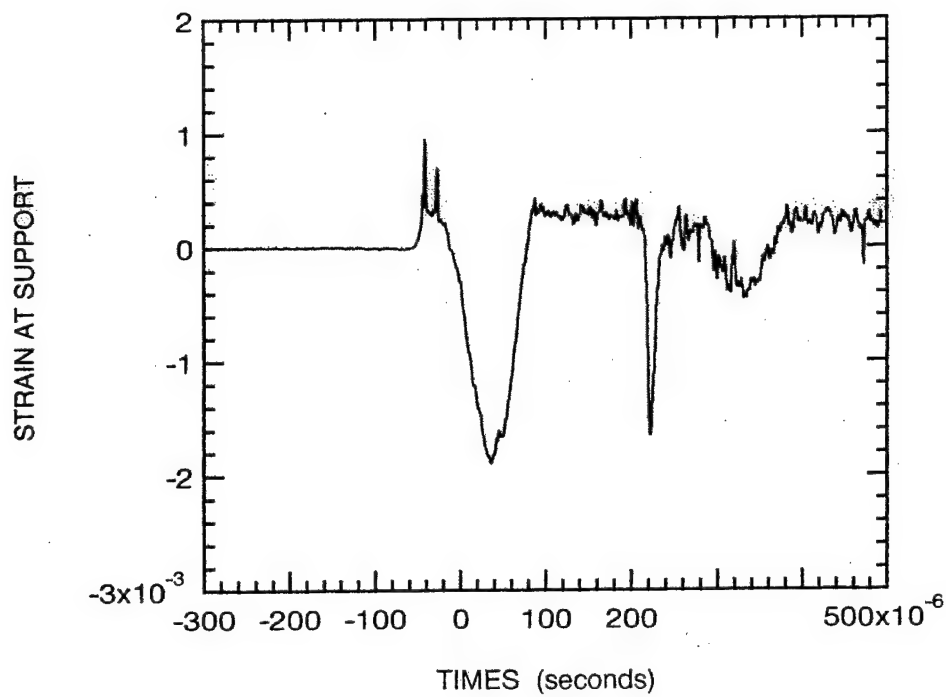


Figure B9. Measured Strain at Support for Specimen 3.

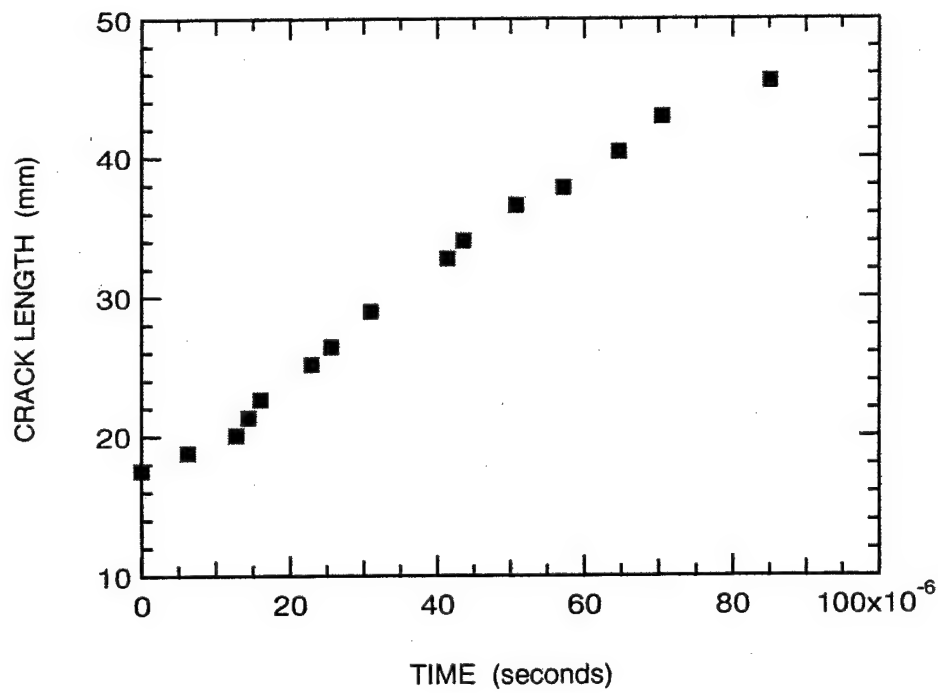


Figure B10. Measured Crack Length History for Specimen 4.

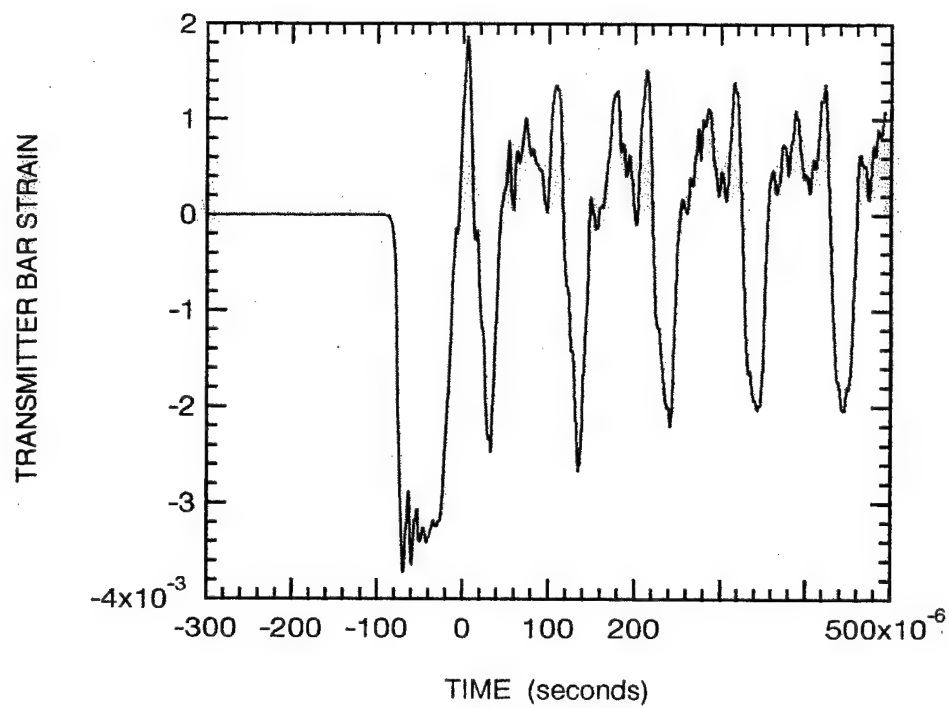


Figure B11. Measured Transmitter Bar Strain for Specimen 4.

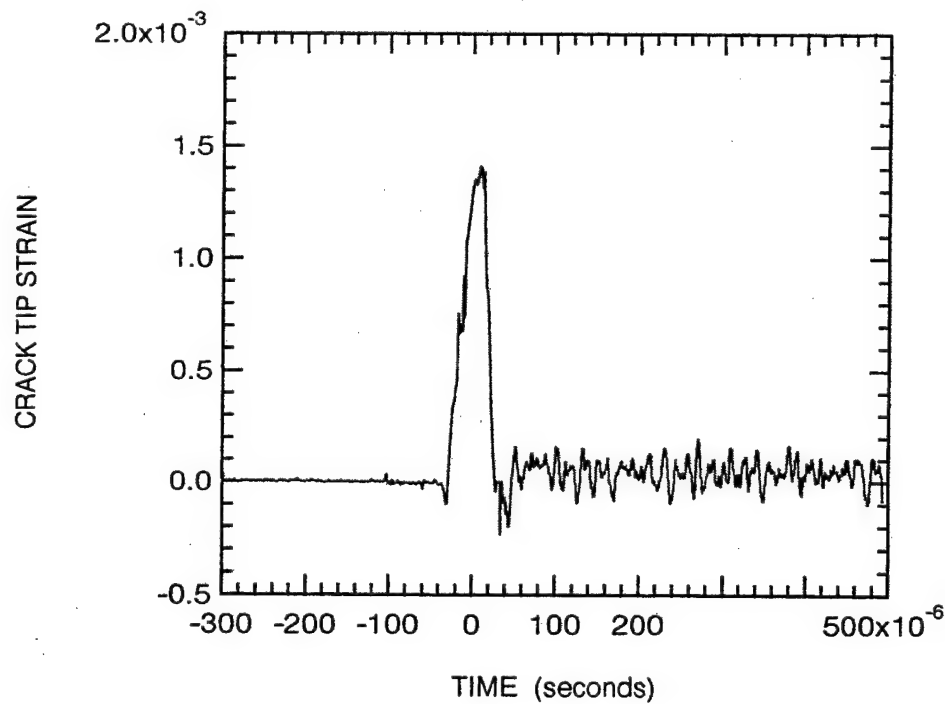


Figure B12. Measured Crack Tip Strain for Specimen 4.

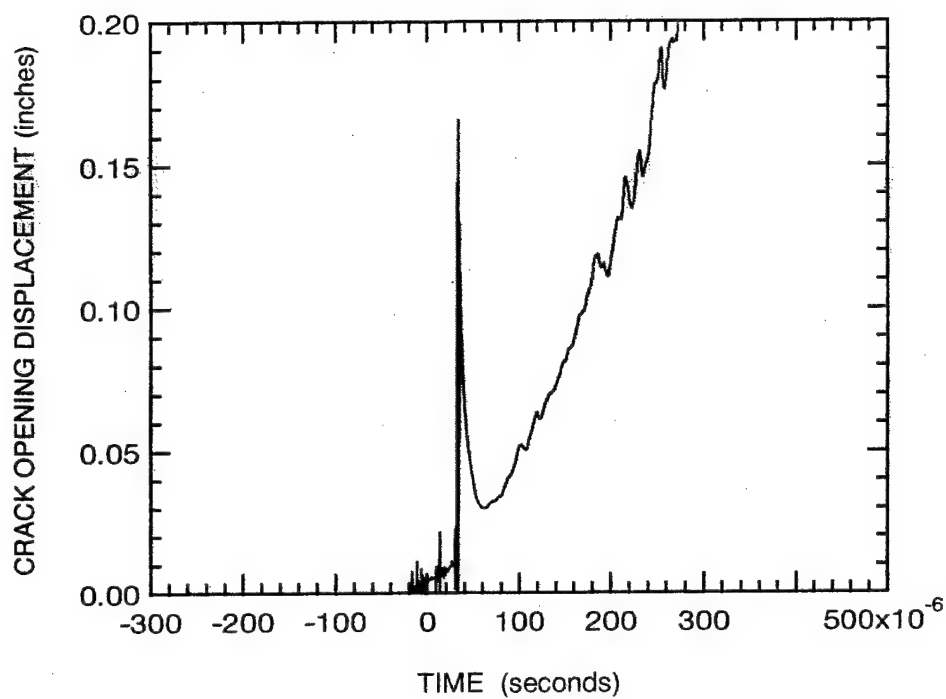


Figure B13. Measured Crack Opening Displacement for Specimen 4.

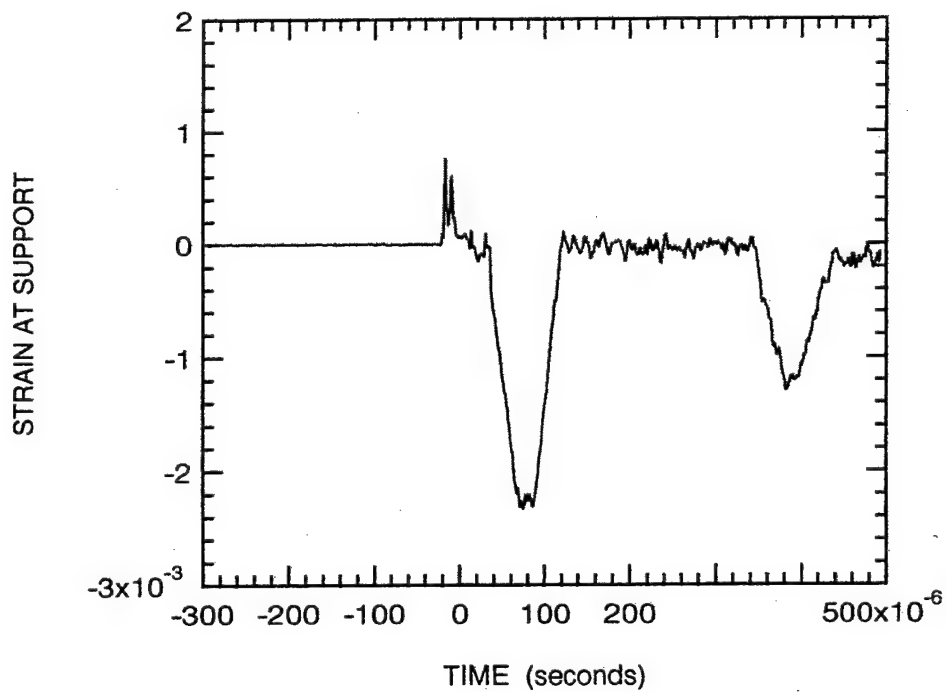


Figure B14. Measured Strain at Support for Specimen 4.

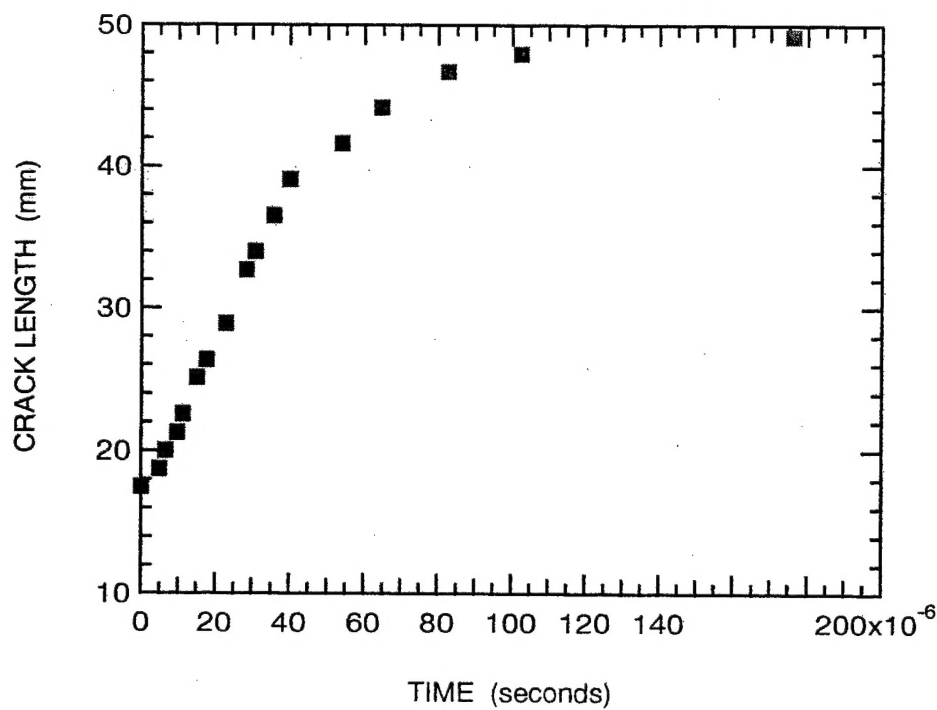


Figure B15. Measured Crack Length History for Specimen 5.

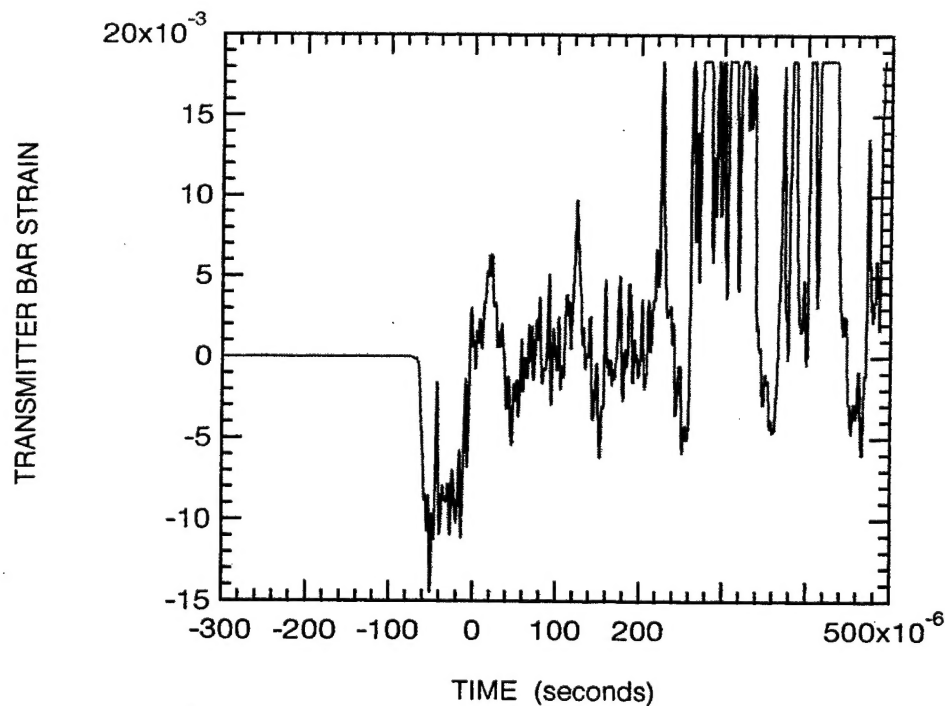


Figure B16. Measured Transmitter Bar Strain for Specimen 5.

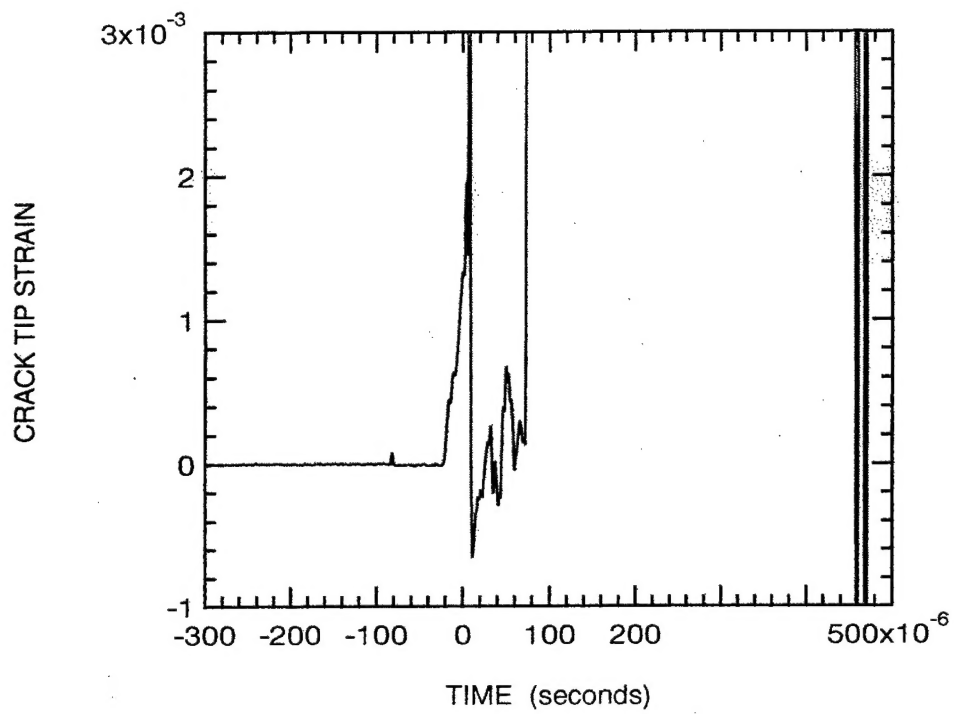


Figure B17. Measured Crack Tip Strain for Specimen 5.

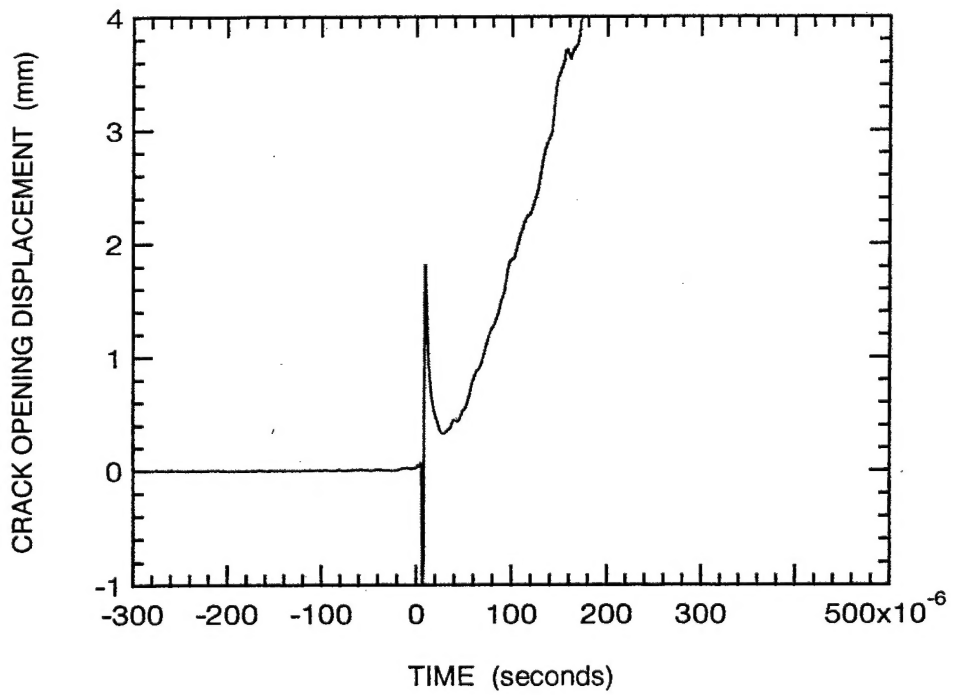


Figure B18. Measured Crack Opening Displacement for Specimen 5.

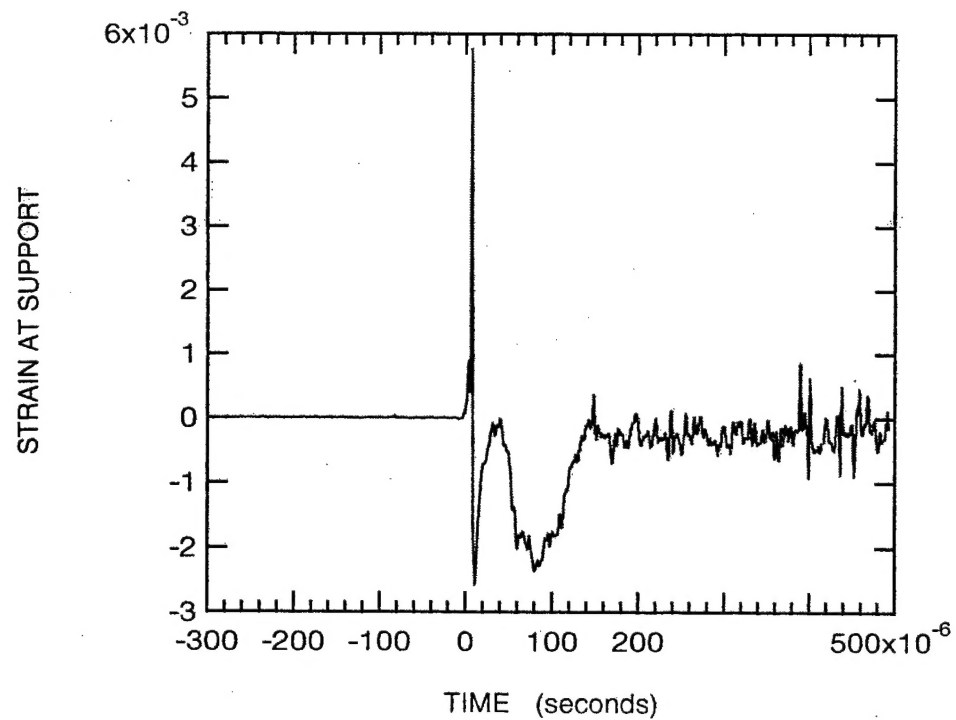


Figure B19. Measured Strain at Support for Specimen 5.

DISTRIBUTION LIST
AFRL-MN-EG-TR-1999-7054

Defense Technical Information Center 1
8725 John J. Kingman Road, Ste 0944
Ft Belvoir, VA 22060-6218

Southwest Research Institute 3
Attn: Dr. C. E. Anderson
P. O. Drawer 28510
San Antonio, TX 78228-0510

Alliant Techsystems, Inc. 2
Attn: Dr. G. R. Johnson
600 Second Street N. E.
Hopkins, MN 55343

EGLIN AFB OFFICES:

AFRL/CA-N	1
AFRL/MNOC-1 (Tech Library)	1
AFRL/MNA	1
AFRL/MNAC (Dr. Cook)	5
AFRL/MNAC (Dr. Belk)	1
AFRL/MNAC (Dr. Lijewski)	1
AFRL/MNMW (Dr. Dilmore)	1